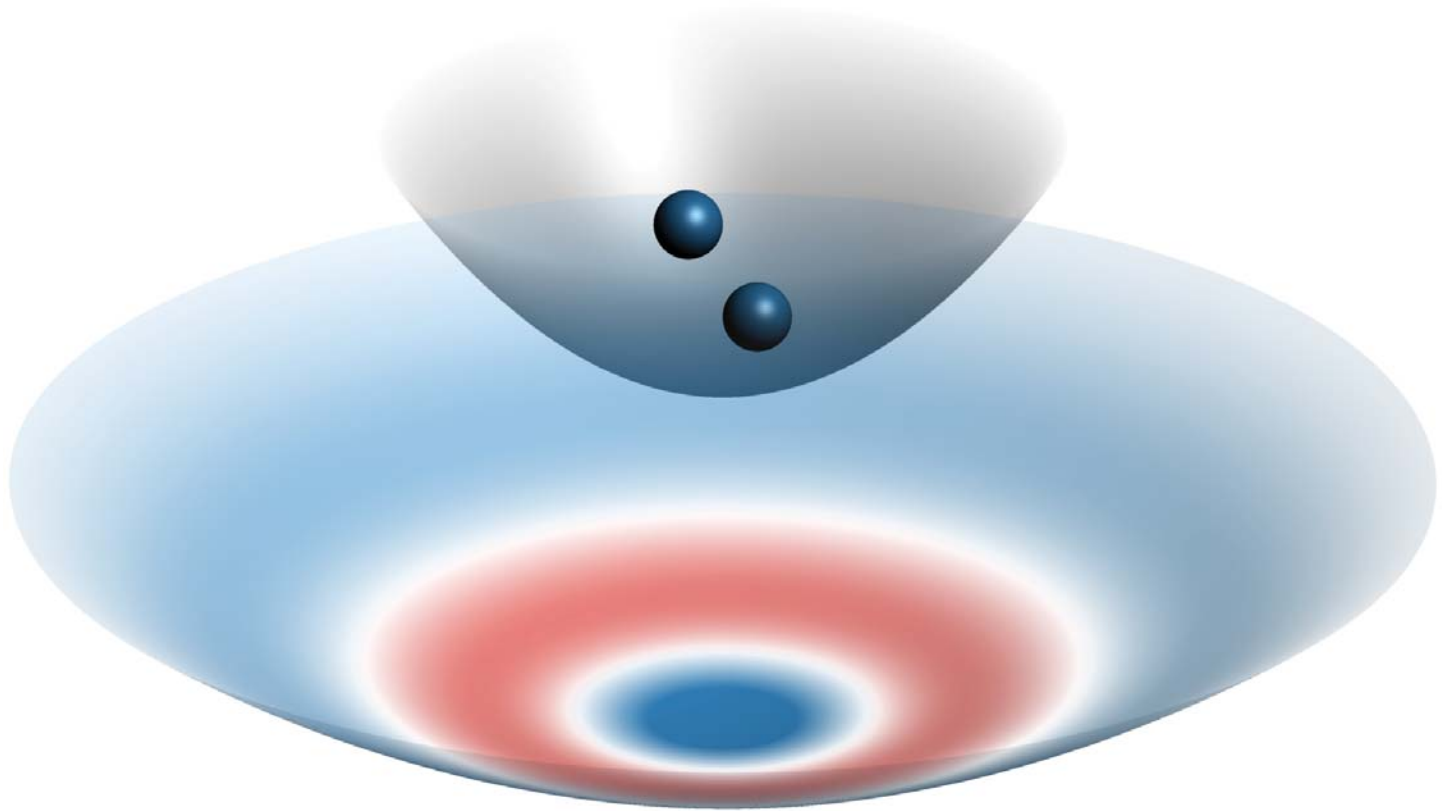


TUNNELING IONIZATION OF DIATOMIC MOLECULES



JENS SVENSMARK
PHD DISSERTATION

Colophon

Tunneling Ionization of Diatomic Molecules

PhD thesis by Jens Svensmark.

The manuscript was typeset using \LaTeX (memoir class). All figures were made using gnuplot (cairolatex terminal) or asymptote.

PDF version

TUNNELING IONIZATION OF
DIATOMIC MOLECULES

JENS SVENSMARK
PHD DISSERTATION
JULY 2016

SUPERVISOR: LARS BOJER MADSEN
CO-SUPERVISOR: OLEG I. TOLSTIKHIN

DEPARTMENT OF PHYSICS AND ASTRONOMY
AARHUS UNIVERSITY

Summary

When a molecule is subject to a strong laser field, there is a probability that an electron can escape, even though the electrons are bound by a large potential barrier. This is possible because electrons are quantum mechanical in nature, and they are therefore able to tunnel through potential barriers, an ability classical particles do not possess. Tunnelling is a fundamental quantum mechanical process, a process that is distinctly non-classical, so solving this tunnelling problem is not only relevant for molecular physics, but also for quantum theory in general.

In this dissertation the theory of tunneling ionization of molecules is presented and the results of numerical calculations are shown. One perhaps surprising result is, that the frequently used Born-Oppenheimer approximation breaks down for weak fields when describing tunneling ionization. An analytic theory applicable in the weak-field limit which supplements the Born-Oppenheimer approximation is also presented.

Dansk resumé

Når et molekyle bliver udsat for et stærkt laser felt, er der en sandsynlighed for at en elektron kan undslippe, også selvom elektronerne er bundet af en stor potentialbarriere. Dette er muligt fordi elektroner er kvantemekaniske af natur, og de er derfor i stand til at tunnelere igennem potentialbarrierer, en evne som klassiske partikler ikke besidder. Tunnelering er en grundlæggende kvantemekanisk proces, en proces som utvetydigt er ikke-klassisk, så løsning af dette tunneleringsproblem er ikke kun relevant for molekylfysik, men også for kvanteteori generelt.

I denne afhandling vil teorien for tunnelionisering blive præsenteret og resultaterne af numeriske beregninger vises. Et muligvis overraskende resultat er, at den hyppigt anvendte Born-Oppenheimer approksimation bryder sammen for svage felter i beskrivelsen af tunnelionisation. En analytisk teori som kan anvendes i svag-felts grænsen til at supplementere Born-Oppenheimer approksimationen præsenteres også.

Preface

This thesis summarizes work done during my PhD at the Department of Physics and Astronomy, Aarhus University from August 2012 to July 2016. The PhD was supported by the ERC-StG (Project No. 277767-TDMET).

Units

Atomic units (a.u.) $\hbar = m_e = e = 1$ are used throughout this thesis, unless otherwise stated.

Acknowledgements

First, I would like to thank my supervisor Lars for making this all of this possible, and for his ideas and help with the project. I would also like to thank my co-supervisor Oleg, whose technical and physical insights and attention to detail was essential for the success of the project.

For the past 4 years I have shared an office with my alter-ego, Jens E. Bækthøj, whom I would like to thank for 4 years of more or less fruitful discussions on physics and various other subjects, and for proofreading this thesis. Andrew C. J. Wade, Lun Yue, Christian K. Andersen and Jørgen Rørstad I would also like to thank for equally diverse and fruitful discussions.

A special thanks goes to our group secretary Grete Flarup, for assistance with navigating the bureaucracy of Aarhus University.

List of publications

- [1] J. Svensmark, O. I. Tolstikhin, and L. B. Madsen, *Coulomb and dipole effects in tunneling ionization of molecules including nuclear motion*, Phys. Rev. A **91**, 013408, Jan 2015.

- [2] J. Svensmark, O. I. Tolstikhin, and L. B. Madsen, *Theory of dissociative tunneling ionization*, Phys. Rev. A **93**, 053426, May 2016.

List of abbreviations

- a.u.** Atomic unit(s)
- BO** Born-Oppenheimer
- CTP** Coulomb tail potential
- DVR** Discrete-variable representation
- FRP** Finite range potential
- HHG** High-harmonic generation
- KER** Kinetic energy release
- SAEA** Single-active-electron approximation
- SCP** Soft-core Coulomb potential
- SS** Siegert State
- SVD** Slow variable discretization (not to be confused with singular value decomposition, which is not used in this thesis)
- TDSE** Time-dependent Schrödinger equation
- TISE** Time-independent Schrödinger equation
- WFAT** Weak-field asymptotic theory

Contents

1	Introduction	1
1.1	Outline of the Thesis	5
2	Siegert States	6
2.1	Tunneling Potential	12
2.2	Summary	14
3	Three-Body Coordinates	15
3.1	Center-of-Mass Coordinates	15
3.2	Jacobi (Relative) Coordinates	17
4	Tunneling Ionization of Molecules	21
4.1	Simple Picture of Tunneling Ionization	21
4.2	Formal Theory	22
4.3	Weak-Field Asymptotic Theory	28
4.4	Born-Oppenheimer Approximation	35
5	Tunneling Ionization of Molecules in 3D	44
5.1	Formal Theory	44
5.2	Weak-Field Asymptotic Theory	50
5.3	Born-Oppenheimer Approximation	56
5.4	One and Three Dimensions Compared	58
6	Numerical Methods	60
6.1	Reduction to a Multi-Channel Eigenvalue Problem	60
6.2	Spatial Basis: Discrete Variable Representation	61
6.3	Slow Variable Discretization	74
6.4	R-Matrix	78
6.5	Complex Rotation	83
7	Bound Ionic States	88

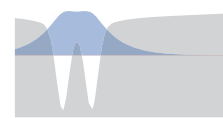
7.1	Model Potentials	88
7.2	Results	90
7.3	Conclusion	107
8	Dissociative Tunneling Ionization	109
8.1	Illustrative 1D Calculations	109
8.2	Conclusion	123
9	Dissociation and Bound Ionic States	124
9.1	H_2^+ Morse and CTP Potentials (M1)	124
9.2	SCP Model (M2)	131
9.3	Another SCP (M3)	132
A	Asymptotic Expansion	144
A.1	The $c_4 = 0$ Case	144
A.2	The $c_4 \neq 0$ Case	146
B	WKB Approximation	149
C	Reflection Approximation	151
D	Continuum Normalization	156
E	Soft-coulomb Potential	158
	Bibliography	160

1 Introduction

Molecules are the building blocks of which most things are built. How these molecules are formed and broken is studied in the discipline of chemistry. This discipline has evolved over many years, from alchemists failing at producing gold to today, where it is probably difficult to imagine a modern society without fertilizers, plastics, medicine and the countless other applications of chemistry. Chemistry affords a good description of both the reactants entering a chemical reaction, and the products that result from it. The details of the dynamics that take place during a chemical reaction is, however, not something that traditional chemistry can describe in detail. These details are typically not that important, since the reactions happen extremely fast, faster than other process we could possible compare them with, so we are not able to see those details anyways. Developing an intuition based on empirical observations as to which products will result from a given reaction has been enough to drive the development of chemistry into a field of science that is now essential for the modern society.

In recent years laser technology has advanced tremendously [3], and it is today possible to generate intense laser pulses in the femtosecond ($\text{fs}=10^{-15}\text{s}$) range. These laser pulses are so fast that their duration is comparable to the speed at which chemical reactions occur. This makes it possible to interfere with a chemical reaction as it happens and thereby control it. The implications of this could be considerable, as control of chemical processes could make it possible to create molecules that is otherwise impossible or very difficult to make. The femtosecond laser pulses not only have a very short duration, they are also very strong, with field-strengths comparable with the Coulomb field that binds the electrons to the nuclei, so the study of the interaction of these pulses with molecules has been dubbed strong-field physics.

When an atom or a molecule is subjected to a femtosecond laser pulse it can, under the right circumstances, produce an even shorter light pulse,

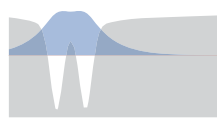


one whose length should be measured in attoseconds ($as=10^{-18}$ s) rather than femtoseconds. The production of these very short light pulses rely on the process of high-harmonic generation (HHG) [4], which is a highly non-linear process in which an atom or a molecule that is subjected to a femtosecond laser pulse emit radiation of a much higher frequency than that of the original femtosecond pulse.

The HHG process can be simply understood on the basis of the semi-classical three-step model [5]. Here the interaction between the femtosecond laser and the molecule is partitioned in the following three steps. First, an electron is tunnel ionized and leaves the molecule. Second, after the electron has left the molecule, it is accelerated freely in the electric field of the laser, and is eventually led back to the molecule from which it came, but now with additional kinetic energy, which it received from acceleration in the laser field. Third, the electron collides with the molecule. A number of things can happen in this collision. One possibility is that the electron simply scatters off the molecule and flies away. Another is that the electron recombines with the molecule, and the excess kinetic energy of the electron is emitted as a photon. The latter of these is what gives HHG.

The first step in the three-step model is the tunneling ionization of an electron. It is, however, not in all situations where an electron is ionized that one can think of it as tunneling ionization. Tunneling occurs when the field is slowly varying, that is when it has a small frequency, but is simultaneously very strong. To see this, we first note that the time it takes for the electron to tunnel, to the extent that the concept of such a time makes sense, can be estimated in a classical way as follows. The distance the electron has to travel under the barrier is roughly given by $z = I_p/F$, where I_p is the ionization potential of the molecule and F is the electric field strength of the laser. If we assume that the electron moves at the velocity $v = \sqrt{2I_p}$, then the time it takes for the electron to tunnel is $T_{\text{tunnel}} = (I_p/F)/v = v/(2F)$. The laser field oscillate at the angular frequency ω , so the inverse $T_{\text{Laser}} = 1/\omega$ gives a time over which the laser field changes appreciably. The ratio of these two is called the Keldysh parameter [6] and is given by¹ $\gamma = 2T_{\text{tunnel}}/T_{\text{Laser}} = v\omega/F$. When this is a lot larger than 1 it takes more time for the electron to tunnel than it takes for the laser to change direction of its field, and we would not expect the tunneling picture to give a good description of the ionization process.

¹The factor of 2 is purely conventional, and not terribly important, since this is an order of magnitude estimate anyways.



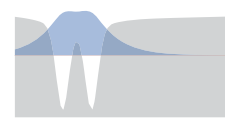
Conversely, if the Keldysh parameter is a lot smaller than 1 the tunneling picture should be accurate.

In addition to the use of tunneling theory in describing the HHG process, tunneling ionization itself is a fundamental process, and the study of it in its own right is interesting. Tunneling is a fundamental concept of quantum mechanics, one that is almost unavoidably taught in introductory quantum mechanics courses. The reason for this is probably that tunneling is a truly quantum mechanical phenomenon, a place in which quantum mechanics is set apart from classical theory, which can often be used to describe quantum results quite well. However, even though most physicists have been introduced to the concept of tunneling, the very technical nature of stationary tunneling states, and the complicated behaviour of a time-dependent tunneling process, mean that few people have seen detailed examples of tunneling beyond Dirac delta and other simple potentials. Other than such potentials, tunneling is considered mostly at a phenomenological level.

In this thesis we consider what happens when a molecule is subject to a constant electric field. In such a field a potential barrier forms, through which the electron can tunnel. We solve the time-independent Schrödinger equation (TISE). Since we only want to consider electrons leaving the molecule we impose outgoing-wave boundary conditions. The solutions to the TISE that fulfill this outgoing-wave boundary condition are called Siegert states (SS) [7–9]. Chapter 2 contains an introduction to these states.

The interaction between the nuclei and electrons in molecules are mediated by the electric Coulomb force, and the forces act in the same manner, and with the same strength, on the nuclei and the electrons. The masses of the nuclei and the electrons are, however, vastly different. The minimal ratio of masses is found in hydrogen, where the proton/electron mass ratio is 1836. The large difference between the electron and nuclei masses mean that we can treat each type of particle differently. In atomic systems the nuclei is considered as a point charge, whose position is almost unchanged by how the electrons move. The centre-of-mass motion of the whole atom almost² coincides with that of the nucleus, and this motion we transform away in the beginning of most treatments anyways.

²In fact, for hydrogenic atoms where there is only 1 electron, the problem exactly separates into a center-of-mass and a relative coordinate problem, and the nuclear mass do not alter the analytic form of any results, and only enters in the reduced mass. For multi-electron systems there are mass-polarization terms that somewhat complicates this story.



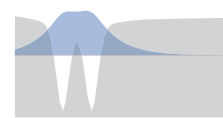
For molecules the situation is rather different, since even after we transform away the center-of-mass motion, at least one relative nucleus-nucleus degree of freedom remains. The difference of the masses for the nuclear and electronic degrees of freedom means that treating such a system numerically is fraught with peril, as anyone who ever tried to integrate stiff differential equations would know. But, the large mass difference also provides us with opportunities for simplifying the treatment of molecules, both on a numerical and on an interpretive level. Almost ubiquitous with molecular physics is the Born-Oppenheimer approximation. This approximation appears formally in the limit of infinite nuclear mass, and in this limit the nuclear and electronic degrees of freedom partly decouple³, which allows for separate treatments of each.

The BO approximation is today used in almost whenever some treatment of molecules is given. This is so, because it is hugely successful at describing molecular systems. There are however cases where it breaks down. Well known examples include Rydberg systems and conical intersections. Perhaps less well known is that the BO approximation also breaks down for weak fields when describing tunneling ionization. This was shown in Ref. [10], where a physical explanation for this breakdown was also given [see also Sec. 4.4.4]. The present thesis is in fact an elaboration and extension of the theory presented in Ref. [10].

For describing the breakdown of BO we have chosen to adopt the single-active-electron approximation (SAEA). In this approximation, we assume that only one electron is active, and all other electrons are frozen. The active electron then interacts with the nuclei through an effective potential, which can for instance be obtained through a Hartree-Fock calculation, or chosen to have some specific analytic form. We can use this approximation because we are mainly interested in the interaction between the electrons and nuclei, and not the interaction between the electrons.

The present thesis contains a series of numerical studies of the tunneling ionization process of a molecule in a static electric field. Parts of the thesis is devoted to the detailed description of the numerical methods used to do this [Chap. 6 mainly]. The numerical studies should be supplemented by a sound analytic understanding of the tunneling ionization process, not only in the form of a thorough analytic formulation of the the-

³The full problem decouples to a nuclear and an electronic problem, where the electronic problem has a parametric dependence on the nuclear coordinate, and the solutions of the electronic problem act as an effective potential for the nuclear problem.



ory [which is done in Sec. 4.2], but also by extending the degree of analytic detail by considering certain limits. One such limit is the weak field limit, in which the so-called weak-field asymptotic theory (WFAT) [11, 12] has been developed. WFAT is an analytic framework for obtaining ionization rates in the weak-field limit. The rates obtained in the WFAT are expressed in terms of analytic expressions that depend solely on properties of the field-free states, so one does not need to solve the tunneling problem numerically in order to obtain the tunneling ionization rates. It is today a fairly routine task to determine field-free states of even quite complex molecules using the standard methods of quantum chemistry. Solving the tunneling ionization problem is, however, by no means standard in any larger systems (or in most small systems for that matter).

1.1 Outline of the Thesis

This thesis describes the theory of tunneling ionization of diatomic molecules, and numerical studies of this process. It is structured as follows:

Chapter 2 introduces Siegert states, since these are perhaps not well known to most readers.

Chapter 3 introduces the relative Jacobi coordinates that will be used in the remainder of the thesis, and derives the Hamiltonian in these coordinates.

Chapter 4 describes the theory of tunneling ionization with one electronic dimension, including the WFAT and BO approximations.

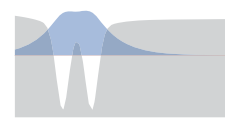
Chapter 5 describes the same tunneling ionization theory as chapter 4, only with three electronic dimension instead of one.

Chapter 6 introduces the numerical methods used in the calculations.

Chapter 7 presents and discusses numerical results for potentials that only allow for bound states of the molecular ion. The content of this chapter roughly corresponds to the content of Ref. [1].

Chapter 8 presents and discusses numerical results for potentials that only allow for continuum states of the molecular ion. The content of this chapter roughly corresponds to the content of Ref. [2].

Chapter 9 presents and discusses numerical results for potentials that allow for both bound and continuum states of the molecular ion.



2 Siegert States

In this thesis we consider solutions to the time-independent Schrödinger equation with outgoing-wave boundary conditions. These solutions are known as Siegert states (SS), and since the properties of these states are perhaps not well known, the SS will be illustrated with some simple examples in this chapter.

Let us consider the 1D time-independent Schrödinger equation (TISE)

$$(H - E)\psi(x) = 0, \quad (2.1)$$

with Hamiltonian

$$H = -\frac{1}{2m} \frac{d^2}{dx^2} + V(x), \quad (2.2)$$

and potential (see Fig. 2.1)

$$V(x) = \begin{cases} \infty & x < 0 \\ -V_0 & 0 < x < a \\ 0 & a < x \end{cases} \quad (2.3)$$

The general solution to this problem can be written in the form

$$\psi(x) = \begin{cases} Ae^{iqx} + Be^{-iqx} & 0 < x < a \\ Ce^{ikx} + De^{-ikx} & a < x, \end{cases} \quad (2.4)$$

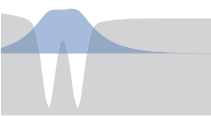
where

$$k = \sqrt{2mE}, \quad (2.5a)$$

$$q = \sqrt{2m(E + V_0)}. \quad (2.5b)$$

Since the potential is infinite at $x < 0$ we impose the boundary condition

$$\psi(0) = 0, \quad (2.6)$$



which implies $A = -B$. We further require that the wave function be continuous and continuously differentiable at $x = a$ which gives the conditions

$$A(e^{iqa} - e^{-iqa}) = Ce^{ika} + De^{-ika}, \quad (2.7a)$$

$$Aiq(e^{iqa} + e^{-iqa}) = ik(Ce^{ika} - De^{-ika}). \quad (2.7b)$$

Adding to these three conditions [Eqs. (2.6), (2.7)] a suitable normalization condition we have 4 conditions that specify the coefficients A, B, C and D . Nothing fixes the energy, which can take any value.

If we consider a bound state with $E < 0$ we require that it be regular, which gives the boundary condition

$$\psi(x)|_{x \rightarrow \infty} = 0. \quad (2.8)$$

In this case k is purely imaginary, and we choose to consider the square root branch such that $\text{Im } k > 0$. With this choice the boundary condition Eq. (2.8) implies that $D = 0$. This combined with Eqs. (2.7) leads to

$$ik \tan(qa) = q. \quad (2.9)$$

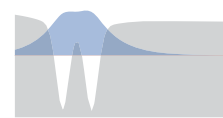
Together with Eqs. (2.5) this equation puts restrictions on the possible values of E . Because we imposed the additional boundary condition Eq. (2.8), only a discrete set of energies are allowed for $E < 0$. For $E > 0$ all energies are allowed, since here we have not imposed a fifth boundary condition. Figure 2.1(a) shows the wave function $\psi(x)$ of these discrete energy levels in the potential $V(x)$. The continuum states with $E > 0$ are also shown in this figure. A modulation of the continuum states along the direction of the energy axis is visible. The continuum states are normalized such that¹

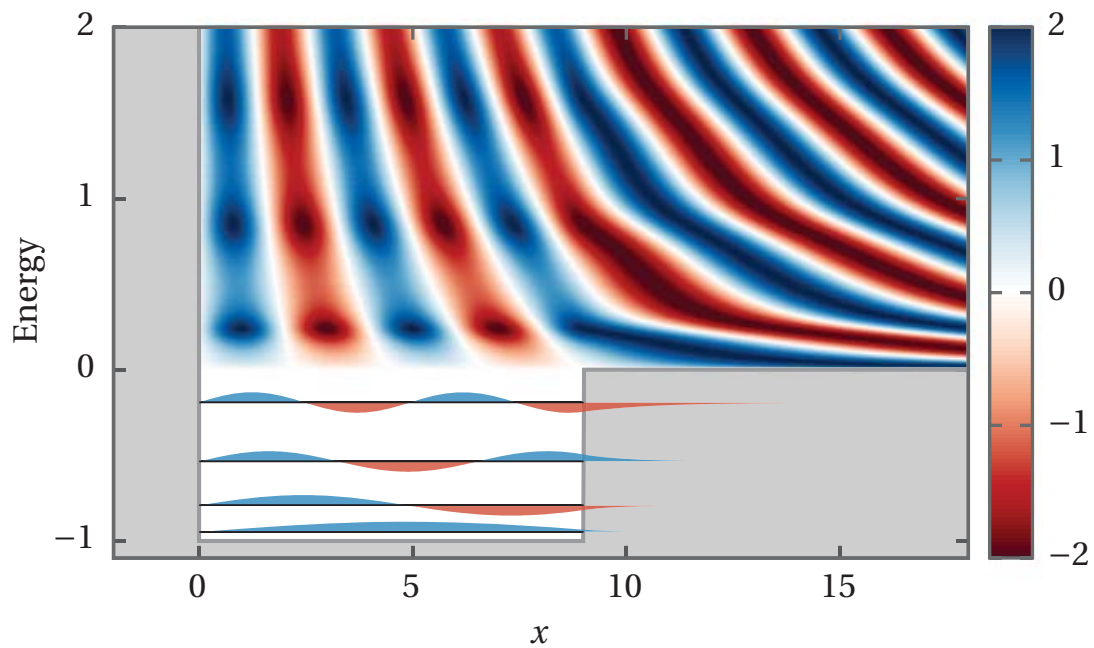
$$\psi(x)|_{x \rightarrow \infty} = 2 \sin(kx + \delta), \quad (2.10)$$

where δ is a free parameter. With this normalization the conditions that the wave function should be continuous and continuously differentiable in $x = a$ [Eqs. (2.7)] imply that the coefficient A is given by

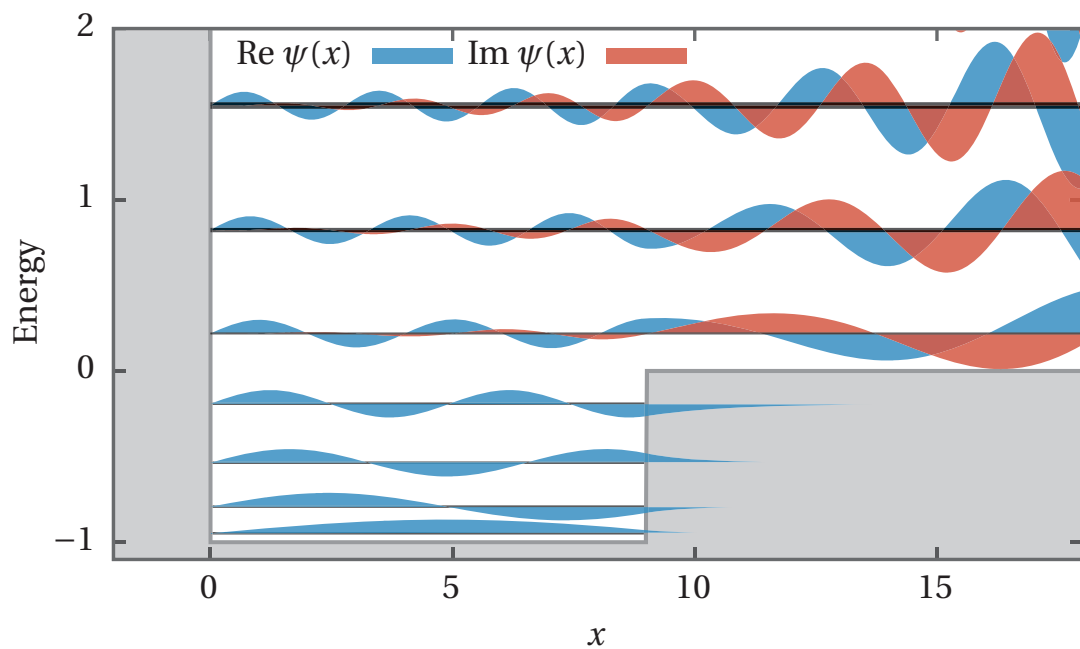
$$A = -\frac{i}{\sin(qa)} \sin \left[\tan^{-1} \left(\frac{k}{q} \tan(qa) \right) \right]. \quad (2.11)$$

¹This normalization is equivalent to δ normalization, see App. D.



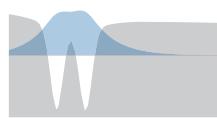


(a) Illustration of bound and continuum states. The continuum states have been normalized according to Eq. (2.10). Blue (red) colors indicate positive (negative) values.



(b) Illustration of bound states and Siegert States. For the Siegert states the thickness of the line indicates the size of the rate Γ . Blue (red) colors indicate real (imaginary) part of the wave function. In Adobe Acrobat Reader, clicking this figure will show an animation of the time-evolution of these states $e^{-i(E-E_0)t}\psi(x)$, where $E_0 = \min V(x)$.

Figure 2.1: The gray line that encloses the gray area indicates the potential $V(x)$ [Eq. (2.3)] with parameters $a = 9$ and $V_0 = 1$.



The modulation seen in the $x < a$ part of the continuum wave function is due to the energy dependence of the coefficient A as given by Eq. (2.11).

The picture presented so far, where we have a set of bound states for $E < V(\infty)$ and a continuum for $E > V(\infty)$, is the picture most people are familiar with. Instead of having an unspecified boundary condition for the $E > 0$ states at $x \rightarrow \infty$, we could choose to impose outgoing-wave boundary conditions. For the flat potentials considered here this can be written as

$$\frac{1}{\psi(x)} \frac{d}{dx} \psi(x) \Big|_{x>a} = ik. \quad (2.12)$$

In the example we have considered, the wave function [Eq. (2.4)] is already written in terms of incoming and outgoing waves, so imposing outgoing wave boundary conditions in this case simply amounts to setting $D = 0$. This additional condition means that the energy is now restricted, and it becomes discretized. In fact, since the condition $D = 0$ coincides with the regularity condition for the bound states, the discretization condition for the SS is Eq. (2.9), only now we seek solutions with $E > 0$. It turns out that no real solutions with $E > 0$ exists, but complex solutions with $\text{Re } E > 0$ do exist.

As the astute reader might have observed, by inserting the quantization condition Eq. (2.9) in the expression for the coefficient A [Eq. (2.11)], we see that the coefficient A has poles at energies that fulfill this quantization condition. This can also be seen in Fig. 2.2, where the norm square of the normalization coefficient A is shown as a function of complex energy.

The complex energy is a special property of the Siegert states; by choosing the outgoing-wave boundary condition the energy turns complex. We will use the notation

$$\mathcal{E} = \text{Re } E, \quad (2.13a)$$

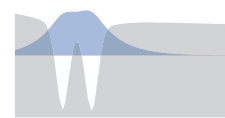
$$\Gamma = -2 \text{Im } E. \quad (2.13b)$$

To interpret the imaginary part of the energy let us first consider the time-dependent Schrödinger equation (TDSE) with a time-independent Hamiltonian

$$i \frac{\partial}{\partial t} \psi(x, t) = H \psi(x, t). \quad (2.14)$$

One solution of this TDSE is

$$\psi(x, t) = e^{-iEt} \psi(x), \quad (2.15)$$



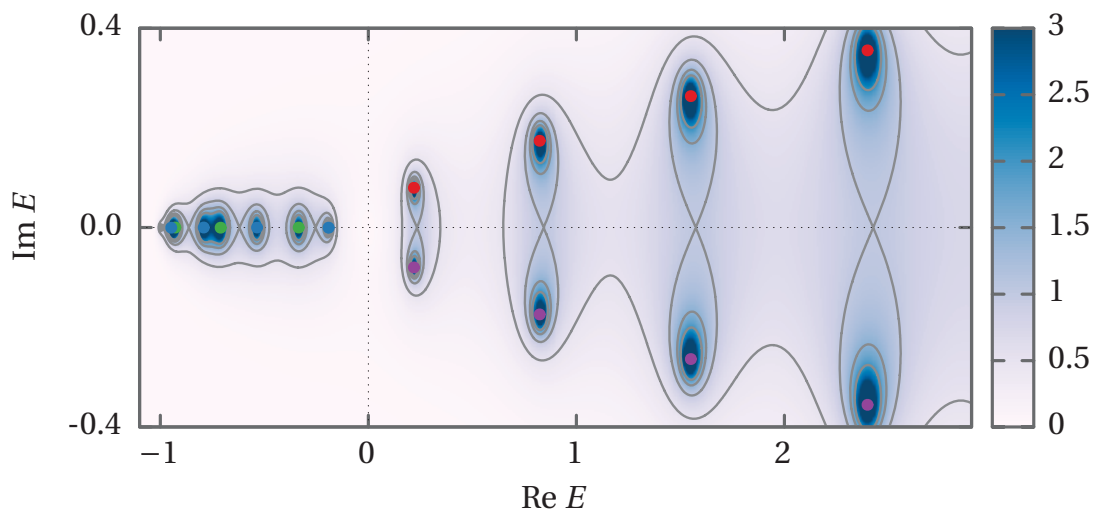


Figure 2.2: Norm square of the normalization coefficient $|A|^2$ [Eq. (2.11)] as a function of complex energy. The dots show the Siegert resonances at energies that fulfill Eq. (2.9), these coincide with the poles of A . The coloring of the dots is the same as in Fig. 2.3. The maxima of $|A|^2$ along the real energy axis do not exactly coincide with the real part of the Siegert resonance energies (this is not easy to see on the scale of the present figure).

where $\psi(x)$ is a solution to the TISE [Eq. (2.1)]. The norm square of the wave function decays as

$$|\psi(x, t)|^2 = e^{2\text{Im}Et} |\psi(x)|^2 \quad (2.16)$$

$$= e^{-\Gamma t} |\psi(x)|^2. \quad (2.17)$$

If we consider the time derivative of this norm square

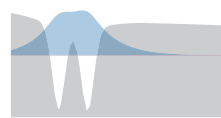
$$\frac{\partial}{\partial t} |\psi(x, t)|^2 = -\Gamma |\psi(x, t)|^2, \quad (2.18)$$

we get a rate equation, with Γ as the rate. We can also relate this time derivative to the probability current

$$\frac{\partial}{\partial t} |\psi(x, t)|^2 = \frac{\partial}{\partial x} j(x), \quad (2.19)$$

where the probability current is given by

$$j(x) = \frac{1}{2mi} \left(\psi(x) \frac{\partial}{\partial x} \psi^*(x) - \psi^*(x) \frac{\partial}{\partial x} \psi(x) \right). \quad (2.20)$$



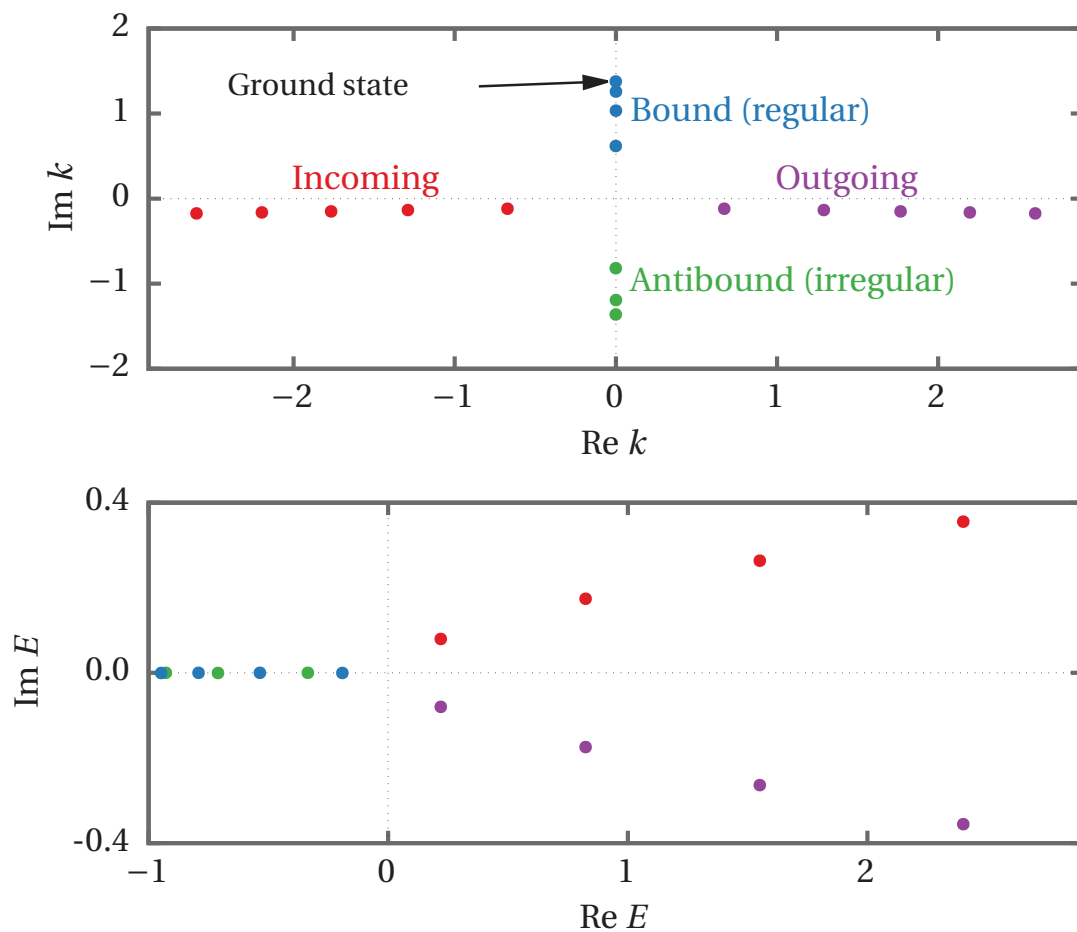
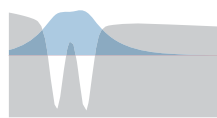


Figure 2.3: Values of k for a potential with $a = 9$ and $V_0 = 1$. The lower panel shows the energy $E = \frac{k^2}{2m}$. This figure is inspired by Fig. 1 in Ref. [13].

We see that associated with the SS is a motion of probability, where the rate Γ describes how quickly the probability is moving. This is a natural consequence of our choice of outgoing-wave boundary conditions, since an outgoing-wave moves outwards, so there must be an overall motion of the wave function outwards. A fascinating aspect of this theory is that the stationary state $\psi(x)$ in a sense describes motion.

In addition to the bound and Siegert state solution to the TISE [Eq. (2.1)], irregular (for $E < 0$) and incoming-wave (for $E > 0$) solutions exist. Figure 2.3 shows the energy and wave number k values for all solutions. We could have chosen to consider $C = 0$ instead of $D = 0$. We would then have obtained the same energies, but the k values would be inverted $k_{C=0} = -k_{D=0}$.



2.1 Tunneling Potential

We have now seen the basic properties of Siegert states. In this thesis Siegert states will be used to describe a tunneling problem, so in this section a very simple tunneling potential will be considered.

We consider a rectangular potential of the form (see Fig. 2.4)

$$V(x) = \begin{cases} \infty & x < 0, \\ 0 & 0 < x < a, \\ V_0 & a < x < b, \\ 0 & b < x. \end{cases} \quad (2.21)$$

The full solution to the TISE [Eq. (2.1)] with this potential is

$$\psi(x) = \begin{cases} A(e^{ikx} - e^{-ikx}) & 0 < x < a, \\ Ce^{iqx} + De^{-iqx} & a < x < b, \\ Fe^{ikx} + Ge^{-ikx} & b < x, \end{cases} \quad (2.22)$$

with

$$k = \sqrt{2mE}, \quad (2.23a)$$

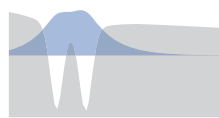
$$q = \sqrt{2m(E - V_0)}, \quad (2.23b)$$

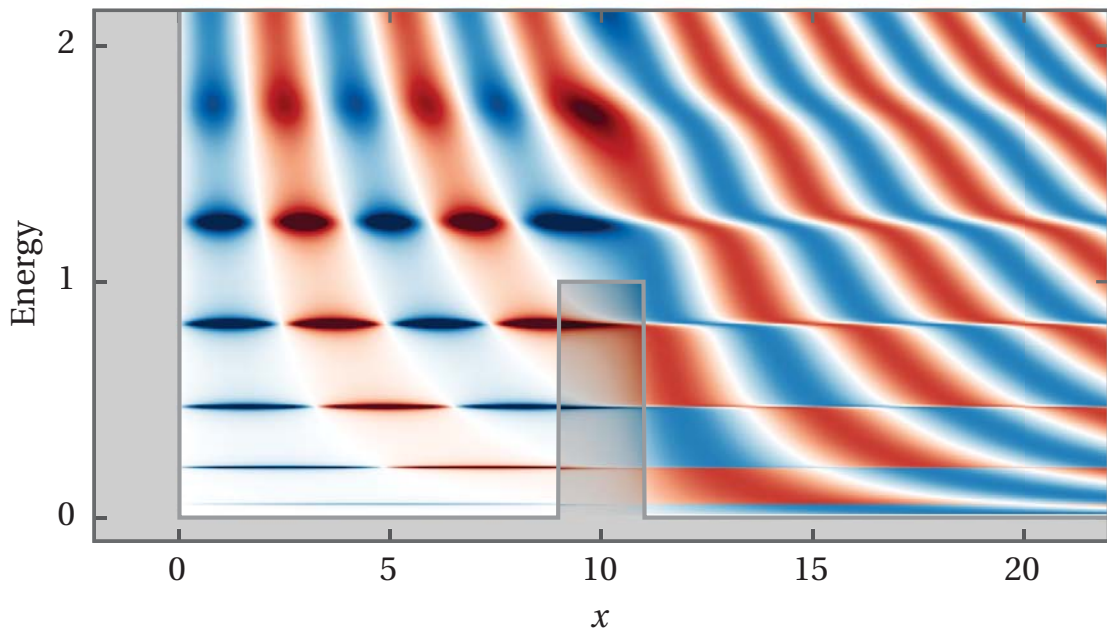
and we have already used the boundary condition Eq. (2.6) to simplify the $0 < x < a$ part. We require that the wave function be continuous and continuously differentiable at both $x = a$ and $x = b$. These 4 conditions together with a normalization condition specify the 5 coefficients A, C, D, F, G , but as before they do not put any restrictions on the energy E , which can take any value greater than zero. Figure 2.4(a) shows these continuum states with the normalization Eq. (2.10).

Imposing outgoing-wave boundary conditions, which in this case corresponds to requiring $G = 0$, gives the following discretization condition

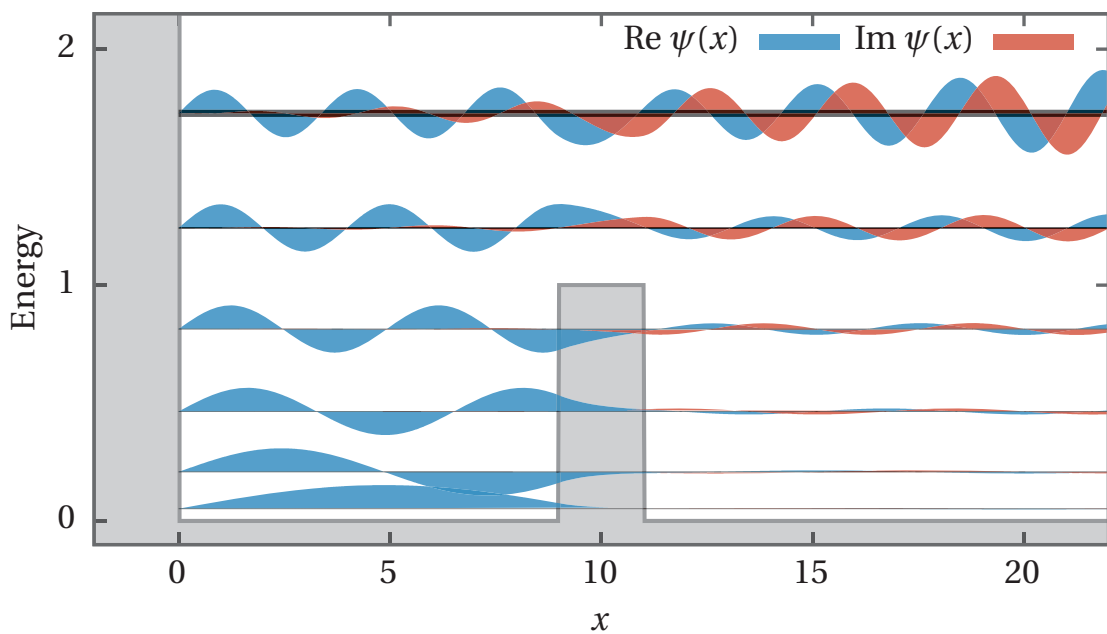
$$e^{-i2qa} \frac{q + k\sigma}{q - k\sigma} = e^{-i2qb} \frac{q + k}{q - k} \quad (2.24)$$

where $\sigma = \frac{e^{ika} + e^{-ika}}{e^{ika} - e^{-ika}} = -i \cot(ka)$. These SS are shown in Fig. 2.4(b). It can be seen that the exponentially decaying part of the solution dominates in the tunneling region for the quasi-bound states with $E < V_0$. Fig. 2.5 shows the wave numbers and energies of the SSs.



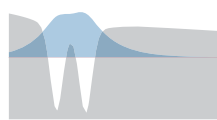


(a) Continuum states, see caption of Fig. 2.1(a).



(b) Siegert states, see caption of Fig. 2.1(b). In Adobe Acrobat Reader, clicking this figure will show an animation.

Figure 2.4: The gray line indicates the tunneling potential [Eq. (2.22)] with parameters $V_0 = 1$, $a = 9$ and $b = 11$.



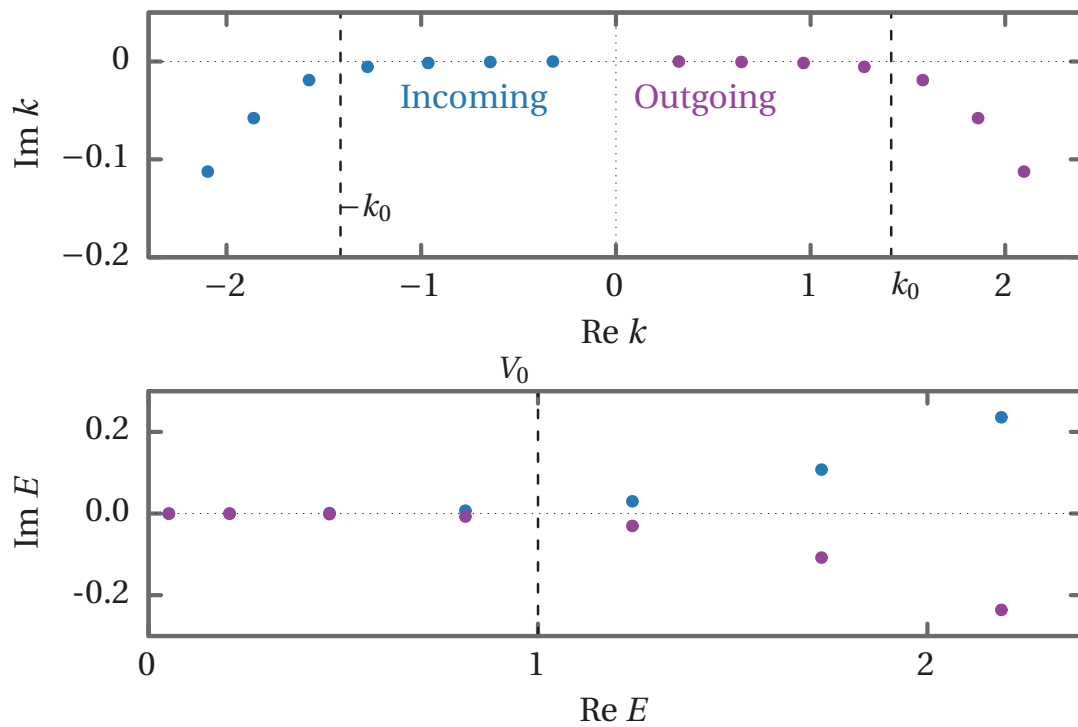
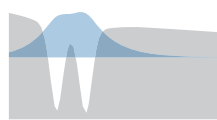


Figure 2.5: Values of k and E for $V_0 = 1$, $a = 9$, $b = 11$ (same parameters as in Fig. 2.4). $k_0 = \sqrt{2mV_0}$ is the wave number that corresponds to the energy at the top of the barrier V_0 . The energy comes in complex conjugate pairs, where one is outgoing and one is incoming.

2.2 Summary

In this chapter we have explored the basic properties Siegert states, which are solutions to the TISE with outgoing-wave boundary conditions. These states have a complex energy; the imaginary part of this energy is a rate describing how quickly the wave function moves.



3 Three-Body Coordinates

Within the SAEA a diatomic molecule is effectively a three-body system. In this chapter the coordinates used to describe such systems in this thesis are presented.

We consider a system of three particles labeled $i = 1, 2, 3$ with the masses m_i , charges q_i and lab-frame coordinates \mathbf{x}_i . Particles 1 and 2 are nuclei, while particle 3 is an electron. The particles interact with each other through central force potentials of the form $V(|\mathbf{x}_i - \mathbf{x}_j|, q_i q_j)$. They also interact with a constant external electric field \mathbf{F} . The lab-frame Hamiltonian is then given by¹

$$H = \sum_i \frac{1}{2m_i} \nabla_{\mathbf{x}_i}^2 - \sum_i q_i \mathbf{F} \cdot \mathbf{x}_i + \sum_{i < j} V(|\mathbf{x}_i - \mathbf{x}_j|, q_i q_j). \quad (3.1)$$

In the following we shall transform this Hamiltonian to other coordinate systems.

3.1 Center-of-Mass Coordinates

First we introduce the center-of-mass coordinates. The center of mass is defined by

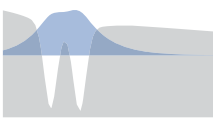
$$\mathbf{r}_{\text{cm}} = \frac{1}{m_{\text{tot}}} \sum_i m_i \mathbf{x}_i. \quad (3.2)$$

where $m_{\text{tot}} = \sum_i m_i$. The center-of-mass coordinates \mathbf{r}_i are then defined relatively to this center of mass as

$$\mathbf{r}_i = \mathbf{x}_i - \mathbf{r}_{\text{cm}}. \quad (3.3)$$

The center-of-mass coordinates are not independent of each other. By

¹The negative sign in the field interaction term is there since this term originates from the length gauge electric field interaction in the dipole approximation.



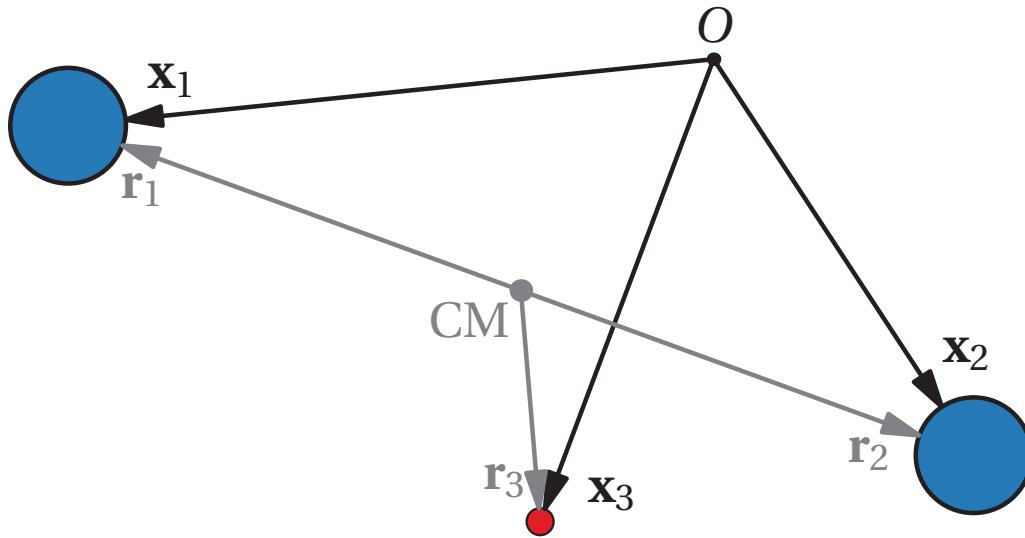


Figure 3.1: Sketch of laboratory frame coordinates \mathbf{x}_i and center-of-mass coordinates \mathbf{r}_i .

inserting Eq. (3.3) in Eq. (3.2) one can obtain

$$\sum_i m_i \mathbf{r}_i = 0. \quad (3.4)$$

This expresses that the center of mass is at the origin of the center-of-mass coordinates.

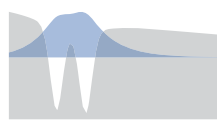
In matrix-form the linear transformation between lab-frame and center-of-mass coordinates can be expressed as

$$\mathbf{r}_i = \sum_j \Lambda_{ij} \mathbf{x}_j \quad (3.5)$$

where

$$\Lambda_{ij}^{\text{COM}} = \delta_{ij} - \frac{m_j}{m_{\text{tot}}}. \quad (3.6)$$

This transformation is not invertible since the center-of-mass coordinates has less degrees-of-freedom than the lab-frame coordinates. This can also be seen explicitly by performing row reduction of the Λ matrix. We can transform from the lab-frame coordinates to the center-of-mass coordinates, but information about the center-of-mass is lost in the transformation, such that we cannot go back.



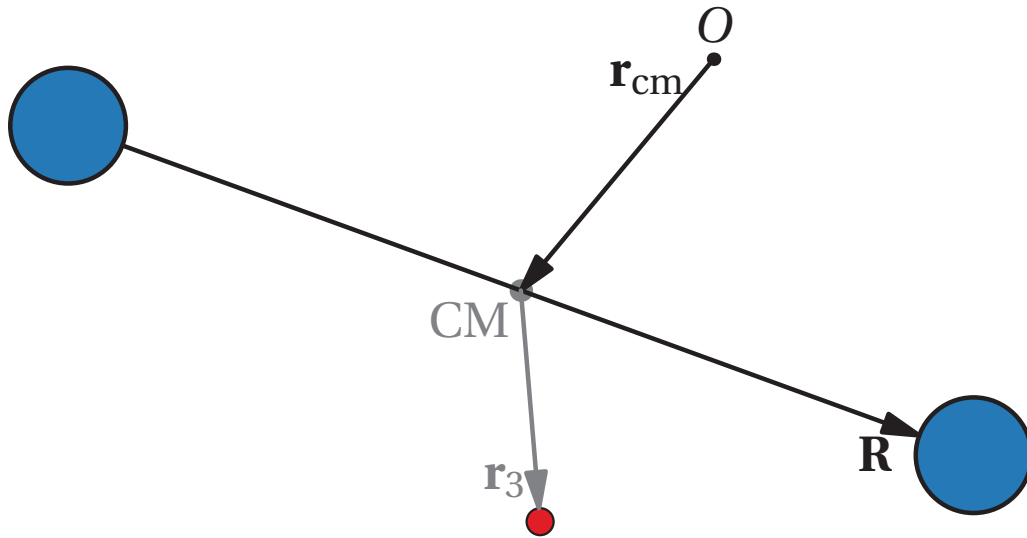


Figure 3.2: Sketch of the Jacobi coordinates \mathbf{R} , \mathbf{r}_3 and \mathbf{r}_{cm} .

3.2 Jacobi (Relative) Coordinates

The redundancy of the center-of-mass coordinates make them an unattractive choice for calculations. We will instead introduce relative Jacobi coordinates. We introduce the relative nuclear coordinate

$$\mathbf{R} = \mathbf{x}_2 - \mathbf{x}_1 = \mathbf{r}_2 - \mathbf{r}_1, \quad (3.7)$$

and define a set of Jacobi coordinates related to the lab-frame coordinates through the linear transformation

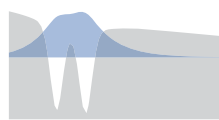
$$\begin{pmatrix} \mathbf{r}_{\text{cm}} \\ \mathbf{R} \\ \mathbf{r}_3 \end{pmatrix} = \frac{1}{m_{\text{tot}}} \begin{pmatrix} m_1 & m_2 & m_3 \\ -m_{\text{tot}} & m_{\text{tot}} & 0 \\ -m_1 & -m_2 & -m_3 + m_{\text{tot}} \end{pmatrix} \begin{pmatrix} \mathbf{x}_1 \\ \mathbf{x}_2 \\ \mathbf{x}_3 \end{pmatrix}. \quad (3.8)$$

As opposed to the center-of-mass transformation [Eq. (3.6)] this transformation is invertible with inverse

$$\left(\Lambda^{\text{Jacobi}}\right)^{-1} = \frac{1}{m_1 + m_2} \begin{pmatrix} m_1 + m_2 & -m_2 & -m_3 \\ m_1 + m_2 & m_1 & -m_3 \\ m_1 + m_2 & 0 & m_1 + m_2 \end{pmatrix}. \quad (3.9)$$

3.2.1 Transformation Properties of Differential Operators

The kinetic energy in the Hamiltonian [Eq. (3.1)] is a differential operator in the lab-frame coordinates. In order to transform this to other coordinate systems we need to know how such differential operators transform.



Suppose we have a linear coordinate transformation from the lab-frame to some other frame

$$\mathbf{s}_i = \sum_j \Lambda_{ij} \mathbf{x}_j. \quad (3.10)$$

Using the chain rule we can then write the differential operator

$$\frac{\partial}{\partial(x_i)_l} = \sum_j \sum_n \frac{\partial(s_j)_n}{\partial(x_i)_l} \frac{\partial}{\partial(s_j)_n} \quad (3.11a)$$

$$= \sum_j \Lambda_{ji} \frac{\partial}{\partial(s_j)_l} \quad (3.11b)$$

with the indices $l, n = x, y, z$. Notice that the order of the indices of the Λ matrix is interchanged compared to the transformation Eq. (3.10). We see that derivatives transform with the transposed transformation matrix. Using this we can write the kinetic energy

$$K = \sum_i \sum_l \frac{1}{2m_i} \frac{\partial}{\partial(r_i)_l} \frac{\partial}{\partial(x_i)_l} \quad (3.12a)$$

$$= \sum_i \sum_l \frac{1}{2} \frac{1}{m_i} \sum_j \Lambda_{ji} \frac{\partial}{\partial(s_j)_l} \sum_k \Lambda_{ki} \frac{\partial}{\partial(s_k)_l} \quad (3.12b)$$

$$= \sum_{j,k,l} \frac{1}{2} \left(\sum_i \frac{1}{m_i} \Lambda_{ji} \Lambda_{ki} \right) \frac{\partial}{\partial(s_j)_l} \frac{\partial}{\partial(s_k)_l}. \quad (3.12c)$$

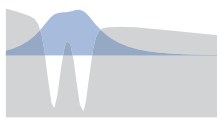
It would be desirable if the kinetic energy in the \mathbf{s}_i coordinates only contains pure second derivatives $\frac{d^2}{d(s_k)_l^2}$, and no cross-terms $\frac{\partial}{\partial(s_j)_l} \frac{\partial}{\partial(s_k)_l}$, $j \neq k$. That the kinetic energy is to have no cross terms is equivalent to that the quantity in the parentheses in Eq. (3.12c)

$$A_{jk} \equiv \sum_i \frac{1}{m_i} \Lambda_{ji} \Lambda_{ki} = \sum_{i,l} \Lambda_{ji} \frac{\delta_{il}}{m_i} \Lambda_{lk}^T \quad (3.13)$$

is diagonal $A_{jk} = \delta_{jk} m_j$. For appropriately mass scaled coordinates this is equivalent to the coordinate transformation matrix being orthogonal.

For the Jacobi coordinates [Eq. (3.8)]

$$A^{\text{Jacobi}} = \frac{1}{m_{\text{tot}}} \begin{pmatrix} 1 & 0 & 0 \\ 0 & \left(\frac{1}{m_1} + \frac{1}{m_2}\right) m_{\text{tot}} & 0 \\ 0 & 0 & \frac{m_1+m_2}{m_3} \end{pmatrix}. \quad (3.14)$$



Using this result we can write the kinetic energy operator in Jacobi coordinates

$$T = \frac{1}{2m_{\text{tot}}}\nabla_{\mathbf{r}_{\text{cm}}}^2 + \frac{1}{2}\left(\frac{1}{m_1} + \frac{1}{m_2}\right)\nabla_{\mathbf{R}}^2 + \frac{m_1 + m_2}{2m_3m_{\text{tot}}}\nabla_{\mathbf{r}_3}^2 \quad (3.15a)$$

$$= \frac{1}{2m_{\text{tot}}}\nabla_{\mathbf{r}_{\text{cm}}}^2 + \frac{1}{2M}\nabla_{\mathbf{R}}^2 + \frac{1}{2m}\nabla_{\mathbf{r}}^2 \quad (3.15b)$$

where we defined the reduced masses

$$M = \frac{1}{\frac{1}{m_1} + \frac{1}{m_2}} = \frac{m_1 m_2}{m_1 + m_2}, \quad (3.16a)$$

$$m = m_3 \frac{m_1 + m_2}{m_{\text{tot}}}, \quad (3.16b)$$

and the mass-scaled coordinate

$$\mathbf{r} = \frac{m_3}{m}\mathbf{r}_3. \quad (3.17)$$

3.2.2 Potential Terms

The potentials we consider fall into two types; central forces acting between the particles dependent on the distance between the particles and the product of their charges

$$\sum_{i < j} V(|\mathbf{x}_i - \mathbf{x}_j|, q_i q_j),$$

and interaction with an external electric field

$$-\mathbf{F} \cdot \sum q_i \mathbf{x}_i.$$

Using the inverse Jacobi transformation [Eq. (3.9)] it can be shown that

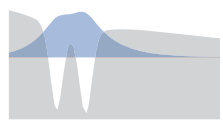
$$\mathbf{x}_2 - \mathbf{x}_1 = \mathbf{R} \quad (3.18a)$$

$$\mathbf{x}_3 - \mathbf{x}_1 = \mathbf{r} + \frac{m_2}{m_1 + m_2}\mathbf{R} \quad (3.18b)$$

$$\mathbf{x}_3 - \mathbf{x}_2 = \mathbf{r} - \frac{m_1}{m_1 + m_2}\mathbf{R}. \quad (3.18c)$$

Note that the center-of-mass coordinate \mathbf{r}_{cm} does not enter in any of these relative quantities. The field term can be written

$$\begin{aligned} -\mathbf{F} \cdot \sum q_i \mathbf{x}_i &= -\mathbf{F} \cdot \left(\sum_i q_i \mathbf{r}_{\text{cm}} + \frac{q_2 m_1 - q_1 m_2}{m_1 + m_2} \mathbf{R} - \left[\frac{q_1 + q_2}{m_1 + m_2} - \frac{q_3}{m_3} \right] m \mathbf{r} \right) \\ &= \mathbf{F} \cdot \left(-\sum_i q_i \mathbf{r}_{\text{cm}} + Q \mathbf{R} + q \mathbf{r} \right), \end{aligned} \quad (3.19)$$



where we introduced the effective charges

$$Q = \left(\frac{q_1}{m_1} - \frac{q_2}{m_2} \right) M, \quad (3.20a)$$

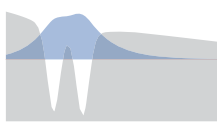
$$q = \left(\frac{q_1 + q_2}{m_1 + m_2} - \frac{q_3}{m_3} \right) m. \quad (3.20b)$$

3.2.3 Total Hamiltonian

The center-of-mass coordinate \mathbf{r}_{cm} additively separates from the \mathbf{R} and \mathbf{r} coordinates in both the kinetic [Eq. (3.15b)] and potential energy [Eq. (3.19)]. This means that we can use a product ansatz to separate this coordinate from the others. The remaining Hamiltonian takes the form

$$H = \frac{1}{2M} \nabla_{\mathbf{R}}^2 + \frac{1}{2m} \nabla_{\mathbf{r}}^2 + \mathbf{F} \cdot (Q\mathbf{R} + q\mathbf{r}) + V(|\mathbf{R}|, q_1 q_2) \\ + V\left(\left|\mathbf{r} + \frac{m_2}{m_1 + m_2} \mathbf{R}\right|, q_1 q_3\right) + V\left(\left|\mathbf{r} - \frac{m_1}{m_1 + m_2} \mathbf{R}\right|, q_2 q_3\right). \quad (3.21)$$

This is the Hamiltonian that we will work with in the remainder of the thesis.



4 Tunneling Ionization of Molecules

In this chapter we consider a diatomic molecule exposed to a static electric field in the single-active electron approximation. Here we will consider a one-dimensional (1D) model of a molecule, with one electronic and one nuclear degree of freedom. In the next chapter a full 3D theory will be developed.

4.1 Simple Picture of Tunneling Ionization

Before considering the full theory in all its gory details, let us first look at the process of tunneling ionization in a simple picture. Fig. 4.1 shows a 1D

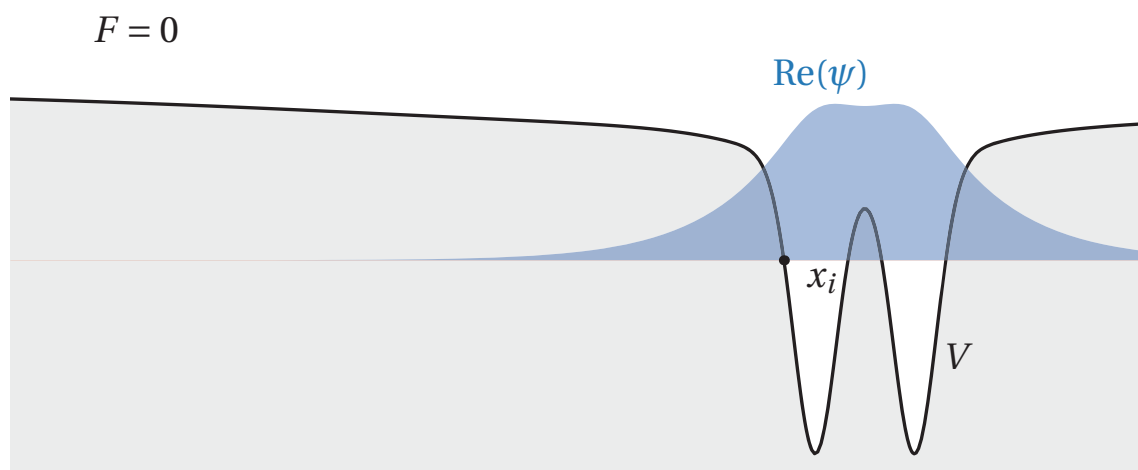
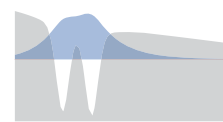


Figure 4.1: Field-free wave function ψ for a fixed R positioned at its energy in the molecular potential V as a function of x . x_i marks the left most classical turning point, where $V(x_i) = E$. The gray area indicates the classically forbidden region.



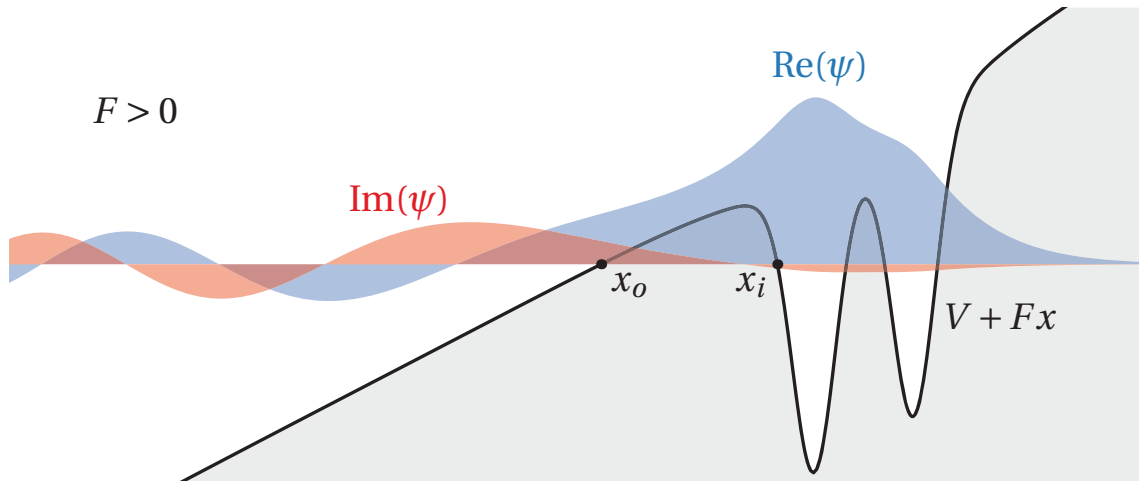


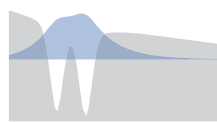
Figure 4.2: Wave function ψ for a fixed R positioned at its energy E as a function of x in the molecular potential V modified by the linear field potential Fx . x_i and x_o marks the inner and outer classical turning points respectively. In Adobe Acrobat Reader, clicking this figure will show an animation of the time-evolution of this state $e^{-i(E-E_0)t}\psi$, where $E_0 = \min_x V(x, R_0)$.

cut of a typical potential felt by an electron in a diatomic molecule for a fixed internuclear distance R . The wave function ψ is primarily located in the wells of the potential, and decays exponentially in the classically forbidden regions. Fig. 4.2 illustrates what happens if a static electric field is applied to this molecule. The addition of the linear field potential Fx causes the potential to bend down for negative x . This opens a classically allowed region at sufficiently large negative x , into which the wave function can tunnel through the tunneling region delimited by the classical turning points x_i and x_o . The shown wave function is chosen to have an outgoing-wave boundary condition, since we only want to consider an electron leaving the molecule, not one that enters it.

4.2 Formal Theory

We will now develop a detailed theory for tunneling ionization in molecules. Using the Jacobi coordinates from Chap. 3 we can write the TISE

$$[H(z, R) - E(F)]\Psi(z, R) = 0, \quad (4.1)$$



with the Hamiltonian

$$H(z, R) = -\frac{1}{2M} \frac{d^2}{dR^2} - \frac{1}{2m} \frac{d^2}{dz^2} + FQR + Fqz + U(R) + V(z, R), \quad (4.2)$$

where we have changed the notation for the potentials slightly from Chap. 3, such that the interaction between the nuclei is described by the potential $U(R)$, and the interaction between the nuclei and the electron has been collected in the potential

$$V(\mathbf{r}, \mathbf{R}) = V_1 \left(\mathbf{r} + \frac{m_2}{m_1 + m_2} \mathbf{R} \right) + V_2 \left(\mathbf{r} - \frac{m_1}{m_1 + m_2} \mathbf{R} \right). \quad (4.3)$$

We wish to solve this TISE [Eq. (4.1)] subject to outgoing-wave boundary conditions in the electronic coordinate z . This choice of boundary condition means that we want to find a Siegert state. As described in Chapter 2 such a state has a complex energy, and we normalize it by

$$\int_0^\infty \int_{-\infty}^\infty \psi^2(z, R) dz dR = 1. \quad (4.4)$$

This normalization contains no complex conjugation, which is somewhat unconventional, but it is often used in the context of Siegert states (see the discussion after Equation (23) in Ref. [11]).

We assume that the nuclei cannot pass through each other, so we restrict the nuclear coordinate to $0 < R$ and impose the zero boundary condition

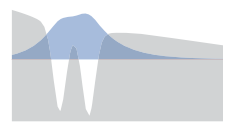
$$\Psi(z, R = 0) = 0. \quad (4.5)$$

Before the exact form of the outgoing-wave boundary conditions in the electronic coordinate can be specified we must first consider the asymptotic behaviour of Eq. (4.1).

4.2.1 Large $|z|$ Limit

We assume that in the limit where the electron is far away from the molecule, the potential describing the electron-nuclear interaction is dominated by the monopole term of the multipole expansion

$$V(z, R)|_{r \rightarrow \infty} = -\frac{Z}{|z|} + O(z^{-2}), \quad (4.6)$$



where $Z = q_1 + q_2$ is the total charge of the system left behind when the electron has left. The only thing that couples the electronic z and nuclear R degrees of freedom is this potential, so in this asymptotic region the Hamiltonian additively separates in electronic z and nuclear R coordinates, and by insertion of the ansatz $\Psi(z, R) = f(z)g(R)$ in Eq. (4.1) we obtain the separated equations

$$\left[-\frac{1}{2m} \frac{d^2}{dz^2} + Fqz - \frac{Z}{|z|} - E_z \right] f(z) = 0, \quad (4.7a)$$

$$\left[-\frac{1}{2M} \frac{d^2}{dR^2} + FQR + U(R) - E_R \right] g(R) = 0, \quad (4.7b)$$

with the separation constants

$$E = E_z + E_R. \quad (4.8)$$

Nuclear Problem

We impose the zero boundary condition for the nuclear equation (4.7b)

$$g(R=0) = 0. \quad (4.9)$$

Depending on the form of $U(R)$ Eq. (4.7b) can have bound solutions, continuum solutions or both. For the bound states we use the index $\nu = 0, 1, \dots$, and write the energy $E_R = E_\nu$. The continuum states we index by their wave number $E_R = \frac{k^2}{2M}$.

$$E_R = E_\nu \quad \nu = 0, 1, \dots \quad \text{Bound states} \quad (4.10a)$$

$$E_R = \frac{k^2}{2M} \quad k \geq 0 \quad \text{Continuum states} \quad (4.10b)$$

where we assumed¹

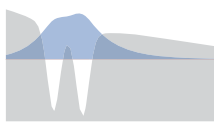
$$\lim_{R \rightarrow \infty} FQR + U(R) = 0. \quad (4.11)$$

The corresponding states are then labelled by

$$g_\nu(R) \quad \text{Bound states} \quad (4.12a)$$

$$g(R, k) \quad \text{Continuum states.} \quad (4.12b)$$

¹If the limit on the left-hand side is finite, the zero point of the energy can be shifted such that the limit becomes 0. If the limit is ∞ there is no continuum. If the limit is $-\infty$ there are no bound states, but this case has not been considered in this thesis.



The continuum states correspond to a molecule that is dissociating after the electron has left. We choose the following orthonormality relations

$$\int_0^\infty g_\nu(R) g_{\nu'}(R) dR = \delta_{\nu\nu'}, \quad (4.13a)$$

$$\int_0^\infty g(R, k) g(R, k') dR = 2\pi\delta(k - k'), \quad (4.13b)$$

$$\int_0^\infty g_\nu(R) g(R, k) dR = 0. \quad (4.13c)$$

The normalization of the continuum states $g(R, k)$ is equivalent to [see App. D]

$$g(R, k)_{R \rightarrow \infty} = 2 \sin(kR + \delta). \quad (4.14)$$

These conditions completely specify the solutions to the nuclear problem.

Electronic Problem

Now for the electronic problem. For $F > 0$ the electrons are ejected in the $-z$ direction, so we want to look at the asymptotic of Eq. (4.7a) in that limit. Consider the transformed coordinate $\bar{z} = -z$ in terms of which we have

$$\left[\frac{d^2}{d\bar{z}^2} + 2mFq\bar{z} + 2m\frac{Z}{|\bar{z}|} + 2mE_z \right] f(-\bar{z}) = 0. \quad (4.15)$$

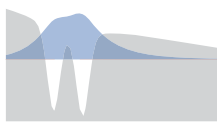
By applying the results of App. A to this equation we get that the leading order term of the asymptotic outgoing-wave solution to Eq. (4.7a) takes the form

$$f(z)|_{z \rightarrow -\infty} = \frac{m^{1/4}}{(2Fq(-z))^{1/4}} \exp \left[i \frac{(2m)^{1/2}}{(Fq)^{1/2}} \left(\frac{2}{3} Fq(-z)^{3/2} + E_z(-z)^{1/2} \right) \right]. \quad (4.16)$$

This expression defines the outgoing-wave boundary condition, which was mentioned after Eq. (4.1). In the $z \rightarrow \infty$ limit we require that the wave function should be regular and decay

$$f(z)|_{z \rightarrow \infty} = \frac{m^{1/4}}{(2Fqz)^{1/4}} \exp \left[-\frac{(2m)^{1/2}}{(Fq)^{1/2}} \left(\frac{2}{3} Fqz^{3/2} - E_z z^{1/2} \right) \right]. \quad (4.17)$$

Note that Eqs. (4.16) and (4.17) represent particular choices of boundary conditions. We could have chosen opposite signs in the exponents, or



some linear combination of the shown functions and the ones with opposite sign in the exponents. This completes the formulation of boundary conditions, and we can write the full wave function in the asymptotic region as

$$\Psi(z, R)|_{z \rightarrow -\infty} = \sum_{\nu} C_{\nu} g_{\nu}(R) f_{\nu}(z) + \int_0^{\infty} C(k) g(R, k) f(z, k) \frac{dk}{2\pi}, \quad (4.18)$$

where C_{ν} and $C(k)$ are asymptotic expansion coefficients. By projecting on the $g_{\nu}(R)$ or $g(R, k)$ states and using the orthonormality of these we can express the asymptotic coefficients in terms of the wave function

$$C_{\nu} = \frac{1}{f_{\nu}(z)} \int_0^{\infty} g_{\nu}(R) \Psi(z, R) dR \Big|_{z \rightarrow \infty}, \quad (4.19a)$$

$$C(k) = \frac{1}{f(z, k)} \int_0^{\infty} g(R, k) \Psi(z, R) dR \Big|_{z \rightarrow \infty}. \quad (4.19b)$$

We will use the notation $C(E_R)$ to indicate either of these

$$C(E_R) = \frac{1}{f(z)} \int_0^{\infty} g(R) \Psi(z, R) dR \Big|_{z \rightarrow \infty}, \quad (4.20)$$

where $g(R)$ can be either $g_{\nu}(R)$ or $g(R, k)$.

The full wave function is thus expanded in terms of nuclear bound and continuum channels indexed by ν and k respectively. As we saw in Chapter 2 the SS has a probability current that satisfies an equation of continuity [9]

$$\frac{\partial}{\partial z} j_z(z, R) + \frac{\partial}{\partial R} j_R(z, R) = \Gamma |\Psi(z, R)|^2, \quad (4.21)$$

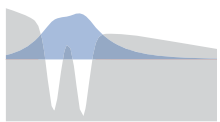
where the currents are defined by

$$j_z(z, R) = \frac{1}{i2m} \left(\Psi \frac{\partial}{\partial z} \Psi^* - \Psi^* \frac{\partial}{\partial z} \Psi \right), \quad (4.22a)$$

$$j_R(z, R) = \frac{1}{i2M} \left(\Psi \frac{d}{dR} \Psi^* - \Psi^* \frac{d}{dR} \Psi \right). \quad (4.22b)$$

By inserting the wave function [Eq. (4.18)] into Eq. (4.21) and integrating over R and some range of z one obtains

$$\left[\sum_{\nu} |C_{\nu}|^2 j_{\nu}(z, R) + \int_0^{\infty} |C(k)|^2 j(z, k) \frac{dk}{2\pi} \right]_{z_{\min}}^{z_{\max}} = \Gamma \cdot [1 + O(F)], \quad (4.23)$$



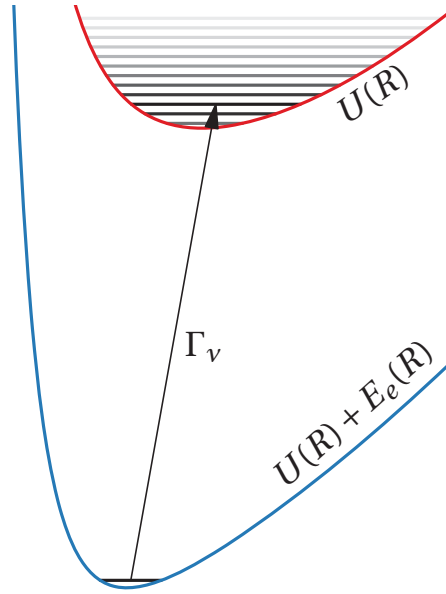


Figure 4.3: Illustration of partial rates.

where the channel currents are defined by

$$j_v(z) = \frac{1}{i2m} \left(f_v(z) \frac{d}{dz} f_v^*(z) - f_v^*(z) \frac{d}{dz} f_v(z) \right) \quad (4.24a)$$

$$j(z, k) = \frac{1}{i2m} \left(f(z, k) \frac{d}{dz} f^*(z, k) - f^*(z, k) \frac{d}{dz} f(z, k) \right). \quad (4.24b)$$

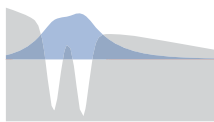
The region in z we integrate over is chosen such that $z_{\min} \ll 0 \ll z_{\max}$ and $\int_{z_{\min}}^{z_{\max}} \int_0^{\infty} |\Psi(z, R)|^2 dR dz = 1 + O(F)$. The contribution from the positive z_{\max} can be disregarded since the wave function decays exponentially in this region. Inserting the asymptotic expansion Eq. (4.16) in the channel current [Eq. (4.24a)] one can show that for $\frac{|\text{Re } E_z|}{2Fq} \ll |z| \ll \frac{Fq}{8m(\text{Im } E_z)^2}$ the asymptotic current is

$$j(z)|_{z < 0} = 1, \quad (4.25)$$

where $j(z)$ indicates either $j_v(z)$ or $j(z, k)$. The pre-exponential factor in Eq. (4.16) was in fact chosen such that the channel current takes this particularly simple form. From this we see that

$$\Gamma|_{F \rightarrow 0} = \sum_v |C_v|^2 + \int_0^{\infty} |C(k)|^2 \frac{dk}{2\pi}. \quad (4.26)$$

We can define the norm square of the individual asymptotic expansion



coefficients as partial rates

$$\Gamma_\nu = |C_\nu|^2, \quad (4.27a)$$

$$P(k) = |C(k)|^2, \quad (4.27b)$$

where the asymptotic coefficients were written in Eqs. (4.20). The first of these we can think of as a rate for going to the vibrational state ν of the molecular ion, see Fig. 4.3. The latter of these describe the distribution of probability current as a function of the energy of dissociating nuclei and will be called the kinetic energy release (KER) spectrum. It is convenient to write Eq. (4.26) in the form

$$\Gamma(F)|_{F \rightarrow 0} = \Gamma^{\text{bound}} + \Gamma^{\text{cont}}, \quad (4.28a)$$

$$\Gamma^{\text{bound}} \equiv \sum_\nu \Gamma_\nu, \quad (4.28b)$$

$$\Gamma^{\text{cont}} \equiv \int_0^\infty P(k) \frac{dk}{2\pi}. \quad (4.28c)$$

The rate and these partial rates are the main observables of interest. For these we shall now describe approximate expressions.

4.3 Weak-Field Asymptotic Theory

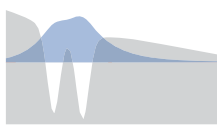
Weak-field asymptotic theory (WFAT) provides an analytic expression for the rate in the weak-field limit, based entirely on properties of the field-free state. In this section we will derive the WFAT expressions. The basic idea of the, rather technical, derivation is to match the field-free and weak-field wave functions in a matching region where $-z$ has large values, but not too large, such that the potentials in the two cases are similar. Since the electron is ejected in the negative z direction, we consider $z < 0$ in this section. The derivation follows that given in Refs. [1, 11].

In the field-free case $F = 0$ the asymptotic wave function is of the form

$$\Psi(z, R)|_{|z| \rightarrow \infty} = \sum_\nu D_\nu g_\nu(R) f_\nu^{(0)}(z) + \int_0^\infty D(k) g(R, k) f^{(0)}(z, k) \frac{dk}{2\pi}, \quad (4.29)$$

where $D_\nu, D(k)$ are field-free asymptotic coefficients and $f^{(0)}(z)$ is the leading order term of the asymptotic solution to Eq. (4.7a) [see App. A]

$$f^{(0)}(z) = |z|^{mZ/\varkappa} e^{-\varkappa|z|}, \quad \varkappa = \sqrt{-2mE_z^{(0)}}, \quad (4.30)$$



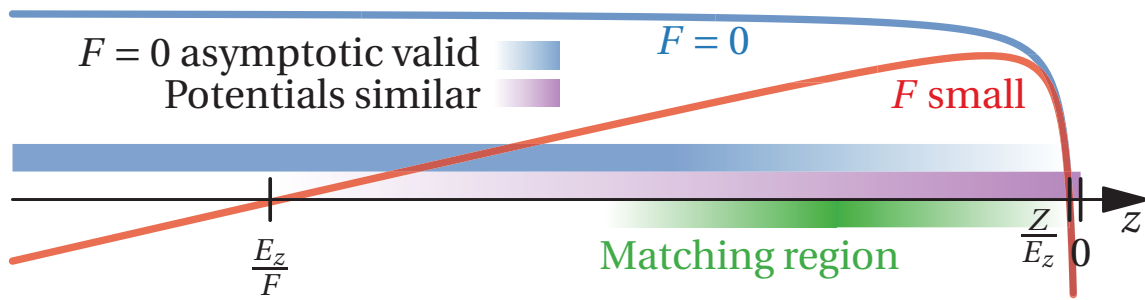


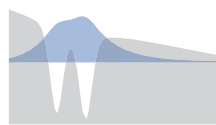
Figure 4.4: The potential $Fz - \frac{Z}{|z|} - E_z$ of Eq. (4.7a) is shown as a function of z , for $F = 0$ and a small value of F . On the z axis the values Z/E_z and E_z/F are indicated. These are quite close to the inner and outer classical turning points respectively, in fact in the $F \rightarrow 0$ limit they coincide with these. Different regions of z are indicated by colored bands around the z axis. These regions are all 'fuzzy', since they are defined by relations of the type $z \gg$ or $z \ll$, and a definite limit to them cannot be found, which is why they are shown with a color gradient. In the $|z| \ll |E_z|/F$ (purple) region, the potentials are similar. The $F = 0$ asymptotic Eq. (4.30) is valid in the (blue) region $|z| \gg Z/|E_z|$. The overlap of these regions is the (green) matching region.

where $E_z^{(0)}$ is the field-free electronic energy. The field-free asymptotic coefficients can be expressed by the integrals

$$D_\nu = \frac{1}{f_\nu^{(0)}(z)} \int_0^\infty g_\nu(R) \Psi(z, R) dR \Big|_{|z| \rightarrow \infty} \quad (4.31a)$$

$$D(k) = \frac{1}{f^{(0)}(z, k)} \int_0^\infty g(R, k) \Psi(z, R) dR \Big|_{|z| \rightarrow \infty}. \quad (4.31b)$$

The key element in the WFAT is the so-called connection formula, which relates the field free asymptotic coefficients $D_\nu, D(k)$ with their weak-field counterparts $C_\nu, C(k)$. The link between these is established by matching the field-free and weak-field wave functions in a matching region [see Fig. 4.4]. The matching is possible when $-Fqz \ll |E_z|$, since then the field-free and weak-field potentials are almost identical, and consequently the wave functions locally of the same form. In order for us to use the asymptotic form Eq. (4.16) we must additionally require that



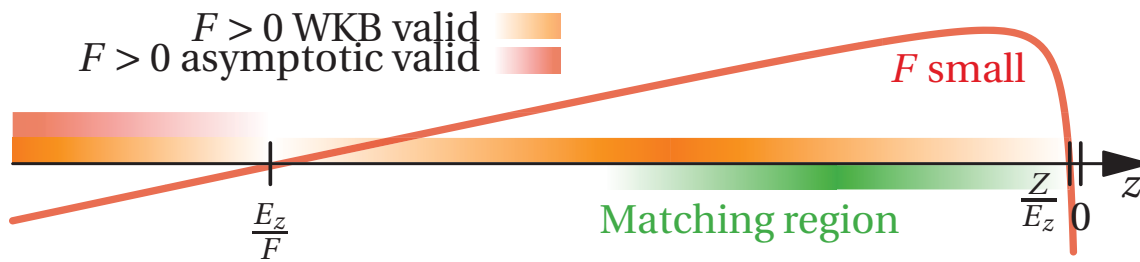


Figure 4.5: Same as figure 4.4, only with other regions highlighted. In the $F > 0$ case the WKB is valid everywhere, except near the turning points, and the weak-field asymptotic expansion Eq. (4.16) is valid away from the outer turning point.

$Z \ll -z|E_z|$. The matching region is thus delimited by the requirements

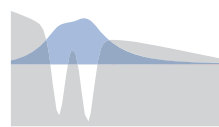
$$\frac{Z}{|E_z|} \ll -z \ll \frac{|E_z|}{Fq}. \quad (4.32)$$

For sufficiently weak F such a matching region exists, and it is for these small F that WFAT is applicable. From Eq. (4.32) we see that for WFAT to be applicable F must fulfill

$$F \ll \frac{E_z^2}{qZ}. \quad (4.33)$$

When matching the field-free and weak-field wave functions in the matching region (4.32) we can use Eq. (4.30) for the field-free wave function. The asymptotic of the weak-field state [Eq. (4.16)] is, however, not valid here, since the matching region is within the tunneling region of the weak-field state (see Fig. 4.5). In order to link the field-free and weak-field wave functions we will first use a WKB² approximation [see App. B] for the weak-field state in the matching region, and match this with the field-free state. A weak-field WKB function will then be matched to the asymptotic weak-field state [Eq. (4.16)]. The two WKB functions cannot be connected on the real axis, since WKB fails at the classical turning point between the two regions, but this problem can be circumvented by an analytic continuation of the WKB wave function into the complex plane z around the turning point [see Fig. 4.6].

²Wentzel-Kramers-Brillouin (WKB) or semi-classical theory is covered in many textbooks on quantum mechanics, e.g. Landau & Lifshitz [14] or Griffiths [15].



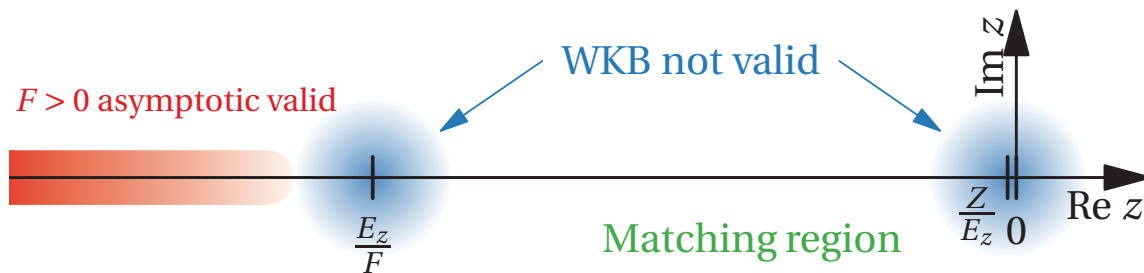


Figure 4.6: Complex z plane. The WKB is valid everywhere except near the classical turning points. The region where WKB is not valid is indicated by the blue circles. By analytically continuing the WKB into the complex plane around the turning points, the coefficient found from matching with the field-free state in the matching region can be related to the weak-field asymptotic state on the far side of the outer turning point.

4.3.1 WKB Wave Function

We now derive the WKB wave function. We expand the electronic energy to first order in field strength

$$E_z = E_z^{(0)} - \mu F + O(F^2), \quad (4.34)$$

where the dipole moment can be calculated from the field-free wave function through the integral

$$\mu = - \left[\int_0^\infty dR \int dz (QR + qz) \Psi^2(z, R) - \int_0^\infty dR QR g^2(R) \right]. \quad (4.35)$$

It is convenient to define the following scaled quantities

$$\tilde{z} = -2\sqrt{m}z, \quad (4.36a)$$

$$\tilde{Z} = \sqrt{m}Z, \quad (4.36b)$$

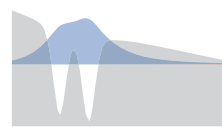
$$\tilde{F} = \frac{q}{\sqrt{m}}F, \quad (4.36c)$$

$$\tilde{\mu} = \frac{\sqrt{m}}{q}\mu, \quad (4.36d)$$

$$\tilde{\kappa} = \frac{1}{\sqrt{m}}\kappa. \quad (4.36e)$$

We cast Eq. (4.7a) using these quantities in the form used in WKB

$$\left[\frac{d^2}{d\tilde{z}^2} + p^2(\tilde{z}) \right] f(\tilde{z}) = 0, \quad (4.37)$$



where the classical momentum is of the same form as in Ref. [11]

$$p^2(\tilde{z}) = \frac{\tilde{F}\tilde{z}}{4} + \frac{E_z}{2} + \frac{\tilde{Z}}{|\tilde{z}|} + O(\tilde{z}^{-2}). \quad (4.38)$$

The WKB² wave function is given by [Eq. (B.11)]

$$f(\tilde{z}) = \frac{C_{\text{WKB}} e^{iS(\tilde{z})}}{p^{1/2}(\tilde{z})}, \quad (4.39)$$

where the classical action is defined by

$$S(\tilde{z}) = \int_{\tilde{z}_o}^{\tilde{z}} p(\tilde{z}') d\tilde{z}'. \quad (4.40)$$

The lower limit of the integral can in principle be chosen arbitrarily, different choices of this can be absorbed into the constant C_{WKB} . To fix C_{WKB} we will make a choice of this limit, and a convenient choice is the outer turning point \tilde{z}_o of the potential in Eq. (4.7a), which fulfills

$$p(\tilde{z}_o) = 0. \quad (4.41)$$

The WKB is accurate when the condition

$$\left| \frac{d}{d\tilde{z}} \frac{1}{p(\tilde{z})} \right| \ll 1 \quad (4.42)$$

is fulfilled. In order to match the WKB wave function [Eq. (4.39)] with the asymptotics of the wave function we will need to simplify the WKB wave function by considering the weak-field and large \tilde{z} limits.

It is convenient to introduce the re-scaled variable

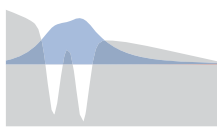
$$x = \frac{\tilde{F}\tilde{z}}{\tilde{\varkappa}^2} = -2 \frac{mqFz}{\varkappa^2}, \quad \tilde{z} = \frac{\tilde{\varkappa}^2 x}{\tilde{F}}, \quad (4.43)$$

where \varkappa was defined in Eq. (4.30). In terms of this variable the classical momentum [Eq. (4.38)] takes the form

$$p^2(x) = \frac{\tilde{\varkappa}^2 x}{4} + \frac{-\frac{1}{2}\tilde{\varkappa}^2 - \tilde{\mu}\tilde{F} + O(F^2)}{2} + \frac{\tilde{F}\tilde{Z}}{\tilde{\varkappa}^2 x} + O(\tilde{z}^{-2}). \quad (4.44)$$

We now consider the limit of small F , and simultaneously the limit of large \tilde{z} , since we only care about what happens in the asymptotic region

$$F \rightarrow 0, \quad \tilde{z} = O(F^{-1}), \quad x = O(F^0). \quad (4.45)$$



In this limit the classical momentum simplifies to

$$p^2(x) = \frac{\tilde{\varkappa}^2}{4} \left[x - 1 + \frac{2}{\tilde{\varkappa}^2} \left(-\tilde{\mu} + \frac{2\tilde{Z}}{\tilde{\varkappa}^2 x} \right) \tilde{F} \right] + O(F^2). \quad (4.46)$$

The outer turning point \tilde{z}_o [Eq. (4.41)] is in this limit given by³

$$x_o = 1, \quad \tilde{z}_o = \frac{\tilde{\varkappa}^2}{\tilde{F}}. \quad (4.47)$$

The condition Eq. (4.42) for the applicability of WKB reduces in this limit to

$$|x - 1| \gg \frac{\tilde{F}^{2/3}}{\tilde{\varkappa}^2}, \quad (4.48)$$

which means the WKB wave function [Eq. (4.39)] is valid when we are not too close to the outer turning point $x_o = 1$.

In the limit (4.45) the action [Eq. (4.40)] takes the form

$$S(\tilde{z}) = \frac{\tilde{\varkappa}^3}{2\tilde{F}} \left[\frac{2}{3}(x-1)^{3/2} - \frac{2\tilde{F}}{\tilde{\varkappa}^2} \left(\tilde{\mu}(x-1)^{1/2} - \frac{2Z}{\tilde{\varkappa}^2} \arctan(x-1)^{1/2} \right) + O(F^2) \right]. \quad (4.49)$$

WKB Wave Function in the Matching Region

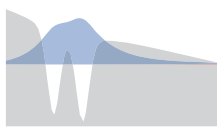
We now consider the WKB wave function in the matching region [Eq. (4.32)] at intermediate \tilde{z} . In terms of x the matching region is delimited by $\frac{4\tilde{F}\tilde{Z}}{\tilde{\varkappa}^4} \ll x \ll 1$. In this region the action [Eq. (4.49)] takes the form

$$S(\tilde{z}) = i \frac{\tilde{\varkappa}^3}{2\tilde{F}} \left[-\frac{2}{3} + x - \frac{2\tilde{F}}{\tilde{\varkappa}^2} \left(\tilde{\mu} + \frac{\tilde{Z}}{\tilde{\varkappa}^2} \ln \frac{x}{4} \right) + O(F^2) \right] \quad (4.50a)$$

$$= -i \frac{\tilde{\varkappa}^3}{3\tilde{F}} + i \frac{\tilde{\varkappa}\tilde{z}}{2} - i\tilde{\varkappa}\tilde{\mu} - i \frac{\tilde{Z}}{\tilde{\varkappa}} \ln \frac{\tilde{F}\tilde{z}}{4\tilde{\varkappa}^2} + O(F^1). \quad (4.50b)$$

Note that the action is purely imaginary, since the matching region is located in the tunneling region of the weak-field state. The classical momentum is given in this region by $p(z) = i\tilde{\varkappa}/2$, which is most easily seen by calculating $p(\tilde{z}) = S'(\tilde{z})$ and using $\frac{2\tilde{Z}}{|\tilde{E}_z|} \ll \tilde{z}$. By matching the WKB wave

³The inner turning point is also defined by Eq. (4.41), but since it is located at small \tilde{z} , it cannot be described in the present limit. The electronic Schrödinger Equation (4.7a) is anyways asymptotic, so we cannot trust anything for small \tilde{z} .



function [Eq. (4.39)] in this region to the asymptotic of the field-free wave function [Eq. (4.30)] we obtain

$$C_{\text{WKB}} = D \cdot (2\sqrt{m})^{-\tilde{Z}/\tilde{\kappa}} \left(\frac{\tilde{\kappa}}{2}\right)^{1/2} \exp\left(-\frac{\tilde{\kappa}^3}{3\tilde{F}} - \tilde{\kappa}\tilde{\mu} - \frac{\tilde{Z}}{\tilde{\kappa}} \ln \frac{\tilde{F}}{4\tilde{\kappa}^2} + i\frac{\pi}{4}\right), \quad (4.51)$$

where D indicates either D_ν or $D(k)$.

WKB Wave Function Beyond the Outer Turning Point

The WKB wave function can be analytically continued from the matching region $x \ll 1$ to the asymptotic region $x \gg 1$, where the asymptotic wave function (4.16) is applicable. The analytic continuation is done through the upper half plane of the complex x plane, staying away from the outer turning point, such that the condition Eq. (4.42) is fulfilled. Since the WKB wave functions in the regions are connected, the constant C_{WKB} appearing in Eq. (4.39) is the same in both cases. In the $x \gg 1$ region the action [Eq. (4.49)] takes the form

$$S(\tilde{z}) = \frac{\tilde{\kappa}^3}{2\tilde{F}} \left[\frac{2}{3}x^{3/2} - x^{1/2} - \frac{2\tilde{F}}{\tilde{\kappa}^2} \left(\tilde{\mu}x^{1/2} - \frac{\pi\tilde{Z}}{\tilde{\kappa}^2} \right) + O(F^2) \right] \quad (4.52)$$

$$= \frac{\tilde{F}^{1/2}\tilde{z}^{3/2}}{3} - \left(\frac{\tilde{\kappa}^2}{2} + \tilde{F}\tilde{\mu} \right) \left(\frac{\tilde{z}}{\tilde{F}} \right)^{1/2} + \frac{\pi\tilde{Z}}{\tilde{\kappa}} + O(F^1). \quad (4.53)$$

The classical momentum takes the form $p(\tilde{z}) = S'(\tilde{z}) = \frac{\tilde{F}^{1/2}\tilde{z}^{1/2}}{2}$. By matching the WKB wave function [Eq. (4.39)] with the $F \neq 0$ asymptotic [Eq. (4.16)] we obtain

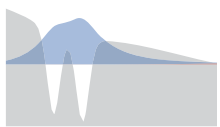
$$C = C_{\text{WKB}} \frac{2^{1/2}}{m^{1/4}} \exp\left(i\frac{\pi\tilde{Z}}{\tilde{\kappa}}\right). \quad (4.54)$$

where C indicates either C_ν or $C(k)$.

We now insert the WKB coefficient C_{WKB} that was found by matching the WKB to the field-free state in the matching region [Eq. (4.51)] in the above expression, which yields

$$C = D \frac{2^{1/2}}{m^{1/4}} \left(\frac{\tilde{\kappa}}{2}\right)^{1/2} \left(\frac{2\tilde{\kappa}^2}{\sqrt{m\tilde{F}}}\right)^{\frac{\tilde{z}}{\tilde{\kappa}}} \exp\left(-\frac{\tilde{\kappa}^3}{3\tilde{F}} - \tilde{\kappa}\tilde{\mu} + i\frac{\pi}{4} + i\frac{\pi\tilde{Z}}{\tilde{\kappa}}\right). \quad (4.55)$$

This equation is called the connection formula, and it is the central result of WFAT. It links the field free asymptotic coefficients D to the weak-field



asymptotic coefficients C . Written in terms of the original quantities [see Eq. (4.36)] it is

$$C = D \left(\frac{\varkappa}{m} \right)^{1/2} \left(\frac{2\varkappa^2}{mFq} \right)^{\frac{mZ}{\varkappa}} \exp \left(-\frac{\varkappa^3}{3mFq} - \frac{1}{q} \varkappa \mu + i \frac{\pi}{4} + i \frac{m\pi Z}{\varkappa} \right). \quad (4.56)$$

The partial rates [Eqs. (4.27)] in WFAT can be written

$$\Gamma_v^{\text{WFAT}} = G_v^2 W_v(F) [1 + O(F)], \quad (4.57a)$$

$$P^{\text{WFAT}}(k) = G^2(k) W(F, k) [1 + O(F)], \quad (4.57b)$$

where the field factor $W(F)$ and structure factors $G_v, G(k)$ are defined by

$$W(F) = \frac{\varkappa}{m} \left(\frac{2\varkappa^2}{mFq} \right)^{2\frac{mZ}{\varkappa}} \exp \left(-\frac{2\varkappa^3}{3mFq} \right), \quad (4.58a)$$

$$G_v = D_v e^{-\varkappa \mu}, \quad (4.58b)$$

$$G(k) = D(k) e^{-\varkappa \mu}, \quad (4.58c)$$

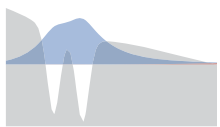
where $W(F)$ can be either $W_v(F)$ or $W(F, k)$. The WFAT partial rates [Eq. (4.57)] are thus partitioned into two factors. The structure factor is obtainable from the field free state and describes the structure of this, while the field factor contains all the field dependence. The total WFAT rate can be found by

$$\Gamma^{\text{WFAT}}(F) = \sum_v \Gamma_v^{\text{WFAT}} + \int_0^\infty P^{\text{WFAT}}(k) \frac{dk}{2\pi}. \quad (4.59)$$

4.4 Born-Oppenheimer Approximation

The Born-Oppenheimer (BO) approximation is very widely used in the treatment of molecules. It is based on the notion, that since the nuclei are a lot heavier than the electrons, the motion of the nuclei should be a lot slower than that of the electrons. The nuclei therefore do not see the detailed motion of the electrons, but only experience a mean field based on the electrons average locations.

Formally the BO approximation appears in the limit of infinite nuclear mass $m_1, m_2 \rightarrow \infty$. In this limit the reduced electron mass and charge becomes $m = 1 = q$. The wave function obtains a separable form



$\Psi_{BO}(z, R) = \psi_e(z; R)\chi(R)$, where the components fulfill the BO equations

$$\left[-\frac{1}{2} \frac{d^2}{dz^2} + Fz + V(z, R) - E_e(R; F) \right] \psi_e(z; R) = 0, \quad (4.60a)$$

$$\left[-\frac{1}{2M} \frac{d^2}{dR^2} + FQR + U(R) + E_e(R; F) - E_{BO}(F) \right] \chi(R) = 0. \quad (4.60b)$$

We impose the zero-boundary condition

$$\chi(R=0) = 0, \quad (4.61)$$

for the nuclear problem [Eq. (4.60b)], and outgoing-wave boundary conditions for the electronic problem [Eq. (4.60a)]. The electronic BO problem [Eq. (4.60a)] is seen to be on the same form as the asymptotic electronic Eq. (4.7a) for large $|z|$, so we can use the same asymptotic expansion [Eq. (4.16)], only we replace the energy E_z with the electronic energy $E_e(R; F)$ and put $m = 1, q = 1$. This allows us to write the electronic wave function for $F > 0$ in the form

$$\psi_e(z; R)|_{z \rightarrow -\infty} = C(R)f(z; R), \quad (4.62)$$

where $C(R)$ are asymptotic coefficients and the outgoing-wave is given by

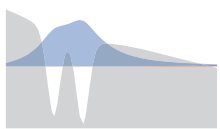
$$f(z; R) = \frac{1}{(2F|z|)^{1/4}} \exp \left[i \frac{2^{1/2}}{F^{1/2}} \left(\frac{2}{3} F|z|^{3/2} + E_e(R; F)|z|^{1/2} \right) \right]. \quad (4.63)$$

This choice of outgoing-wave boundary condition means that once again we have a SS with energy $E_e(R; F) = \mathcal{E}(R; F) - \frac{i}{2}\Gamma_e(R; F)$. The total rate of the BO state is given by the imaginary part of the BO energy as $\Gamma_{BO} = -2\text{Im}E_{BO}(F)$. This rate we can think of as an average of the electronic rate $\Gamma_e(R; F)$. In fact, by projecting Eq. (4.60b) on $\chi^*(R)$ we obtain

$$E_{BO}(F) = \int_0^\infty \chi^*(R) \left[-\frac{1}{2M} \frac{d^2}{dR^2} + FQR + U(R) + E_e(R; F) \right] \chi(R) dR. \quad (4.64)$$

Since the kinetic energy is a Hermitian operator its expectation value with respect to any state is real, even for a complex state⁴. Thus the only thing

⁴This can be shown by the following manipulation of the inner product, where K is Hermitian $\langle \chi | K | \chi \rangle = \frac{1}{2} (\langle \chi | K | \chi \rangle + \langle K \chi | \chi \rangle) = \frac{1}{2} (\langle \chi | K | \chi \rangle + \langle \chi | K | \chi \rangle^*) = \text{Re}(\langle \chi | K | \chi \rangle)$.



imaginary on the right hand side of Eq. (4.64) is in the electronic energy and we can write

$$\Gamma_{\text{BO}}(F) = -2 \text{Im} E_{\text{BO}}(F) = \int_0^\infty |\chi(R)|^2 \Gamma_e(R; F) dR. \quad (4.65)$$

There is a flux of probability associated with the SS, through which we can relate the electronic rate to the asymptotic coefficient [see Sec. 4.2.1]

$$\Gamma_e(R; F)|_{F \rightarrow 0} = |C(R)|^2. \quad (4.66)$$

We wish to find expressions for the partial rates in the BO approximation, so we insert the BO wave function in the expression for the asymptotic coefficients [Eq. (4.20)]

$$C^{\text{BO}}(E_R) = \int_0^\infty g(R) C(R) \frac{f(z; R)}{f(z)} \chi(R) dR \Big|_{z \rightarrow \infty}. \quad (4.67)$$

If we assume that the electronic energy E_z is the same as the electronic energy $E_e(R; F)$ this reduces to

$$C^{\text{BO}}(E_R) = \int_0^\infty g(R) C(R) \chi(R) dR. \quad (4.68)$$

Note that there is no explicit reference to the electron coordinate in this expression. We will use this expression to define BO partial rates analogously to Eq. (4.27)

$$\Gamma_\nu^{\text{BO}} = |C_\nu^{\text{BO}}|^2, \quad (4.69a)$$

$$P^{\text{BO}}(k) = |C^{\text{BO}}(k)|^2, \quad (4.69b)$$

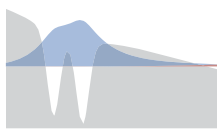
where

$$C_\nu^{\text{BO}} = \int_0^\infty g_\nu(R) C(R) \chi(R) dR, \quad (4.70a)$$

$$C^{\text{BO}}(k) = \int_0^\infty g(R, k) C(R) \chi(R) dR. \quad (4.70b)$$

4.4.1 Reflection Principle

In order to evaluate the integrals in Eqs. (4.70) we can use the so-called reflection principle (RP) [16, 17]. This principle essentially states, that the spectrum can be obtained by reflection of the wave function times some field coupling factor in the potential of the molecular ion. It can be



formulated for bound state integrals [Eq. (4.70a)], but it does not appear to be accurate in this case, so we will only formulate it for the continuum integral Eq. (4.70b). Central to the reflection principle is the reflection approximation [see App. C], which states that the continuum state solutions $g(R, k)$ of the asymptotic nuclear problem Eq. (4.7b) can be approximated by [Eq. (C.22)]

$$g(R, k) = \sqrt{-2\pi \frac{dR_t}{dk}} \delta(R - R_t), \quad (4.71)$$

where R_t is the turning point⁵ of the potential $U(R)$ of Eq. (4.7b) defined by

$$U(R_t) = \frac{k^2}{2M}. \quad (4.72)$$

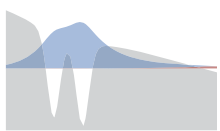
The reflection approximation is exact in the limit $M \rightarrow \infty$, so it is compatible with the BO approximation which also appears in the limit of infinite nuclear mass. Using the reflection principle we can write the spectrum [Eq. (4.69b)] as

$$P^{\text{BO+RP}}(k) = -2\pi \frac{dR_t}{dk} \Gamma_e(R_t; F) |\chi(R_t)|^2. \quad (4.73)$$

The reflection principle thus predicts that the spectrum is given by the product of some Jacobian factor, the nuclear wave function and the electronic rate, evaluated in the R that corresponds to k through reflection in $U(R)$.

The reflection principle has been used in a number of time-dependent cases [16–19]. If the time-scale on which the laser moves electrons is shorter the time scale of nuclear motion, we can assume that the nuclear wave function makes a Franck-Condon transition to an excited electronic state. The probability amplitude in this excited state is then given by the product of the nuclear wave function and a dipole coupling factor. If we assume the excited electronic state is dissociative, the spectrum can then be obtained through an integral of the form (C.1), such that the reflection approximation can be used. The variations of the dipole coupling factor with R are typically not very large, and do not have the violent exponential dependence on R that the electronic rate $\Gamma_e(R)$ has. We therefore approximate the dipole coupling as constant, and thus obtain that the spectrum

⁵We assume that there is only one turning point for the k considered.



directly reflects the initial nuclear wave function. In our time-independent tunneling case the exponential dependence of $\Gamma_e(R)$ on R means that we cannot make such an approximation, and must consider the effect of the R dependence of $\Gamma_e(R)$.

4.4.2 WFAT in BO

The WFAT can also be applied within the framework of BO. Specifically, we can employ it to the electronic equation (4.60a) to find an approximation for the electronic rates [Eq. (4.66)]. This is in fact exactly what was done in Ref. [11], where the frozen-nuclei approximation was used. First we note that the field-free electronic wave function can be asymptotically expanded

$$\psi_e^{(0)}(z; R)|_{z \rightarrow \infty} = D(R) f^{(0)}(z; R), \quad (4.74)$$

where $D(R)$ are the field-free asymptotic expansion coefficients and

$$f^{(0)}(z; R) = z^{Z/\kappa(R)} e^{-\kappa(R)z}, \quad \kappa(R) = \sqrt{-2E_e(R; F=0)}. \quad (4.75)$$

The electronic energy is expanded in field strength

$$E_e(R; F) = E_e(R; 0) - \mu(R)F + O(F^2), \quad (4.76)$$

where

$$\mu(R) = - \int_{-\infty}^{\infty} \psi_e^{(0)}(z; R) q z \psi_e^{(0)}(z; R) dz. \quad (4.77)$$

The WFAT can now be developed in the same way as in Sec. 4.3. This yields

$$\Gamma_e^{\text{WFAT}}(R) = G^2(R) W(F; R), \quad (4.78)$$

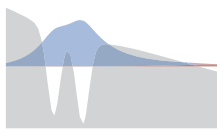
where the field factor $W(F; R)$ and structure factor $G(R)$ are defined by

$$W(F; R) = \kappa(R) \left(\frac{2\kappa^2(R)}{F} \right)^{\frac{2Z}{\kappa(R)}} \exp\left(-\frac{2\kappa^3(R)}{3F} \right) \quad (4.79a)$$

$$G = D(R) e^{-\kappa(R)\mu(R)}. \quad (4.79b)$$

The total BO rate with this partial rate is then

$$\Gamma_{\text{WFAT in BO}}(F) = \int_0^{\infty} |\chi(R)|^2 \Gamma_e^{\text{WFAT}}(R) dR. \quad (4.80)$$



4.4.3 Simple Model for Location of Spectrum Maximum

Combining the reflection principle with WFAT in BO we can build a simple model that predicts the energy at which the spectrum has its maximum.

First we write up approximations for the nuclear wave function. We can describe the nuclear wave function in two regions. Either close to the equilibrium distance R_0 , or at large R . In the first region we do a harmonic expansion of the potential around R_0 and obtain a Gaussian nuclear wave function

$$\chi^{\text{Gauss}}(R) = \chi_0 \exp(-b(R - R_0)^2), \quad (4.81)$$

where χ_0 is a constant of normalization⁶, $b = \frac{1}{2} \sqrt{M[U''(R_0) + E_e''(R_0)]}$ and R_0 is the minimum location of the BO potential, determined by $U'(R_0) + E_e'(R_0) = 0$.

In the second region at large R we are in the classically forbidden region of the BO potential: $U(R) + E_e(R; F) - E_{\text{BO}}(F) > 0$. Here we can describe the nuclear wave function $\chi(R)$ by the WKB wave function [see App. B]

$$\chi^{\text{WKB}}(R) = \frac{C}{p^{1/2}} e^{-\int p \, dR}, \quad (4.82)$$

where the classical momentum is given by $p = \sqrt{2M(U(R) + E_e(R; F) - E_{\text{BO}})}$.

In the reflection approximation [Eq. (4.73)] the spectrum is determined by the product of the electronic rate and the nuclear wave function. Both the Gaussian and WKB wave functions are partitioned into an exponential and a pre-exponential part. The same is the case for the electronic WFAT rate [Eq. (4.78)]. We can therefore partition the spectrum in the same way

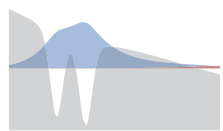
$$P^{\text{BO+RP}}(k) = a(R_t) \exp[e(R_t)] \quad (4.83a)$$

$$e^{\text{Gauss}}(R) = -2 \frac{\varkappa(R)^3}{3F} - 2b(R - R_0)^2, \quad (4.83b)$$

$$e^{\text{WKB}}(R) = -2 \frac{\varkappa(R)^3}{3F} - 2 \int p \, dR. \quad (4.83c)$$

where the Jacobian factor is considered as part of the pre-exponential factor $a(R)$. We now make two additional approximations. First we choose to only consider the exponential dependence of Eq. (4.83), so we assume

⁶ $\chi_0 = \left(\frac{2b}{\pi}\right)^{1/4}$, but the normalization isn't important here.



the pre-exponential factor is constant. Second we assume that the electronic energy $E_e(R; F)$ and its derivatives, as well as $E_{\text{BO}}(F)$, only has a weak dependence on F , and replace these by their values at $F = 0$. The only dependence on F in the exponents (4.83) is then contained in the F^{-1} factor of the first term. The only dependence on M is the \sqrt{M} factor in the second term.

We wish to determine the R_t for which the spectrum has its maximum. If we only consider the exponential dependence of the spectrum this maximum is determined by the condition

$$\frac{\partial}{\partial R} e(R)|_{R=R_{\max}} = 0. \quad (4.84)$$

The derivatives of the exponents are given by

$$\frac{\partial}{\partial R} e^{\text{Gauss}}(R) = 2 \frac{1}{F} \varkappa(R) \frac{\partial}{\partial R} E_e(R; 0) - 2\sqrt{M} \sqrt{U''(R_0) + E_e''(R_0)} (R - R_0), \quad (4.85a)$$

$$\frac{\partial}{\partial R} e^{\text{WKB}}(R) = 2 \frac{1}{F} \varkappa(R) \frac{\partial}{\partial R} E_e(R; 0) - 2\sqrt{M} \sqrt{2(U(R) + E_e(R; F) - E_{\text{BO}})}. \quad (4.85b)$$

We define the functions

$$f_0^{\text{Gauss}}(R) \equiv \frac{\sqrt{-2E_e(R; 0)}}{\sqrt{U''(R_0) + E_e''(R_0, 0)}} \frac{1}{R - R_0} \frac{\partial}{\partial R} E_e(R; 0), \quad (4.86a)$$

$$f_0^{\text{WKB}}(R) \equiv \sqrt{\frac{-E_e(R; 0)}{U(R) + E_e(R; 0) - E_{\text{BO}}}} \frac{\partial}{\partial R} E_e(R; 0). \quad (4.86b)$$

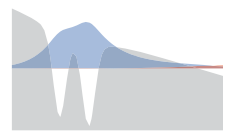
These functions only depend on R and are independent of F and M . The condition for maximum of the spectrum (4.84) is equivalent with

$$f_0(R_{\max}) = F\sqrt{M}. \quad (4.87)$$

Inverting the $f_0(R)$ function then gives the location of the maximum R_{\max} as a function of $F\sqrt{M}$. The energy at which the spectrum has its maximum can then be determined by inverting

$$U(R_{\max}) = E_R. \quad (4.88)$$

The only ingredient that this method uses for determining the maximum of the spectrum is the BO curves of the molecule and its molecular ion. The method can therefore be applied to more general cases than the 1D model considered in this chapter, since it only requires knowledge of the BO curves.



4.4.4 Validity of the BO

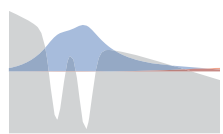
Since the Born-Oppenheimer approximation is an approximation, we would expect that there is a regime of parameters where it will not do well. It is well known that the BO approximation fails at describing Rydberg states and since it is an adiabatic theory, it fails when non-adiabatic couplings are non-negligible, which happens near conical intersections. It turns out that when considering tunneling ionization the BO approximation breaks down for weak field strengths. This is perhaps surprising, since one might naively expect that not a lot should happen at weak field strengths. This breakdown of the BO approximation for weak field-strengths was first reported in Ref. [10]; in this section we will summarize the explanation given there for this breakdown.

The BO approximation appears in the limit of infinite nuclear mass, and use of this approximation is justified since the nuclei are at least 1836 times heavier than the electrons. The heavy mass of the nuclei means that the electrons move a lot faster than the nuclei. Another way to say this is that the typical time-scale of electron motion is a lot shorter than the typical time-scale for nuclear motion. If, however, the electron should move far away from the nuclei it will spend a lot of time doing this, and even though it moves a lot faster than the nuclei, if it moves sufficiently far away, the time scale of the electronic motion can become longer than that of the nuclear motion. If this happens the BO approximation breaks down. This also explains why the BO approximation breaks for Rydberg states, since here the electron is far from the nuclei. We will now estimate how far away from the nuclei the electrons should move before this starts to happen.

A typical electron velocity can be estimated as $v_e = \sqrt{-2E_e(R_0; 0)}$, where R_0 is the equilibrium internuclear distance, which for H_2^+ is $R_0 = 2 \text{ a.u.}$. A typical time scale for the nuclear motion can be estimated as $T = \frac{1}{2\omega_e}$, where ω_e is obtained by expanding the BO potential around R_0 to second order $U(R) + E_e(R; 0) \approx U(R_0) + E_e(R_0; 0) + \frac{1}{2}M\omega_e^2(R - R_0)^2$. Using these estimates Ref. [10] defines a critical distance [see Fig. 4.7]

$$z_{\text{BO}} = v_e T = \frac{v_e}{2\omega_e}, \quad (4.89)$$

such that for $|z| < z_{\text{BO}}$ we expect BO to work well, while for $|z| > z_{\text{BO}}$ we expect it to break down. Since the magnitude of the wave function is essentially unchanged after the tunneling, the BO approximation is expected to work well when the outer turning point is within this z_{BO}



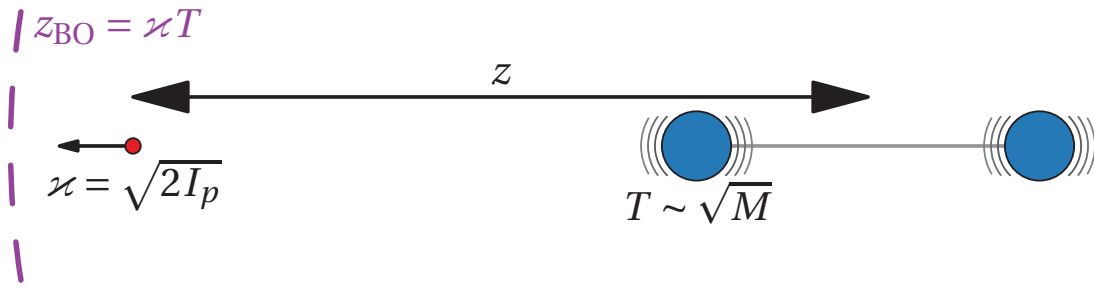
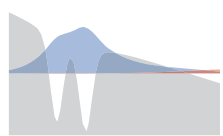


Figure 4.7: The motion of the nuclei happens at a time scale T . The electron moves with velocity $\varkappa = \sqrt{2I_p}$, where I_p is the ionization potential. The product of these gives a distance z_{BO} , beyond which we expect BO to breakdown.

distance. The outer turning point is approximately located at $z_o = \frac{E_e(R_0;0)}{F}$, so by equating the critical BO distance with the outer a turning point a critical field

$$F_{\text{BO}} = 2\varkappa_e \omega_e \quad (4.90)$$

can be estimated, such that the BO approximation is expected to give good results for larger fields, but fail for smaller fields.



5 Tunneling Ionization of Molecules in 3D

In this chapter we extend the theory of the last chapter to three electronic dimensions. All the numerical work in the following chapters are done in one electronic dimension, so it is not necessary to read this chapter in order to read the remainder of the thesis. The content of this chapter is similar to that of Chapter 4, and extensive reference is made to Chap. 4 when the same formulations can be used.

5.1 Formal Theory

As in Chap. 4, we write the Hamiltonian using the Jacobi coordinates from Chap. 3

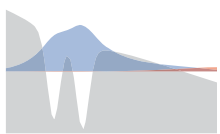
$$H(\mathbf{r}, \mathbf{R}) = -\frac{1}{2M} \nabla_{\mathbf{R}}^2 - \frac{1}{2m} \nabla_{\mathbf{r}}^2 + \mathbf{F} \cdot (Q\mathbf{R} + q\mathbf{r}) + U(R) + V(\mathbf{r}, \mathbf{R}). \quad (5.1)$$

We wish to solve the time-independent Schrödinger equation

$$[H(\mathbf{r}, \mathbf{R}) - E(F)] \Upsilon(\mathbf{r}, \mathbf{R}) = 0. \quad (5.2)$$

First we assume that the molecule has been aligned such that its internuclear axis \mathbf{R} has some particular direction in space. Such an alignment can for instance be achieved by inducing a rotational wave packet using an alignment pulse, as described in Ref. [20]. We additionally assume that the external field is linearly polarized in the z direction such that $\mathbf{F} = F\hat{\mathbf{z}}$. For $F = 0$ we assume that $\Upsilon(\mathbf{r}, \mathbf{R})$ is invariant under rotations around the \mathbf{R} vector. Due to the azimuthal symmetry of the molecule only the polar angle β between \mathbf{R} and \mathbf{F} matters. We can write the wave function

$$\Upsilon(\mathbf{r}, \mathbf{R}) = A(\beta) \frac{1}{R} \Psi(\mathbf{r}, R, \beta), \quad (5.3)$$



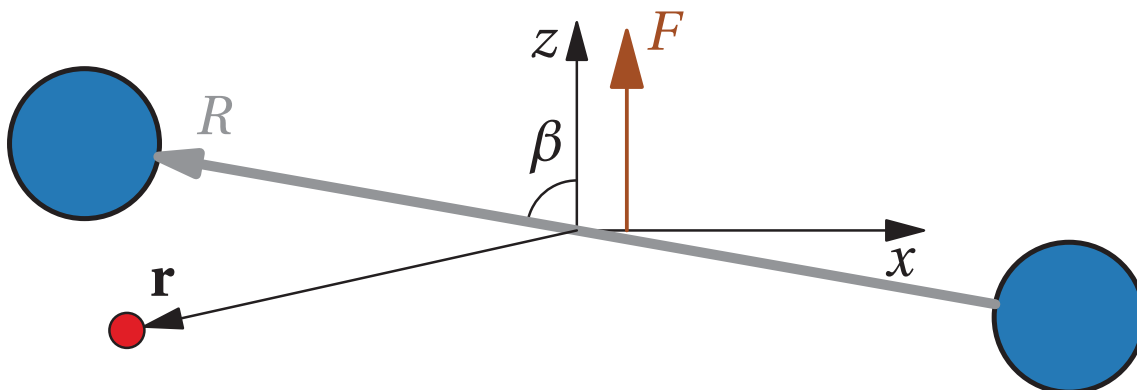


Figure 5.1: Sketch of the coordinates used.

where $A(\beta)$ is a function that is sharply peaked around some particular angle. It can be thought of as a linear combination of many angular functions $Y_{JM}(\Omega_R)$ in the nuclear coordinate, and its exact form depends on the alignment pulse used. With this alignment, β takes the role as an external parameter, and we omit explicit reference to it in the following.

The TISE now takes the form

$$[H(\mathbf{r}, R) - E(F)] \Psi(\mathbf{r}, R) = 0 \quad (5.4)$$

with the Hamiltonian

$$H(\mathbf{r}, R) = -\frac{1}{2M} \frac{d^2}{dR^2} - \frac{1}{2m} \nabla_{\mathbf{r}}^2 + F(QR_z + qz) + U(R) + V(\mathbf{r}, R), \quad (5.5)$$

where R_z is the z component of \mathbf{R} . We wish to solve this TISE subject to outgoing-wave boundary conditions in the electronic coordinate \mathbf{r} . This choice of boundary condition means that we want to find a Siegert state. As described in Chapter 2 such a state has a complex energy.

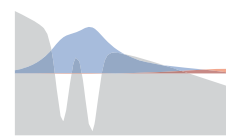
We assume that the nuclei cannot pass through each other, so we restrict the nuclear coordinate to $0 < R$ and impose the zero boundary condition

$$\Psi(\mathbf{r}, R = 0) = 0. \quad (5.6)$$

Before the exact form of the outgoing-wave boundary conditions in the electronic coordinate can be specified we must first consider the asymptotic behaviour of Eq. (5.4).

5.1.1 Large r Limit

We assume that in the limit where the electron is far away from the molecule, the potential describing the electron-nuclear interaction is dominated by



the monopole term of the multipole expansion

$$V(\mathbf{r}, R)|_{r \rightarrow \infty} = -\frac{Z}{r} + O(r^{-2}), \quad (5.7)$$

where $Z = q_1 + q_2$ is the total charge of the system left behind when the electron has left. The only thing that coupled the electronic \mathbf{r} and nuclear R degrees of freedom was this potential, so in this asymptotic region the Hamiltonian additively separates in electronic \mathbf{r} and nuclear R coordinates, and by insertion of the ansatz $\Psi(\mathbf{r}, R) = f(\mathbf{r})g(R)$ in Eq. (5.4) we obtain the separated equations

$$\left[-\frac{1}{2m} \nabla_{\mathbf{r}}^2 + Fqz - \frac{Z}{r} - E_{\mathbf{r}} \right] f(\mathbf{r}) = 0, \quad (5.8a)$$

$$\left[-\frac{1}{2M} \frac{d^2}{dR^2} + FQR_z + U(R) - E_R \right] g(R) = 0, \quad (5.8b)$$

with the separation constants

$$E = E_{\mathbf{r}} + E_R. \quad (5.9)$$

The nuclear problem is of the same form as in Chap. 4, and the discussion of this problem in Sec. 4.2.1 also applies for the 3D case.

Parabolic Coordinates for the Electronic Problem

Let us now consider the electronic problem Eq. (5.8a). This problem has a spherically symmetric Coulomb potential and a linear field potential. It is separable in parabolic coordinates, so will therefore rewrite it using these coordinates. First we introduce the following scaled quantities

$$\tilde{\mathbf{r}} = \sqrt{m}\mathbf{r}, \quad (5.10a)$$

$$\tilde{F} = \frac{q}{\sqrt{m}}F, \quad (5.10b)$$

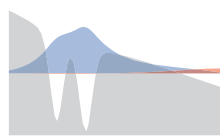
$$\tilde{Z} = \sqrt{m}Z. \quad (5.10c)$$

In terms of these quantities Eq. (5.8a) is of the same form as Eq. (1) of Ref. [11]. We can therefore write the problem in parabolic coordinates in the same way as done in Ref. [11]. We define our parabolic coordinates by

$$\xi = \tilde{r} + \tilde{z}, \quad 0 \leq \xi < \infty \quad (5.11a)$$

$$\eta = \tilde{r} - \tilde{z}, \quad 0 \leq \eta < \infty \quad (5.11b)$$

$$\varphi = \arctan \frac{\tilde{y}}{\tilde{x}}, \quad 0 \leq \varphi < 2\pi. \quad (5.11c)$$



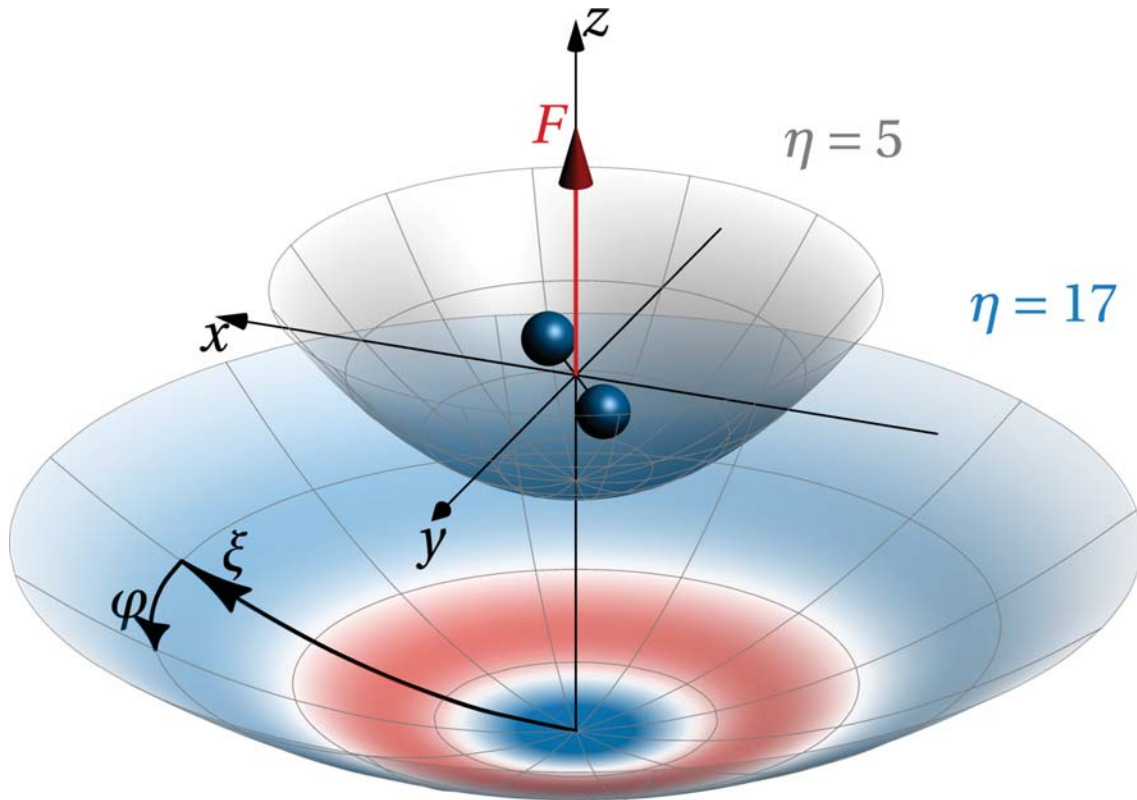


Figure 5.2: Parabolic coordinates. The paraboloids show surfaces of constant η . For fixed η , the ξ and φ coordinates designate locations in the paraboloid. The red/blue colors in the lower paraboloid illustrate a parabolic channel function $\Phi_\mu(\xi, \varphi)$ [Eq. (5.15a)]. These functions 'live' in the paraboloids. Due to the curvature of the paraboloids their extent is finite. This means that η is the only coordinate we need to consider at infinity.

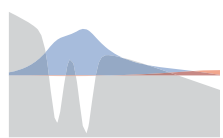
These coordinates are illustrated in Fig. 5.2. Using these we can rewrite Eq. (5.8a) as

$$\left[\frac{\partial}{\partial \eta} \eta \frac{\partial}{\partial \eta} + \mathcal{B}(\eta) + \frac{E_{\mathbf{r}} \eta}{2} + \frac{\tilde{F} \eta^2}{4} \right] f(\mathbf{r}) = 0, \quad (5.12)$$

where

$$\mathcal{B}(\eta) = \frac{\partial}{\partial \xi} \xi \frac{\partial}{\partial \xi} + \frac{\eta + \xi}{4\xi\eta} \frac{d^2}{d\varphi^2} + \tilde{Z} + \frac{E_{\mathbf{r}} \xi}{2} - \frac{\tilde{F} \xi^2}{4}. \quad (5.13)$$

In the limit of large η the operator $\mathcal{B}(\eta)$ becomes independent on η



and only depends on ξ and φ

$$\mathcal{B} \equiv \mathcal{B}(\eta)|_{\eta \rightarrow \infty} = \frac{\partial}{\partial \xi} \xi \frac{\partial}{\partial \xi} + \frac{1}{4\xi} \frac{d^2}{d\varphi^2} + \tilde{Z} + \frac{E_r \xi}{2} - \frac{\tilde{F} \xi^2}{4}. \quad (5.14)$$

Note that this limit implies the limit $r \rightarrow \infty$ (but not conversely). For $\tilde{F} \geq 0$ this operator has a purely discrete spectrum. This is important, since it means that we do not need to consider the limit $\xi \rightarrow \infty$. Only the η coordinate can go to infinity; this coordinate takes the role as the tunneling coordinate. In the $\eta \rightarrow \infty$ limit Eq. (5.12) is separable, and we can write the separated equations¹

$$\left[\frac{\partial}{\partial \xi} \xi \frac{\partial}{\partial \xi} + \frac{1}{4\xi} \frac{d^2}{d\varphi^2} + \tilde{Z} + \frac{E_r \xi}{2} - \frac{\tilde{F} \xi^2}{4} - \beta_\mu \right] \Phi_\mu(\xi, \varphi) = 0, \quad (5.15a)$$

$$\left[\frac{\partial}{\partial \eta} \eta \frac{\partial}{\partial \eta} + \beta_\mu + \frac{E_r \eta}{2} + \frac{\tilde{F} \eta^2}{4} \right] h_\mu(\eta) = 0. \quad (5.15b)$$

The parabolic channel functions $\Phi_\mu(\xi, \varphi)$ are normalized according to

$$\int_0^\infty \int_0^{2\pi} \Phi_\mu(\xi, \varphi) \Phi_{\mu'}(\xi, \varphi) d\varphi d\xi = \delta_{\mu\mu'}. \quad (5.16)$$

These solutions to Eq. (5.15a) are required to be regular at $\xi = 0$ and fulfill periodic boundary conditions in φ . They are analogous to spherical harmonics, which describe what happens on spheres of constant r , where locations are designated by coordinates θ, φ . Correspondingly, the parabolic channel functions describe what happens in paraboloids of constant η , where locations are designated by the ξ, φ coordinates.

It is convenient to introduce the reduced function

$$f_\mu(\eta) = \eta^{1/2} h_\mu(\eta), \quad (5.17)$$

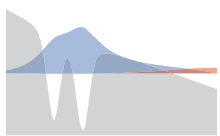
such that Eq. (5.15b) becomes

$$\left[\frac{d^2}{d\eta^2} + \frac{\tilde{F} \eta}{4} + \frac{E_r}{2} + \frac{\beta_\mu}{\eta} + O(\eta^{-2}) \right] f_\mu(\eta) = 0. \quad (5.18)$$

For $F > 0$ the leading order term of the asymptotic solution to these equations [see App. A] is

$$f(\eta) \equiv f_\mu(\eta) = \frac{m^{1/4} 2^{1/2}}{(\tilde{F} \eta)^{1/4}} \exp \left[\frac{i \tilde{F}^{1/2} \eta^{3/2}}{3} + \frac{i E_r \eta^{1/2}}{\tilde{F}^{1/2}} \right]. \quad (5.19)$$

¹Usually ν is used for the parabolic channel index. Due to similarity of ν with the vibrational index ν , the letter μ will be used instead in this thesis.



Note that this expression is in fact independent on μ . This expression defines the outgoing-wave boundary condition. This completes the formulation of boundary conditions, and we can write the full wave function in the asymptotic region as

$$\begin{aligned} \Psi(\mathbf{r}, R)|_{\eta \rightarrow \infty} = & \eta^{-1/2} \sum_{\mu} \sum_{\nu} C_{\mu\nu} g_{\nu}(R) f(\eta) \Phi_{\mu}(\xi, \varphi) \\ & + \eta^{-1/2} \sum_{\mu} \int_0^{\infty} C_{\mu}(k) g(R, k) f(\eta) \Phi_{\mu}(\xi, \varphi) \frac{dk}{2\pi}, \end{aligned} \quad (5.20)$$

where $C_{\mu\nu}$ and $C_{\mu}(k)$ are asymptotic expansion coefficients. Note that $f(\eta)$ and $\Phi_{\mu}(\xi, \varphi)$ depend on the nuclear energy and therefore on ν and k in the sum and integral respectively. By projecting on the $\Phi_{\mu}(\xi, \varphi)$ and $g_{\nu}(R)$ or $g(R, k)$ states and using the orthonormality of these we can write the asymptotic coefficients in terms of the wave function

$$C_{\mu\nu} = \frac{1}{\eta^{-1/2} f(\eta)} \int_0^{\infty} g_{\nu}(R) \langle \Phi_{\mu}(\xi, \varphi) | \Psi(\mathbf{r}, R) \rangle_{(\xi, \varphi)} dR \Big|_{\eta \rightarrow \infty}, \quad (5.21a)$$

$$C_{\mu}(k) = \frac{1}{\eta^{-1/2} f(\eta)} \int_0^{\infty} g(R, k) \langle \Phi_{\mu}(\xi, \varphi) | \Psi(\mathbf{r}, R) \rangle_{(\xi, \varphi)} dR \Big|_{\eta \rightarrow \infty}. \quad (5.21b)$$

We will use the notation $C_{\mu}(E_R)$ to indicate either of these

$$C_{\mu}(E_R) = \frac{1}{\eta^{-1/2} f(\eta)} \int_0^{\infty} g(R) \langle \Phi_{\mu}(\xi, \varphi) | \Psi(\mathbf{r}, R) \rangle_{(\xi, \varphi)} dR \Big|_{\eta \rightarrow \infty}, \quad (5.22)$$

where $g(R)$ can be either $g_{\nu}(R)$ or $g(R, k)$. Note that $g(R)$, $\Phi_{\mu}(\xi, \varphi)$ and $f(\eta)$ all depends on the nuclear energy E_R considered.

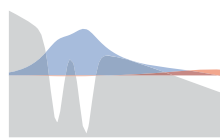
The full wave function is thus expanded in terms of nuclear bound and continuum channels indexed by ν and k respectively, and additionally in terms of parabolic channels indexed by μ . As we saw in Chapter 2 the SS has a probability current that satisfies an equation of continuity [9]

$$\nabla_{\mathbf{r}} \mathbf{j}_{\mathbf{r}}(\mathbf{r}, R) + \frac{\partial}{\partial R} j_R(\mathbf{r}, R) = \Gamma |\Psi(\mathbf{r}, R)|^2, \quad (5.23)$$

where the currents are defined by

$$\mathbf{j}_{\mathbf{r}}(\mathbf{r}, R) = \frac{1}{i2m} (\Psi \nabla_{\mathbf{r}} \Psi^* - \Psi^* \nabla_{\mathbf{r}} \Psi), \quad (5.24a)$$

$$j_R(\mathbf{r}, R) = \frac{1}{i2M} \left(\Psi \frac{d}{dR} \Psi^* - \Psi^* \frac{d}{dR} \Psi \right). \quad (5.24b)$$



Using the asymptotic expansion Eq. (5.19) one can show that in the weak-field limit the total rate is given by²

$$\Gamma|_{F \rightarrow 0} = \sum_{\mu} \sum_{\nu} |C_{\mu\nu}|^2 + \sum_{\mu} \int_0^{\infty} |C_{\mu}(k)|^2 \frac{dk}{2\pi} \quad (5.25)$$

We can define the norm square of the individual asymptotic expansion coefficients as partial rates

$$\Gamma_{\mu\nu} = |C_{\mu\nu}|^2, \quad (5.26a)$$

$$P_{\mu}(k) = |C_{\mu}(k)|^2. \quad (5.26b)$$

The latter of these describe the distribution of probability current as a function of the energy of dissociating nuclei and will be called the spectrum. The rate and these partial rates are the main observables of interest, for which we shall now describe approximate expressions.

5.2 Weak-Field Asymptotic Theory

See the 1D Sec. 4.3 for a detailed discussion of WFAT. Here we mainly list the points in the derivation that are different.

In the field-free case $F = 0$ the asymptotic wave function is of the form

$$\begin{aligned} \Psi(\mathbf{r}, R)|_{\eta \rightarrow \infty} = & \eta^{-1/2} \sum_{\mu} \sum_{\nu} D_{\mu\nu} g_{\nu}(R) f_{\mu}^{(0)}(\eta) \Phi_{\mu}^{(0)}(\xi, \varphi) \\ & + \eta^{-1/2} \sum_{\mu} \int_0^{\infty} D_{\mu}(k) g(R, k) f_{\mu}^{(0)}(\eta) \Phi_{\mu}^{(0)}(\xi, \varphi) \frac{dk}{2\pi}, \end{aligned} \quad (5.27)$$

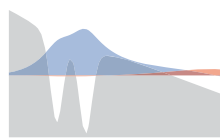
where $\beta_{\mu}^{(0)}$ and $\Phi_{\mu}^{(0)}(\xi, \varphi)$ are the asymptotic adiabatic eigenvalues and eigenfunctions solving Eq. (5.15a) for $F = 0$. The leading order term of the asymptotic solution to Eq. (5.15b) is in this field-free case of the form [see App. A]

$$f_{\mu}^{(0)}(\eta) = \eta^{\beta_{\mu}^{(0)}/\varkappa} e^{-\varkappa\eta/2}, \quad \varkappa = \sqrt{-2E_{\mathbf{r}}^{(0)}}, \quad (5.28)$$

where $E_{\mathbf{r}}^{(0)}$ is the field-free electronic energy. Note that these depend on μ , as opposed to $f(\eta)$ from Eq. (5.19)³. In the 3D case the matching region is

²The factor in front of the exponential in Eq. (5.19) is in fact chosen such that no extra constant appears in this expression.

³This is because the term β_{μ}/η in Eq. (5.18) is not neglectable compared to the constant term, when there is no η^1 present.



delimited by (see Eq. (4.32))

$$\frac{2|\beta_\mu|}{|E_{\mathbf{r}}|} \ll \eta \ll \frac{2|E_{\mathbf{r}}|}{\tilde{F}}. \quad (5.29)$$

WFAT is applicable when

$$\tilde{F} \ll \frac{E_{\mathbf{r}}^2}{|\beta_\mu|}. \quad (5.30)$$

5.2.1 WKB Wave Function

We now turn to deriving this WKB wave function. We expand the energy to first order in field strength

$$E_{\mathbf{r}} = E_{\mathbf{r}}^{(0)} - \mu_z \tilde{F} + O(F^2), \quad (5.31)$$

where the dipole moment can be calculated from the field-free wave function through the integral

$$\mu_z = - \left[\int_0^\infty dR \int d^3\mathbf{r} (QR_z + qz) \Psi^2(\mathbf{r}, R) - \int_0^\infty dR QR_z g^2(R) \right]. \quad (5.32)$$

We cast Eq. (5.18) in the form used in WKB

$$\left[\frac{d^2}{d\eta^2} + p^2(\eta) \right] f_\mu(\eta) = 0, \quad (5.33)$$

where

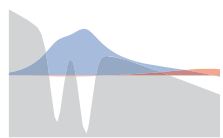
$$p^2(\eta) = \frac{\tilde{F}\eta}{4} + \frac{E_{\mathbf{r}}}{2} + \frac{\beta_\mu}{\eta} + O(\eta^{-2}). \quad (5.34)$$

The WKB wave function is given by [Eq. (B.11)]

$$f_\mu(\eta) = \frac{C_{\text{WKB}} e^{iS(\eta)}}{p^{1/2}(\eta)} \quad (5.35)$$

where the classical action is defined by

$$S(\eta) = \int_{\eta_0}^{\eta} p(\eta') d\eta', \quad (5.36)$$



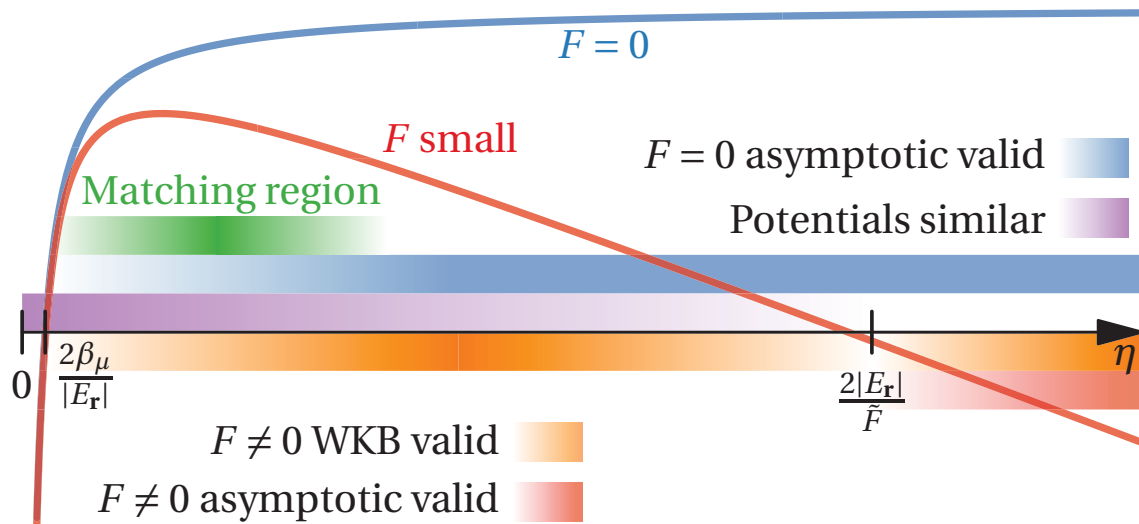
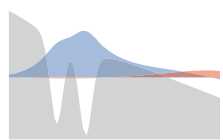


Figure 5.3: This figure shows the potential $-\frac{1}{2} \left[\frac{\tilde{F}\eta}{4} + \frac{E_r}{2} + \frac{\beta_\mu}{\eta} \right]$ of Eq. (5.18), as a function of η , for $F = 0$ and a small value of F . On the η axis the values $2\beta_\mu/|E_r|$ and $2|E_r|/\tilde{F}$ are indicated. These are quite close to the inner and outer classical turning points respectively, in fact in the $F \rightarrow 0$ limit they coincide with these. Different regions of η are indicated by colored bands around the η axis. These regions are all 'fuzzy', since they are defined by relations of the type $\eta \gg$ or $\eta \ll$, and a definite limit to them cannot be found, which is why they are shown with a color gradient. In the $\eta \ll 2|E_r|/\tilde{F}$ (purple) region, the potentials are similar. The $F = 0$ asymptotic Eq. (5.28) is valid in the (blue) region $\eta \gg 2\beta_\mu/|E_r|$. The overlap of these regions is the matching region. In the $F \neq 0$ case the WKB (orange region) is valid everywhere, except near the turning points, and the weak-field asymptotic expansion Eq. (5.19) is valid outside the outer turning point (red region).



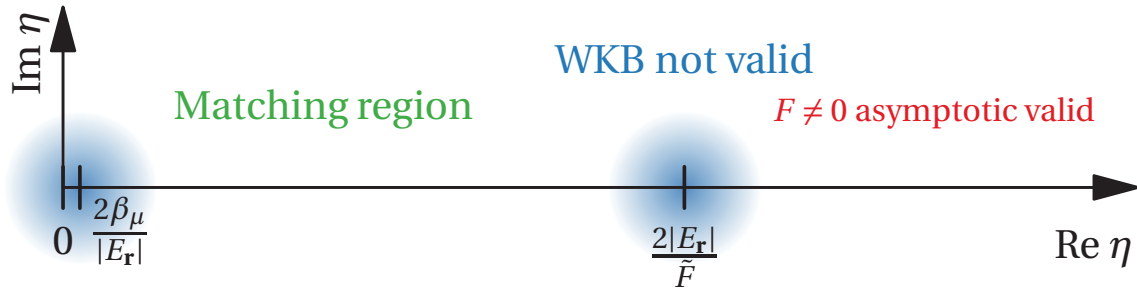


Figure 5.4: Complex η plane. The WKB is valid everywhere except near the classical turning points. The region where WKB is not valid is indicated by the blue circles. By analytically continuing the WKB into the complex plane around the turning points, the coefficient found from matching with the field-free state in the matching region can be related to the weak-field asymptotic state on the far side of the outer turning point.

with η_o chosen as the outer turning point. The WKB is accurate when the condition

$$\left| \frac{d}{d\eta} \frac{1}{p(\eta)} \right| \ll 1 \quad (5.37)$$

is fulfilled. In order to match the WKB wave function [Eq. (5.35)] with the asymptotics of the wave function we need to simplify the WKB wave function by considering the weak-field and large η limits.

It is convenient to introduce the re-scaled variable

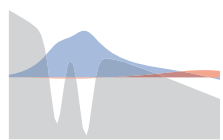
$$x = \frac{\tilde{F}\eta}{\varkappa^2}, \quad \eta = \frac{\varkappa^2 x}{\tilde{F}}, \quad (5.38)$$

where \varkappa was defined in Eq. (5.28). In terms of this variable the classical momentum takes the form

$$p^2(x) = \frac{\varkappa^2 x}{4} + \frac{-\frac{1}{2}\varkappa^2 - \mu_z \tilde{F} + O(F^2)}{2} + \frac{\tilde{F}\beta_\mu}{\varkappa^2 x} + O(\eta^{-2}). \quad (5.39)$$

We now consider the limit of small F , and simultaneously the limit of large η , since we only care about what happens in the asymptotic region

$$F \rightarrow 0, \quad \eta = O(F^{-1}), \quad x = O(F^0). \quad (5.40)$$



In this limit the classical momentum simplifies to

$$p^2(x) = \frac{\varkappa^2}{4} \left[x - 1 + \frac{2}{\varkappa^2} \left(-\mu_z + \frac{2\beta_\mu^{(0)}}{\varkappa^2 x} \right) \tilde{F} \right] + O(F^2). \quad (5.41)$$

The outer turning point η_o is in this limit given by

$$x_o = 1, \quad \eta_o = \frac{\varkappa^2}{\tilde{F}}. \quad (5.42)$$

The condition Eq. (5.37) for the applicability of WKB reduces in this limit to

$$|x - 1| \gg \frac{\tilde{F}^{2/3}}{\varkappa^2}, \quad (5.43)$$

which means the WKB wave function [Eq. (5.35)] is valid when we are not too close to the outer turning point $x_o = 1$.

In the limit (5.40) the action [Eq. (5.36)] takes the form

$$S(\eta) = \frac{\varkappa^3}{2\tilde{F}} \left[\frac{2}{3}(x-1)^{3/2} - \frac{2\tilde{F}}{\varkappa^2} \left(\mu_z(x-1)^{1/2} - \frac{2\beta_\mu^{(0)}}{\varkappa^2} \arctan(x-1)^{1/2} \right) + O(F^2) \right]. \quad (5.44)$$

WKB Wave Function in the Matching Region

We now consider the WKB in the matching region [Eq. (5.29)] at intermediate η . In terms of x the matching region is delimited by $|\beta_\mu| \tilde{F}/E_r^2 \ll x \ll 1$. In this region the action [Eq. (5.44)] takes the form

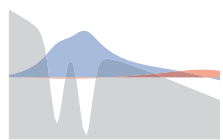
$$S(\eta) = i \frac{\varkappa^3}{2\tilde{F}} \left[-\frac{2}{3} + x - \frac{2\tilde{F}}{\varkappa^2} \left(\mu_z + \frac{\beta_\mu^{(0)}}{\varkappa^2} \ln \frac{x}{4} \right) + O(F^2) \right] \quad (5.45a)$$

$$= -i \frac{\varkappa^3}{3\tilde{F}} + i \frac{\varkappa\eta}{2} - i \varkappa\mu_z - i \frac{\beta_\mu^{(0)}}{\varkappa} \ln \frac{\tilde{F}\eta}{4\varkappa^2} + O(F^1). \quad (5.45b)$$

Note that the action is purely imaginary, since the matching region is located in the tunneling region of the weak-field state. The classical momentum is given in this region by $p(\eta) = i\varkappa/2$, which is most easily seen by calculating $p(\eta) = S'(\eta)$ and using $\frac{2|\beta_\mu|}{|E_r|} \ll \eta$. By matching the WKB wave function [Eq. (5.35)] in this region to the asymptotic of the field-free wave function [Eq. (5.28)] we obtain

$$C_{\text{WKB}} = D_\mu \left(\frac{\varkappa}{2} \right)^{1/2} \exp \left(-\frac{\varkappa^3}{3\tilde{F}} - \varkappa\mu_z - \frac{\beta_\mu^{(0)}}{\varkappa} \ln \frac{\tilde{F}}{4\varkappa^2} + i \frac{\pi}{4} \right), \quad (5.46)$$

where D_μ indicates either $D_{\mu\nu}$ or $D_\mu(k)$.



WKB Wave Function Beyond the Outer Turning Point

The WKB wave function can be analytically continued from the matching region $x \ll 1$ to the asymptotic region $x \gg 1$, where the asymptotic Eq. (5.19) is applicable. The analytic continuation is done through the upper half plane of the complex x plane, staying away from the outer turning point, such that the condition Eq. (5.37) is fulfilled. Since the WKB wave functions in the regions are connected, the constant C_{WKB} appearing in Eq. (5.35) is the same in both cases. In the $x \gg 1$ region the action [Eq. (5.44)] takes the form

$$S(\eta) = \frac{\varkappa^3}{2\tilde{F}} \left[\frac{2}{3}x^{3/2} - x^{1/2} - \frac{2\tilde{F}}{\varkappa^2} \left(\mu_z x^{1/2} - \frac{\pi\beta_\mu^{(0)}}{\varkappa^2} \right) + O(F^2) \right] \quad (5.47)$$

$$= \frac{\tilde{F}^{1/2}\eta^{3/2}}{3} - \left(\frac{\varkappa^2}{2} + \tilde{F}\mu_z \right) \left(\frac{\eta}{\tilde{F}} \right)^{1/2} + \frac{\pi\beta_\mu^{(0)}}{\varkappa} + O(F^1). \quad (5.48)$$

The classical momentum takes the form $p(\eta) = S'(\eta) = \frac{\tilde{F}^{1/2}\eta^{1/2}}{2}$. By matching the WKB wave function [Eq. (5.35)] with the $F \neq 0$ asymptotic [Eq. (5.19)] we obtain

$$C_\mu = C_{\text{WKB}} m^{-1/4} \exp\left(i \frac{\pi\beta_\mu^{(0)}}{\varkappa} \right). \quad (5.49)$$

where C_μ indicates either $C_{\mu\nu}$ or $C_\mu(k)$.

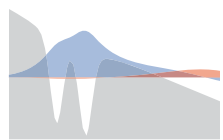
We now insert the WKB coefficient C_{WKB} which was found by matching the WKB to the field-free state in the matching region [Eq. (5.46)] in the above expression, which yields

$$C_\mu = D_\mu \left(\frac{\varkappa}{2m^{1/2}} \right)^{1/2} \left(\frac{4\varkappa^2}{\tilde{F}} \right)^{\frac{\beta_\mu^{(0)}}{\varkappa}} \exp\left(-\frac{\varkappa^3}{3\tilde{F}} - \varkappa\mu_z + i\frac{\pi}{4} + i\frac{\pi\beta_\mu^{(0)}}{\varkappa} \right). \quad (5.50)$$

This equation is called the connection formula, and it is the central result of WFAT. It links the field free asymptotic coefficients D_μ to the weak-field asymptotic coefficients C_μ . The partial rates [Eqs. (5.26)] in WFAT can be written

$$\Gamma_{\mu\nu}^{\text{WFAT}} = G_{\mu\nu}^2 W_{\mu\nu}(F), \quad (5.51a)$$

$$P_\mu^{\text{WFAT}}(k) = G_\mu^2(k) W_\mu(F, k), \quad (5.51b)$$



where the field factor $W_\mu(F)$ and structure factors $G_{\mu\nu}, G_\mu(k)$ are defined by

$$W_\mu(F) = \frac{\varkappa}{2m^{1/2}} \left(\frac{4\varkappa^2}{\tilde{F}} \right)^{2\frac{\beta_\mu^{(0)}}{\varkappa}} \exp\left(-\frac{2\varkappa^3}{3\tilde{F}}\right), \quad (5.52a)$$

$$G_{\mu\nu} = D_{\mu\nu} e^{-\varkappa\mu_z}, \quad (5.52b)$$

$$G_\mu(k) = D_\mu(k) e^{-\varkappa\mu_z}, \quad (5.52c)$$

where $W_\mu(F)$ can be either $W_{\mu\nu}(F)$ or $W_\mu(F, k)$. The WFAT partial rates [Eq. (5.51)] are thus partitioned into two factors. The structure factor is obtainable from the field free state and describes the structure of this, while the field factor contains all the field dependence.

5.3 Born-Oppenheimer Approximation

See Sec. 4.4 for discussion of the BO approximation. In 3D the BO wave function takes the form $\Psi_{BO}(\mathbf{r}, R) = \psi_e(\mathbf{r}; R)\chi(R)$, where the components fulfill the BO equations

$$\left[-\frac{1}{2}\nabla_{\mathbf{r}}^2 + Fz + V(\mathbf{r}, R) - E_e(R; F) \right] \psi_e(\mathbf{r}; R) = 0, \quad (5.53a)$$

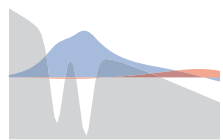
$$\left[-\frac{1}{2M}\frac{d^2}{dR^2} + FQR_z + U(R) + E_e(R; F) - E_{BO}(F) \right] \chi(R) = 0. \quad (5.53b)$$

The electronic problem [Eq. (5.53a)] is seen to be on the same form as the asymptotic electronic Equation (5.8a), so Eq. (5.53a) can be written in parabolic coordinates and expanded in the $\eta \rightarrow \infty$ limit in the same way as Eq. (5.8a), only we replace the energy $E_{\mathbf{r}}$ with the electronic energy $E_e(R; F)$ and put $m = 1, q = 1$. This allows us to write the electronic wave function for $F > 0$ in the form

$$\psi_e(\mathbf{r}; R)|_{\eta \rightarrow \infty} = \sum_{\mu} \eta^{-1/2} C_{\mu}(R) f(\eta; R) \Phi_{\mu}(\xi, \varphi; R), \quad (5.54)$$

where $C_{\mu}(R)$ are asymptotic coefficients and the outgoing-wave is given by

$$f(\eta; R) = \frac{2^{1/2}}{(F\eta)^{1/4}} \exp\left[\frac{iF^{1/2}\eta^{3/2}}{3} + \frac{iE_e(R; F)\eta^{1/2}}{F^{1/2}} \right]. \quad (5.55)$$



This choice of outgoing-wave boundary condition means that once again we have a SS with energy $E_e(R; F) = \mathcal{E}(R; F) - \frac{i}{2}\Gamma_e(R; F)$. We define the partial electronic rate by

$$\Gamma_{e,\mu}(R) = |C_\mu(R)|^2. \quad (5.56)$$

As in Chap. 2 there is a flux of probability associated with the SS, through which we can relate the electronic rate to the asymptotic coefficient

$$\Gamma_e(R; F)|_{F \rightarrow 0} = \sum_{\mu} \Gamma_{e,\mu}(R). \quad (5.57)$$

We wish to find expressions for the partial rates in the BO approximation, so we insert the BO wave function in the expression for the asymptotic coefficients [Eq. (5.22)]

$$C_{\mu}^{\text{BO}}(E_R) = \sum_{\nu} \int_0^{\infty} g(R) C_{\nu}(R) \frac{f(\eta; R)}{f(\eta)} \langle \Phi_{\mu}(\xi, \varphi) | \Phi_{\nu}(\xi, \varphi; R) \rangle_{(\xi, \varphi)} \chi(R) dR \Big|_{\eta \rightarrow \infty}. \quad (5.58)$$

If we assume that the electronic energy $E_{\mathbf{r}}$ is the same as the electronic energy $E_e(R; F)$ this reduces to

$$C_{\mu}^{\text{BO}}(E_R) = \int_0^{\infty} g(R) C_{\mu}(R) \chi(R) dR. \quad (5.59)$$

Note that there is no explicit reference to the electron coordinate in this expression. We will use this expression to define BO partial rates

$$\Gamma_{\mu\nu}^{\text{BO}} = |C_{\mu\nu}^{\text{BO}}|^2, \quad (5.60a)$$

$$P_{\mu}^{\text{BO}}(k) = |C_{\mu}^{\text{BO}}(k)|^2, \quad (5.60b)$$

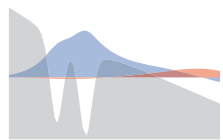
where

$$C_{\mu\nu}^{\text{BO}} = \int_0^{\infty} g_{\nu}(R) C_{\mu}(R) \chi(R) dR, \quad (5.61a)$$

$$C_{\mu}^{\text{BO}}(k) = \int_0^{\infty} g(R, k) C_{\mu}(R) \chi(R) dR. \quad (5.61b)$$

5.3.1 Reflection Principle

Since it only refers to the nuclear coordinate, the reflection principle can be developed in the exactly same way as in Sec. 4.4.1, only including the parabolic index μ where relevant.



5.3.2 WFAT in BO

See discussion in Sec.4.4.2. First we note that the field-free electronic wave function can be asymptotically expanded

$$\psi_e^{(0)}(\mathbf{r}; R)|_{\eta \rightarrow \infty} = \sum_{\mu} \eta^{-1/2} D_{\mu}(R) f_{\mu}^{(0)}(\eta; R) \Phi_{\mu}^{(0)}(\xi, \varphi; R), \quad (5.62)$$

where

$$f_{\mu}^{(0)}(\eta; R) = \eta^{\beta_{\mu}^{(0)}(R)/\varkappa(R)} e^{-\varkappa(R)\eta/2}, \quad \varkappa(R) = \sqrt{-2E_e(R; F=0)}, \quad (5.63)$$

and $\beta_{\mu}^{(0)}$ and $\Phi_{\mu}^{(0)}(\xi, \varphi; R)$ are the eigenvalues and eigenfunctions solving Eq. (5.15a) with $E_e(R; F=0)$ replacing $E_{\mathbf{r}}$. The WFAT can now be developed in the same way as in Sec. 5.2. This yields

$$\Gamma_{e,\mu}^{\text{WFAT}}(R) = G_{\mu}^2(R) W_{\mu}(F; R), \quad (5.64)$$

where the field factor $W_{\mu}(F; R)$ and structure factor $G_{\mu}(R)$ are defined by

$$W_{\mu}(F; R) = \frac{\varkappa(R)}{2} \left(\frac{4\varkappa^2(R)}{F} \right)^{2 \frac{\beta_{\mu}^{(0)}(R)}{\varkappa(R)}} \exp\left(-\frac{2\varkappa^3(R)}{3F} \right), \quad (5.65a)$$

$$G_{\mu} = D_{\mu}(R) e^{-\varkappa(R)\mu z}. \quad (5.65b)$$

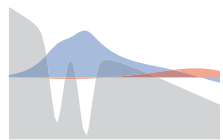
5.4 One and Three Dimensions Compared

There are some subtle differences between the 1D and 3D WFAT expressions obtained. These originate in the use of different coordinates, and therefore different definitions of the asymptotic coefficients. First we note that if we consider $\tilde{x} = \tilde{y} = 0$, or equivalently $\xi = 0$, we get that $\eta = -2\tilde{z} = -2\sqrt{m}z$. Also for fixed x, y we have that

$$\eta|_{z \rightarrow -\infty} \rightarrow -2\tilde{z}. \quad (5.66)$$

We can therefore think of the η coordinate in the 3D theory as corresponding to z of the 1D theory. Most of the 1D equations can be obtained from the 3D expressions by substituting $\eta \rightarrow -2\sqrt{m}z$ and removing the parabolic index μ , which describes what happens in the ξ, φ directions 'transversal' to η .

Another subtle difference between the 1D and 3D formulations is the factor of $2^{1/2}$ that appears in the pre-exponential of the 3D outgoing-wave (5.19), but not in the corresponding 1D asymptotic (4.16). This originates from the fact that we have used a reduced wave function in the η coordinate, see Eq. (5.17).



5.4.1 Hydrogen Atom

As an example let us consider the ground state of the hydrogen atom and compare the 1D and 3D WFAT formulations for this. The reduced mass and charge should be put to $m = q = 1$, and we have the following parameters: $Z = 1, E = -\frac{1}{2}, \kappa = 1, \mu_z = 0$. For the 3D case the parabolic eigenvalue of the dominant state⁴ $\mu = (0, 0)$ is given by $\beta_{(0,0)}^{(0)} = 1/2$. The WFAT rate (5.51) then takes the form

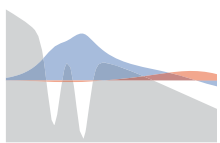
$$\Gamma_{(0,0)}^{\text{WFAT}} = D_{(0,0)}^2 \frac{1}{2} \frac{4}{F} \exp\left(-\frac{2}{3F}\right). \quad (5.67)$$

Formulating the same for 1D is more complicated, since here we cannot avoid the Coulomb singularity. We can however choose to consider a soft-coulomb potential $V(z) = (z^2 + a)^{-1/2}$ which has asymptotic tail z^{-1} and ground state energy $E = -\frac{1}{2}$. For such a potential it would require a numerical calculation to determine the field-free asymptotic coefficient D , but we do not concern ourselves with the value of this coefficient here. Instead we just write the WFAT rate (4.57)

$$\Gamma_v^{\text{WFAT}} = D^2 \left(\frac{2}{F}\right)^2 \exp\left(-\frac{2}{3F}\right). \quad (5.68)$$

We note that the contents of the exponential functions are identical in the two cases. There is a difference in the pre-exponential power function, where the exponent is different in the 3D and 1D cases. This is because the parabolic eigenvalue $\beta_{(0,0)}^{(0)} = 1/2$ is not identical with the asymptotic charge $Z = 1$. This eventually originates from 'fictitious forces' related to the parabolic coordinates.

⁴For details on this quantum number and the parabolic eigenvalue see Ref. [11].



6 Numerical Methods

In this chapter the numerical methods used to find ionization rates and various other properties of the Siegert states are presented. The methods and algorithms described here have been implemented in FORTRAN. The FORTRAN programs are based on code written by my co-supervisor Oleg for an adiabatic basis, but they have been heavily modified by me to make use of a diabatic basis. Additionally I have added the parts of these programs that allow for construction of wave functions. Parts of the material in this chapter also appeared in [1], of which I am the first author.

6.1 Reduction to a Multi-Channel Eigenvalue Problem

In order to solve the TISE (4.1) we introduce a complete set of vibrational states of the molecular ion, the so called *diabatic basis*¹

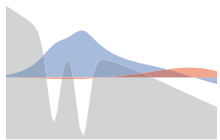
$$\left[-\frac{1}{2M} \frac{d^2}{dR^2} + U(R) + FQR - \varepsilon_v(F) \right] \varphi_v(R) = 0, \quad v = 0, 1, 2, \dots, \quad (6.1)$$

with boundary conditions $\varphi_v(0) = 0$, expressing that we do not allow the nuclei to pass through each other, and $\varphi_v(R_{\max}) = 0$ because we use a box of finite size in R . This is reasonable to do as long as the exact wave function does not have considerable weight around or further out than R_{\max} . The diabatic states $\varphi_v(R)$ coincide with the bound state solutions $g_v(R)$ of Eq. (4.7b) when R_{\max} is sufficiently large.

The diabatic basis functions $\varphi_v(R)$ and their eigenvalues $\varepsilon_v(F)$ are real and the basis functions are orthonormal

$$\int_0^{R_{\max}} dR \varphi_v(R) \varphi_{v'}(R) = \delta_{vv'}. \quad (6.2)$$

¹The term diabatic here does not refer any type of fast motion or rapidly changing variable. It is a name we use simply because the chosen basis is not an adiabatic basis.



The wave function $\Psi(z, R)$ is expressed in the diabatic basis as

$$\Psi(z, R) = \sum_v f_v(z) \varphi_v(R). \quad (6.3)$$

Inserting the wave function (6.3) in the Schrödinger equation (4.1), and projecting on the $\varphi_v(R)$ basis yields

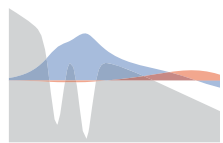
$$\left[-\frac{1}{2m} \frac{d^2}{dz^2} + Fqz + \varepsilon_v(F) - E(F) \right] f_v(z) + \sum_{v'} V_{vv'}(z) f_{v'}(z) = 0, \quad (6.4)$$

where $V_{vv'}(z) = \int_0^\infty dR \varphi_v(R) V(z, R) \varphi_{v'}(R)$. By projecting out the R degree of freedom we thus obtain a system of coupled equations for the *coefficient functions* $f_v(z)$. Let us consider our problem in the limit $|z| \rightarrow \infty$. We assume that our potential in this limit has the Coulomb-form from Eq. (4.6). In this asymptotic limit the potential is independent of R , and the channel equations (6.4) decouple. We wish to solve these channel equations subject to the outgoing-wave boundary condition given by Eq. (4.16), where $E_z = E - \varepsilon_v$.

6.2 Spatial Basis: Discrete Variable Representation

In this section the properties of the discrete variable representation (DVR) [21] basis will be analyzed. We will use two different kinds of these bases for the z and R coordinates. The basis functions of a DVR basis are localized in space, and we can think of it as similar to a grid representation. We want to use these DVR bases to describe functions of a coordinate x on an interval $[x_{\min}, x_{\max}]$. The DVR functions are however more naturally defined using a different variable t on a different interval $[t_{\min}, t_{\max}]$, which depends on the specific DVR considered. We therefore first consider coordinate transformations between the coordinate x and the natural DVR variable t . In this section we will use the bra-ket notation to indicate integration in the x coordinate

$$\langle \cdot \rangle = \int_{x_{\min}}^{x_{\max}} \cdot dx. \quad (6.5)$$



6.2.1 Coordinate Transform

We consider the linear transformation from $t \in [t_{\min}, t_{\max}]$ to $x \in [x_{\min}, x_{\max}]$ given by

$$x = x_{\min} + \frac{x_{\max} - x_{\min}}{t_{\max} - t_{\min}}(t - t_{\min}) \quad (6.6a)$$

$$= x_{\min} + s_x(t - t_{\min}), \quad (6.6b)$$

where

$$s_x = \frac{x_{\max} - x_{\min}}{t_{\max} - t_{\min}}. \quad (6.7)$$

The inverse transformation is given by

$$t = \frac{x - x_{\min}}{s_x} + t_{\min}. \quad (6.8)$$

Integrals are transformed according to

$$\int_{x_{\min}}^{x_{\max}} f(x) dx = s_x \int_{t_{\min}}^{t_{\max}} f(x(t)) dt. \quad (6.9)$$

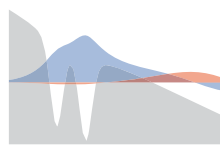
In the rest of this section we will use x and t interchangeably, with the above transformation implicitly included.

6.2.2 Quadrature

A DVR basis is intimately linked with a corresponding Gaussian quadrature [22]. Here we will only list the properties of a Gaussian quadrature, but not prove these. A Gaussian quadrature is a way of approximately evaluating integrals of the form

$$\int_{t_{\min}}^{t_{\max}} \omega(t) F(t) dt \approx \sum_{i=1}^N w_i F(t_i), \quad (6.10)$$

where $\omega(t)$ is some known weight function, and t_i, w_i are called quadrature points (or nodes) and quadrature weights, respectively. These are chosen in an 'optimal' way such that Eq. (6.10) is as close to equality as possible. By optimal is meant that we for a given weight function $\omega(t)$ and interval $[t_{\min}, t_{\max}]$ choose the points and weights such that Eq. (6.10) holds exactly



for all polynomials up to order $2N - 1$. This can be achieved by inserting the monomials t^k as $F(t)$ in Eq. (6.10) and require equality

$$\int_{t_{\min}}^{t_{\max}} \omega(t) t^k dt = \sum_{i=1}^N w_i t_i^k \quad k = 0, \dots, 2N - 1. \quad (6.11)$$

These $2N$ equations fixes the N points t_i and N weights w_i . One can define a set of orthogonal polynomials $p_n(t)$ of degree n associated with the weight function $\omega(t)$ such that

$$\int_{t_{\min}}^{t_{\max}} \omega(t) t^k p_n(t) dt = 0, \quad k = 0, \dots, n - 1. \quad (6.12)$$

Up to a normalization these polynomials are unique. It can be shown that the quadrature points for an N point quadrature are given by the zeros of the $p_N(t)$ polynomial associated with the weight function $\omega(t)$. We shall use these polynomials in the construction of the DVR basis.

6.2.3 DVR Properties

Now that we have introduced the coordinate transformation Eq. (6.6b) and the quadrature we can define the DVR basis. The N functions $\pi_i(t)$ defined on the interval $[t_{\min}, t_{\max}]$ should possess the following three properties to be called a DVR basis

1. Orthonormality:

$$\langle \pi_i | \pi_j \rangle = \delta_{ij} \quad (6.13)$$

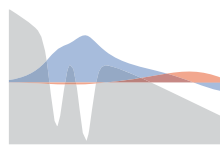
2. Delta property:

$$\pi_i(t_j) = \frac{1}{\sqrt{w_j s_x}} \delta_{ij} \quad (6.14)$$

Where t_j and w_j are the j 'th quadrature point and weight, respectively, of the associated Gaussian quadrature. s_x is the coordinate transformation factor from Eq. (6.7).

3. Integral of arbitrary function $F(x)$

$$\langle \pi_i | F(x) | \pi_j \rangle \approx F(x_i) \delta_{ij}. \quad (6.15)$$



We shall construct our DVR basis functions building on a spectral basis. A spectral basis is one where the basis functions extend over the full interval $[t_{\min}, t_{\max}]$ on which they are defined, as opposed to the DVR basis functions that are localized around their corresponding quadrature points. The orthogonal polynomials associated with the weight function $\omega(t)$ are an example of such spectral functions. Let us denote the N spectral basis functions by $\psi_j(x)$. Following Ref. [23], let us assume that we have constructed a DVR basis $\pi_i(t)$ that fulfill the three DVR properties [Eqs. (6.13)-(6.15)]. Then we can calculate the overlap of these with the spectral basis functions using the quadrature rule (6.10)

$$\langle \psi_k | \pi_j \rangle = s_x \int_{t_{\min}}^{t_{\max}} \psi_k(x) \pi_j(t) dt \quad (6.16a)$$

$$\approx s_x \sum_{n=1}^N w_n \psi_k(x_n) \pi_j(t_n) \quad (6.16b)$$

$$= \sqrt{w_j s_x} \psi_k(x_j). \quad (6.16c)$$

The DVR basis span the same space as the spectral basis, so we can write

$$\pi_j(x) = \sum_{n=1}^N \psi_n(x) \langle \psi_n | \pi_j \rangle \quad (6.17a)$$

$$\approx \sqrt{w_j s_x} \sum_{n=1}^N \psi_n(x) \psi_n(x_j). \quad (6.17b)$$

The transformation between the spectral and DVR bases can be expressed in terms of a matrix T

$$\pi_j(x) = \sum_{n=1}^N T_{jn} \psi_n(x), \quad (6.18a)$$

$$T_{jn} = \sqrt{w_j s_x} \psi_n(x_j). \quad (6.18b)$$

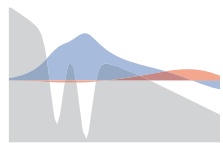
We can also write up matrix elements in the spectral basis as

$$\langle \psi_n | f(x) | \psi_m \rangle = \sum_{i,j} T_{in} T_{jm} \langle \pi_i | f(x) | \pi_j \rangle \quad (6.19a)$$

$$= \sum_{i,j} T_{in} T_{jm} \delta_{ij} f(x_i) \quad (6.19b)$$

$$= \sum_i T_{in} T_{im} f(x_i). \quad (6.19c)$$

In the following we will describe two different kinds of DVR, each based on their own specific quadrature.



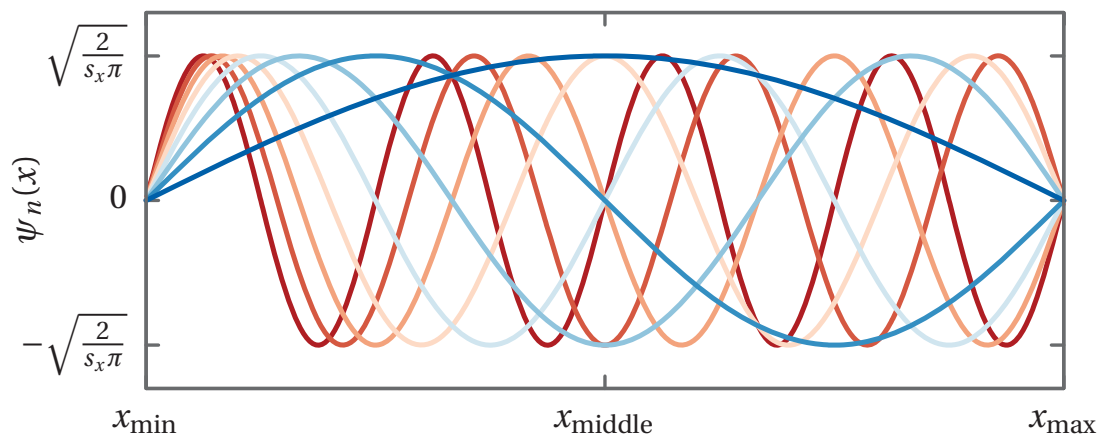


Figure 6.1: Spectral sine functions $\psi_j(x)$ [Eq. (6.20)]. These function extend over the whole interval $[x_{\min}, x_{\max}]$. The first function is colored dark blue, the last dark red, the others in intermediate lighter colors.

6.2.4 Sine-DVR

The spectral basis of the first DVR we consider is in fact not polynomial. In this so called sine-DVR we consider spectral functions of the form [see Fig. 6.1]

$$\psi_n(x) = \sqrt{\frac{2}{\pi s_x}} \sin nt, \quad (6.20)$$

$t_{\min} = 0$, $t_{\max} = \pi$ and

$$t = \frac{x - x_{\min}}{s_x}, \quad (6.21)$$

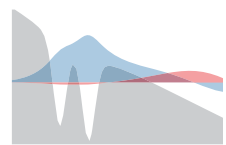
$$s_x = \frac{x_{\max} - x_{\min}}{\pi}. \quad (6.22)$$

The quadrature points associated with this spectral function are the zeros of the $\sin[(N+1)t]$ function

$$t_k = \frac{k\pi}{(N+1)}. \quad (6.23)$$

In order to determine the weights we will look at the Chebyshev quadrature [24, <http://dlmf.nist.gov/3.5.E24>]

$$\int_{-1}^1 g(y) \sqrt{1-y^2} dy = \sum_k w_k g(y_k), \quad (6.24)$$



which has nodes and weights

$$y_k = \cos\left(\frac{k}{N+1}\pi\right), \quad (6.25a)$$

$$\omega_k = \frac{\pi}{N+1} \sin^2\left(\frac{k\pi}{N+1}\right). \quad (6.25b)$$

We wish to transform this to the variable t on the interval $[0, \pi]$, and define

$$h(t) = \frac{f(t)}{\sin^2 t}, \quad (6.26a)$$

$$y = \cos t. \quad (6.26b)$$

Let us now transform the integral

$$\int_0^\pi f(t) dt = \int_0^\pi h(t) \sin^2 t dt \quad (6.27a)$$

$$= \int_{-1}^1 h(\cos^{-1} y) \sqrt{1-y^2} dy. \quad (6.27b)$$

We see that this has the same form as the Chebyshev quadrature, where $g = h \circ \cos^{-1}$, and by applying the Chebyshev quadrature to this integral we obtain

$$\int_0^\pi f(t) dt = \sum_{k=1}^N \frac{\pi}{N+1} \sin^2\left(\frac{k\pi}{N+1}\right) h(\cos^{-1}(y_k)) \quad (6.28a)$$

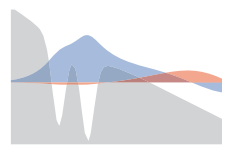
$$= \sum_{k=1}^N \frac{\pi}{N+1} f(t_k), \quad (6.28b)$$

where for $k = 1, \dots, N$ we identify the quadrature nodes and weights

$$t_k = \cos^{-1} y_k = \frac{k\pi}{N+1}, \quad (6.29a)$$

$$w_k = \frac{\pi}{N+1}. \quad (6.29b)$$

The nodes are identical to the zeros of $\sin[(N+1)t]$ [Eq. (6.23)], and we can use the weights above in our sine quadrature. It might seem strange that the Chebyshev quadrature has anything to do with the sine function, but the Chebyshev polynomials and trigonometric functions are in fact intimately linked.



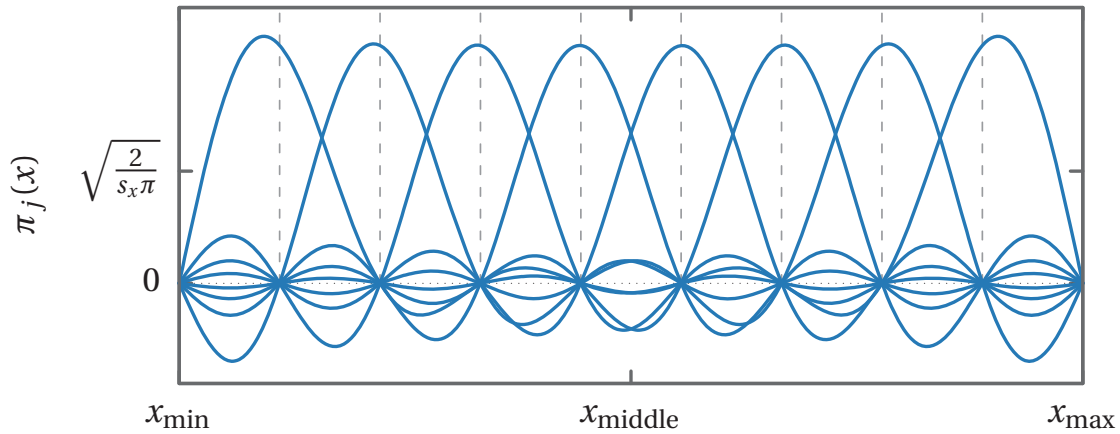


Figure 6.2: Sine-DVR functions π_j [Eq. (6.31a)]. The quadrature points are indicated by vertical dashed lines, and at each of these all but one DVR function go to zero. Each DVR function primarily has weight around its quadrature point. Note, however, that a DVR function does not in general attain its maximum value at its quadrature point.

The transformation matrix [Eq. (6.18b)] from the spectral to the DVR basis takes the form

$$T_{jn} = \sqrt{\frac{2}{N+1}} \sin nt_j, \quad (6.30)$$

and the DVR functions [Eq. 6.18a] can be written

$$\pi_j(x) = \frac{2}{\sqrt{(N+1)\pi s_x}} \sum_{n=1}^N \sin nt \sin nt_j \quad (6.31a)$$

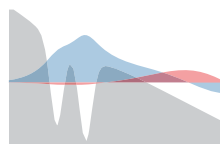
$$= \frac{2}{\pi} \sqrt{\frac{w_j}{s_x}} \sum_{n=1}^N \sin nt \sin nt_j. \quad (6.31b)$$

These functions are illustrated in Fig. 6.2. Note that they all go to zero on the boundary, like the sine functions from which they are built.

Properties

Here we check that the three DVR properties are indeed fulfilled by the functions $\pi_j(x)$ [Eq. (6.31a)]

Property 1. First we note that by writing the sine functions as complex exponential function (Eulers formula) and recognizing the resulting



expression as two geometric series one can show

$$\sum_n^N \sin nt_k \sin nt_j = \frac{N+1}{2} \delta_{jk}, \quad (6.32)$$

where t_k and t_j are quadrature points from Eq. (6.23). We will also need the integral

$$\int_0^\pi \sin nt \sin mt dt = \frac{\pi}{2} \delta_{mn}. \quad (6.33)$$

Now we can calculate the overlap of the DVR functions

$$\begin{aligned} \langle \pi_i | \pi_j \rangle &= \frac{4}{(N+1)\pi} \sum_{m,n=1}^N \sin mt_i \sin nt_j \int_0^\pi \sin nt \sin mt dt \\ &= \delta_{ij}. \end{aligned} \quad (6.34)$$

Property 2. We use the result Eq. (6.32)

$$\pi_i(x_j) = \frac{2}{\pi} \sqrt{\frac{w_j}{s_x}} \sum_{n=1}^N \sin nt_j \sin nt_i \quad (6.35a)$$

$$= \frac{1}{\sqrt{w_i s_x}} \delta_{ij}. \quad (6.35b)$$

Property 3. Here we first apply the quadrature Eq. (6.28b), and then use property 2

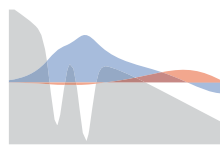
$$\begin{aligned} \langle \pi_i | F(x) | \pi_j \rangle &\approx s_x \sum_k w_k \pi_i(x_k) F(x_k) \pi_j(x_k) \\ &= F(x_i) \delta_{ij}. \end{aligned} \quad (6.36)$$

So the sine-DVR functions [Eq. (6.31a)] indeed possesses the three DVR properties.

Kinetic Energy

We want to calculate kinetic energy matrix elements in the DVR basis given by

$$K_{ij} = \left\langle \pi_i \left| -\frac{1}{2} \frac{d^2}{dx^2} \right| \pi_j \right\rangle. \quad (6.37)$$



Here we put the mass to 1, rescaling the kinetic energy with the actual mass is trivial and can be done at a later stage. First we note that for the spectral functions (6.20)

$$\frac{d^2}{dx^2}\psi_n(x) = -s_x^{-2}n^2\psi_n(x). \quad (6.38)$$

So the matrix element becomes

$$K_{ij} = - \sum_{n,m=1}^N T_{in}T_{jm} \left\langle \psi_n \left| \frac{1}{2} \frac{d^2}{dx^2} \right| \psi_m \right\rangle \quad (6.39a)$$

$$= \frac{1}{2s_x^2} \sum_{n,m=1}^N m^2 T_{in}T_{jm} \langle \psi_n | \psi_m \rangle \quad (6.39b)$$

$$= \frac{1}{2s_x^2} \sum_{n=1}^N n^2 T_{in}T_{jn}. \quad (6.39c)$$

6.2.5 Legendre DVR

We now consider another DVR, the Legendre DVR, where the spectral functions are defined in terms of Legendre polynomials. Legendre polynomials are defined on the interval $t \in [-1, 1]$ with the weight function $\omega(t) = 1$, and they are given by Rodrigues' formula

$$P_n(t) = \frac{1}{2^n n!} \left(\frac{d}{dt} \right)^n (t^2 - 1)^n. \quad (6.40)$$

These polynomials are illustrated in Fig. 6.3. In this case the coordinate scaling factor [Eq. (6.7)] is

$$s_x = \frac{x_{\max} - x_{\min}}{2}. \quad (6.41)$$

The Legendre polynomials obey the recurrence relations

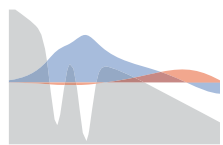
$$(2n+1)P_n(t) = P'_{n+1}(t) - P'_{n-1}(t) \quad (6.42a)$$

$$(n+1)P_{n+1}(t) = (2n+1)tP_n(t) - nP_{n-1}(t) \quad (6.42b)$$

$$(1-t^2)P'_n(t) = nP_{n-1}(t) - n t P_n(t), \quad (6.42c)$$

where $p'(t) = \frac{d}{dt}p(t)$ and have the orthogonality relation

$$\int_{-1}^1 P_m(t)P_n(t)dt = \frac{2}{2n+1}\delta_{mn}. \quad (6.43)$$



The quadrature points are the i 'th root of $P_N(t)$ denoted t_i . The weights for the associated quadrature can be written

$$w_i = \frac{2}{NP_{N-1}(t_i)P'_N(t_i)}. \quad (6.44)$$

We also define the rescaled Legendre polynomials

$$p_n(t) = \sqrt{\frac{2n+1}{2}} P_n(t). \quad (6.45)$$

These functions are orthonormal, see Eq. (6.43). From Eq. (6.42b) the following recurrence relations can be shown

$$p_n(t) = t \frac{\sqrt{4n^2-1}}{n} p_{n-1}(t) - \left(1 - \frac{1}{n}\right) \sqrt{\frac{n+1/2}{n-3/2}} p_{n-2}(t). \quad (6.46a)$$

$$p'_n(t) = \frac{1}{1-t^2} \left(n \sqrt{\frac{2n+1}{2n-1}} p_{n-1}(t) - n t p_n(t) \right) \quad (6.46b)$$

The quadrature weights can be written as

$$w_i = \frac{\sqrt{4N^2-1}}{N p_{N-1}(t_i) p'_N(t_i)}. \quad (6.47)$$

We now define our spectral functions in terms of the rescaled Legendre polynomials

$$\psi_n(x) = \sqrt{\frac{1}{s_x}} p_{n-1}(t), \quad n = 1, \dots, N. \quad (6.48)$$

These are orthonormal with respect to integration in x

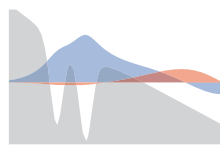
$$\langle \psi_m | \psi_n \rangle = \delta_{mn}. \quad (6.49)$$

The transformation matrix [Eq. (6.18b)] takes the form

$$T_{jn} = \sqrt{w_j} p_{n-1}(t_j) \quad (6.50)$$

The DVR basis is explicitly given by

$$\pi_j(x) = \sum_{n=1}^N \sqrt{\frac{w_j}{s_x}} p_{n-1}(t_j) p_{n-1}(t), \quad (6.51)$$



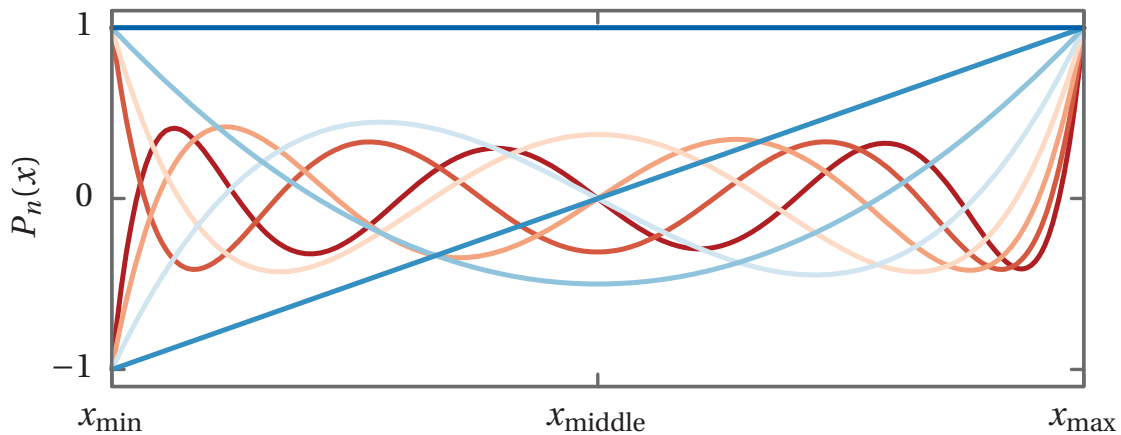


Figure 6.3: Legendre polynomials, from which the spectral functions $\psi_j(x)$ [Eq. (6.48)] are built. The first polynomial is colored dark blue, the last dark red, the others in intermediate lighter colors.

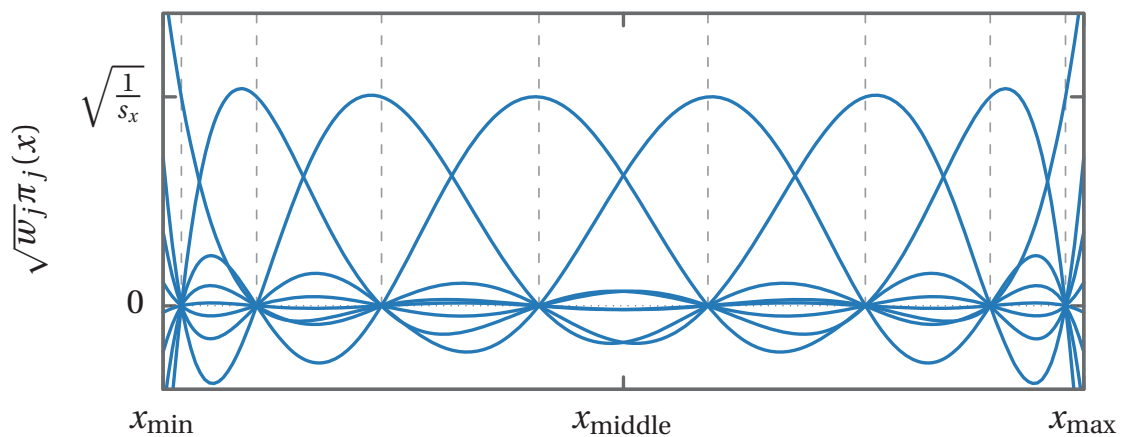
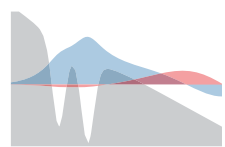


Figure 6.4: Legendre-DVR functions π_j [Eq. (6.51)]. At each quadrature point all the other DVR functions go to zero. Each DVR function primarily has weight around its quadrature point. The DVR functions have been multiplied by the square root of the weight to make the plot look more balanced.



and is illustrated in Fig. 6.4. Note that these functions do not go to zero on the boundary.

Notice that the symmetry of the Legendre polynomials $P_n(-t) = (-1)^n P_n(t)$ implies $t_{N+1-i} = -t_i$ and therefore

$$T_{N+1-i,n} = (-1)^{n-1} T_{in}. \quad (6.52)$$

This implies that

$$\pi_j(-x) = \sum_{n=1}^N (-1)^{n-1} T_{N+1-j,n} (-1)^{n-1} \psi_n(x) \quad (6.53a)$$

$$= \pi_{N+1-j}(x). \quad (6.53b)$$

In the next section we will need the DVR basis functions evaluated at the boundaries of the interval $[x_{\min}, x_{\max}]$.

$$\pi_j(x) = \sum_{n=1}^N T_{jn} \sqrt{\frac{n-1/2}{s_x}} \cdot \begin{cases} 1 & x = x_{\max} \\ (-1)^{n-1} & x = x_{\min}. \end{cases} \quad (6.54)$$

Kinetic Energy

We also need to find the kinetic energy matrix elements

$$K_{ij} = \frac{1}{2m} \int_{x_{\min}}^{x_{\max}} \frac{d}{dx} \pi_i(x) \frac{d}{dx} \pi_j(x) dx \quad (6.55a)$$

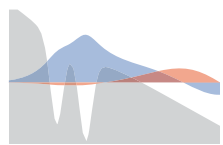
$$= \frac{1}{2m} \sum_{n,m=1}^N T_{in} T_{jm} \int_{x_{\min}}^{x_{\max}} \frac{d}{dx} \psi_n(x) \frac{d}{dx} \psi_m(x) dx \quad (6.55b)$$

$$= \frac{1}{2m} \frac{1}{s_x^2} \sum_{n,m=1}^N T_{in} T_{jm} \int_{-1}^1 p'_{n-1}(t) p'_{m-1}(t) dt. \quad (6.55c)$$

We want to evaluate the integral in this last expression. The following is similar to a derivation in Ref. [25]. From the recurrence relation (6.42a) we know that the derivative of a Legendre polynomial is expressible as a linear combination of lower order Legendre polynomials²

$$p'_m(t) = \sum_{k=0}^{m-1} a_{mk} p_k(t). \quad (6.56)$$

²It also follows from the fact that any polynomial of a given order can be written as a linear combination of Legendre polynomials up to that order.



From the orthogonality of the Legendre polynomials we get

$$a_{mk} = \int_{-1}^1 dt p'_m(t) p_k(t), \quad (6.57)$$

and

$$a_{mk} + a_{km} = \int_{-1}^1 dt (p_m(t) p_k(t))' \quad (6.58a)$$

$$= p_m(1) p_k(1) - p_m(-1) p_k(-1) \quad (6.58b)$$

$$= \frac{1}{2} \sqrt{2m-1} \sqrt{2k-1} (1 - (-1)^{m-k}). \quad (6.58c)$$

The coefficients a_{mk} thus have the values

$$a_{mk} = \begin{cases} \sqrt{2m-1} \sqrt{2k-1}, & \text{if } k = m-1, m-3, \dots \geq 1 \\ 0 & \text{otherwise.} \end{cases} \quad (6.59)$$

The integral of the derivative of the rescaled Legendre polynomials thus takes the form

$$\int_{-1}^1 p'_{n-1}(t) p'_{m-1}(t) dt = \sum_{k=1}^{m-1} a_{mk} \sum_{l=1}^{n-1} a_{nl} \delta_{kl}. \quad (6.60)$$

The kinetic energy becomes

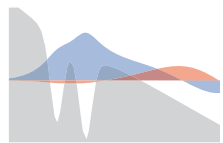
$$K_{ij} = \frac{1}{2m} \frac{1}{s_x^2} \sum_{n,m=1}^N \sum_{k=1}^{m-1} a_{mk} T_{jm} \sum_{l=1}^{n-1} a_{nl} T_{in} \delta_{kl}. \quad (6.61)$$

We can extend the sums ending with $m-1$ and $n-1$ respectively to N , since $a_{nk} = 0$ for $k \geq n$. We thus obtain

$$K_{ij} = \frac{1}{2m} \frac{1}{s_x^2} \sum_{k=1}^N b_{jk} b_{ik} \quad (6.62)$$

where

$$b_{ik} = \sum_{n=1}^N a_{nk} T_{in}. \quad (6.63)$$



6.2.6 Comparison of Sine and Legendre DVR

For both the sine and Legendre DVR the weight function $\omega(t) = 1$. The quadrature points and weights are, however, different in the two forms of DVR. In sine-DVR the quadrature points are evenly distributed over the interval $[x_{\min}, x_{\max}]$, and the weights are the same for all quadrature points. In Legendre DVR, on the other hand, the quadrature points are not evenly distributed; more quadrature points are present near the boundary of the interval $[x_{\min}, x_{\max}]$, and less points are to be found in the middle of the interval. The Legendre weights are pairwise the same, but otherwise different for each quadrature point.

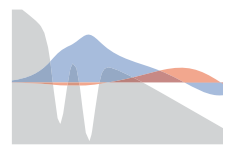
One essential difference between the two DVR's is the boundary condition they fulfill at the end of the interval on which they are defined. The sine-DVR functions go to zero on the interval boundary, but the Legendre-DVR functions do not. The sine-DVR will be applied to solve the diabatic problem [Eq. (6.1)] in the R -coordinate. These diabatic states should also go to zero on the boundary of the interval they are considered, so this is a suitable choice of basis. The z -coordinate, on the other hand, is divided into a series of sectors (more on this below). The solutions in each of these sectors must be connected at the boundaries of the sectors, and it is therefore important to use a basis which is non-zero at the boundary. The Legendre-DVR is such a basis.

6.3 Slow Variable Discretization

In this section the method used to locally solve the Schrödinger equation in each sector will be described. The method is called slow variable discretization (SVD), and it was originally developed in Ref. [26] to avoid problems with non-adiabatic couplings in adiabatic theories. In this thesis we employ a diabatic basis, and thus we do not have the same problems with non-adiabatic couplings, but the SVD nevertheless provides a convenient framework for formulating the R-matrix propagation equations that we will consider in the next section.

First we note that the Hamiltonian of the TISE [Eq. (4.1)] can be partitioned as follows

$$H = K + \tilde{V}(z) + h, \quad (6.64)$$



where

$$h = -\frac{1}{2M} \frac{d^2}{dR^2} + U(R) + FQR, \quad (6.65a)$$

$$K = -\frac{1}{2m} \frac{d^2}{dz^2}, \quad (6.65b)$$

$$\tilde{V}(z) = V(z, R) + Fqz. \quad (6.65c)$$

We now consider coordinates within a sector $z \in [z^-, z^+]$. Within this sector the Hamiltonian Eq. (6.64) is not Hermitian, but it would be convenient for us to work with a Hermitian Hamiltonian. To construct a Hermitian Hamiltonian we introduce the Bloch operator

$$\mathcal{L} = \frac{1}{2m} [\delta(z - z^+) - \delta(z - z^-)] \frac{d}{dz}. \quad (6.66)$$

When doing integrals of the type $\int_{z^-}^{z^+} dz$ with this operator it is implied that we consider $\lim_{\varepsilon \rightarrow 0} \int_{z^- - \varepsilon}^{z^+ + \varepsilon} dz$, such that the delta functions are included. We now consider the eigenvalue problem

$$[H + \mathcal{L} - \bar{E}] \bar{\psi} = 0. \quad (6.67)$$

The Bloch operator ensures hermicity of the Hamiltonian $H + \mathcal{L}$ associated with Eq. (6.67) by cancelling surface terms appearing when one does partial integration. These surface terms originate from the kinetic energy. In the following we consider Eq. (6.67) and will later connect it to Eq. (4.1).

We now expand the wave function in terms of DVR function $\pi_i(z)$

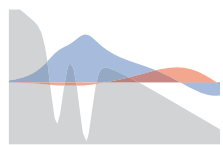
$$\bar{\psi}(z, R) = \sum_{i=1}^N \pi_i(z) \Phi_i(R) \quad (6.68)$$

where the $\Phi_i(R)$ functions are further expanded in terms of diabatic states [solutions of Eq. (6.1)]

$$\Phi_i(R) = \sum_{v=1}^M c_{iv} \varphi_v(R). \quad (6.69)$$

By inserting the expansion (6.68) into Eq. (6.67) and projecting on $\pi_i(z)$ we obtain

$$0 = \sum_{j=1}^N [K_{ij} + \tilde{V}(z_i) \delta_{ij} - \bar{E} \delta_{ij}] \Phi_j(R) + h \Phi_i(R) \quad (6.70)$$



where we have used the properties of the DVR basis, including

$$\int_{z^-}^{z^+} \pi_i(z) \tilde{V}(z) \pi_j(z) dz \approx \tilde{V}(z_i) \delta_{ij}, \quad (6.71)$$

and introduced the (hermitized) matrix elements of the kinetic energy

$$K_{ij} = \int_{z^-}^{z^+} \pi_i(z) [K + \mathcal{L}] \pi_j(z) dz \quad (6.72a)$$

$$= \frac{1}{2m} \int_{z^-}^{z^+} \frac{d}{dz} \pi_i(z) \frac{d}{dz} \pi_j(z) dz. \quad (6.72b)$$

We can expand Eq. (6.70) further by inserting the expansion (6.69), projecting on $\varphi_u(R)$ and using Eq. (6.1)

$$0 = \sum_{j=1}^N \sum_{v=1}^M [K_{ij} \delta_{uv} + \tilde{V}_{vu}(z_i) \delta_{ij}] c_{jv} + [\varepsilon_u - \bar{E}] c_{iu} \quad (6.73)$$

where

$$\tilde{V}_{vu}(z_i) = \int_0^{R_{\max}} \varphi_v(R) V(z_i; R) \varphi_u(R) dR + F q z_i \delta_{uv}. \quad (6.74)$$

Eq. (6.73) is a linear eigenvalue problem. We use the indices n, m to label eigenvalues \bar{E}_n and eigenvectors (with elements c_{jv}^n). The eigenvectors are normalized according to

$$\sum_{j=1}^N \sum_{v=1}^M c_{jv}^n c_{jv}^m = \delta^{nm}. \quad (6.75)$$

We can write wave functions corresponding to the eigenvectors

$$\bar{\psi}_n(z, R) = \sum_{i=1}^N \sum_{v=1}^M c_{iv}^n \pi_i(z) \varphi_v(R), \quad (6.76)$$

with the corresponding energy \bar{E}_n . This we can also write

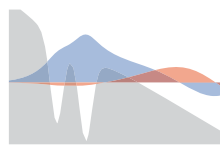
$$\bar{\psi}_n(z, R) = \sum_{v=1}^M F_{nv}(z) \varphi_v(R), \quad (6.77)$$

where

$$F_{nu}(z) = \sum_{i=1}^N c_{iu}^n \pi_i(z). \quad (6.78)$$

In particular we see that evaluating the expansion function F_{nu} at a quadrature point yields

$$F_{nv}(z_j) = \frac{1}{\sqrt{w_j s_x}} c_{jv}^n. \quad (6.79)$$



6.3.1 Relating Back to Full Wave Function

We now wish to express the solution Ψ to the original TISE (4.1) in terms of the hermitized sector basis functions $\bar{\psi}_n$ that are solutions of Eq. (6.76). First we consider

$$\langle \bar{\psi}_n | \mathcal{L} | \Psi \rangle_{z,R} = \langle \bar{\psi}_n | H + \mathcal{L} - H | \Psi \rangle_{z,R} \quad (6.80a)$$

$$= \langle \bar{\psi}_n | \bar{E}_n - E | \Psi \rangle_{z,R} \quad (6.80b)$$

where we use the notation

$$\langle \cdot \rangle_{z,R} = \int_{z^-}^{z^+} \int_0^{R_{\max}} \cdot dR dz, \quad (6.81)$$

and have used the Hermiticity of the operator $H + \mathcal{L}$ to apply it to the left. We now use that the $\bar{\psi}_n(z, R)$ form a complete basis

$$\Psi(z, R) = \sum_n \langle \Psi | \bar{\psi}_n \rangle_{z,R} \bar{\psi}_n(z, R) \quad (6.82a)$$

$$= \sum_n \frac{\langle \bar{\psi}_n | \mathcal{L} | \Psi \rangle_{z,R}}{\bar{E}_n - E} \bar{\psi}_n(z, R) \quad (6.82b)$$

Let us take a look closer look at

$$\langle \bar{\psi}_n | \mathcal{L} | \Psi \rangle_{z,R} = \frac{1}{2m} \sum_{\nu=1}^M F_{n\nu}(z) \left\langle \varphi_\nu \left| \frac{d}{dz} \right| \Psi \right\rangle_R \Big|_{z=z^-}^{z=z^+} \quad (6.83)$$

where we used the expansion Eq. (6.77) and the notation

$$\langle \cdot \rangle_R = \int_0^{R_{\max}} \cdot dR. \quad (6.84)$$

If we assume that we have a set of boundary conditions

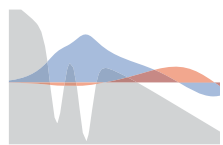
$$d_\nu^\pm = \left\langle \varphi_\nu \left| \frac{\partial}{\partial z} \right| \Psi \right\rangle_R \Big|_{z=z^\pm} \quad (6.85)$$

we can write the wave function

$$\Psi(z, R) = \frac{1}{2m} \sum_n \frac{\bar{\psi}_n(z, R)}{\bar{E}_n - E} \sum_{\nu=1}^M (F_{n\nu}(z^+) d_\nu^+ - F_{n\nu}(z^-) d_\nu^-). \quad (6.86)$$

The coefficient functions $f_\nu(z)$ introduced in the wave function expansion Eq. (6.3) can be expressed in terms of the SVD quantities as

$$f_\nu(z) = \langle \varphi_\nu | \Psi \rangle_R = \frac{1}{2m} \sum_n \frac{F_{n\nu}(z)}{\bar{E}_n - E} G_n(z_{\text{sec}}), \quad (6.87)$$



where

$$G_n(z_{\text{sec}}) = \sum_{\nu} (F_{n\nu}(z^+)d_{\nu}^+ - F_{n\nu}(z^-)d_{\nu}^-). \quad (6.88)$$

The notation (z_{sec}) indicates that $G_n(z_{\text{sec}})$ depends on in which sector z is in, but it is otherwise independent of z .

6.4 R-Matrix

Now that we formulated how to locally diagonalize the hermitized Hamiltonian within each sector using the SVD method we can write down the object that we are really interested in, namely the R-matrix. The R-matrix \mathcal{R} is defined by

$$\langle \varphi_{\nu}(R) | \Psi(z, R) \rangle_R = \sum_{u=1}^M \mathcal{R}_{\nu u}(z) \left\langle \varphi_u(R) \left| \frac{\partial}{\partial z} \right| \Psi(z, R) \right\rangle_R. \quad (6.89)$$

We can think of the R -matrix as a matrix if we consider the coefficient functions

$$f_{\nu}(z) = \langle \varphi_{\nu}(R) | \Psi(z, R) \rangle_R \quad (6.90)$$

as a vector \mathbf{f} . Equation (6.89) can then be written as a matrix equation

$$\mathbf{f} = \mathcal{R}(z) \frac{d}{dz} \mathbf{f}. \quad (6.91)$$

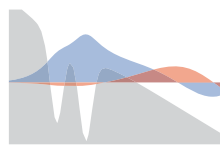
One can think of the R-matrix as essentially the ratio of the wave function and its derivative; the inverse of the logarithmic derivative.

6.4.1 Propagation Equation

Projecting equation (6.86) [this equation was derived using the TISE (4.1)] on diabatic states φ_{ν} and using the expansion (6.77) we get

$$f_{\nu}(z) = \sum_{u=1}^M \frac{1}{2m} \sum_n \left(\frac{F_{n\nu}(z)F_{nu}(z^+)}{\bar{E}_n - E} d_u^+ - \frac{F_{n\nu}(z)F_{nu}(z^-)}{\bar{E}_n - E} d_u^- \right). \quad (6.92)$$

If we consider this at the boundary of the sector z^a , where $a, b = \pm$ are indices used to indicate either the upper or lower boundary of the sector



we get

$$f_v(z^a) = \sum_{u=1}^M (\mathcal{R}_{vu}^{a+} d_u^+ - \mathcal{R}_{vu}^{a-} d_u^-) \quad (6.93a)$$

$$= \sum_{u=1}^M (a\mathcal{R}_{vu}^{aa} d_u^a + b\mathcal{R}_{vu}^{ab} d_u^b), \quad (6.93b)$$

where $b = -a$, such that b designates the boundary that is not a , and

$$\mathcal{R}_{vu}^{ab} = \frac{1}{2m} \sum_n \frac{F_{nv}(z^a) F_{nu}(z^b)}{\bar{E}_n - E}. \quad (6.94)$$

Inserting the same boundary point in the definition of the R-matrix [(6.89)] we obtain the relation

$$\sum_{u=1}^M \mathcal{R}_{vu}(z^a) d_u^a = \sum_{u=1}^M (a\mathcal{R}_{vu}^{aa} d_u^a + b\mathcal{R}_{vu}^{ab} d_u^b). \quad (6.95)$$

In matrix form this can be written

$$\mathcal{R}(z^a) \mathbf{d}^a = a\mathcal{R}^{aa} \mathbf{d}^a + b\mathcal{R}^{ab} \mathbf{d}^b. \quad (6.96)$$

Manipulating this equation we obtain

$$\mathbf{d}^a = b [\mathcal{R}(z^a) - a\mathcal{R}^{aa}]^{-1} \mathcal{R}^{ab} \mathbf{d}^b. \quad (6.97)$$

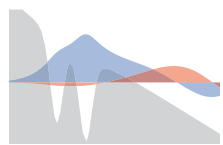
In this expression we can interchange a and b . Doing this and inserting the result in Eq. (6.96) yields

$$\mathcal{R}(z^a) \mathbf{d}^a = a\mathcal{R}^{aa} \mathbf{d}^a - \mathcal{R}^{ab} [\mathcal{R}(z^b) - b\mathcal{R}^{bb}]^{-1} \mathcal{R}^{ba} \mathbf{d}^a. \quad (6.98)$$

Since this is true for any derivative vector \mathbf{d}^a we can write the matrix equation

$$\mathcal{R}(z^a) = a\mathcal{R}^{aa} - \mathcal{R}^{ab} [\mathcal{R}(z^b) - b\mathcal{R}^{bb}]^{-1} \mathcal{R}^{ba}. \quad (6.99)$$

This equation is the main result of this section. It describes how to propagate the R-matrix from the sector boundary b to the sector boundary a . The matrices \mathcal{R}^{ab} that are used to make the propagation are calculated based on the local SVD diagonalization. Since the potentials we consider are (at least) continuous, the wave function and by extension the coefficient function $f_v(z)$ must be at least continuously differentiable.



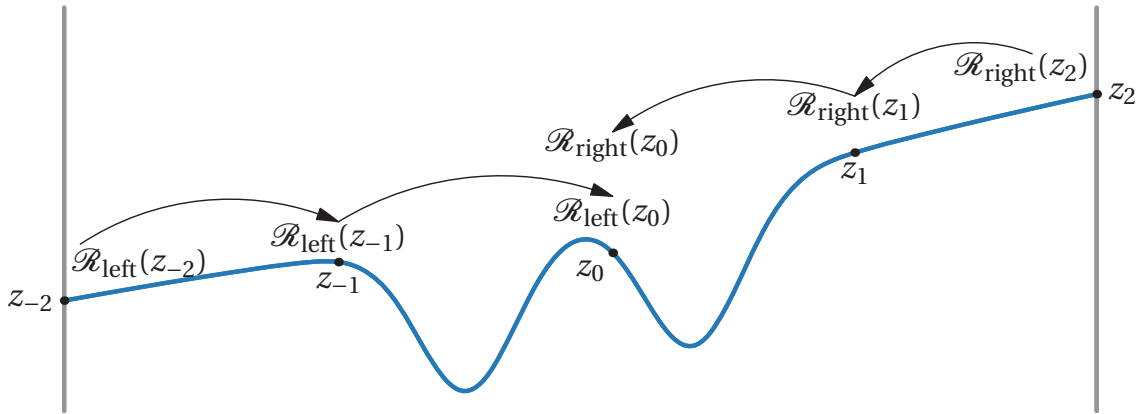


Figure 6.5: Illustration of R-matrix propagation. The indicated values of z are sector boundaries.

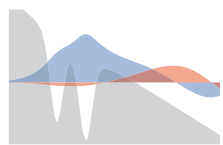
The R-matrix is defined in terms of the coefficient functions and their derivatives [Eq. (6.89)], and this must therefore be continuous. This must also be the case at the sector boundaries, so the R-matrix found at the boundary of one sector must be the same as the R-matrix determined at the corresponding boundary in the neighbouring sector. In this way we can propagate the R-matrix not only through sectors, but between sectors, and thus to everywhere on the z -axis.

Now we have devised a way to propagate the R-matrix, but which R-matrix should we propagate? In order to apply our R-matrix propagation scheme we need some initial R-matrix. Let us consider the problem in the asymptotic limit at large $|z|$, where the z and R degrees of freedom decouple. In this limit there is no coupling between the ν -channels, that describe the R -coordinate, and the R-matrix takes the diagonal form

$$\mathcal{R}_{\nu\nu'}(z)|_{|z|\rightarrow\infty} = \frac{f_\nu(z)}{\frac{d}{dz}f_\nu(z)}\delta_{\nu\nu'}. \quad (6.100)$$

The values of the coefficient function and its derivative can be found using the asymptotic expansions of Appendix A. In this way we can construct the asymptotic R-matrix in the 'left' region where $-z$ is very large, and the 'right' region where z is very large. These can then be propagated inwards through sectors until they meet at some matching sector boundary whose coordinate we denote z_0 . From the continuity of the coefficient function and its derivative together with the definition of the R-matrix [Eq. (6.89)] we obtain

$$[\mathcal{R}_{\text{right}}(z_0) - \mathcal{R}_{\text{left}}(z_0)] \mathbf{d} = 0, \quad (6.101)$$



where $\mathcal{R}_{\text{right}}(z), \mathcal{R}_{\text{left}}(z)$ are the R-matrices obtained from propagation of the asymptotic R-matrices from the left and right ends of the z -axis respectively, see Fig. 6.5. If the derivative \mathbf{d} is non-zero³, we must have that the matrix $\mathcal{R}_{\text{right}}(z_0) - \mathcal{R}_{\text{left}}(z_0)$ is singular, which is equivalent to

$$\det[\mathcal{R}_{\text{right}}(z_0) - \mathcal{R}_{\text{left}}(z_0)] = 0. \quad (6.102)$$

There is one missing ingredient in this procedure, though. In order to construct the asymptotic expansions we need to know the energy, see Eq. (4.16). The energy is, however, what we are trying to find, so it seems we are at an impasse. If we can somehow obtain a guess for the energy E_{guess} , we can still carry through with the whole procedure as described, only as long as the energy we guess is not the correct energy we cannot expect that the determinant in Eq. (6.102) is zero. However, if we consider this determinant as a function of the energy

$$\varepsilon(E) = \det[\mathcal{R}_{\text{right}}(z_0) - \mathcal{R}_{\text{left}}(z_0)], \quad (6.103)$$

then we can use the Newton-Raphson zero-finding algorithm to find the energy where this is zero. If our initial guess for the energy was close enough this should hopefully yield the correct, physical energy.

The Newton-Raphson algorithm is an iterative procedure, which is derived by initially expanding the function one wants to find a zero for to first order

$$\varepsilon(E_{n+1}) \approx \varepsilon(E_n) + \varepsilon'(E_n)(E_{n+1} - E_n). \quad (6.104)$$

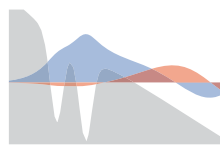
We then set $\varepsilon(E_{n+1}) = 0$ and solve for E_{n+1}

$$E_{n+1} = \frac{\varepsilon(E_n)}{\varepsilon'(E_n)} + E_n. \quad (6.105)$$

A complication is that we do not know the derivative $\varepsilon'(E_n)$, but this can be circumvented by using a numerical derivative $\varepsilon'(E_n) \approx \frac{\varepsilon(E_n) - \varepsilon(E_{n-1})}{E_n - E_{n-1}}$. For the first step some value is more or less arbitrarily chosen for $E_n - E_{n-1}$.

The initial guess for the energy is found from a direct diagonalization of the Hamiltonian for $F = 0$ using a sine-DVR basis for both the z and R

³In cases where $\mathbf{d} = 0$ at the matching point this method fails. The matching point can however be chosen freely. For instance, in the case where $F = 0$ this derivative vector is zero at $z = 0$, so here we should choose some other value.



coordinates⁴. In this $F = 0$ case the wave function goes to zero for $|z| \rightarrow \infty$, which is compatible with the sine-DVR. Since the energy is continuous in F , $E(F = 0)$ is close to the energy at small F , and $E(F = 0)$ can therefore be used as an initial guess for the energy at some small F . Once the energy at this small F has been found, it can be used as initial guess for the energy at a slightly larger F . This procedure can be repeated to find the energies for any given F , conditioned that it converges all the way.

An example of energies obtained using this R-matrix propagation method is shown in Fig. 7.5.

6.4.2 Construction of Wave Function

Not only the energy can be found using R-matrix propagation. It is also possible to construct the wave function [Eq. (6.86)]. In order to do this we need to know the derivative vectors \mathbf{d} at the sector boundaries. From Eq. (6.97) we see that this derivative vector can be propagated through a sector by

$$\mathbf{d}^a = \mathcal{D}^a \mathbf{d}^b \quad (6.106)$$

where the derivative propagation matrix is given by

$$\mathcal{D}^a = b [\mathcal{R}(z^a) - a\mathcal{R}^{aa}]^{-1} \mathcal{R}^{ab}. \quad (6.107)$$

We can use Eq. (6.106) to find the derivative vectors everywhere from some initial derivative vector. This initial derivative vector can be found by noting that Eq. (6.101) can be written

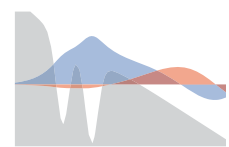
$$[\mathcal{R}_{\text{right}}(z_0) - \mathcal{R}_{\text{left}}(z_0)] \mathbf{d} = \mathbf{0d}. \quad (6.108)$$

So, we can find an initial derivative vector as the eigenvector of the matrix $\mathcal{R}_{\text{right}}(z_0) - \mathcal{R}_{\text{left}}(z_0)$ that belongs to the eigenvalue 0.

6.4.3 Summary of R-matrix Method

Here we give a short of summary of how the different methods described in this chapter are combined to exactly solve the TISE (4.1). The contents

⁴In the numerical implementation the diabatic basis [Eq. (6.1)] is found using a sine-DVR basis in R , and a sine-DVR basis in z is then used to solve the coupled Eqs. (6.4). This method of first doing one partial diagonalization before the full diagonalization is called pre-diagonalization.



of this section is taken from Ref. [1]. To solve Eq. (6.4), which is a projected version of the TISE, we use the R-matrix propagation technique. This method consists of dividing the z axis into a series of sectors. A spatial Legendre DVR [25] basis is chosen in each sector, and the local Hamiltonian is diagonalized by means of the SVD method [26]. Based on this diagonalization the R-matrix can be propagated from sector to sector. Details of this is described in the appendix of [9].

Before we can propagate the R-matrix we need some initial R-matrix. This is obtained asymptotically. Since the channel equations (6.4) decouple in the large $|z|$ limit the R-matrix is diagonal and has the form

$$\mathcal{R}_{\nu\nu'}(z; E)|_{|z|\rightarrow\infty} = \frac{f_\nu(z)}{\frac{d}{dz}f_\nu(z)}\delta_{\nu\nu'}. \quad (6.109)$$

The coefficient function $f_\nu(z)$ and its derivative can be found in this asymptotic region using the asymptotic expansion of App. A.

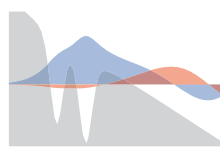
The method we employ is the following; first we pick some initial energy based on a direct diagonalization of the field-free Hamiltonian. Then we take a small step in field strength and find the asymptotic R-matrices at the right and left ends of our box. These are then propagated through the sectors until they meet at some matching point x_0 near the center of the box. Since the potentials considered are smooth, the coefficient functions must be continuous and their derivatives like so. This implies that the matrix difference of the R-matrices propagated from the left and from the right must have a zero eigenvalue, such that this difference matrix is singular

$$\det[\mathcal{R}_{\text{left}}(z_0; E) - \mathcal{R}_{\text{right}}(z_0; E)] = 0. \quad (6.110)$$

We then find the zero of this determinant by doing a simple Newton search with the energy E as variable. In each step a new guess for the energy is obtained, which is then used to construct the asymptotic R-matrices etc. This proceeds until the energy giving the zero eigenvalue is found. Then a new step in F is made and the procedure is repeated, this time using the present energy as a guess for the new energy.

6.5 Complex Rotation

As a supplement to the R-matrix propagation method described above I have also used the complex rotation method. This consists of rotating the



electron coordinate z into the complex plane, in such a way that all the boundary conditions for the wave function gives a decaying wave function for $|z| \rightarrow \infty$. This allows us to do a diagonalization in a box, which is a lot simpler and easier to implement than the R-matrix method. The trade-off is that complex rotation only yields a total rate, and not partial rates, or a wave function for that matter. In this thesis complex rotation has been used as a crude tool to test whether the R-matrix propagation is working correctly, by checking that the total rates obtained with the two different methods are the same.

In the complex rotation method we consider the electronic coordinate as a complex variable. In order to use the complex rotation method we must require that the potential $V(z, R)$ is holomorphic in z . Then the wave function and its double derivative should also be holomorphic and can be analytically continued to the complex z plane. We write the TISE (4.1) in the form

$$\frac{H\Psi}{\Psi} = E. \quad (6.111)$$

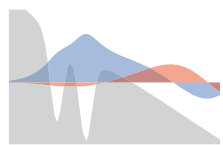
Except for any possible zeros of Ψ , the left hand side in this expression is holomorphic, and so is the constant E . The identity theorem for holomorphic functions then gives us, that since Eq. (6.111) is fulfilled for real z (and the real axis definitely contains at least one accumulation point), it must be fulfilled for all complex z , when using the analytic continuation of Ψ . Since the energy is constant on the real axis of z , it must also be constant in the full complex z plane.

The energy is defined not only by the TISE, but also by the boundary conditions Eqs. (4.16) and (4.17). These can also be analytically continued to the complex z plane. In complex rotation we choose to consider a particular line of the complex z plane, at an angle θ to the real axis. This we can write

$$z = xe^{i\theta}, \quad (6.112)$$

where x is a real variable and θ is a constant. Inserting this in the Hamiltonian (4.2) yields

$$H^{\text{CR}} = -\frac{1}{2M} \frac{d^2}{dR^2} - \frac{1}{2m} e^{-i2\theta} \frac{d^2}{dx^2} + F(QR + qxe^{i\theta}) + U(R) + V(xe^{i\theta}, R). \quad (6.113)$$



The boundary conditions Eqs. (4.16) and (4.17) becomes

$$f(xe^{i\theta})|_{x \rightarrow -\infty} = \frac{m^{1/4}}{(2Fq(-xe^{i\theta}))^{1/4}} \quad (6.114a)$$

$$\times \exp \left[i \frac{(2m)^{1/2}}{(Fq)^{1/2}} \left(\frac{2}{3} Fq(-x)^{3/2} e^{i3\theta/2} + E_z(-x)^{1/2} e^{i\theta/2} \right) \right]$$

$$f(xe^{i\theta})|_{x \rightarrow \infty} = \frac{m^{1/4}}{(2Fqxe^{i\theta})^{1/4}} \exp \left[-\frac{(2m)^{1/2}}{(Fq)^{1/2}} \left(\frac{2}{3} Fqx^{3/2} e^{i3\theta/2} - E_z^{1/2} x e^{i\theta/2} \right) \right]. \quad (6.114b)$$

We would like these to decay in the limits $|x| \rightarrow \infty$. Whether this happens is determined by the real part of the exponential. If it is negative we have decay, if it is positive we have growth. In the $|x| \rightarrow \infty$ limits the exponent in both Eqs. (6.114a) and (6.114b) are dominated by the first term. The real part of this term in the $x \rightarrow -\infty$ limit is

$$\operatorname{Re} \left(i \frac{(2m)^{1/2}}{(Fq)^{1/2}} \frac{2}{3} Fq(-x)^{3/2} e^{i3\theta/2} \right) = -\sin \left(\frac{3\theta}{2} \right) \frac{(2m)^{1/2}}{(Fq)^{1/2}} \frac{2}{3} Fq(-x)^{3/2}. \quad (6.115)$$

For this to be negative we must require that

$$\sin \left(\frac{3\theta}{2} \right) > 0. \quad (6.116)$$

Similarly for the limit $x \rightarrow \infty$

$$\operatorname{Re} \left(-\frac{(2m)^{1/2}}{(Fq)^{1/2}} \frac{2}{3} Fqx^{3/2} e^{i3\theta/2} \right) = -\cos \left(\frac{3\theta}{2} \right) \frac{(2m)^{1/2}}{(Fq)^{1/2}} \frac{2}{3} Fqx^{3/2}, \quad (6.117)$$

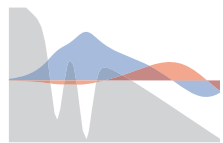
so here we must require

$$\cos \left(\frac{3\theta}{2} \right) > 0. \quad (6.118)$$

We note that the conditions (6.116) and (6.118) are fulfilled by angles in the range

$$\theta \in \left[0, \frac{\pi}{3} \right]. \quad (6.119)$$

So, if we choose an angle θ in the interval (6.119) the wave function decays in both the $x \rightarrow \infty$ and $x \rightarrow -\infty$ limits, and we can use a box of



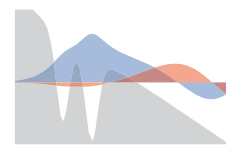
finite size in x to diagonalize the complex Hamiltonian (6.113). In cases where the potential asymptotically goes to zero rather than having the form Fx , the choice of the rotation angle θ that ensures asymptotic decay of the wave function depends on the angle that the complex energy makes with the real energy axis. One says that the θ angle should be chosen such that it exposes the given complex energy. In our case the Fx term dominates over the energy term in the asymptotic potential and therefore in the asymptotic wave function, so we do not need to consider the energy at all when choosing θ .

In the exact analytic formulation the choice of θ does not matter, as long as we choose it in the interval (6.119), the wave function will decay. In a numerical calculation the precise choice of θ can be more important, since the choice of θ determines how fast the wave function decays. It should thus be chosen such that the wave function has decayed sufficiently when it reaches the boundary of the box.

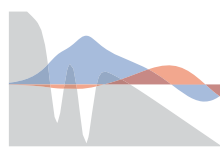
Another important thing to keep in mind when doing a numerical calculation is that we must inevitably use a finite, truncated basis, and the use of such a basis introduces spurious solutions that do not correspond to physical states. For a normal, real diagonalization (where $\theta = 0$) of a Hermitian Hamiltonian this is usually not a big problem; since such a method is variational the eigenvalues are nicely ordered and the spurious states should only appear high up in the spectrum. However, when the Hamiltonian has undergone a complex rotation, it is no longer Hermitian and all bets are off. The spurious states can now come close to the physical states in energy, and we should be quite careful with how we sort the energies, to make sure that we correctly assign an energy to a given state.

Let us assume that we have done a set of complete complex rotation diagonalizations at a series of equidistant field strengths $F_i = i\Delta F$, $i = 0, 1, \dots$. For each F we have a set of energies $E_k(F_i)$. At $F = 0$ these energies are ordered by the normal ordering of the real numbers $E_0(F_0) < E_1(F_0) < \dots < E_n(F_0) < E_{n+1}(F_0) < \dots$. At each F the energies are assigned to a particular state n by choosing the state that has the minimal complex distance $|E_k(F_i) - E_n(F_{i-1})|$ to the state n at the previous field strength, starting at $F = 0$. If the distance between field strengths ΔF is too large this procedure fails when two energies cross or come too close to each other. A refinement of the method uses a linear projection from the previous field strength, such that the distance $|E_k(F_i) - (E_n(F_{i-1}) + [E_n(F_{i-1}) - E_n(F_{i-2})])|$ should be minimal instead.

In this section we have only considered rotations of the electronic coordinate z , and not the nuclear coordinate R . This is because we do



not specify any asymptotic boundary conditions for the R coordinate, that is, we consider a continuum in the R coordinate. We could also have chosen to impose outgoing-wave boundary conditions in the R -coordinate (Siegert state boundary condition), and then we could use complex rotation in the R -coordinate by following the same procedure as described above.



7 Bound Ionic States

In this chapter we consider $U(R)$ potentials with no continuum. This means that the molecule cannot dissociate, and after ionization the molecule is in a bound ionic state. Large parts of the material in this chapter is the same as in Ref. [1], of which I am first author.

7.1 Model Potentials

In this section the analytic form of the model potentials used to describe the interaction between the nuclei $U(R)$, and the effective one-electron potential $V(x, R)$, are presented.

The internuclear interaction is modeled by the potential

$$U(R) = \frac{A}{R^2} + B + CR^2, \quad (7.1)$$

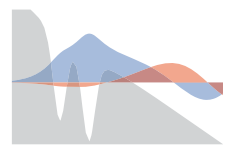
with coefficients $A = 0.26$, $B = -0.732635$ and $C = 0.01625$. These parameters were chosen such that this potential reproduce the minimum of the BO potential of H_2^+ , as shown in Fig. 7.1. This inter-nuclear potential is strictly binding and does not allow for dissociation of the molecule. It is identical to the one used in Refs. [1, 10].

The interaction between the nuclei and the electron is of the form (4.3). In Ref. [10] a finite-range potential (FRP)

$$V_i(z) = -\frac{a}{\cosh^2(bz)}, \quad i = 1, 2, \quad (7.2)$$

with parameters $a = 0.62772$ and $b = 0.857$ was used. In this chapter we additionally consider a Coulomb-tail potential (CTP). It has the form

$$V_i(z) = -q_i \frac{1 - de^{-fz^2}}{\sqrt{z^2 + a^2}} - ce^{-bz^2}, \quad i = 1, 2, \quad (7.3)$$



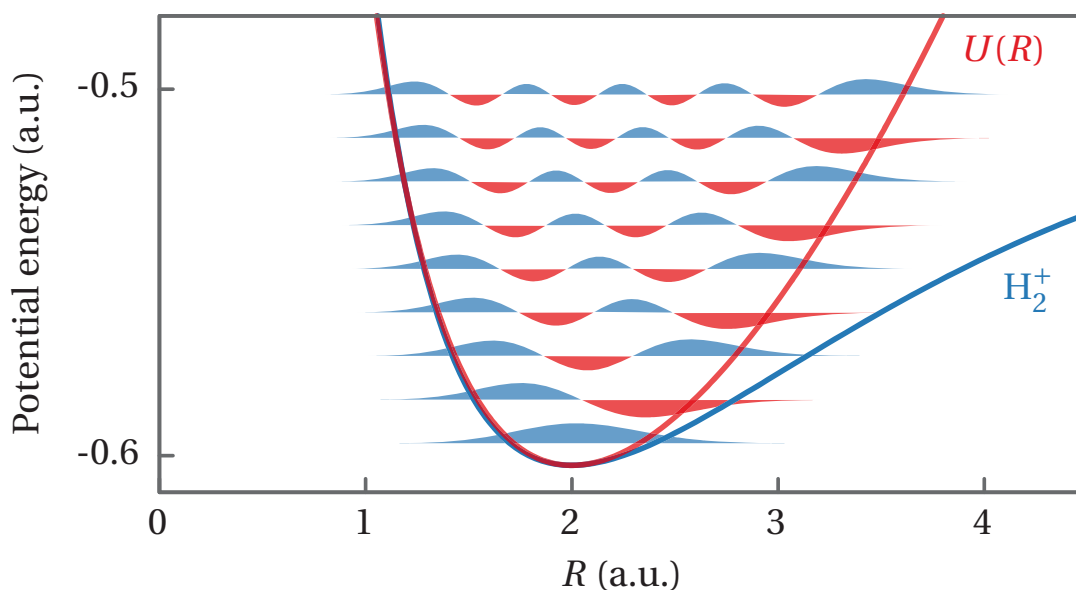


Figure 7.1: Blue curve: BO potential of 3D H_2^+ [27]. Red curve: Model potential of the molecular ion $U(R)$ [Eq. (7.1)], with the vibrational states $\varphi_v(R)$ that solves Eq. (6.1) superimposed. Blue indicates positive values of $\varphi_v(R)$, red indicates negative values.

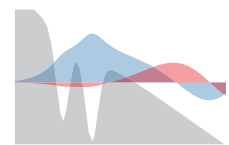
with parameters $a = 1$, $b = 5.46$, $c = 0.931$, $d = 0.633$, $f = 0.0402$ and $q_1 = q_2 = 0.5$. These parameters, as well as those for Eq. (7.2), are chosen such that the BO potential reproduces the BO potential of H_2 [lower (black) lines in Fig. 7.2]. Since we use a SAEA in this description of H_2 , the H_2^+ described by the $U(R)$ potential that appears when the active electron has left has no active electrons.

Although the two FRP and CTP models result in a similar behavior of the BO potentials, they are very different in nature. The FRP (7.2) vanishes exponentially fast at large $|z|$, while the CTP (7.3) takes the form

$$V(z, R)|_{z \rightarrow \pm\infty} = -\frac{q_1 + q_2}{|z|}. \quad (7.4)$$

The potentials also have different behavior at small $|z|$. Figure 7.3 shows the FRP and CTP at the H_2 equilibrium distance $R_0 = 1.4$ and illustrates the qualitative difference, as the FRP has one minimum, whereas the CTP has two.

When the field is non-zero, two distinct classically allowed regions appear. An inner one in the potential well around the nuclei and an outer one in the negative z -direction extending towards minus infinity. As long



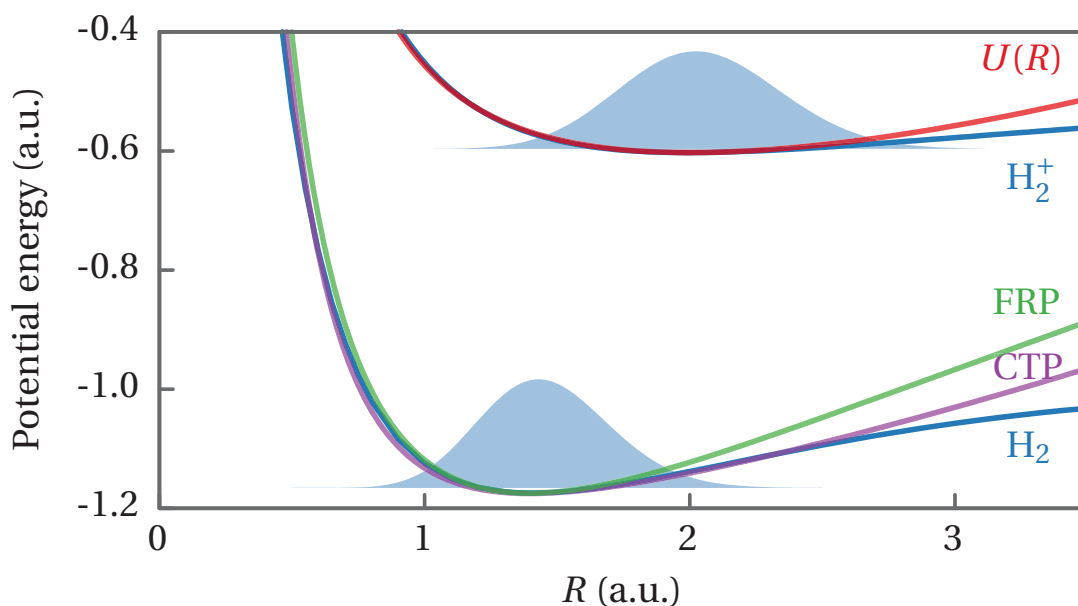
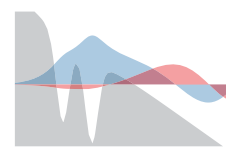


Figure 7.2: Blue lines: BO potentials for H_2^+ [27] and H_2 [28, 29] as functions of the inter-nuclear distance R . Red line: present model inter-nuclear potential $U(R)$ [Eq. (7.1)]. Green line: BO potential for the three-body system $U(R) + E_e(R;0)$ using the FRP [Eq. (7.2)]. Purple line: $U(R) + E_e(R;0)$ using the CTP [Eq. (7.3)]. Shaded areas: lowest vibrational state $\varphi_0(R)$ (upper) and BO vibrational ground state $\chi(R)$ (lower, Eq. (4.60b)) using the CTP.

as these regions are separate we have under-the-barrier ionization, since the electron has to tunnel through a barrier in order to get from the inner to the outer classically allowed region. For sufficiently large field strengths the two regions merge and we have over-the-barrier ionization. By considering plots of the iso-contour $V(z, R) + U(R) + (QR + qz)F = \text{Re}[E(F)]$ we can determine the critical field at which we switch from under-the-barrier to over-the-barrier ionization.

7.2 Results

In Sec. 7.2.1 we consider the FRP and CTP models for H_2 with $q_1 = q_2 = 0.5$, since the charge of the passive electron is distributed across the molecule, and $m_1 = m_2 = 1836$. The goal is to investigate the effect of the Coulomb tail on the wave function and the ionization rate. In Sec. 7.2.2 we consider non-symmetric CTP models for polar molecules and investigate the effect



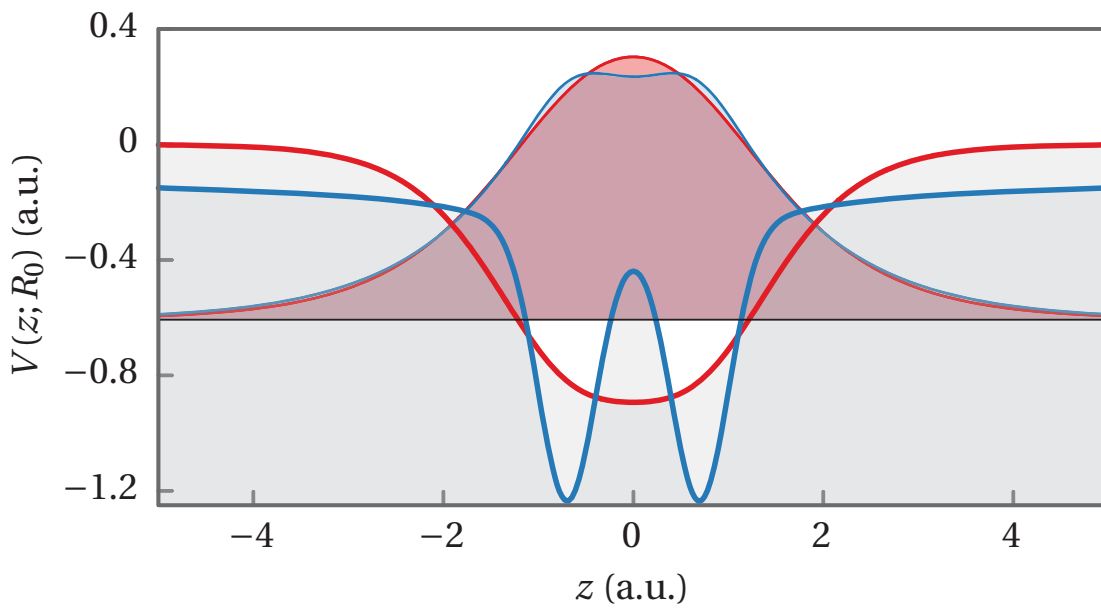
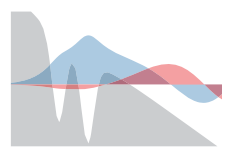


Figure 7.3: Red (blue) line: the FRP [Eq. (7.2)] {CTP [Eq. (7.3)]} at $R_0 = 1.4$. Shaded red (blue) area bounded by red (blue) line: ground-state electronic wave function at this R_0 for the FRP (CTP), the horizontal black line is at the electronic energy $E_e(R_0; 0)$ of these ground states (the energies are indistinguishable on the scale of the figure). The gray shaded area indicates the classically forbidden region.

of the dipole.

7.2.1 Non-polar Model H_2 : Finite-range vs. Coulomb-tail Potential

The upper panel of Fig. 7.4 shows the real part of the energy of the SS that is the analytic continuation along the real F -axis of the field-free ground-state for the two model potentials. For $F = 0$ the energies of the ground state for the two potentials are close to each other, $E = -1.163269$ for FRP and $E = -1.165766$ for CTP, but as F increases the energy for the CTP becomes lower than that for the FRP. The change of slope of the CTP energy curve at around $F = 0.15$ is due to an avoided crossing with a vibrationally excited state. The energy of the lowest vibrational state of the molecular ion to which the molecule can ionize is $\varepsilon_0(0) = -0.5966$. The lower panel of Fig. 7.4 shows the rate obtained from $\Gamma = -2\text{Im}(E)$ for the



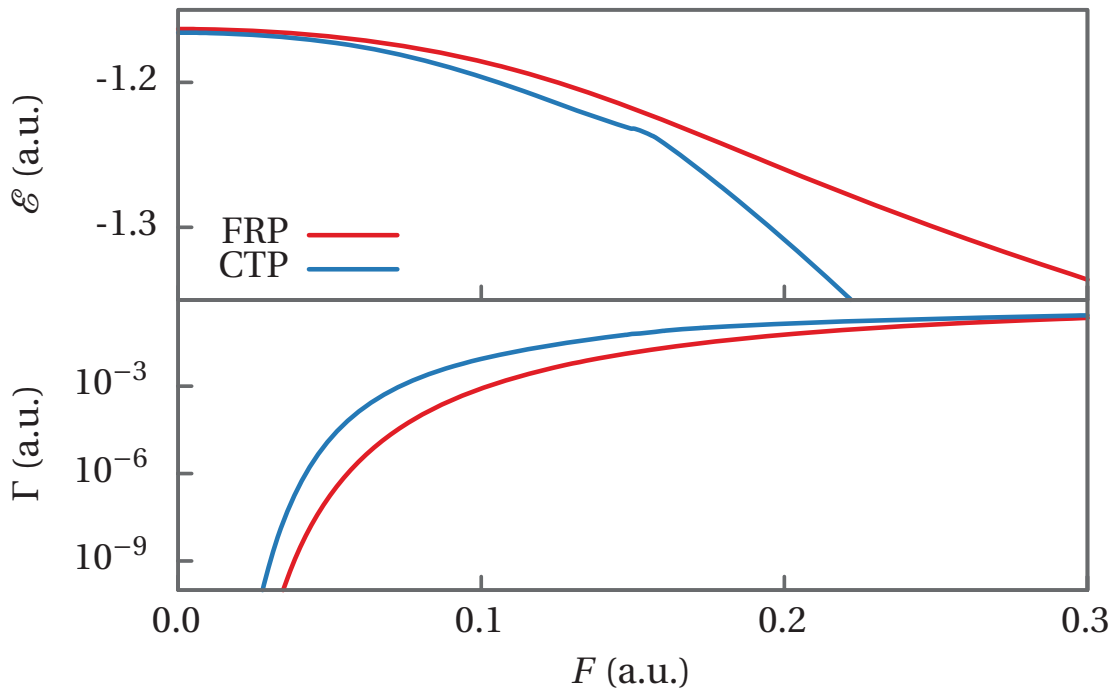
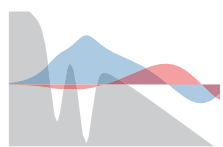


Figure 7.4: Upper panel: Real part of the energy $\mathcal{E} = \text{Re}(E)$, for the SS that is the analytic continuation of the field-free ground-state for the FRP [Eq. (7.2)] and CTP [Eq. (7.3)]. Lower panel: The exact rates $\Gamma = -2\text{Im}(E)$ for the same states.

same state as in the upper panel. The avoided crossing in the CTP curve is not seen since the plot is on a logarithmic scale. The figure shows that the rate is lower for the FRP than for the CTP. The rates obtained from these R-matrix calculations have been verified by use of a complex rotation calculation.

In Fig. 7.5 energies obtained with the R-matrix propagation and complex rotation methods for the CTP are compared. They are seen to completely overlap. In this figure we also see the avoided crossings near $F = 0.15$. The details are somewhat difficult to make out in this figure, so Fig. 7.6 shows a zoom near this field strength. Here we see that the real part of the energy of the ground state crosses the real part of the energy of the first and second excited state. Since the lines cross, there must be a point where the two states have the same energy and are degenerate, so how do we know which state is which after the crossing? Where the states cross in the real part of the energy they are not close to each other in the imaginary part of the energy, so when we consider the complex nature of



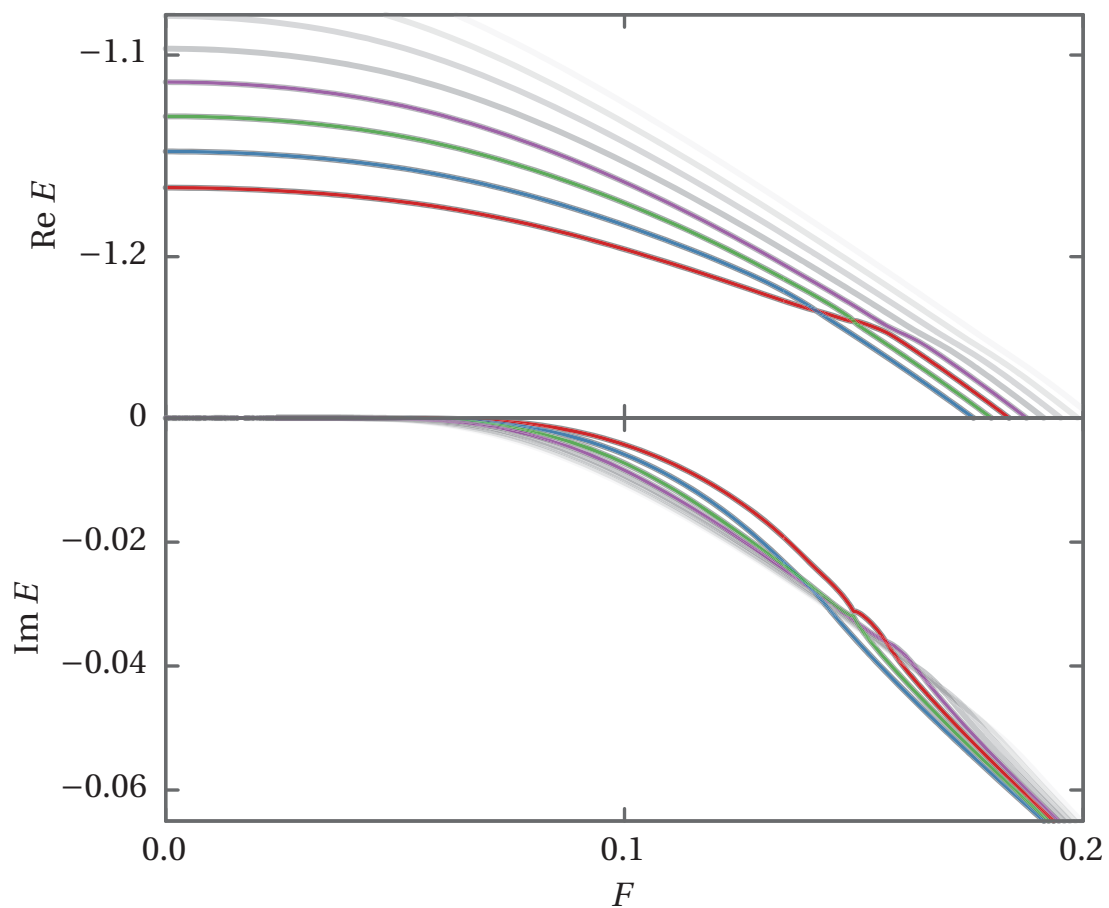
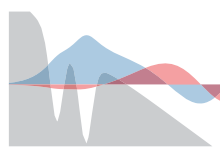


Figure 7.5: Real and imaginary part of energies for the CTP. The colored lines show the R-matrix calculations for the lowest 4 states. The gray lines show the results of a complex rotation calculation for the lowest 8 states, where higher states are more transparent. They completely agree with the R-matrix results, so the lowest 4 complex rotation states are hidden behind the R-matrix lines.



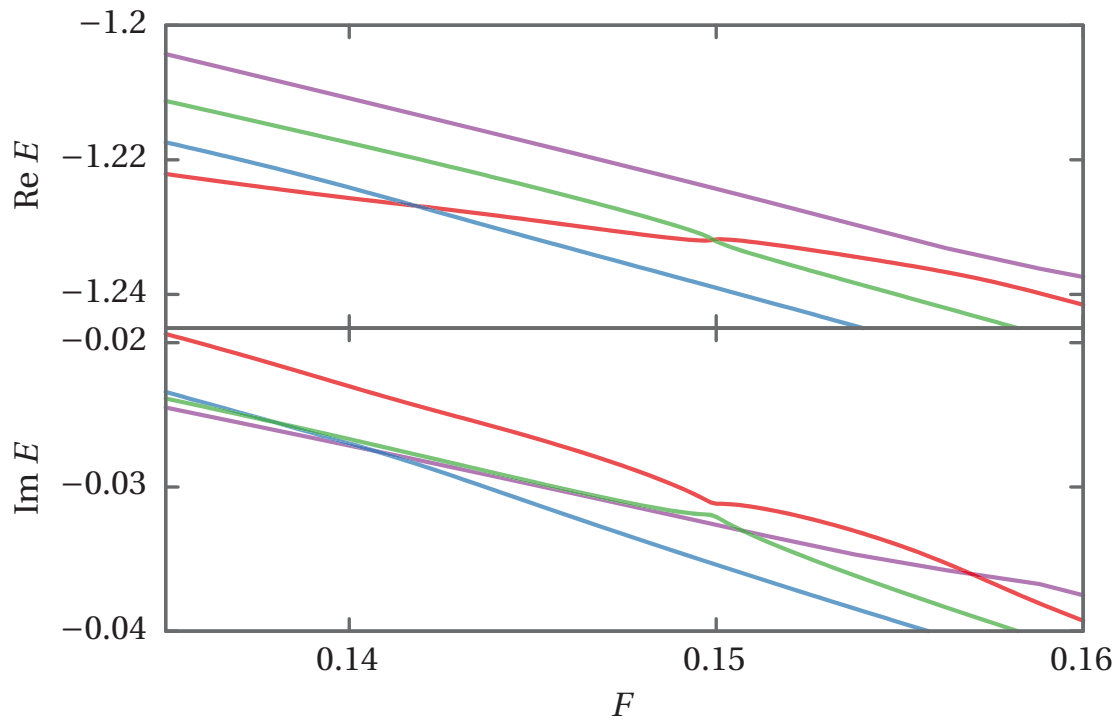
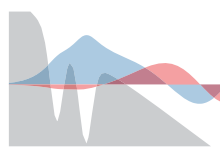


Figure 7.6: Same as Fig. 7.5, only zoomed and without the complex rotation energies.

the energies the states are clearly distinguishable. We may additionally observe that whenever there is a crossing in the real part of the energy, there is an avoided crossing in the imaginary part, and vice versa. The avoided crossings which look like the states are repelling each other are not always visible, particularly if the states are some distance from each other in the relevant energy component. At the crossing between the field-free ground state and second excited state near $F = 0.15$ the imaginary energies are quite close to each other, and the avoided crossing clearly modifies the form of the energy curve.

Another way to visualize the results of the complex rotation is by plotting the solutions in the complex energy plane for fixed F . This is shown in Fig. 7.7. At $F = 0$ all solutions where the imaginary part of the energy is different from zero can clearly not represent a physical state, and any such solutions must be artificial, spurious solutions introduced by the truncated basis. As F is increased from zero the energy of these spurious states change rather quickly compared to the physical states. Some of the spurious states move to larger values of $\text{Re } E$, some move to smaller, but the details of the complicated dynamics of these spurious is difficult to



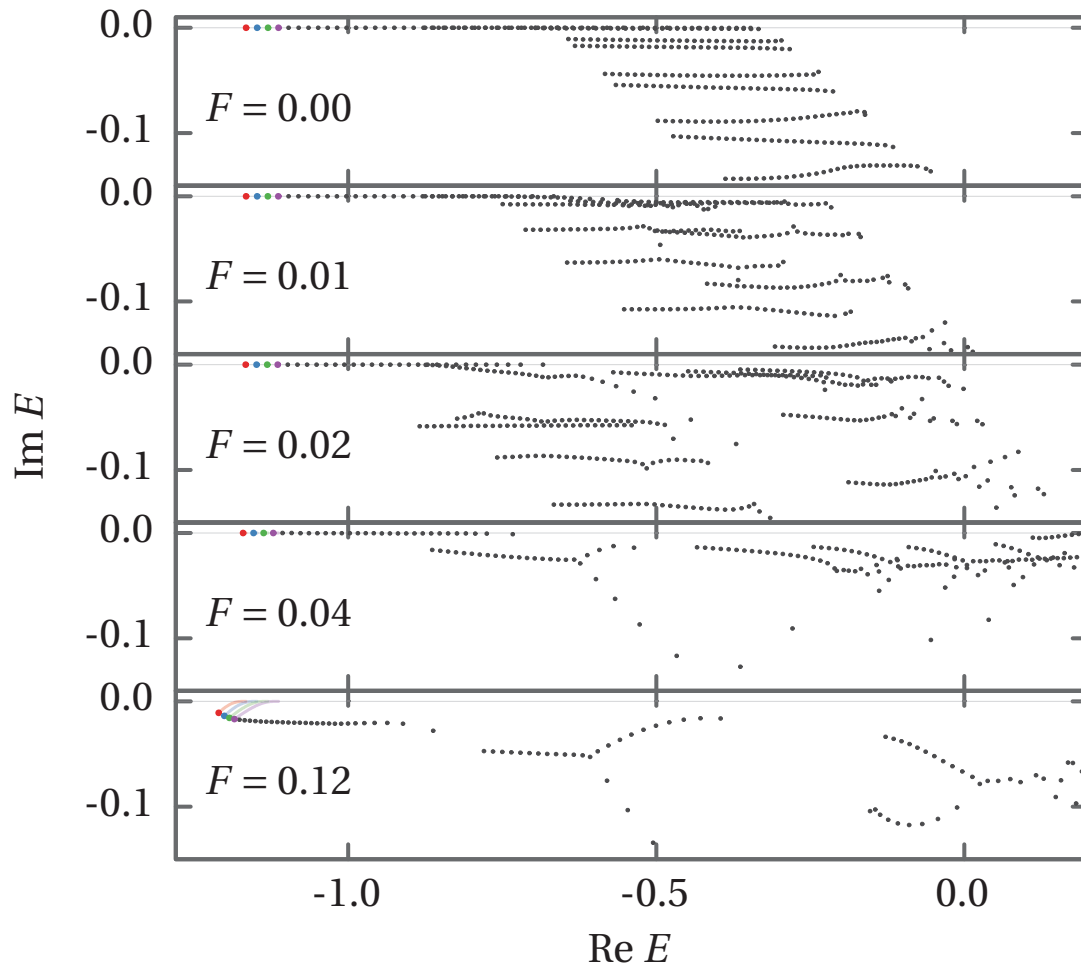
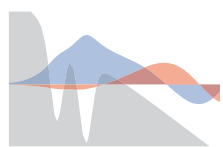


Figure 7.7: Energies of complex rotation solutions for selected field strengths. The colored dots indicate the 4 states that at $F = 0$ has the lowest real part of the energy. For these 4 states traces are shown that indicate their energies at smaller F . In Adobe Acrobat Reader, clicking this figure will show an animation.



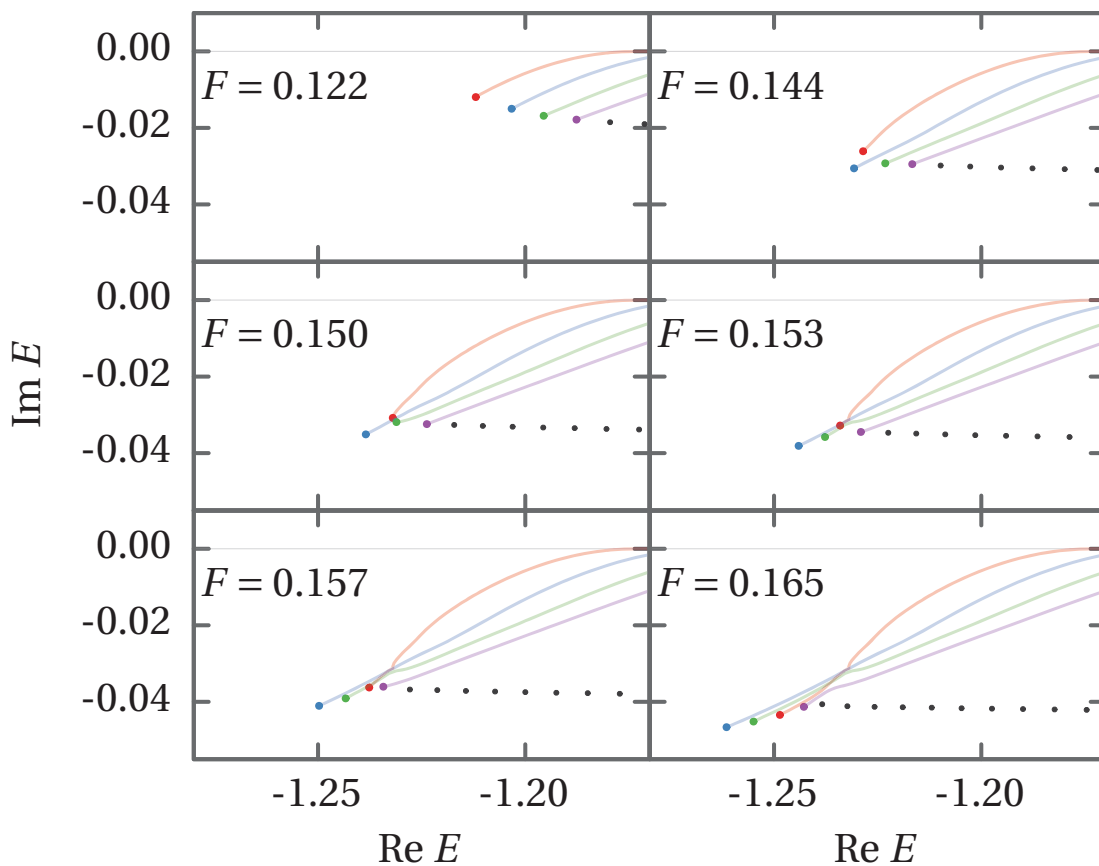
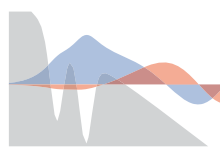


Figure 7.8: Energies of complex rotation solutions for selected field strengths, as in Fig. 7.7, but for different F and E . In Adobe Acrobat Reader, clicking this figure will show an animation.

capture with snapshots like those in Fig. 7.7. For sufficiently large F the spurious states moving towards smaller $\text{Re } E$ will have $\text{Re } E$ comparable to or smaller than the physical states, which will give problems if one sorts the energies according to $\text{Re } E$.

The avoided crossings of the states around $F = 0.15$ is shown as snapshots in F in Fig. 7.8. Here we see that the traces of the states cross, and for some values of F the real part the energy of some of these states coincide, but there is no value of F such that both the real and imaginary part of the energy coincides simultaneously.

Interestingly it seems that the nodal structure in the R coordinate reflects the ordering of the real part of the energy. This is shown in Fig. 7.9. The first column, e.g., shows how the state that is the analytic continuation of the ground state, changes from having no nodes at $F = 0.11$ to having 2



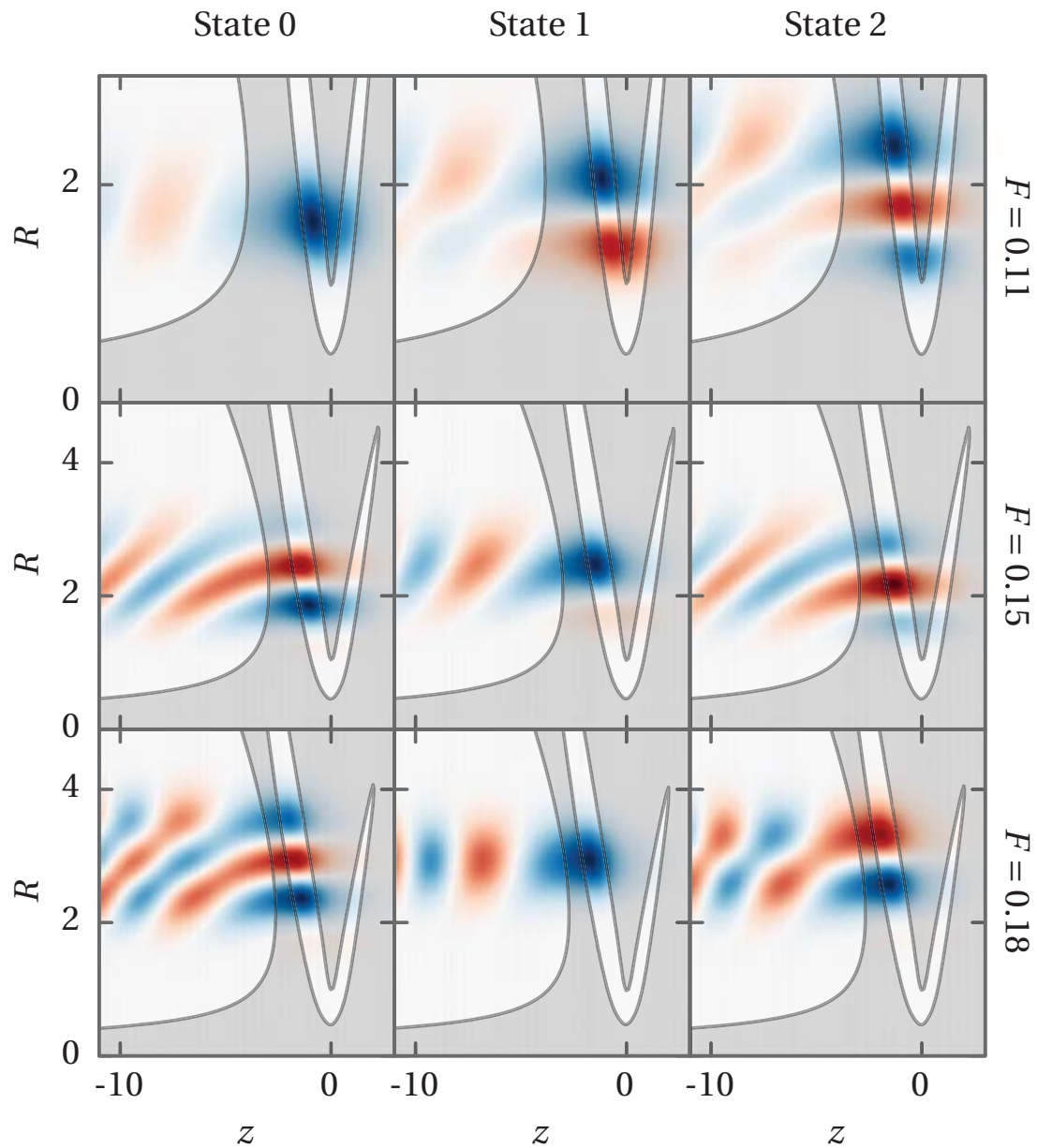
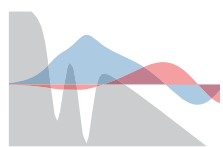


Figure 7.9: Real part of the wave function. The field strength is fixed across the rows. The same state is considered along the columns. We see that the nodal structure in the R coordinate is permuted as one goes from smaller to larger field strengths, which corresponds to the crossings in Fig. 7.6. The gray line is an iso-contour showing where $V(z, R) + U(R) + Fqz = \text{Re}[E(F)]$. It marks the boundary between the classically allowed and forbidden (the gray area) regions.



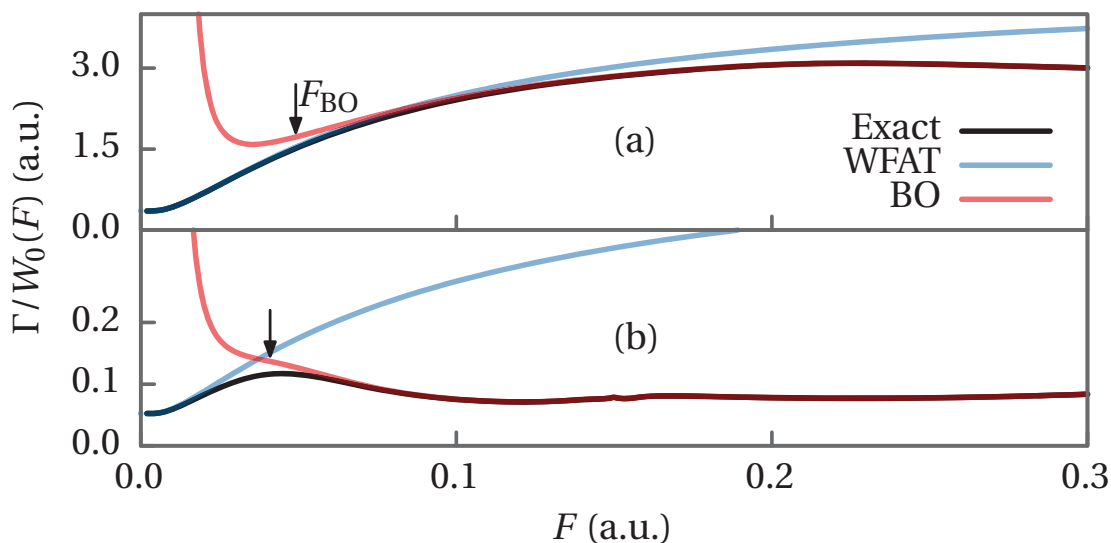


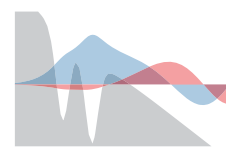
Figure 7.10: Total ionization rates of the ground state divided by the field factor for the zeroth channel $W_0(F)$ [Eq. (4.58a)]. Black lines are exact rates, blue lines are WFAT rates and red lines are BO rates. Arrows indicate the boundary of the region of validity of the BO approximation [Eq. (4.90)]. (a) is for the FRP [Eq. (7.2)] and (b) is for the CTP [Eq. (7.3)].

nodes at $F = 0.18$. At this larger field strength it is the second excited state when considering the real part of the energy [Fig. 7.5]. The other states are seen to also change their nodal structure, such that it is consistent with the ordering of the real part of the energies.

The exact ionization rates are shown in Fig. 7.10, together with BO and WFAT rates. The BO rates were obtained from $\Gamma_{\text{BO}} = -2\text{Im}(E_{\text{BO}})$, where the BO energies E_{BO} were obtained by solving the BO Equations (4.60). For the FRP the field strength at which we expect the BO approximation to break down [Eq. (4.90)] is $F_{\text{BO}} \approx 0.05$, whereas for the CTP it is around $F_{\text{BO}} \approx 0.04$. The difference is due to differences in the curvature of the BO curve $U(R) + E_e(R; 0)$, this difference is also evident in Fig. 7.2. In Fig. 7.10 we see that the BO approximation indeed works well for $F > F_{\text{BO}}$, but fails for $F < F_{\text{BO}}$, as discussed in Sec. 4.4.4.

The WFAT rate is the sum of the partial rates [Eq. (4.59)]. The critical field at which we switch from under-the-barrier to over-the-barrier ionization has been estimated by the method described in the end of Sec. 7.1 to be about 0.1745 for the FRP and 0.247 for the CTP.

Figure 7.10(a) shows total rates for the FRP. This potential was also

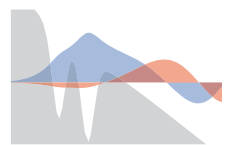


used in Ref. [10], and the results are the same. One remarkable feature in Fig. 7.10(a) is that the exact and WFAT results agree over a very large range of F , up to around $F = 0.1$. Figure 7.10(b) shows the corresponding rates for the CTP. Here the exact and WFAT rates start to differ at somewhat smaller F , around 0.02. One might be tempted to conclude that the difference between these potentials is entirely due to the Coulomb-tail, but other factors also play a role, as will be explained.

We have made additional calculations with a modified version of the CTP to investigate the role of the long-range part of the potential in the accuracy of the WFAT approximation. This modified CTP is the same as the CTP within 10 a.u. of the origin, but outside these 10 a.u. the potential is multiplied by a Gaussian such that it quickly goes to zero. This augmented potential is hence the same as the CTP at short range where most of the wave function is located, but it does not have a Coulomb-tail. The results of these calculations, which are not shown in the figures, show that the exact and WFAT rates depart from each other as fast as for the CTP, so the difference in performance of the WFAT between the FRP and CTP is not exclusively due to the Coulomb tail.

The form of WFAT considered in this work is called zeroth-order WFAT, since it only considers the wave function to zeroth order in the field. In Ref. [30] the first-order WFAT is developed. In that theory first-order field corrections to the wave function are considered. Determining these first-order corrections is tedious and beyond the scope of this work. Nevertheless, we can make a comment on the size of these corrections. The asymptotic coefficients C_ν in terms of which the partial rates $\Gamma_\nu = |C_\nu|^2$ are defined [Eq. (4.27)] can be obtained exactly from the R-matrix propagation, since we can construct the wave function. These exact partial rates are compared to their WFAT counterparts in Fig. 7.11. The curves in this figure show $\Gamma_\nu / \Gamma_\nu^{\text{WFAT}}$, so from Eq. (4.57) we see that this corresponds to $1 + O(F)$. The error of WFAT for each channel is thus shown by how much each curve departs from unity. In the $F \rightarrow 0$ limit all these curves should approach unity, which they indeed do. Interestingly, we see that the partial rate ratios for the FRP have a very small slope as they approach $F = 0$, while the partial rate ratios for the CTP have a larger slope. This directly shows that the first-order WFAT corrections are larger for the CTP than for the FRP.

A number of factors contribute to the first-order WFAT correction, one of them is wave function distortion caused by the external field [30]. Figure 7.12 shows the wave function in the FRP and CTP at $F = 0.06$, which, as indicated by the shaded gray area in the figure, corresponds



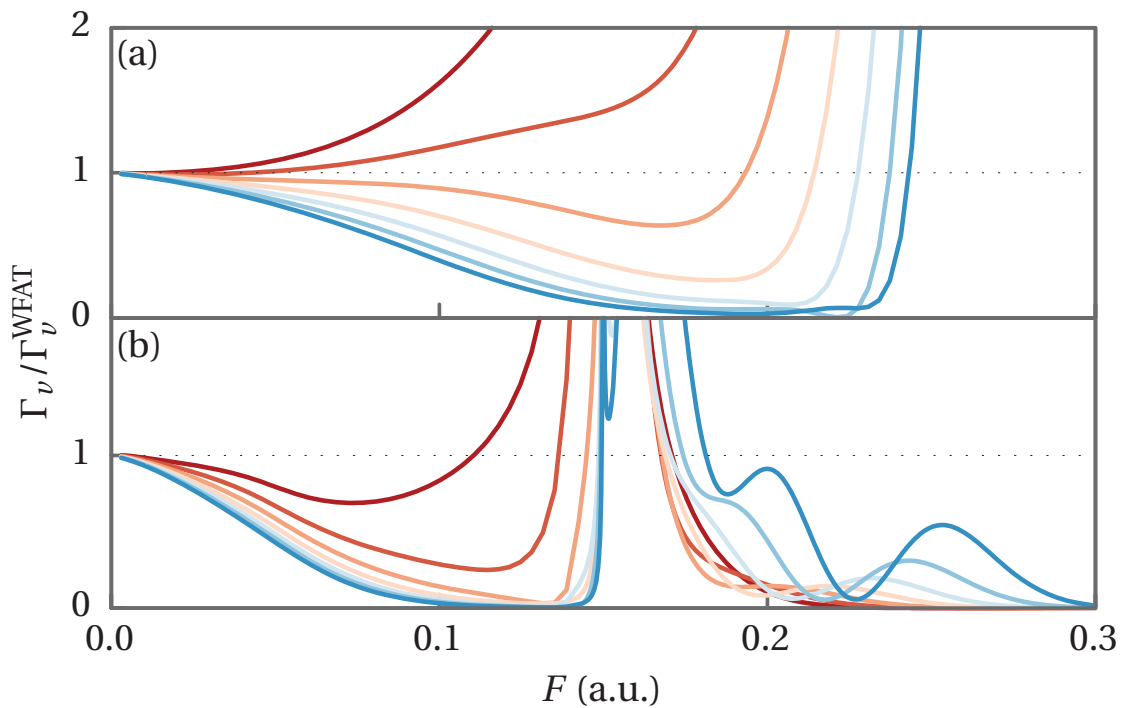
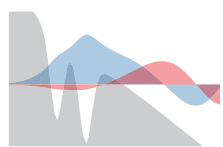
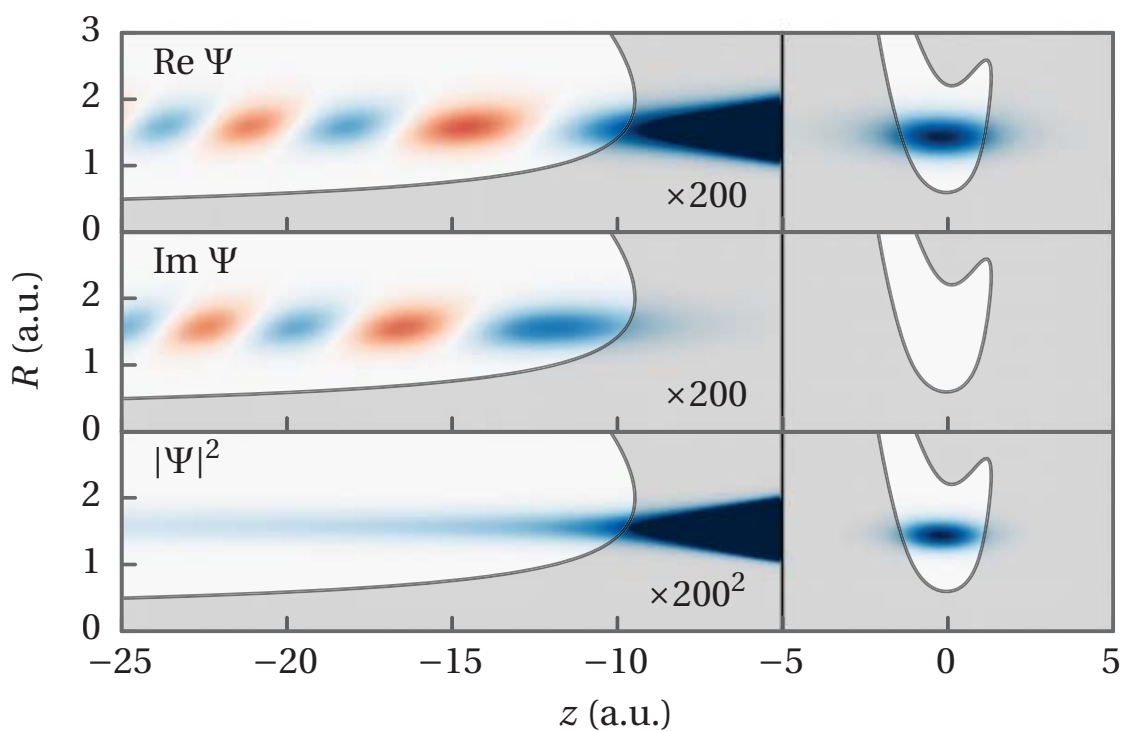


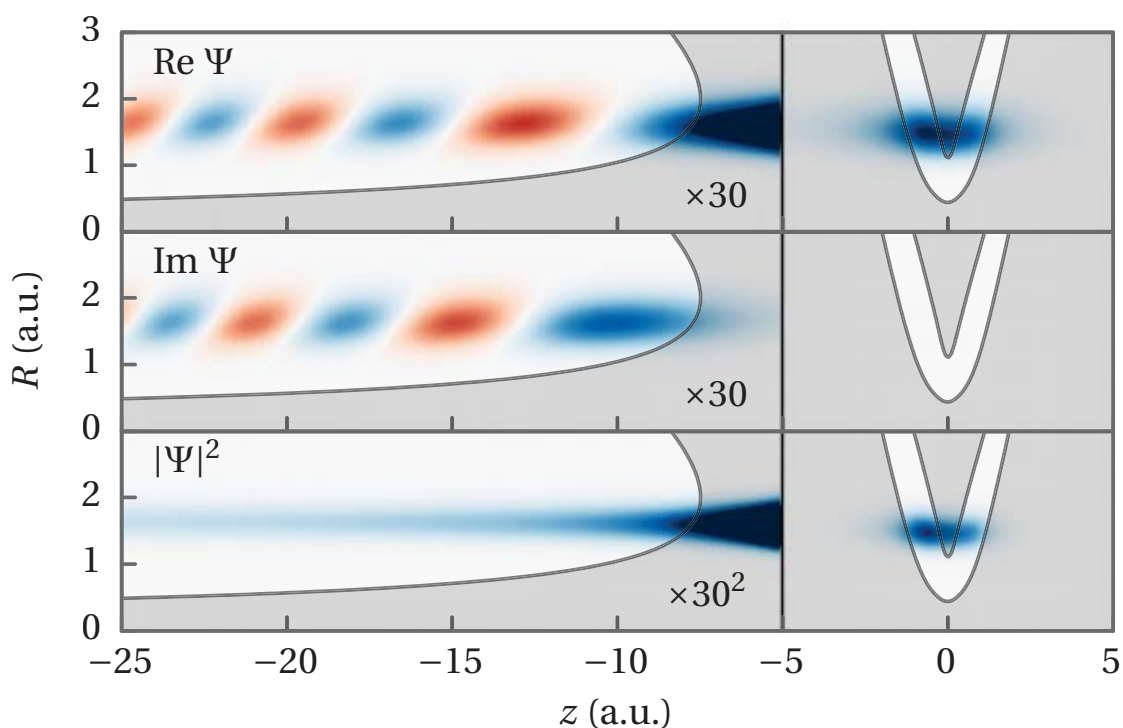
Figure 7.11: Exact partial rates $\Gamma_\nu = |C_\nu|^2$ divided by the WFAT partial rates Γ_ν^{WFAT} [Eq. (4.57)]. The red line is the first channel, the rest follow in order downwards. The dotted horizontal line is a guide for the eye. (a) is for the FRP [Eq. (7.2)] and (b) is for the CTP [Eq. (7.3)].

to under-the-barrier ionization. The figure shows the part of the wave function in the central potential well and the exponential decay in the classically forbidden region from the boundary of the well to around $z \approx 10$. This classically forbidden region contains the matching region used in WFAT to match the field-free and weak-field wave functions. The figure also shows the oscillating outgoing wave extending from the boundary of this tunneling region to $-\infty$. In the central part of the potential the wave function is more asymmetric in the CTP than in the FRP. Also the magnitude of the outgoing wave is different. The wave function is thus distorted more for the CTP than for the FRP. We would therefore expect that this contribution to the first-order WFAT correction is larger for the CTP than for the FRP. The cause for the difference in wave function field distortion between the FRP and CTP is to be found in the form of the potentials. From Fig. 7.3 it is evident that the CTP is lower in the region away from the nuclei than the FRP. It is therefore easier for the wave function to reach this region when the field is applied; a fact reflected in



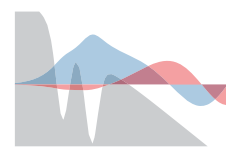


(a) FRP [Eq. (7.2)]



(b) CTP [Eq. (7.3)]

Figure 7.12: Real and imaginary parts as well as norm square of the wave function at $F = 0.06$ in the under-the-barrier regime. The outgoing wave is smaller than the part of the wave function closer to the nuclei, so for $z < -5$ the wave function has been multiplied by a factor of 200 or 30 to make it visible.



the size of the ionization rate, which is larger for the CTP than the FRP (see Fig. 7.4).

Figure 7.13 show the wave function for the two potentials at larger field strengths, corresponding to the over-the-barrier regime. Here the inner and outer classically allowed regions have merged, and the wave functions therefore go directly to oscillating outgoing waves.

Figure 7.14 shows a peculiar case. At a field strength of $F = 0.18$ the two classically allowed regions of the FRP potential are joined, however the majority of the wave function is located at R sufficiently small that the electron still has to tunnel in order to escape from the nuclei.

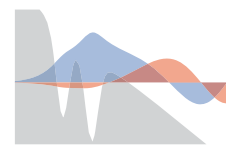
In summary, it appears that the agreement between the exact and WFAT results over an extended interval of F in the case of the FRP is specific for this potential and is likely related to the small amount of wave function distortion for this potential.

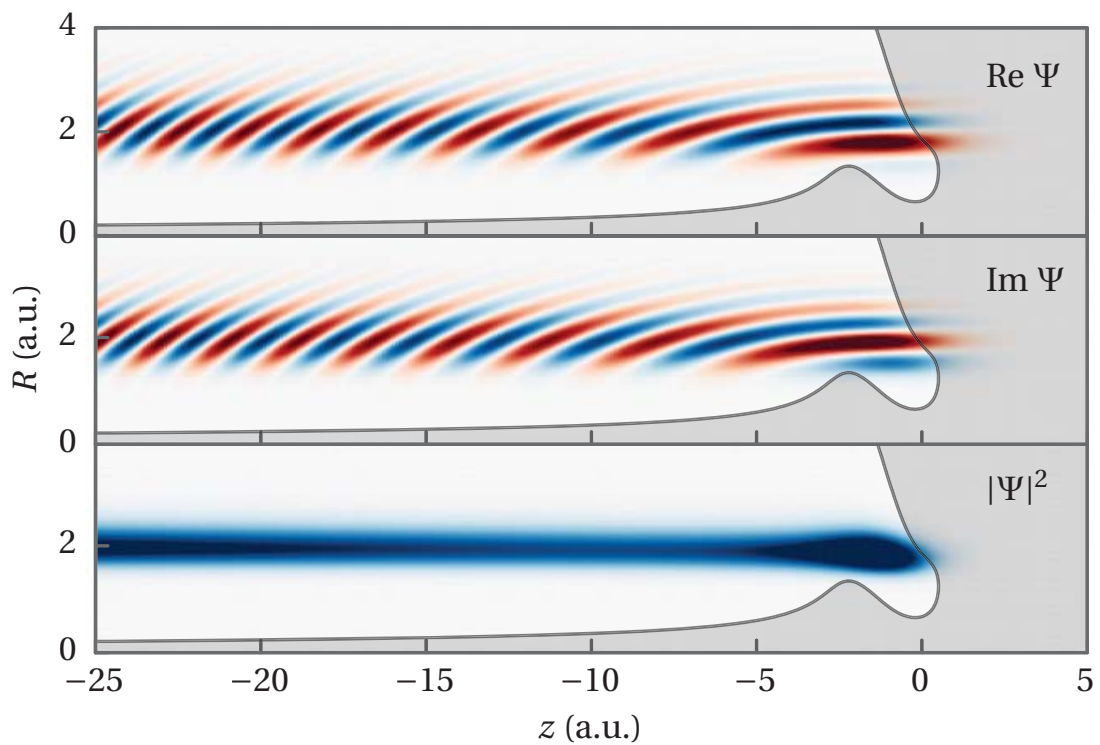
7.2.2 Polar Model Molecules: Dipole Effects

A non-zero dipole moment can be introduced in the CTP model by choosing $q_1 \neq q_2$. We still consider the system in an inertial frame¹ and thus require $q_1 + q_2 = 1$. The case $q_1 = q_2 = 0.5$ corresponds to symmetry in z and the total dipole moment μ is 0 in this case. Note that even when $q_1 = 0$ the potential still has two centers, due to the second term of Eq. (7.3). Figure 7.15 shows the exact rates obtained from calculations using different values of q_1 , with $q_2 = 1 - q_1$, and in Fig. 7.16 the exact rates are compared to their BO and WFAT counterparts.

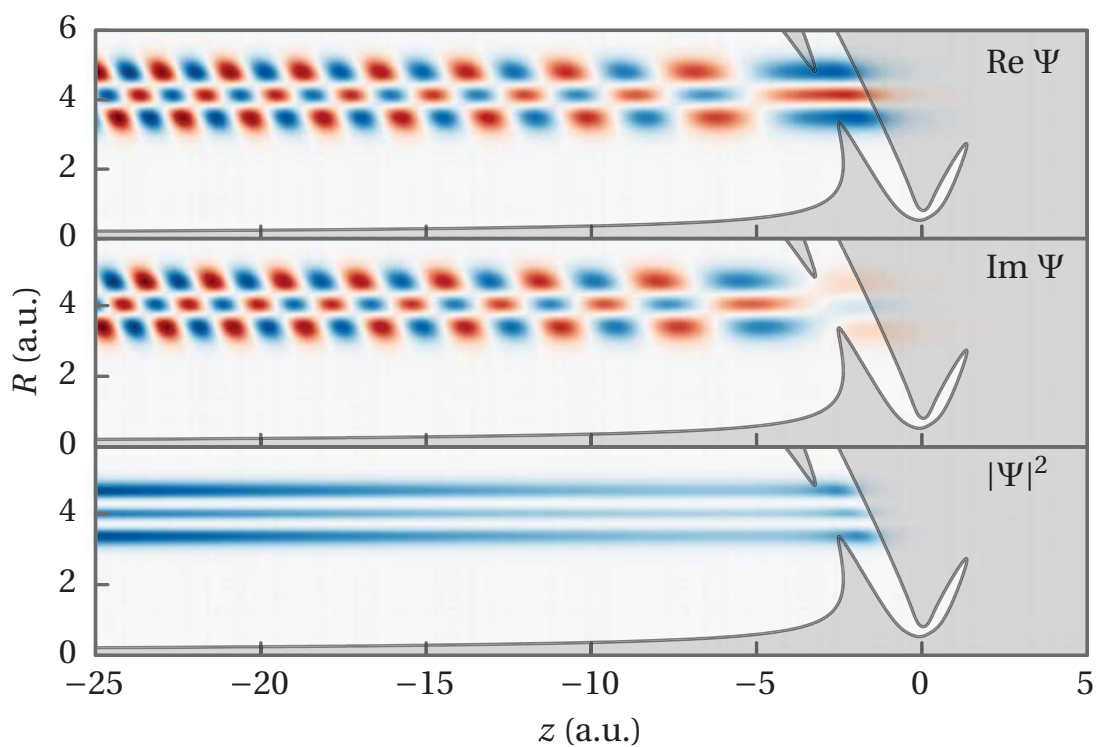
The effect of a non-zero dipole moment on the rate is determined mainly by two effects corresponding to the two factors in Eq. (4.58b). One is that the energy is shifted down when the dipole and the field are parallel, see Eq. (4.34), which should cause the ionization rate to decrease, since the electron then has to cross a higher tunneling barrier. Conversely, if the dipole and field are anti-parallel the rate should be larger. The other effect is due to the shape of the electron distribution. When the dipole and the field are parallel the majority of the electron is located closer to the tunnel exit, and is therefore more likely to tunnel through, giving a larger rate. Conversely, when the dipole and field are anti-parallel the majority of the electron is away from the tunnel exit and the rate is smaller. These two effects act opposite to each other. From Fig. 7.15 it is evident that the

¹If we choose $q_1 + q_2 \neq 1$ the net charge of the whole three-body system would be different from zero, and the external field would give the center-of-mass a net acceleration, making the center-of-mass frame non-inertial.



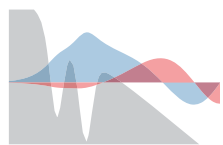


(a) FRP [Eq. (7.2)]



(b) CTP [Eq. (7.3)]

Figure 7.13: Real and imaginary parts as well as norm square of the wave function that is the analytic continuation of the field-free ground states at $F = 0.26$ in the over-the-barrier regime.



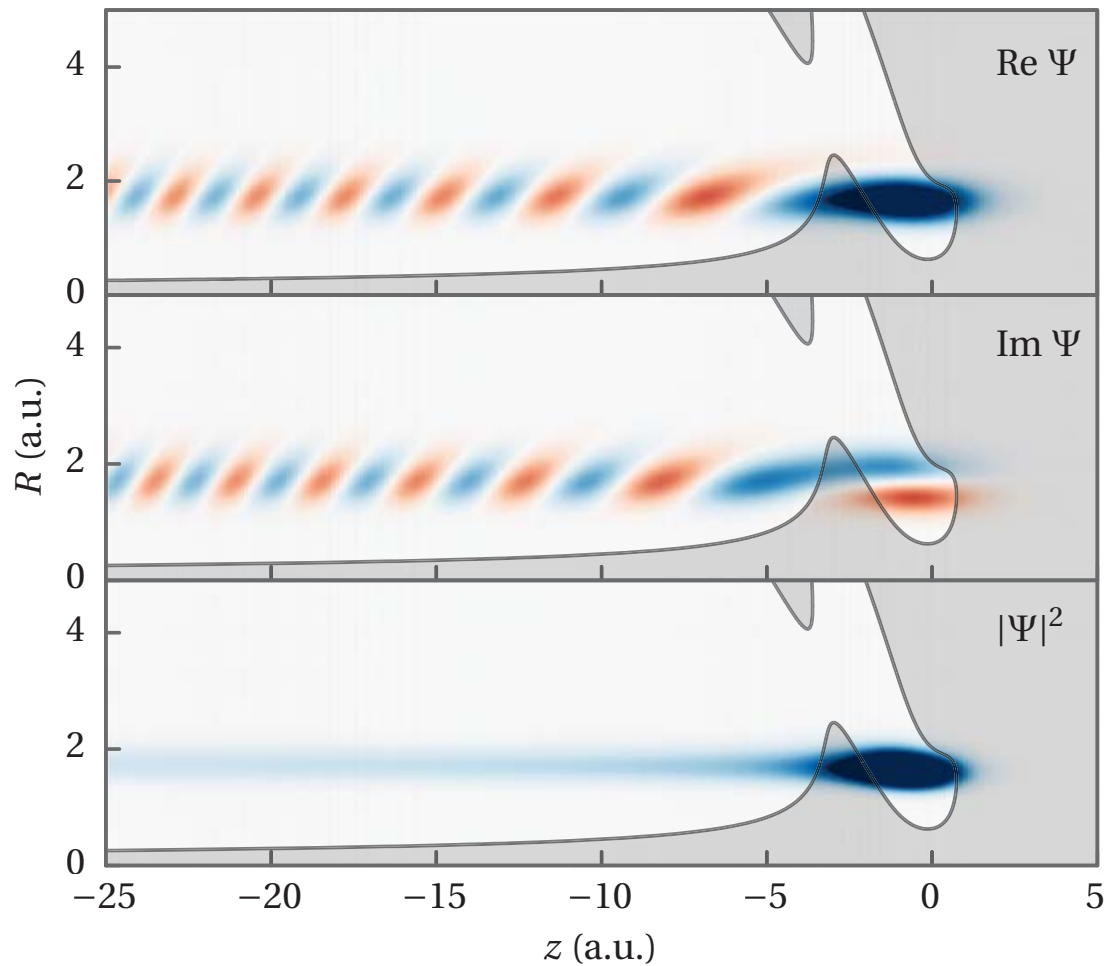
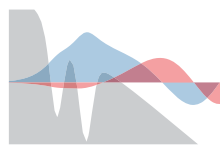


Figure 7.14: Same as Figure 7.13(a), for FRP, but at a different field strength of $F = 0.18$. Here the two classically allowed regions are connected, but the large mass of the nuclei restricts the majority of the wave function to a region in R where it still has to tunnel in order to escape.



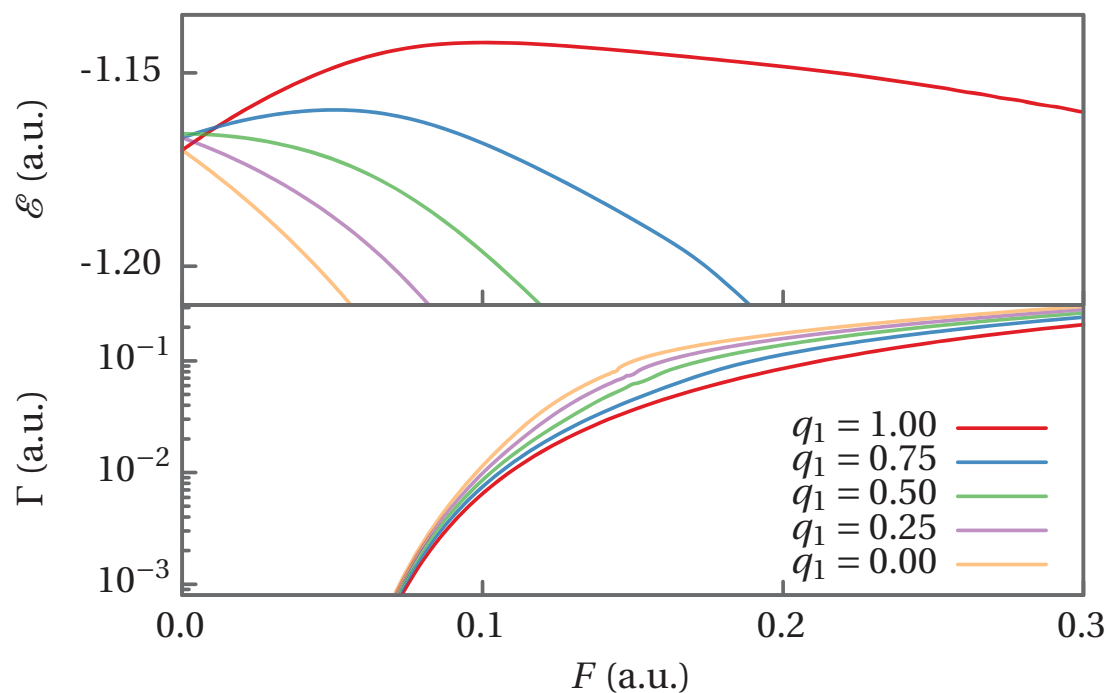
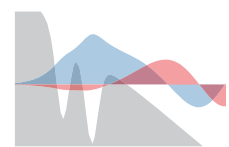


Figure 7.15: Exact real part of the energy and ionization rates for different dipoles using the CTP [Eq. (7.3)]. For $q_1 < 0.5$ the dipole and the field are parallel, for $q_1 > 0.5$ they are anti-parallel. The real part of the energy has a slope at $F = 0$ given by the dipole moment μ of the associated field-free state.

size of the rate is largest when the dipole and the field are parallel, so we conclude that in this case the electron distribution effect is larger than the energy-shift effect. This is similar to experimental findings in CO [31–33].

We see that, as the dipole increases, the WFAT rate departs from the exact rate for smaller F . This behavior is expected. In the WFAT derivation, see Eq. (4.38), we neglected terms in the potential of order $O(z^{-2})$ or higher, which is consistent with the leading-order approximation in F . In the non-dipole case no $O(z^{-2})$ terms exists in the potential so what we neglect in the potential is of order $O(z^{-3})$ or higher. In the dipole cases, on the other hand, a term of order $O(z^{-2})$ is present in the potential, and what we neglect in WFAT is therefore of greater importance [this contributes to the term $O(F)$ in Eq. (4.57)]. In all cases we obtain the expected behavior from BO; agreement at $F > F_{\text{BO}} \approx 0.04$ but difference at $F < F_{\text{BO}}$.

Figure 7.17 shows the partial rates for the different dipole cases. We see that the slope of these curves near $F = 0$, which is the same as the



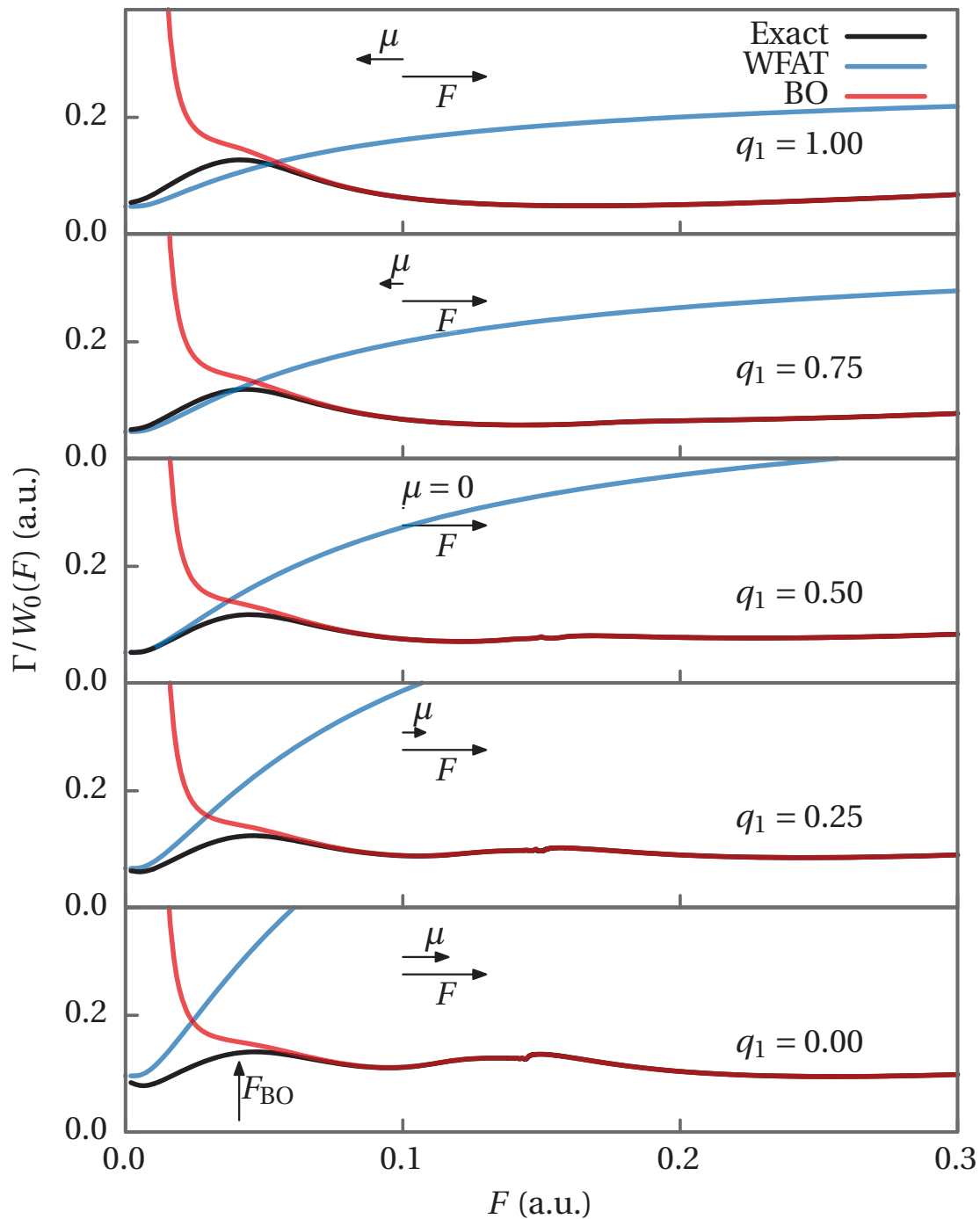
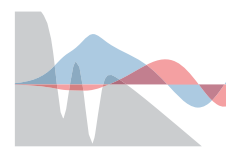


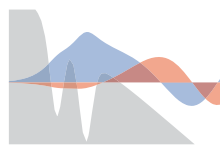
Figure 7.16: Ionization rates for different dipoles using the CTP [Eq. (7.3)]. The horizontal arrows indicate the orientation of the total dipole moment [Eq. (4.35)] with respect to the field. The vertical arrow indicates the boundary of the region of validity of the BO approximation [Eq. (4.90)].



first-order WFAT correction, is indeed smallest for the non-dipole $q_1 = 0.5$ case, and increases for larger dipole moments.

7.3 Conclusion

The present study has extended previous work on the tunneling ionization of molecules in a 1D model with electronic and nuclear motions treated exactly within the limitations of the model [10]. The theory has been generalized to deal with potentials that has a Coulomb-tail, and non-symmetric potentials with non-zero dipole moments modelling the tunneling dynamics in polar molecules. We have shown that inclusion of a Coulomb-tail in the potential and non-zero dipole moments do not change the main conclusions of Ref. [10], namely that the BO approximation breaks down for fields $F < F_{\text{BO}}$, but works for $F > F_{\text{BO}}$ [Eq. (4.90)], and that WFAT works in the weak-field limit. The agreement between the WFAT and exact results over an extended interval of F , seen here and in Ref. [10], seems to be particular for the finite-range model potential and due to the small amount of field distortion for this potential.



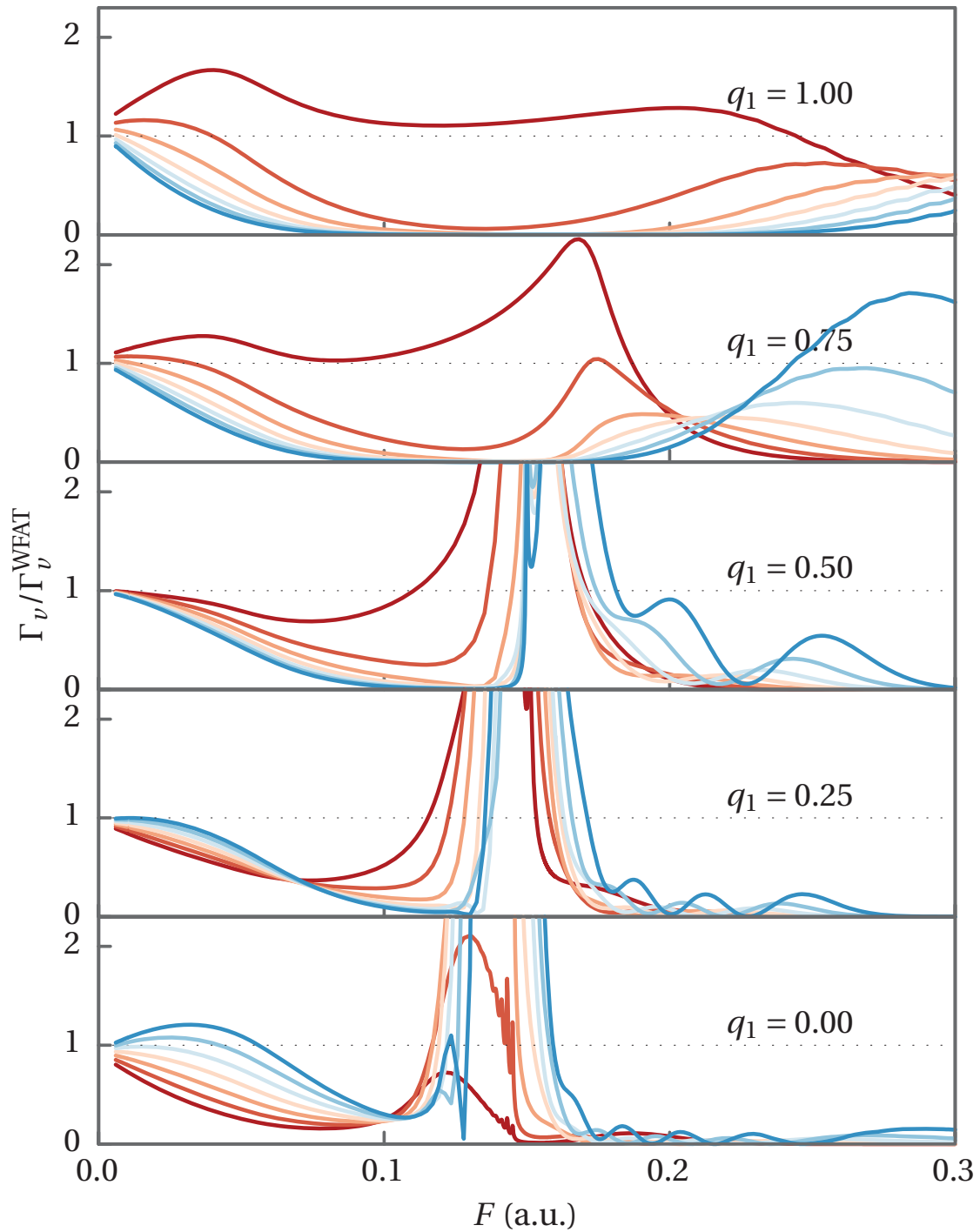
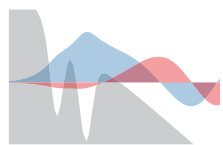


Figure 7.17: Exact partial rates $\Gamma_\nu = |C_\nu|^2$ divided by the WFAT partial rates Γ_ν^{WFAT} [Eq. (4.57)], for different dipoles using the CTP [Eq. (7.3)]. The dark red line is the first channel, the rest follow in order. The dotted horizontal line is a guide for the eye.



8 Dissociative Tunneling Ionization

Large parts of the material in this chapter is the same as in Ref. [2], of which I am first author.

8.1 Illustrative 1D Calculations

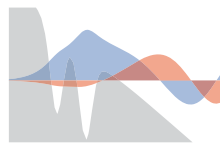
In this section we compare exactly calculated KER spectra with those obtained through the BO approximation [Eq. (4.73)] and the WFAT [Eq. (4.57)]. In the following we will consider a model of H_2^+ as an example. The potentials we consider are

$$U(R) = \frac{1}{R}, \quad (8.1a)$$

$$V(z, R) = -\sum_{\pm} \frac{1}{\sqrt{(z \pm \frac{R}{2})^2 + a(R)}}, \quad (8.1b)$$

and $m_1 = m_2 = 1836$, $q_1 = q_2 = 1$. The interaction between the nuclei and the electrons $V(z, R)$ is described by a soft-core Coulomb potential (SCP). The function $a(R)$ is chosen in such a way that the BO potential derived from this potential reproduces the BO potential energy curve of 3D H_2^+ [34–36], see Fig. 8.1 [also see App. E].

The process we consider in this chapter is dissociative tunneling ionization. Another dissociative process is direct dissociation, where the electron stays with one of the nuclei after they have separated. When the field is not too strong this process can be pictured as the nuclei tunneling through a barrier in the BO potential. We can think of the electronic energy as a sampling of the electron-nuclear potential with the norm square of the electronic wave function as weight factor. This electronic wave function is mainly located in the two wells of the electron-nuclear potential around $z + \frac{R}{2} = 0$ and $z - \frac{R}{2} = 0$ [see Fig. 8.2]. When a positive electric field is applied, the electron will prefer to stay in the lower well around $z + \frac{R}{2} = 0$.



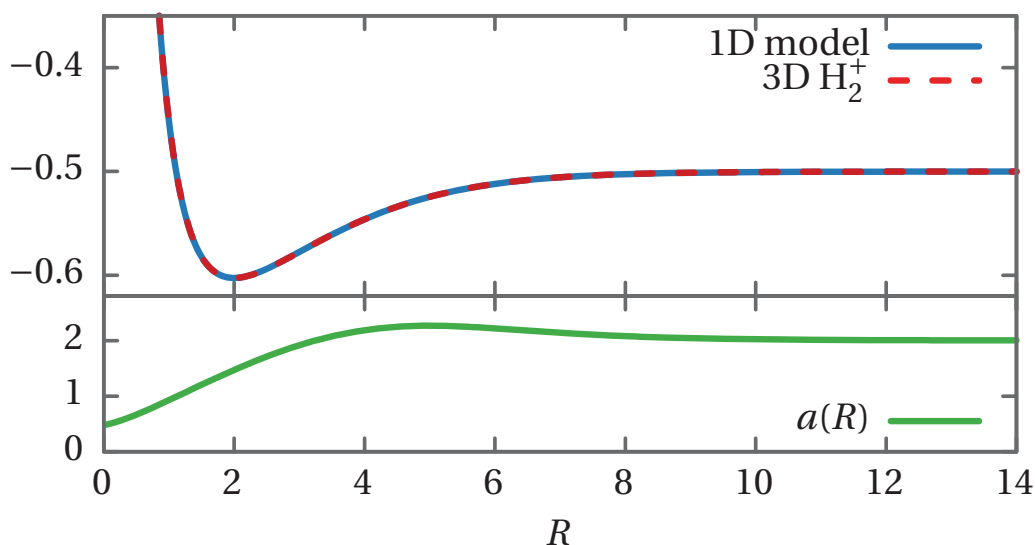


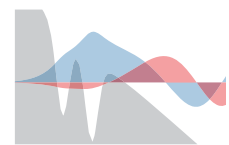
Figure 8.1: BO potential of 3D H_2^+ [27] (dashed red line), and the BO potential $U(R) + E_e(R; F = 0)$ obtained from the potentials (8.1) (blue line). The green line shows the soft-coulomb parameter used in the potential (8.1b) to give the blue curve.

The potential contribution from the field in this well is $qFz = -qFR/2$, so for sufficiently large R , the electronic energy takes the form $E_H - qFR/2$, where E_H is the energy of hydrogen in the present field. As F is increased, the barrier in the BO potential, through which the nuclear wave function has to tunnel, grows smaller and eventually disappears. In our numerical scheme we cannot treat this direct dissociation channel since we use a box in the R -coordinate, on the boundary of which we assume the wave function to be zero. The large mass of the nuclei means, however, that this process can be neglected for low field strengths, where dissociative tunneling ionization will dominate.

A way to treat this pure dissociation channel could be to apply the R-matrix propagation scheme to the nuclear BO Equation (5.53b). The pure dissociation becomes a size-able channel for larger field strengths, so the BO should be applicable.

8.1.1 From Wave Function to KER Spectrum

Figure 8.3 illustrates how the BO approximation can be used in conjunction with the reflection principle to determine the KER spectrum. The



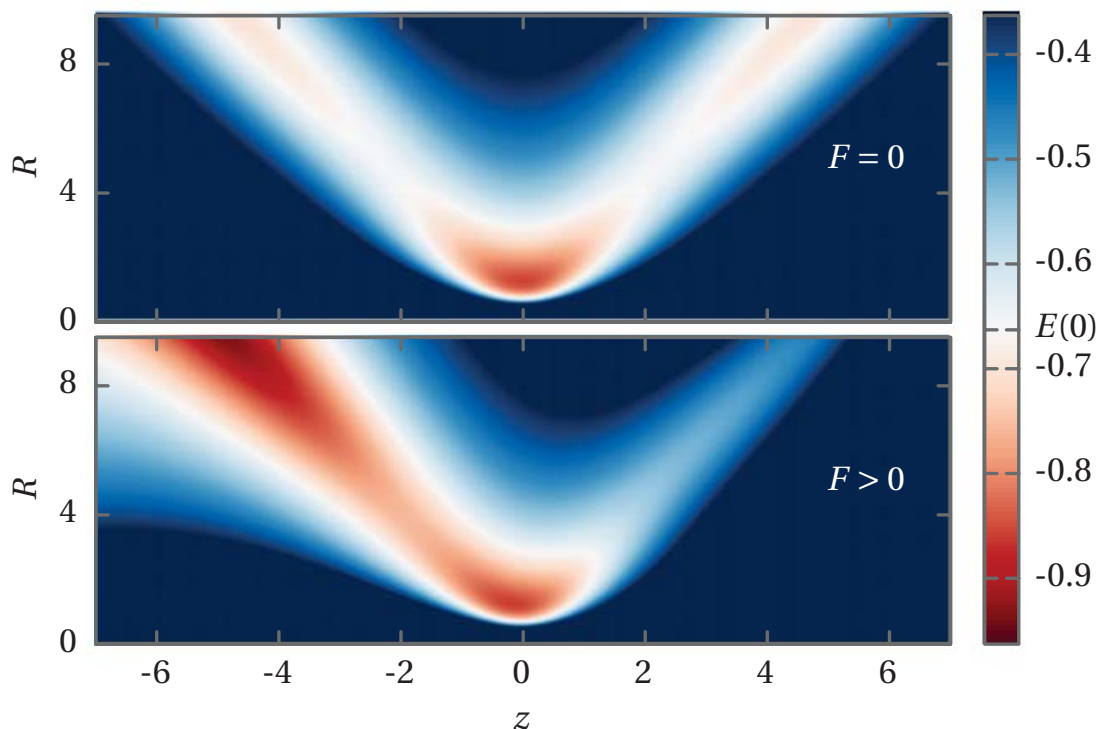
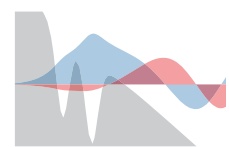


Figure 8.2: Total potential $V(z, R) + U(R) + Fqz$ [Eq. (8.1)] felt by the electron. The color scale is centered around the field-free energy $E(0)$, such that red colors correspond to the classically allowed region, where it is more likely for the wave function to be, and blue colors correspond to classically forbidden, where it is less likely to find the wave function.

figure shows a calculation for the ground state of the H_2^+ model at $F = 0.034$. The field dressed nuclear wave function $|\chi(R)|^2$ is multiplied by the electronic rate $\Gamma_e(R)$. The exponential dependence of the electronic rate $\Gamma_e(R)$ on the internuclear coordinate means that the product $\Gamma_e(R) |\chi(R)|^2$ {see [Eq. (4.73)]} has its maximum at a value of $R \approx 3$, which is significantly different from the maximum of the bare nuclear wave function at $R_0 \approx 2$. This in turn means that the transition to the continuum, which is determined by the product $\Gamma_e(R) |\chi(R)|^2$ and not the bare nuclear wave function, is far from 'vertical' in R with respect to the initial nuclear wave function, and the spectrum peaks at a lower energy around $1/R \approx 0.33$ and not at $1/R_0 \approx 0.5$.

Using WFAT within the BO approximation we can determine in which direction the maximum of the spectrum shifts when the field is varied.



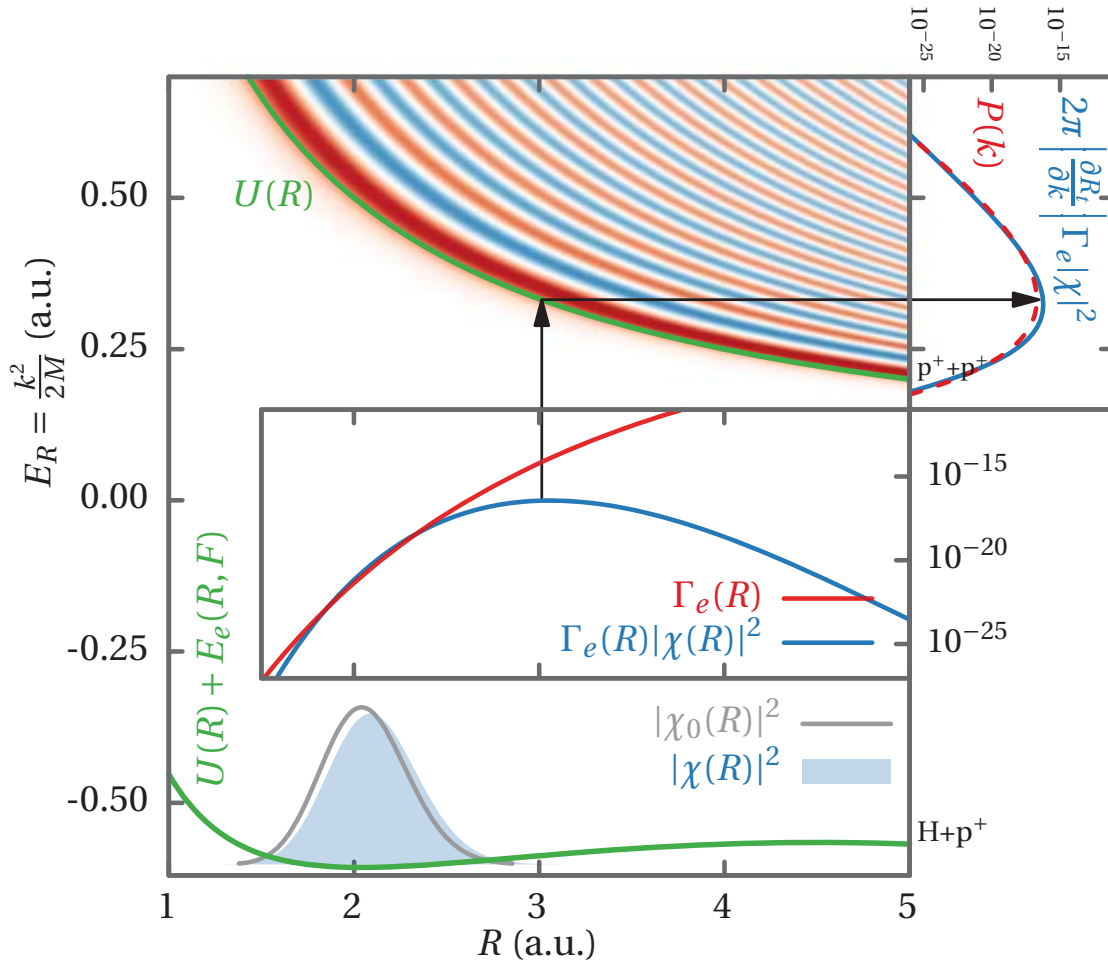
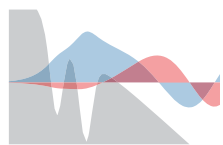


Figure 8.3: The field dressed nuclear wave function $|\chi(R)|^2$ [light blue shaded area in the lower $U(R) + E_e(R; F)$ BO curve] is multiplied by the electronic rate $\Gamma_e(R)$ (red line) and reflected in the dissociative $U(R)$ BO curve to give a KER spectrum (solid blue line in upper right corner, [Eq. (4.73)]), using the relation $U(R) = \frac{k^2}{2M}$ to translate k into R . This is compared to the exact KER spectrum $P(k)$ (red dashed line, [Eq. (4.27)]). A field strength of $F = 0.034$ was used for the calculations shown in this figure. The solid gray line in the lower part of the figure shows the field-free nuclear wave function $|\chi_0(R)|^2$. The surface plot in the upper part of the figure shows the continuum states $g(R, k)$ of the $U(R)$ potential, these are solutions of Eq. (4.7b).

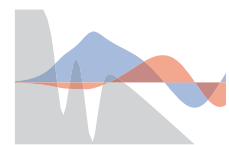


Under these approximations the main dependence of the electronic rate on the field is contained in the exponent $-\frac{2\kappa^3(R)}{3F}$, see Eq. (4.78). The electronic energy $E_e(R; F = 0)$, in terms of which $\kappa(R)$ is defined, generally depends very much on the system considered. In the case of H_2^+ it is a monotonically increasing function of R , since when the two potential wells around each of the nuclei start to overlap the electron is more tightly bound. This in turn means that the electronic rate is an increasing function of R , as can also be seen in Fig. 8.3. When the strength of the field increases, the exponent $-\frac{2\kappa^3(R)}{3F}$ grows, but at the same time the slope of this exponent with respect to R decreases, since $\kappa^3(R)$ is multiplied by a smaller number. The smaller slope means that the location of the maximum of the product $\Gamma_e(R) |\chi(R)|^2$ is shifted less from the maximum of $|\chi(R)|^2$ as the field strength increases, and conversely, as the field strength is decreased the maximum of the product $\Gamma_e(R) |\chi(R)|^2$ is shifted more towards larger R . These shifts are directly reflected in the spectrum, which is given as the reflection of the $\Gamma_e(R) |\chi(R)|^2$ product in the BO and reflection approximations.

Figure 8.4 shows KER spectra obtained using as initial state the first vibrationally excited state of H_2^+ . This is the lowest state with a non-trivial nodal structure in R . In the figure two different field strengths are considered. In the top panel we see that the nodal structure of the nuclear wave function is reflected in the KER spectrum, although one peak is a lot larger than the other. This asymmetry can be understood in the BO approximation, see Eq. (4.73), as due to the fact that the electronic rate $\Gamma_e(R)$ has an exponential dependence on R . In the WFAT it can be understood as resulting from the exponential dependence of the field factor [Eq. (4.58a)] on k . For the lower field strength the structures at $E_R > 0.4$ are not visible as the KER spectrum falls below the numerical precision limit of our calculation.

For the large field strength [Fig. 8.4(a)] we see that the BO KER spectrum has a shape much closer to the exact KER spectrum than for the lower field strength. Also the maximum value of the BO KER spectrum is more than an order of magnitude closer to the maximum value of the exact KER spectrum for the larger field strength, see the caption of Fig. 8.4. The two field strengths of Fig. 8.4 lies on either side of the critical BO field [Eq. (4.90)], which for the system under consideration is $F_{\text{BO}} = 0.0315$. As we increase the field strength further the BO gives even better results.

For the lower field strengths, where BO fails, we can apply the WFAT. In Fig. 8.4 we see that the shape of the WFAT KER spectrum indeed is closer



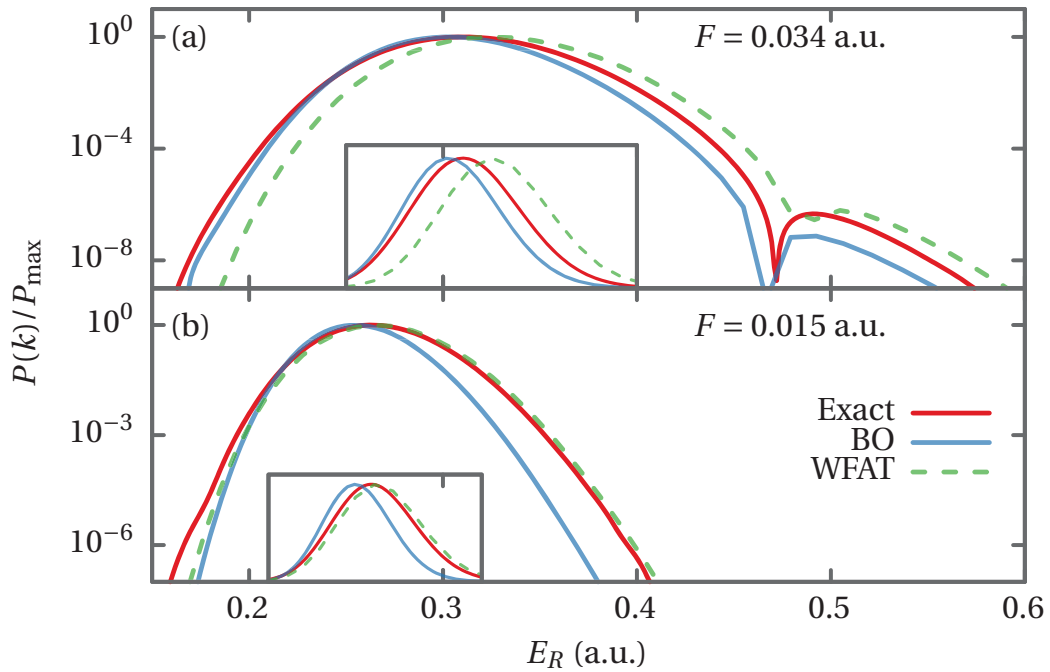
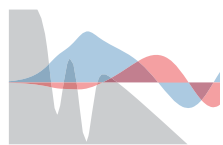


Figure 8.4: KER Spectra normalized to their maxima. Red line: $P(k)$ [Eq. (4.27)]. Blue line: BO combined with reflection principle [Eq. (4.73)]. Green (dashed) line: WFAT [Eq. (4.57)]. The insets show the normalized KER spectra on a linear scale. The critical field for use of BO [Eq. (4.90)] is for H_2^+ : $F_{\text{BO}} = 0.0315$. (a) $P_{\text{max}}^{\text{BO}}/P_{\text{max}}^{\text{Exact}} = 2.32$ and $P_{\text{max}}^{\text{WFAT}}/P_{\text{max}}^{\text{Exact}} = 0.29$. (b) $P_{\text{max}}^{\text{BO}}/P_{\text{max}}^{\text{Exact}} = 95.0$ and $P_{\text{max}}^{\text{WFAT}}/P_{\text{max}}^{\text{Exact}} = 0.54$.

to the exact KER spectrum than the BO KER spectrum for the weaker field strength, and it is also closer in magnitude to the maximum value. For the larger field strength the WFAT KER spectrum is further from the exact KER spectrum in both shape and magnitude.

8.1.2 From KER Spectrum Back to Wave Function

The field dressed nuclear wave function can be imaged from a measurement of the KER spectrum by inverting Eq. (4.73) for fields sufficiently large that the BO approximation applies. To demonstrate this we have taken the exact KER spectrum from our calculation at $F = 0.034$ for the first vibrationally excited state and divided it by the Jacobian factor and the electronic rate to obtain an image of the nuclear density. Since an experi-



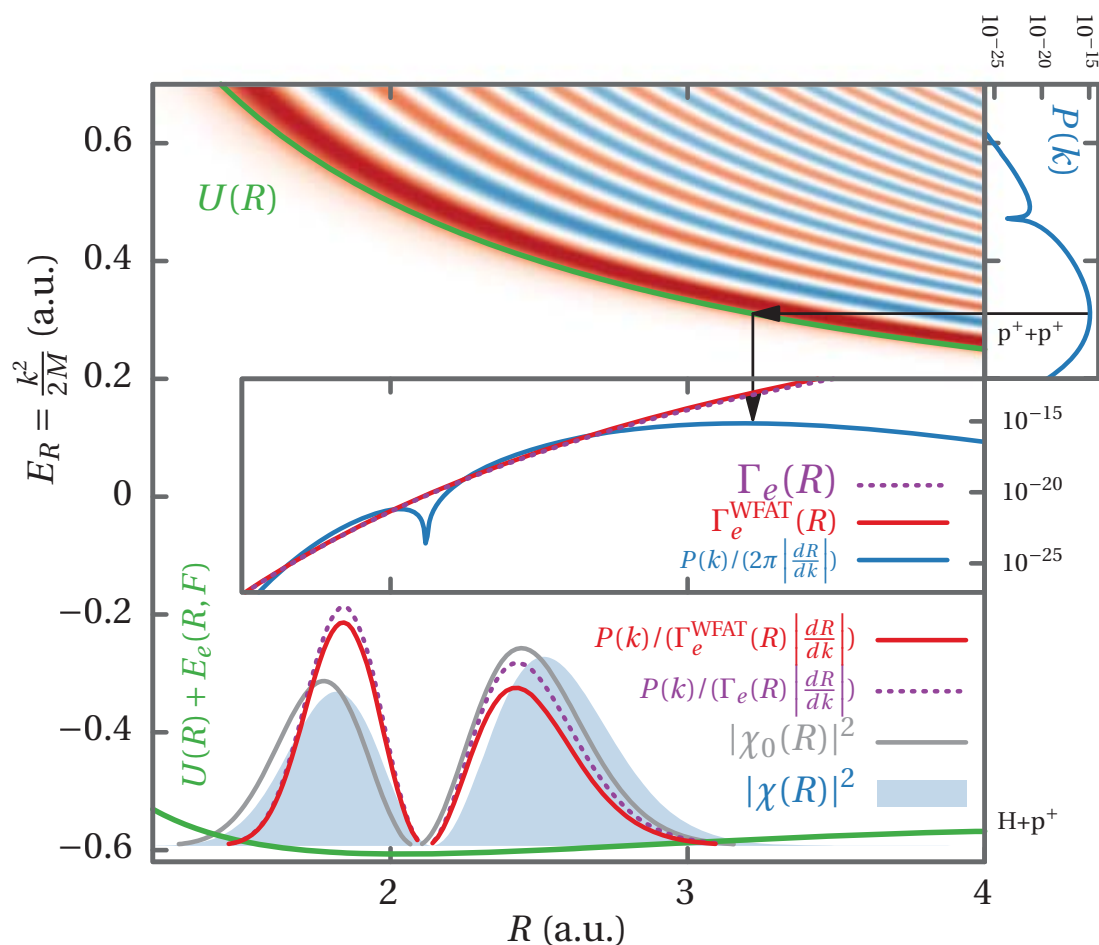
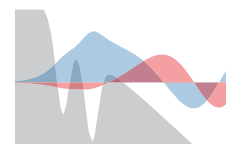


Figure 8.5: From the exact KER spectrum $P(k)$ [upper right corner, Eq. (4.27)] at $F = 0.034$ the magnitude of the asymptotic wave function has been found by reversing the reflection principle, giving $P(k) / \left(2\pi \left| \frac{dR}{dk} \right| \right)$, using the relation $U(R) = \frac{k^2}{2M}$ to translate k into R . From this, the field-dressed nuclear wave function has been imaged by dividing with the electronic rate $\Gamma_e(R)$ and normalizing. In the lowest part of the plot, the dashed (purple) line shows this imaging using the exact electronic rate $\Gamma_e(R) = -2\text{Im}[E_e(R; F)]$, the red line shows the imaging using the BO WFAT approximation $\Gamma_e^{\text{WFAT}}(R)$ [Eq. (4.78)]. The solid gray line shows the field-free nuclear wave function $|\chi_0(R)|^2$. The shaded (light blue) area shows the field-dressed nuclear wave function $|\chi(R)|^2$. The surface plot in the upper part of the figure shows the continuum states $g(R, k)$.



mental KER spectrum is typically not known on an absolute scale, we have then normalized this quantity. In a calculation on a more complicated system than the one considered here the exact electronic rate is often not available, so we also show the result using the WFAT approximation for the electronic rate [Eq. (4.78)]. The results are compared to the nuclear wave function known from the calculation in our model in Fig. 8.5. They do not agree perfectly, but the nodal structure is correctly reproduced.

For smaller field strengths, where the BO is not applicable, this type of imaging is not possible. The KER spectrum, however, does give us access to the asymptotic wave function, as it is the norm square of the expansion coefficients of this, see Eq. (4.18). For the cases we have looked at, the phase of the asymptotic coefficient $C(k)$ varies very little over the range where it has support. In our model we have access to the full wave function, and this we show in Figs. 8.6-8.7. The imaging through the 1D equivalent of Eq. (4.18) would only give access to the part at large negative z .

In the classically allowed region at large negative z the maximum of the wave function follows a classical trajectory. This is a prediction of the WKB theory, which applies as long we are not too close to the turning line. The classical trajectories can be found using Newton's second law

$$m\ddot{z} + \frac{\partial}{\partial z}V(z; R) + Fq = 0, \quad (8.2a)$$

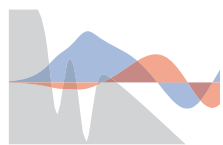
$$M\ddot{R} + \frac{\partial}{\partial R}V(z; R) + \frac{\partial}{\partial R}U(R) = 0. \quad (8.2b)$$

A tempting choice of initial condition for the differential Eqs. (8.2) would be to choose the (z, R) values at the intersection of the outer turning line and the maximum ridge of the wave function, with zero velocity in both z and R direction. However, the WKB fails near the turning line, and therefore we cannot expect the wave function to follow a classical trajectory here. Instead we have chosen as initial condition some point at the maximum of the wave function at a large negative z value away from the turning line. The influence of the $V(z; R)$ potential can be neglected for sufficiently large negative z , in this region we can write the separated energy conservation equations

$$\frac{1}{2}m\dot{z}^2 + Fqz = E - \frac{1}{2M}k^2, \quad (8.3a)$$

$$\frac{1}{2}M\dot{R}^2 + U(R) = \frac{1}{2M}k^2. \quad (8.3b)$$

The initial velocities have then been determined from Eqs. (8.3), using the real part of the total (quantum) energy for E and the k at which the



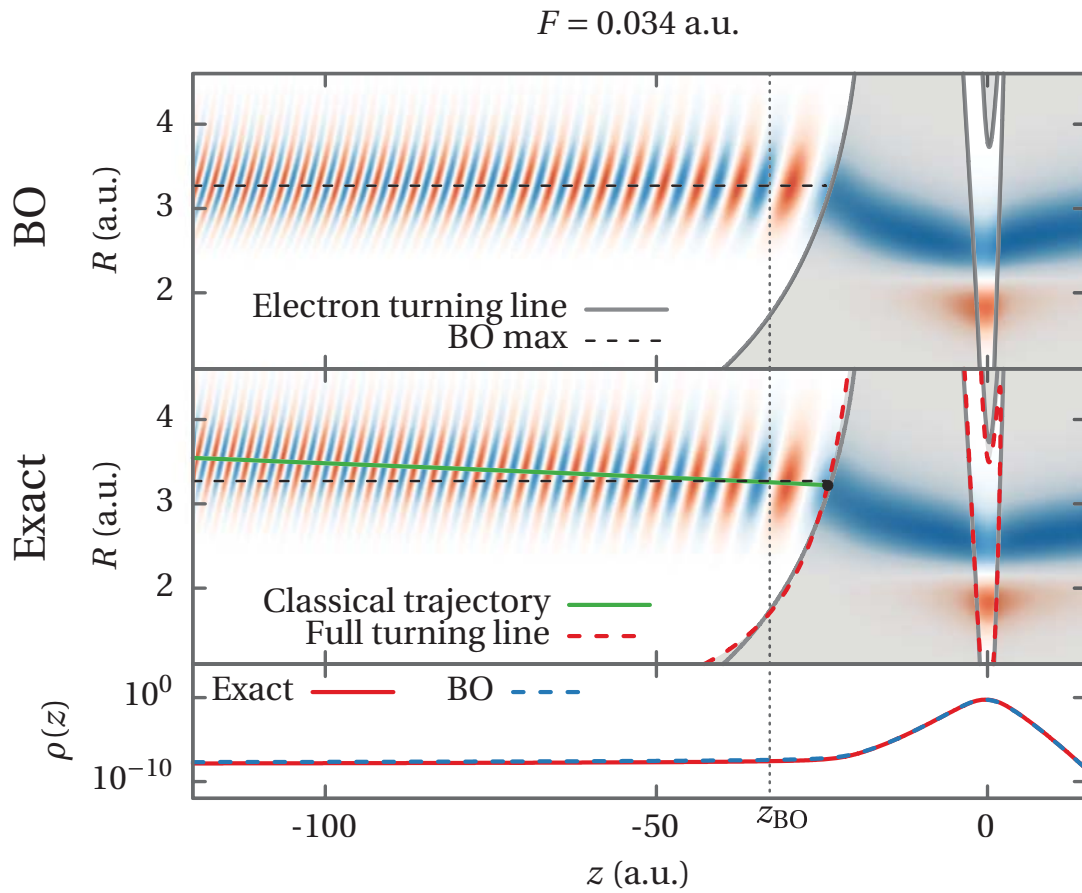
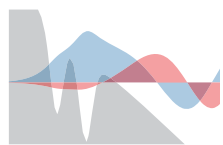


Figure 8.6: Real part of wave function normalized with the electron density $\rho(z) = \int |\Psi(z, R)|^2 dR$. Gray lines: Electronic turning lines $\text{Re}[E_e(R; F)] = V(z, R) + Fqz$. Dashed (red) lines: Full turning lines $\text{Re}[E(F)] = V(z, R) + U(R) + Fqz$. In the upper panels the dashed black line shows a constant value that coincides with the maximum of the BO wave function. In the middle panels the green line additionally shows a classical trajectory that coincides with the maximum of the exact wave function. The black dot at the end of the classical trajectory is the exit point $(z_{k_{\max}}, R_{k_{\max}})$ determined from the maximum of the spectrum k_{\max} (see main text). The critical BO distance [Eq. (4.89)] is shown with a vertical dashed line at $-z_{\text{BO}} = -32.9$.



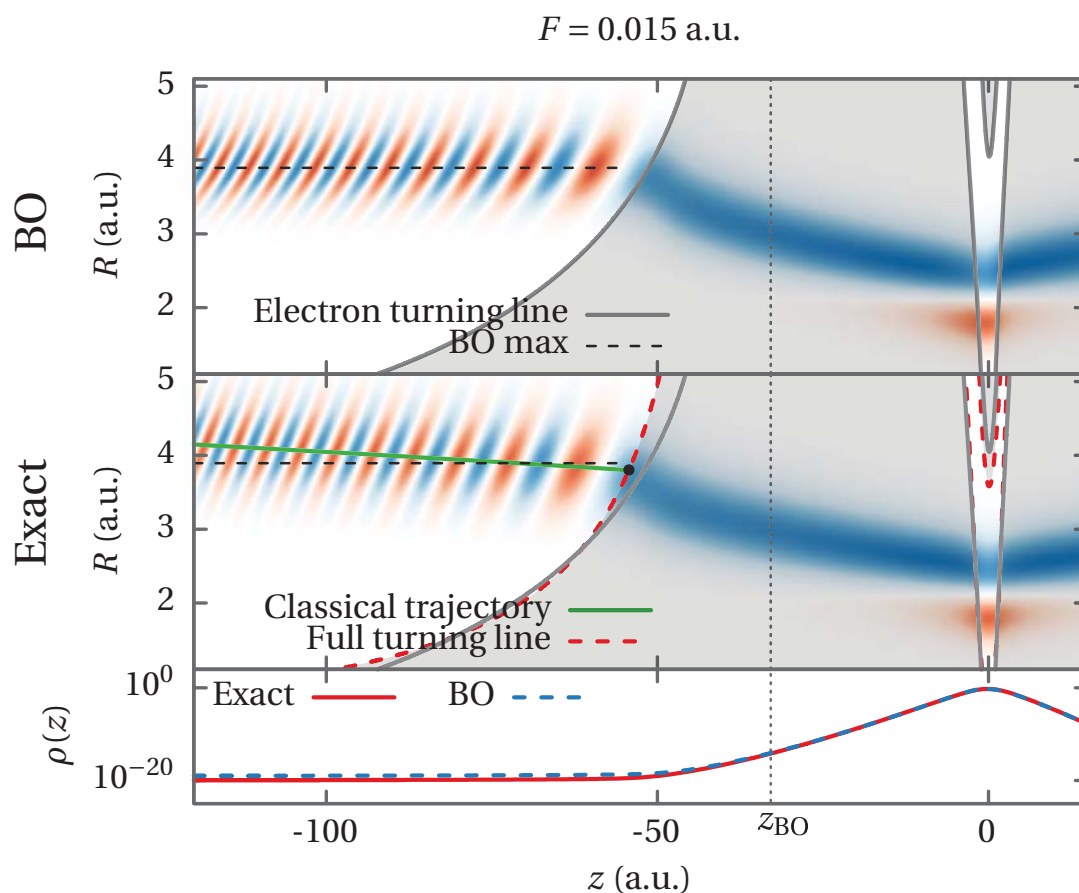
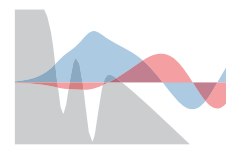


Figure 8.7: Same as Fig. 8.6, only at a different field strength.

KER spectrum $P(k)$ [Eq. (4.27)] peaks. The classical trajectories shown in Figs. 8.6-8.7 were found using such initial conditions, and then propagated inwards.

From Figs. 8.6-8.7 it can be seen that contrary to the exact wave function, the position of the ridge of the BO wave function in R does not change with z . This is expected as the BO approximation appears in the limit of infinite nuclear mass, so classical motion in the nuclear coordinate is not possible. The asymptotic wave function that we can image using Eq. (4.18) is therefore a non-BO wave function.

It might seem strange that the BO is able to give the correct KER spectrum when the spectrum is the norm square of the expansion coefficients of the asymptotic wave function, and the BO gives a wrong description of this asymptotic wave function. However, the fact that the BO wave function does not obtain a probability current (or velocity in the classical



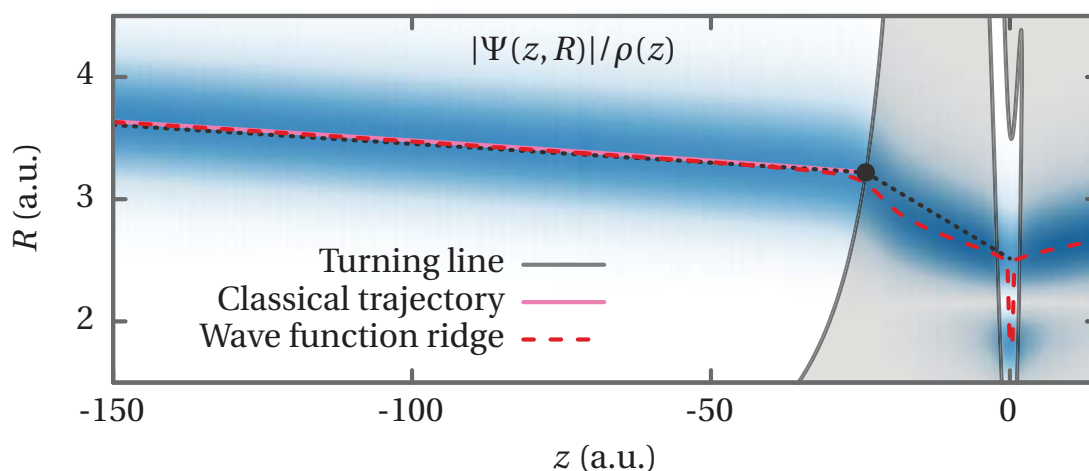
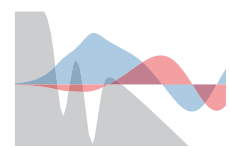


Figure 8.8: Absolute value of wave function normalized with the electron density $\rho(z) = \int |\Psi(z, R)|^2 dR$ for $F = 0.034$. Solid grey lines: Full turning lines $\text{Re}(E(F)) = V(z, R) + U(R) + Fqz$. The long dashed red line shows for each z the R at which the wave function $|\Psi(z, R)|$ has its maximum. The solid pink line shows a classical trajectory [Eq. (8.2)]. The black dot at the end of the classical trajectory is the exit point $(z_{k_{\max}}, R_{k_{\max}})$ determined from the maximum of the spectrum k_{\max} (see main text). The short dashed lines are the simple straight line estimates for the tunneling and initial classical motion described around Eq. (8.4).

picture) in the R -direction does not alter its projection on the continuum states. The important point is whether the BO wave function is similar to the exact wave function as it emerges at the outer turning line after tunneling, and as we have seen, this is the case if the turning line is within the critical BO distance z_{BO} [Eq. (4.89)].

In Figs. 8.6-8.7 we also see that for the larger field strength the tunneling is completed before the critical BO distance is reached, contrary to at the smaller field strength. We see that for the large field strength the electronic and full turning lines agree quite well in the region where most of the wave function is localized, but for the smaller field strength they do not.



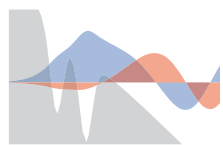
8.1.3 A Refraction Phenomenon

One can notice that a phenomenon reminiscent of light refraction occurs for the wave function around the turning line in Figs. 8.6-8.7. It is evident, that the direction in which the maximum of the wave function 'moves' changes noticeably at the turning line, when the wave function escapes from the classically forbidden tunneling region into the classically allowed region. The change of direction is due to the two different types of 'motion' involved. When the wave function emerges from the tunneling region it has essentially zero average velocity in the R direction. This means that we can apply the reflection principle in reverse on the spectrum to find the $R_{k_{\max}}$ coordinate at which the maximum of the wave function emerges from the tunneling region by the relation $U(R_{k_{\max}}) = \frac{k_{\max}^2}{2M}$, where k_{\max} is the value of k for which the spectrum $P(k)$ has its maximum. The z value corresponding to this $R_{k_{\max}}$ can then be found by considering the turning line $V(z_{k_{\max}}, R_{k_{\max}}) + U(R_{k_{\max}}) + Fqz_{k_{\max}} = \text{Re } E$.

In Fig. 8.8 we see that near the turning line the location of the wave function ridge differs from the classical trajectory. This is expected, since the prediction that the wave function ridge should follow a classical trajectory comes from WKB theory, which fails near the turning line. Nevertheless, we can roughly describe the dissociative tunneling ionization process in two steps. First the system tunnels from the central region around $z = 0$ to the exit point $(z_{k_{\max}}, R_{k_{\max}})$. This motion can roughly be described by a straight line from the maximum of the nuclear wave function $|\chi(R)|^2$ that has the largest R value, since this is the maximum that will dominate the tunneling, to the exit point. Notice that this tunneling is not simply the electron tunneling out, but a correlated process involving both the electronic and nuclear degrees of freedom. In the classically allowed region the initial direction of the wave function from the exit point can be found from the classical trajectory: The initial slope of the classical trajectory that starts at the exit point $(z_{k_{\max}}, R_{k_{\max}})$ with zero velocity in both z and R directions can be found to be

$$\left. \frac{\dot{z}}{\dot{R}} \right|_{\text{exit}} = \frac{M}{m} \frac{\frac{\partial}{\partial z} V(z; R) + Fq}{\frac{\partial}{\partial R} V(z; R) + \frac{\partial}{\partial R} U(R)} \Bigg|_{(z_{k_{\max}}, R_{k_{\max}})} . \quad (8.4)$$

This is not exactly the trajectory that describes the motion of the wave function ridge, but it is quite close. These two directions are different as they come from different types of motion, and hence we see the refraction-like phenomenon at the turning line.



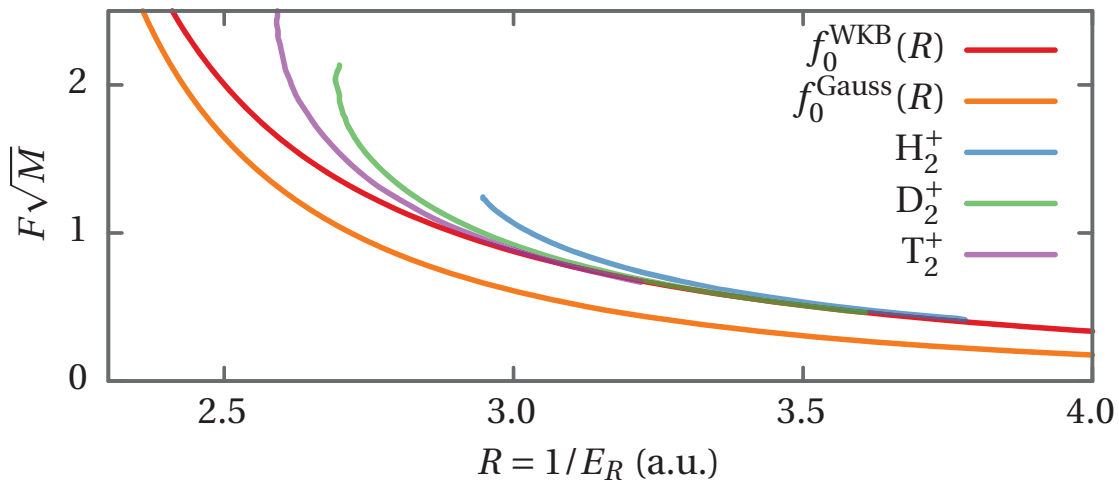
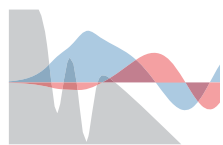


Figure 8.9: The red and orange curves show the f_0 functions defined in Eqs. (4.86). These functions depend only on the field-free BO curves of H_2^+ -like systems, and not on neither field strength or nuclear mass. The R that corresponds to a given combination of nuclear mass and field strength gives the maximum of the spectrum through the relation $1/R = U(R) = E_R$. The blue, green and purple curves in show the maxima of the exact spectra, these spectra are displayed in Fig. 8.10.

8.1.4 Simple Model for Spectrum Maximum

Figure 8.9 shows the f_0 functions from Sec. 4.4.4. These can be used to predict the maxima of the spectra. The maxima of the exact spectra are indicated by the blue, green and purple curves in this figure. We see that the WKB based f_0 function is closer to the exact result than the one based on a Gaussian approximation to the nuclear wave function. This is the case because the values of R relevant are sufficiently large that the WKB approximation is valid, but the Gaussian is no good.

Figure 8.10 shows the spectrum for different nuclear masses, as a function of field strength F . The magnitude of the spectra varies wildly with field strength, so the spectra has been normalized with the total rate at each F . The red lines on top of these spectra indicate the prediction from Sec. 4.4.3 of the maximum of the spectra. They are seen to agree fairly well for smaller field strengths, but less well for larger field strengths. This makes sense, since this prediction is based on electronic WFAT and on approximating electronic energies by their field-free values.



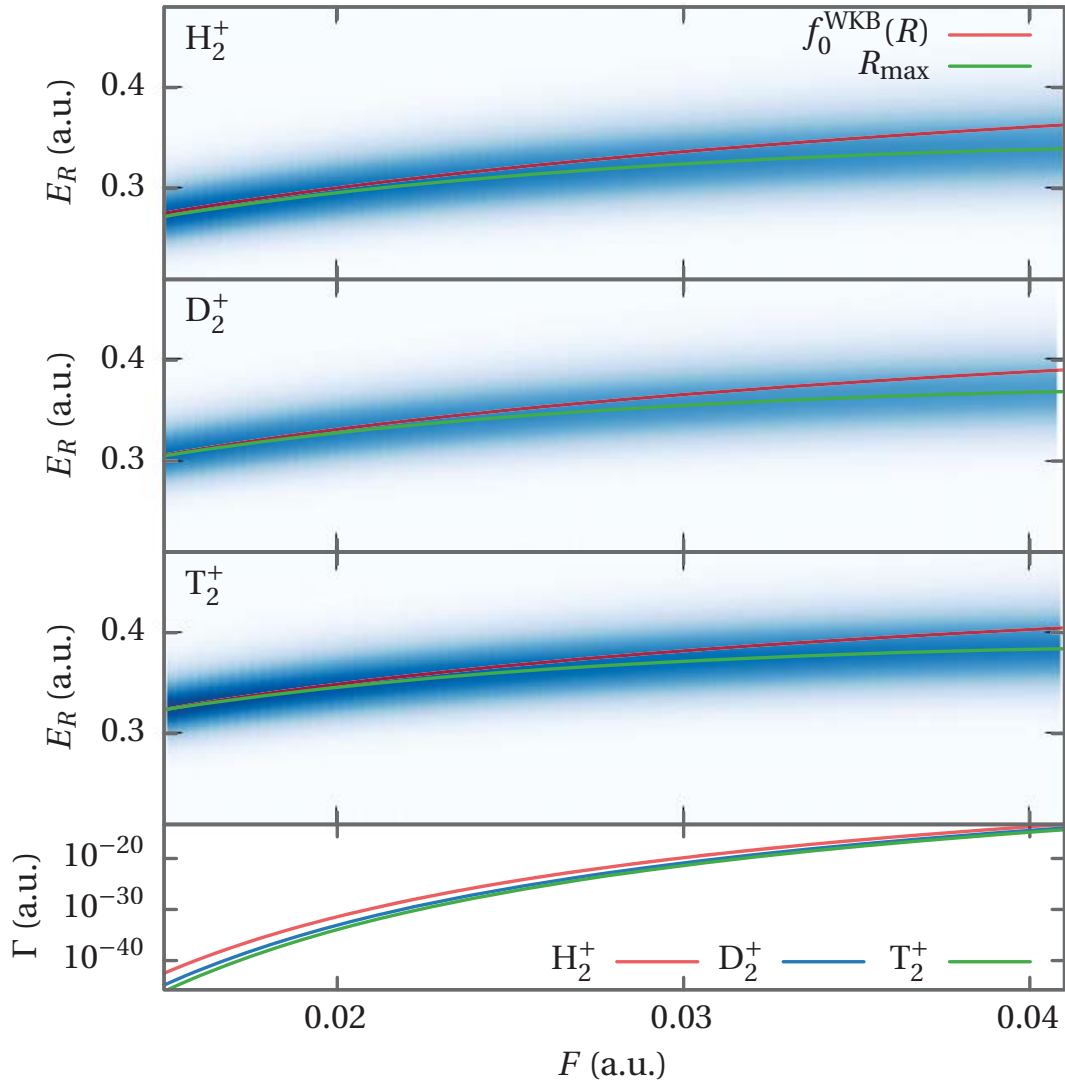
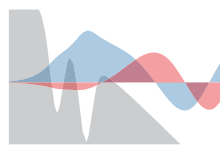
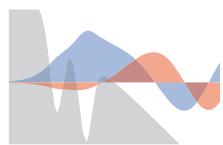


Figure 8.10: The blue surface plots shows $P(k)/\Gamma$, where $P(k)$ are exact spectra [Eq. (4.27)], normalized with the total rate Γ at each F . On top of these the purple line shows the maximum of these spectra, and the red line shows the prediction from Sec. 4.4.3 for this, based on the $f_0(R)$ function [Eq. (4.86)], where $E_R = 1/R$. The lower panel shows the total rate for each system on a logarithmic scale.



8.2 Conclusion

We have formulated theory for the dissociative tunneling ionization process, and derived exact formulas for the KER spectrum, as well as approximations in the framework of the BO and reflection approximations. We have demonstrated that the reflection principle can be used in conjunction with the BO approximation to image the field-dressed nuclear wave function from the KER spectrum. For weaker fields, where the BO approximation fails, the WFAT can be used to find the KER spectrum. We have also demonstrated a qualitative difference between asymptotic BO and exact wave functions, as the latter shows classical motion in the nuclear coordinate, whereas the former does not move at all due to the infinite nuclear mass of the BO approximation. Around the turning line the wave function exhibits a behavior similar to refraction of light at an interface between different media.



9 Dissociation and Bound Ionic States

In this chapter we consider $U(R)$ potentials that allow for both bound and continuum ionic states. We consider three different models using different internuclear $U(R)$ and electron-nuclear $V(z, R)$ potentials. The various models will be identified by the abbreviations M1, M2 and M3. In all of these models some variation of the Morse potential

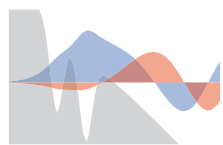
$$U(R) = D_0 [e^{-2\alpha(R-R_0)} - 2e^{-\alpha(R-R_0)}], \quad (9.1)$$

with different parameters is used. The models are built such that they to a varying degree imitate the behaviour of the 3D BO curves of H_2 and H_2^+ . In building these models we have used the Morse potential approximations to the true 3D BO curves, these are shown in Fig. 9.1, with parameters given in the caption. The work described in this chapter is still in progress, and it may therefore not appear as 'polished' as other parts of the thesis.

9.1 H_2^+ Morse and CTP Potentials (M1)

In the first model we use a Morse potential for $U(R)$ with parameters $D_0 = 0.1026$, $R_0 = 2$ and $\alpha = 0.72$, which make this potential reproduce the BO curve of H_2^+ [see Fig. 9.1]. For the $V(z; R)$ potential the CTP potential [Eq. (7.3)] has been used.

Figure 9.2 shows the BO curves resulting from solving the electronic problem Eq. (4.60a) for $F = 0$. On the $U(R)$ potential curve the bound and continuum states associated with this potential [the solutions of Eq. (4.7b)] are shown. It is seen how the change of the nodal structure of the bound state continues in the continuum. The nuclear wave function $\chi(R)$ is multiplied by the asymptotic coefficient $D(R)$ [Eq. (4.70b)] and projected on the ionic states of the $U(R)$ potential to give the BO approximation to



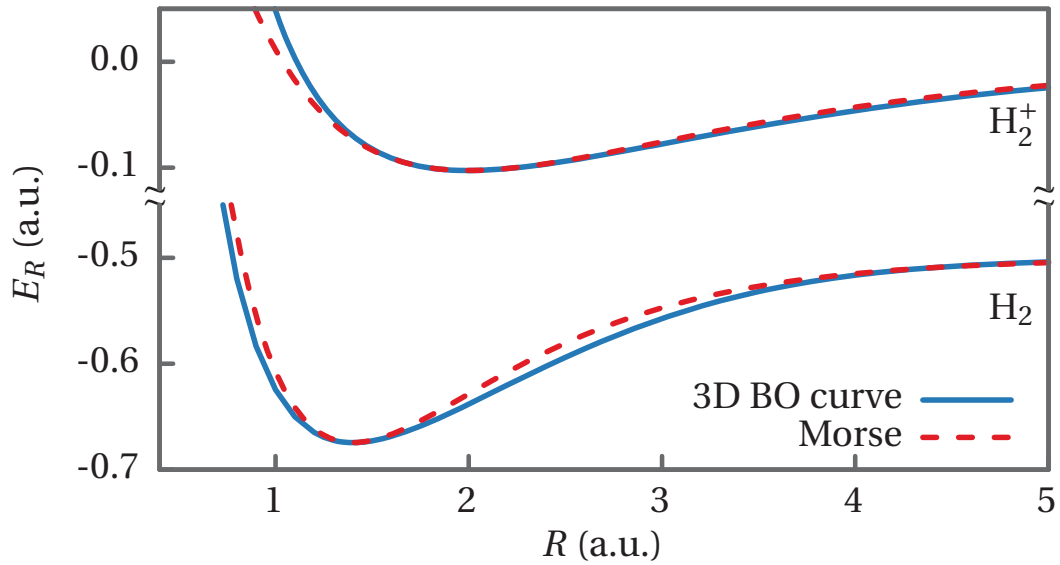


Figure 9.1: The blue curves show the BO potentials of 3D H_2^+ [27] and H_2 [28, 29]. The red curve show Morse potentials with parameters $D_0 = 0.1026$, $R_0 = 2$, $\alpha = 0.72$ for H_2^+ and $D_0 = 0.1745$, $R_0 = 1.4010$, $\alpha = 1.2034$ for H_2 .

the field-free asymptotic expansion coefficients [see Eqs. (4.31),(4.74)]

$$D_\nu^{\text{BO}} = \int_0^\infty dR \chi(R) D(R) g_\nu(R), \quad (9.2a)$$

$$D^{\text{BO}}(k) = \int_0^\infty dR \chi(R) D(R) g(R, k), \quad (9.2b)$$

$$\gamma_\nu^{\text{BO}} = |D_\nu^{\text{BO}}|^2 \quad (9.2c)$$

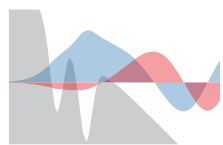
$$p^{\text{BO}}(k) = |D^{\text{BO}}(k)|^2. \quad (9.2d)$$

In Fig. 9.3 these γ_ν^{BO} , $p^{\text{BO}}(k)$ are compared to their exact counterparts [Eq. (4.29)]

$$\gamma_\nu = |D_\nu|^2, \quad (9.3)$$

$$p(k) = |D(k)|^2, \quad (9.4)$$

and they are seen to agree quite well. For $F = 0$ the asymptotic coefficient $D(R)$ only has a weak (non-exponential) dependence on R . The Franck-Condon principle [37] assumes that this coefficient in fact does not depend on R , so we can evaluate the integrals Eqs. (9.2) by assuming $D(R) = D(R_0)$,



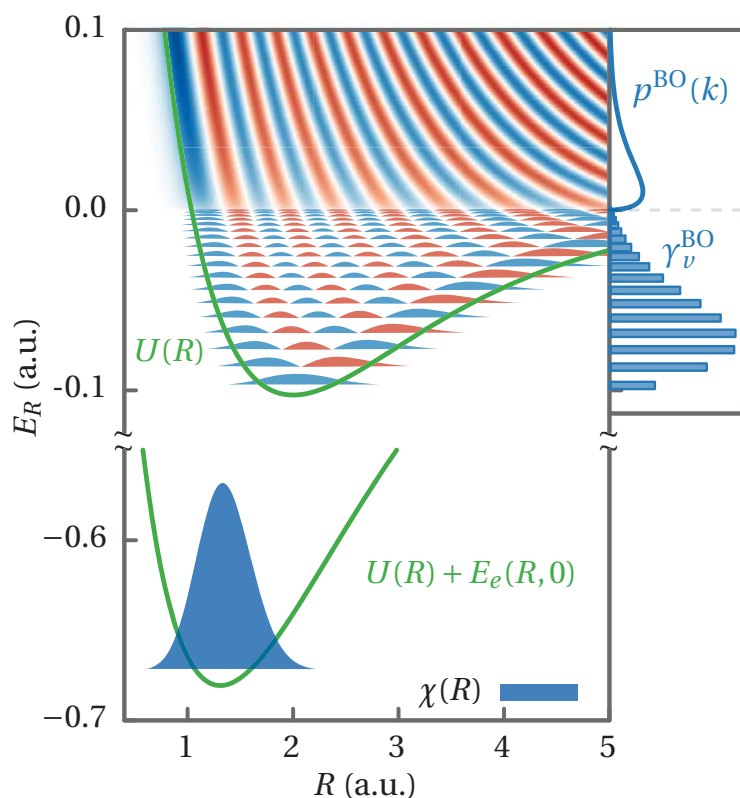


Figure 9.2: BO curves for $F = 0$. The shaded (blue) region near the bottom illustrates the nuclear wave function $\chi(R)$ [Eq. (4.60b)]. The bound $g_\nu(R)$ and continuum $g(R, k)$ states that are solutions of Eq. (4.7b) are illustrated at their energy E_R in the $U(R)$ curve. To the right the norm square of the projection of the product $D(R)\chi(R)$ on the ionic states $g_\nu(R), g(R, k)$ are illustrated [Eqs. (9.2)].

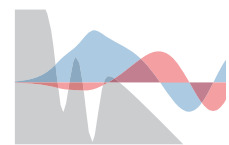
where R_0 is the equilibrium distance of H_2 . We then obtain this asymptotic coefficient times a Franck-Condon overlap and can write

$$\gamma_\nu^{\text{FC}} = |D(R_0)|^2 \left| \int_0^\infty dR \chi(R) g_\nu(R) \right|^2, \quad (9.5a)$$

$$p^{\text{FC}}(k) = |D(R_0)|^2 \left| \int_0^\infty dR \chi(R) g(R, k) \right|^2. \quad (9.5b)$$

These are also shown in Fig. 9.3, and they are seen to agree quite well with the asymptotic coefficients.

Figure 9.4 shows the same as Fig. 9.2, only for a non-zero field strength of $F = 0.053$. It is worth to note that the nuclear wave function $\chi(R)$, which



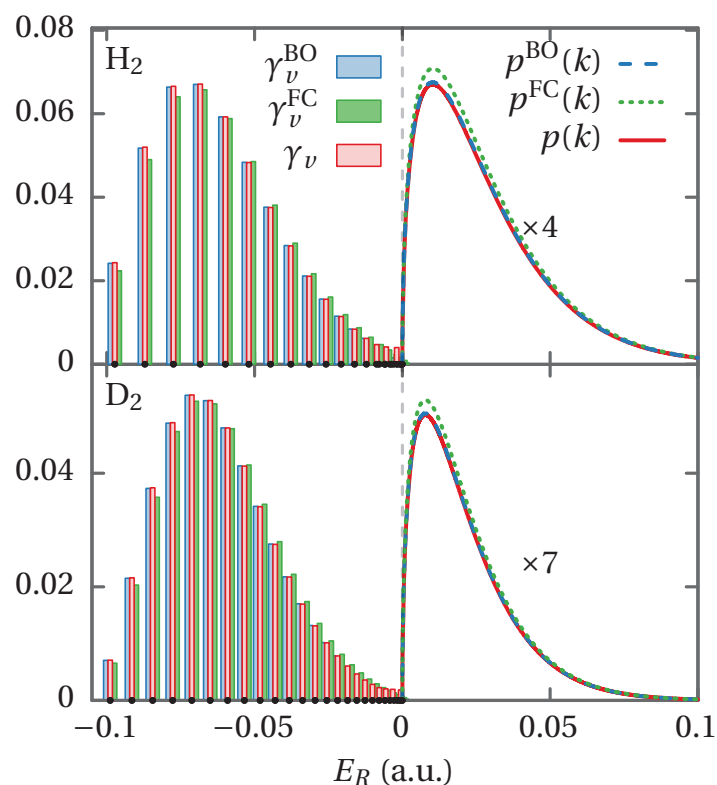
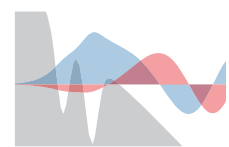


Figure 9.3: Norm square of asymptotic coefficients for $F = 0$. H_2 corresponds to $m_1 = m_2 = 1836$, D_2 corresponds to $m_1 = m_2 = 3672$. The lightly shaded (red) boxes and solid (red) lines show the norm square of the asymptotic coefficients corresponding to bound and continuum states, respectively [Eqs. (9.3)]. The medium shaded (blue) boxes and dashed (blue) lines show the BO approximation for the same [Eq. (9.2)]. These results for H_2 are the same as the upper right part of Fig. 9.2. The dark shaded (green) boxes and short dashed (green) lines show the Franck-Condon overlaps [Eqs. (9.5)]. All lines have been multiplied by a factor indicated in each panel to make them visible on the same scale as the boxes. The dots on the energy axes indicate the energies E_ν of the bound states of the $U(R)$ potential.



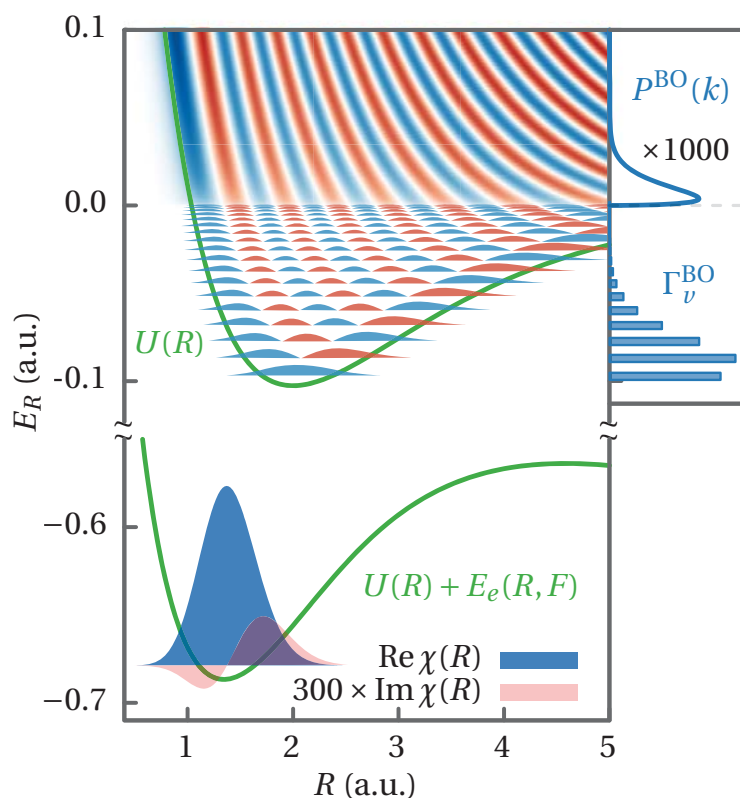
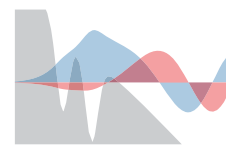


Figure 9.4: BO curves for $F = 0.053$ (a.u.). Similar to Fig. 9.2. Note that the nuclear wave function $\chi(R)$ has a non-zero imaginary part. The subplot to the right shows the BO approximations to the ionization rates and spectrum [Eqs. (4.27)]. The spectrum has been multiplied by 1000 to make it visible on the same scale as the ionization rates.

was calculated by diagonalizing the Hamiltonian of Eq. (4.60b) with complex electronic energies $E_e(R; F)$, has a non-zero imaginary part. Note also that the spectrum is a lot smaller than the ionization rates to the bound states, the difference is a lot larger than the corresponding difference in the field-free case. In the framework of WFAT we can understand this additional difference as originating from the field factor [Eqs. (4.58a)], since states with a larger E_R will have a larger ν , and therefore a smaller value of this field factor.

Figure 9.5 shows the ionization rates and spectra for a small and a larger field strength. As in Refs. [1, 2, 10] we see that for the small field strength the BO results are quite far from the exact, whereas WFAT gives a



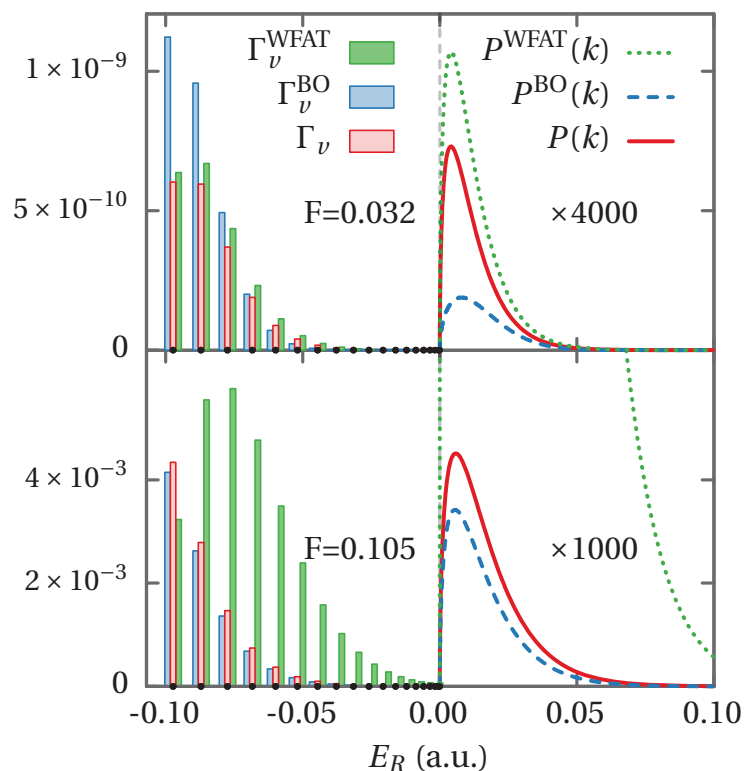
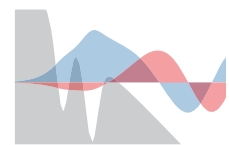


Figure 9.5: Ionization rates and spectra for two selected field strengths with H_2 as initial state. The lightly shaded (red) boxes and solid (red) lines show ionization rates and spectra respectively [Eqs. (4.27)]. The medium shaded (blue) boxes and dashed (blue) lines show the BO approximation for the same [Eqs. (4.69)]. These results for H_2 are the same as the upper right part of Fig. 9.4. The dark shaded (green) boxes and short dashed (green) lines show the WFAT approximation for this [Eqs. (4.57)]. All lines have been multiplied by a factor indicated in each panel to make them visible on the same scale as the boxes. For the larger field strength the WFAT spectrum is orders of magnitude larger than the exact one.

better description, and the other way round for the larger field strength. We also note that the continuum part is again a lot smaller than the bound part.

This is also evident in Fig. 9.6. Here the exact total rate $\Gamma(F)$ is com-



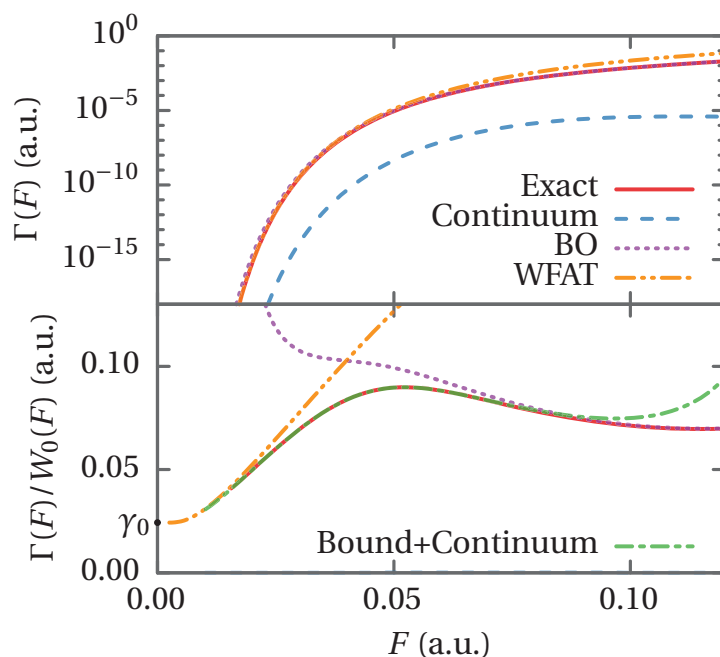
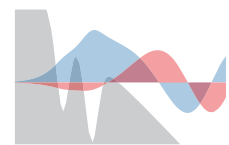


Figure 9.6: Ionization rates as function of field strength for H_2 ($m_1 = m_2 = 1836$). Solid (red) line: Exact rate $\Gamma(F) = -2\text{Im}[E(F)]$. Dashed (blue) line: Continuum rate [Eq. (4.28c)]. Dotted (purple) line: BO rate $\Gamma_{\text{BO}}(F) = -2\text{Im}[E_{\text{BO}}(F)]$. Dashed-dot-dotted (orange) line: WFAT rate [Eq. (4.59)]. In the lower panel the rates have been divided by the WFAT field factor W_0 [Eq. (4.58a)] of the $\nu = 0$ state to make the rates comparable on a linear scale. The dashed-dot-dotted (green) line shows the sum of partial rates [Eq. (4.28a)].

pared to the continuum rate Γ^{cont} [Eq. (4.28c)], and the former is seen to be at least 10^3 times larger than the latter. In this figure the breakdown of the BO in the weak-field limit is also evident. The figure additionally shows the sum of the sum of all the bound partial rates and integral of the continuum spectrum [Eq. (4.28a)], labeled by 'Bound+Continuum', compared to the exact rate $\Gamma(F) = -2\text{Im}(E)$. These only agree in the weak-field limit as indicated in Eq. (4.28a), for sufficiently large fields they differ and the total rate is not the same as the sum of partial rates. The wave function for our model looks almost the same as the wave function in Ref. [1] (or Chapter 7), since in that work only bound ionic states were considered, and in our case the bound ionic states dominate. In the asymptotic region we write



the wave function as a sum of a bound and continuum part [Eq. (4.18)]. In Fig. 9.7 we show the continuum contribution to this sum given by

$$\Psi_{\text{cont}}(z, R) = \int_0^{\infty} C(k) f(z, k) g(R, k) \frac{dk}{2\pi}, \quad (9.6)$$

normalized by the electron density

$$\rho(z) = \int_0^{\infty} |\Psi_{\text{cont}}(z, R)|^2 dR. \quad (9.7)$$

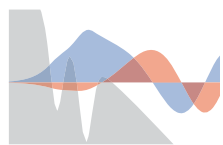
This reconstruction can in principle be done on the basis of an experimentally measured spectrum $P(k)$, by using $C_{\text{Experiment}} = \sqrt{P(k)}$. The phase information in $C(k)$ would then not be known, but in the present case using $|C(k)|$ instead of $C(k)$ yields identical plots. The structure of this wave function might look a bit baffling at first. For a fixed z considered as a function of R it has a number of oscillations and is not a collected wave packet as in Ref. [2] (or Chapter 8). These oscillations can be understood with the help of Fig. 9.4. Here we see that the spectrum $P^{\text{BO}}(k)$ has significant weight over a fairly small range of energies, and the continuum states $g(R, k)$ with these energies only slightly change their nodal structure. There is not sufficient energy spread of the spectrum to build a localized wave packet. This means that the linear combination in Eq. (9.6) should reflect this nodal structure, which is indeed what we see. Superimposed on this nodal structure we also see a motion of the wave function towards larger R as z becomes increasingly more negative. This motion shows how the nuclei dissociate for the part of the wave function that is in the dissociation continuum.

9.2 SCP Model (M2)

We have done the same calculations as in Sec. 9.1, using the same potential for $U(R)$, but using instead of the CTP potential a soft coulomb potential of the form [Eq. (8.1b)]

$$V(z, R) = - \sum_{\pm} \frac{1}{\sqrt{\left(z \pm \frac{R}{2}\right)^2 + a(R)}}, \quad (9.8)$$

where $a(R)$ has been chosen such that $U(R) + E_e(R)$ reproduces the BO curve of H_2 . The CTP potential was constructed such that it combined with the potential Eq. (7.1) would reconstruct the minimum of the H_2



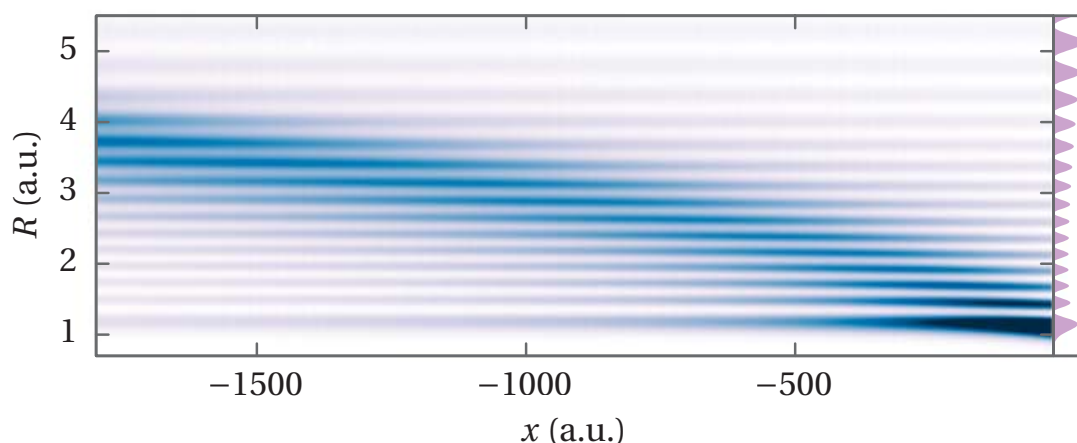


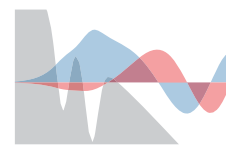
Figure 9.7: Reconstructed continuum wave function $|\Psi_{\text{cont}}(z, R)|^2 / \rho(z)$, at $F = 0.01$. The inset on the right side shows the square of the continuum state $g(R, k)^2$ at the energy where $P(k)$ is maximal.

BO curve, using the method of App. E. However, when the CTP potential is used together with the Morse potential Eq. (9.1) the minimum of the resulting BO curve is shifted to smaller R [see Fig. 9.8], since the two $U(R)$ potentials are different around the equilibrium distance of H_2 (but they are similar around the equilibrium distance of H_2^+). The model described in this section, on the other hand, reproduces the H_2 BO potential everywhere, and it is the model in this thesis that most closely resembles the H_2 molecule.

Figs. (9.9), (9.10), (9.11), (9.12) and (9.13) show the results of calculations using this potential instead of the CTP. In all these figures we see that the probabilities in the continuum spectrum is smaller compared to the bound ionization states than was the case for M1. In M2 the minimum of the $U(R) + E_e(R, 0)$ BO curve is closer to the minimum of the $U(R)$ curve than for M1 [see Fig. 9.8], as a consequence the overlap of the nuclear wave function $\chi(R)$ (or the nuclear wave function times the electronic rate) with the bound states of $U(R)$ is larger for M2, and less weight goes to the continuum states.

9.3 Another SCP (M3)

A third model we have considered is one where we use the Morse potential Eq. (9.1) for $U(R)$, but with parameters $D_0 = 0.1026$, $R_0 = 2.5$ and $\alpha =$



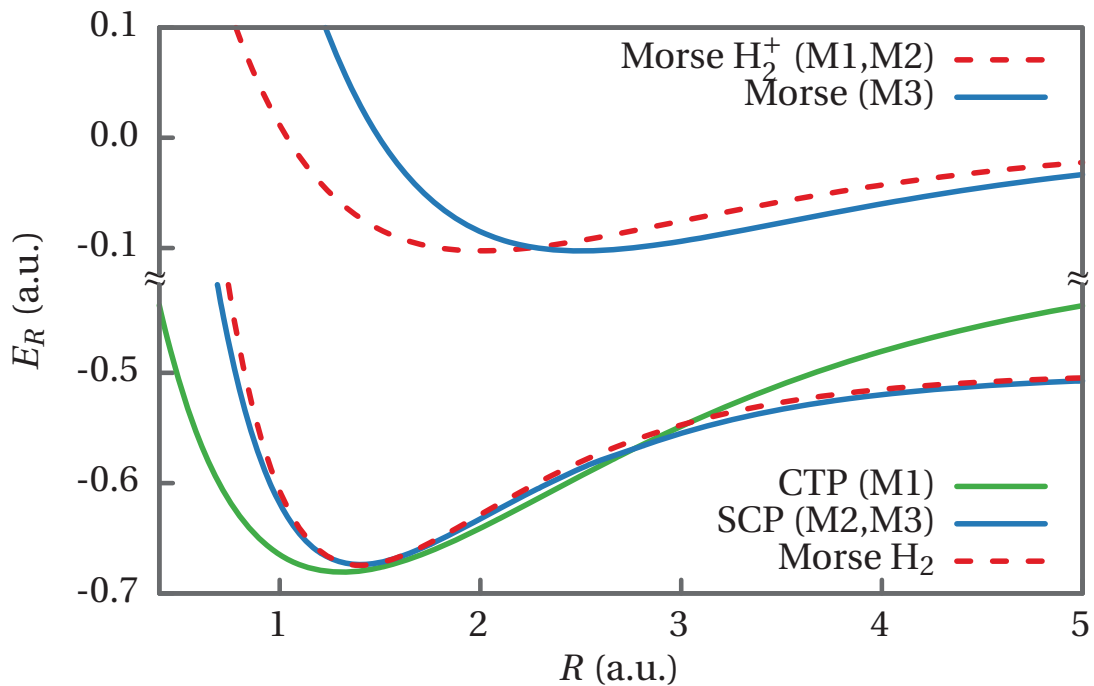
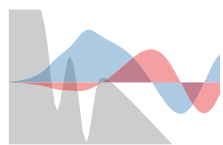


Figure 9.8: BO curves for the various models (M1, M2, M3) used in this chapter. The upper curves are the $U(R)$ potentials. The lower curves show $E_e(R, F=0) + U(R)$ obtained by solving the electronic BO problem [Eq. (4.60a)] using the $V(z, R)$ potential of the given model.

0.69. For the electron-nuclear potential $V(z, R)$ we used the SCP Eq. (8.1b) optimized such that the BO curve of H_2 is reproduced.

Figs. (9.14), (9.15), (9.16), (9.17), (9.18) and (9.19) show the results of calculations using this model. For this model we see that the continuum states have more weight than in both M1 and M2. In M3 the minimum of the BO curve $U(R) + E_e(R, 0)$ is further away from the minimum of $U(R)$ than for both M1 and M2 [see Fig. 9.8], and consequently the overlap between the nuclear wave function (or the nuclear wave function times the electronic rate) and the continuum states is larger for M3 than for either M1 or M2.



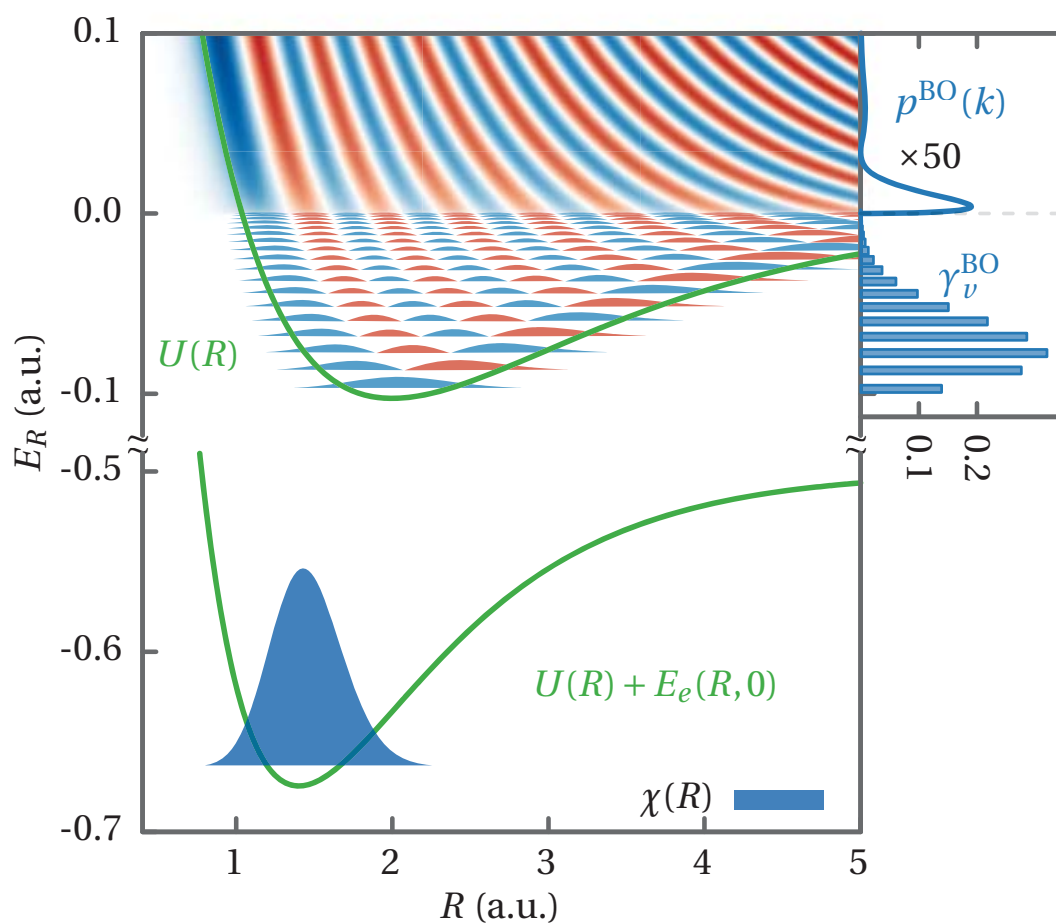
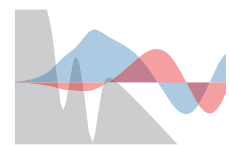


Figure 9.9: Same as Fig. 9.2, but using the potential Eq. (9.8) instead of the CTP (M2).



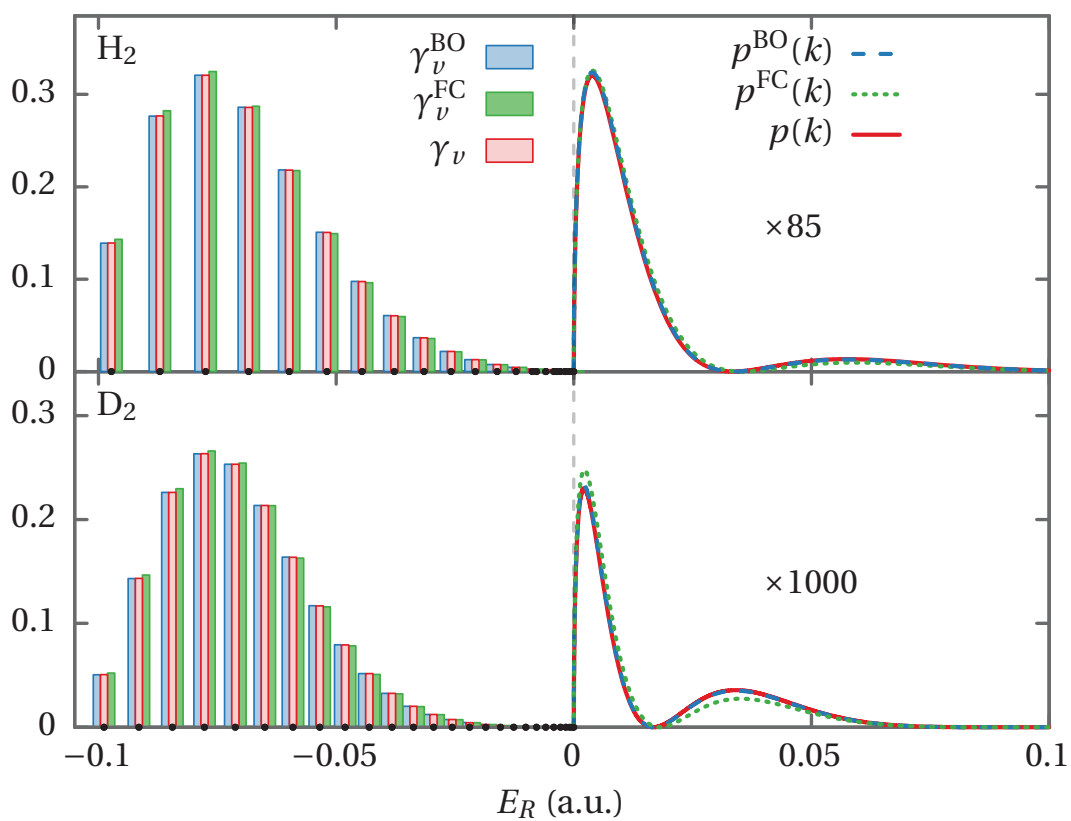
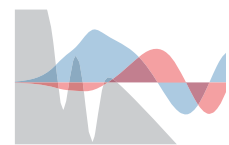


Figure 9.10: Same as Fig. 9.3, but using the potential Eq. (9.8) instead of the CTP (M2).



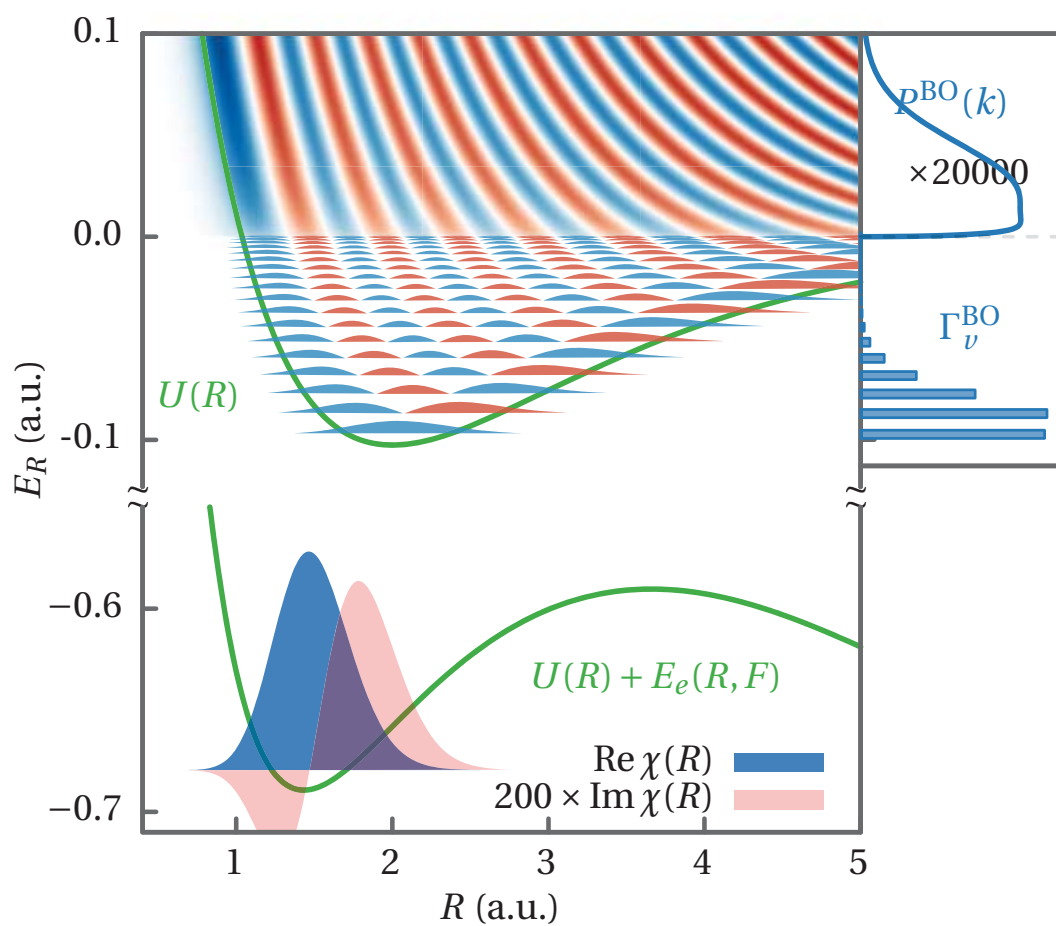
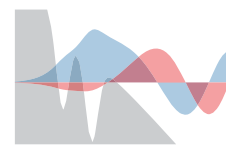


Figure 9.11: Same as Fig. 9.4, but using the potential Eq. (9.8) instead of the CTP (M2).



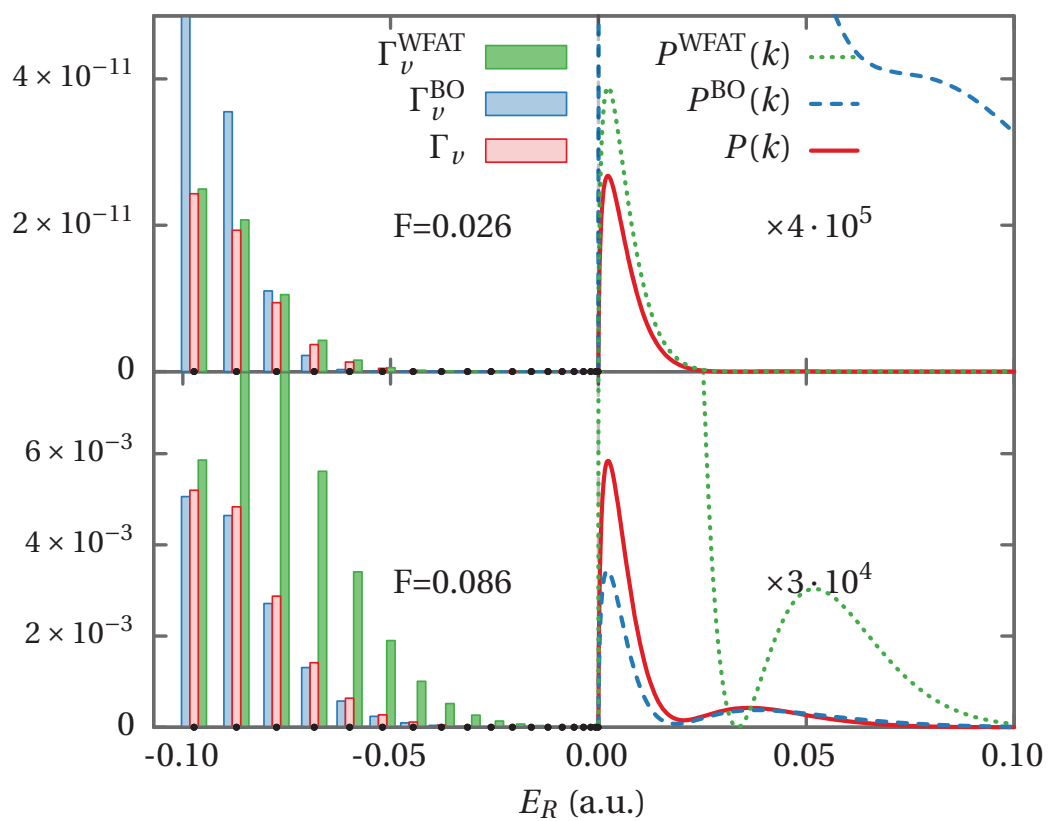
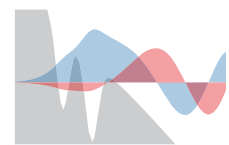


Figure 9.12: Same as Fig. 9.5, but using the potential Eq. (9.8) instead of the CTP (M2).



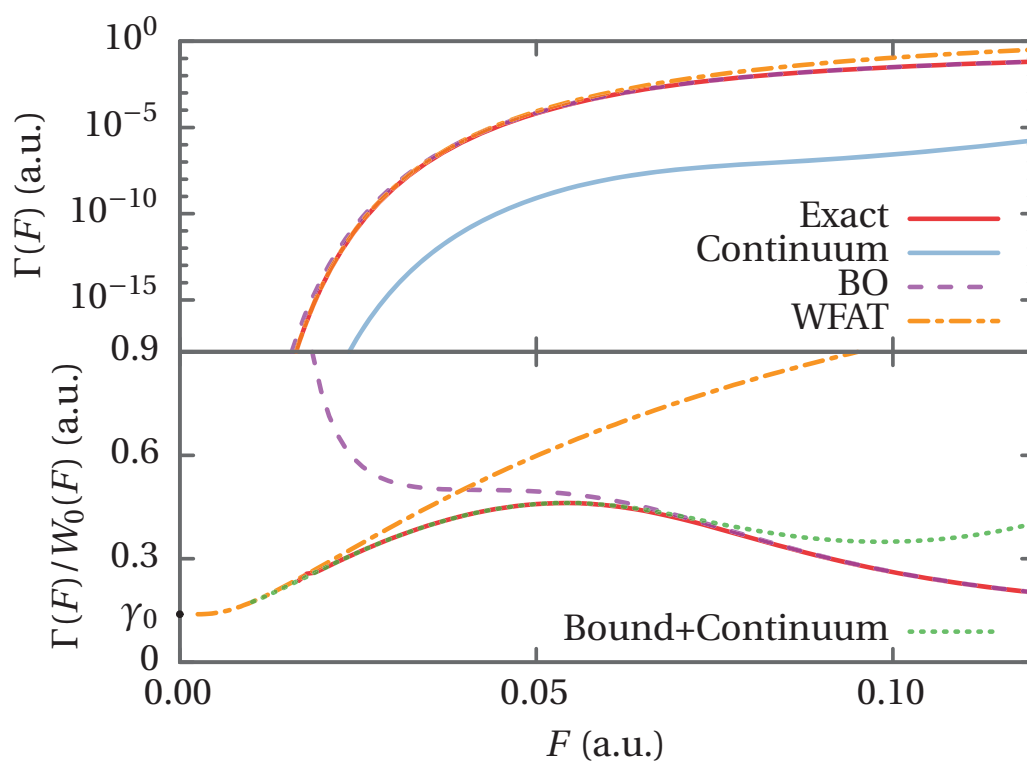
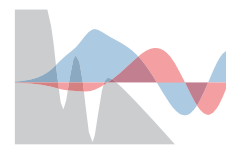


Figure 9.13: Same as Fig. 9.6, but using the potential Eq. (9.8) instead of the CTP (M2).



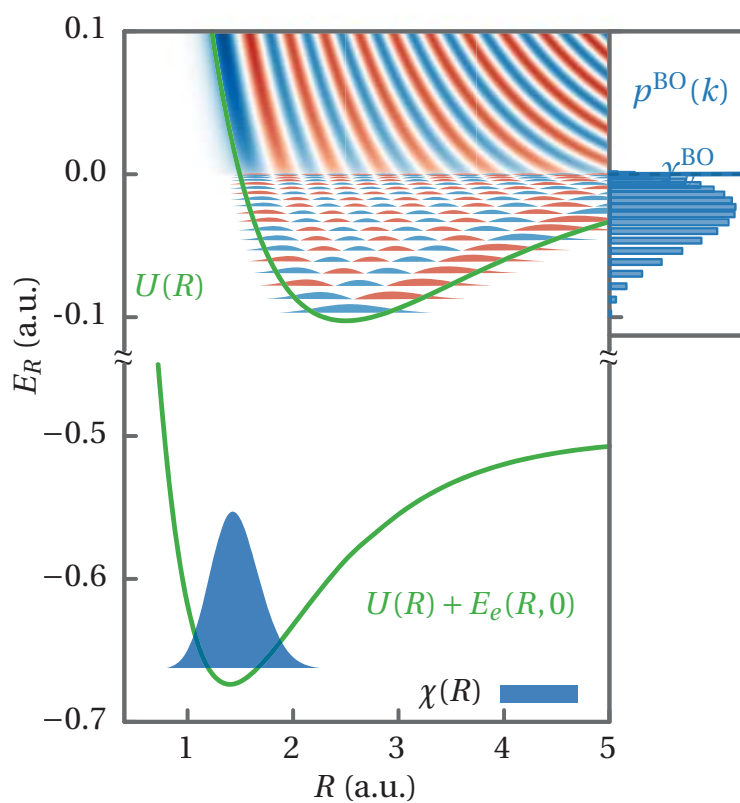
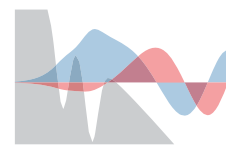


Figure 9.14: Same as Fig. 9.2, but using the potentials of M3.



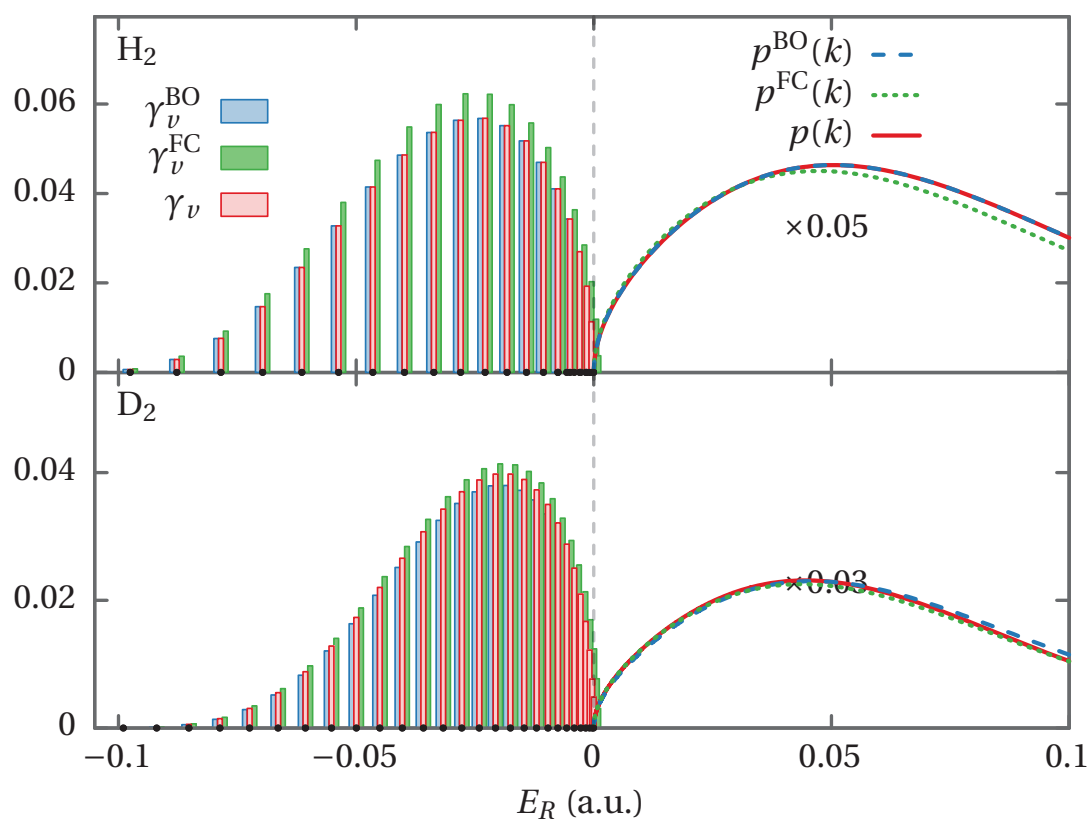
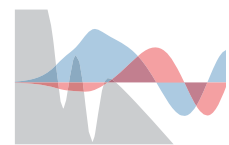


Figure 9.15: Same as Fig. 9.3, but using the potentials of M3.



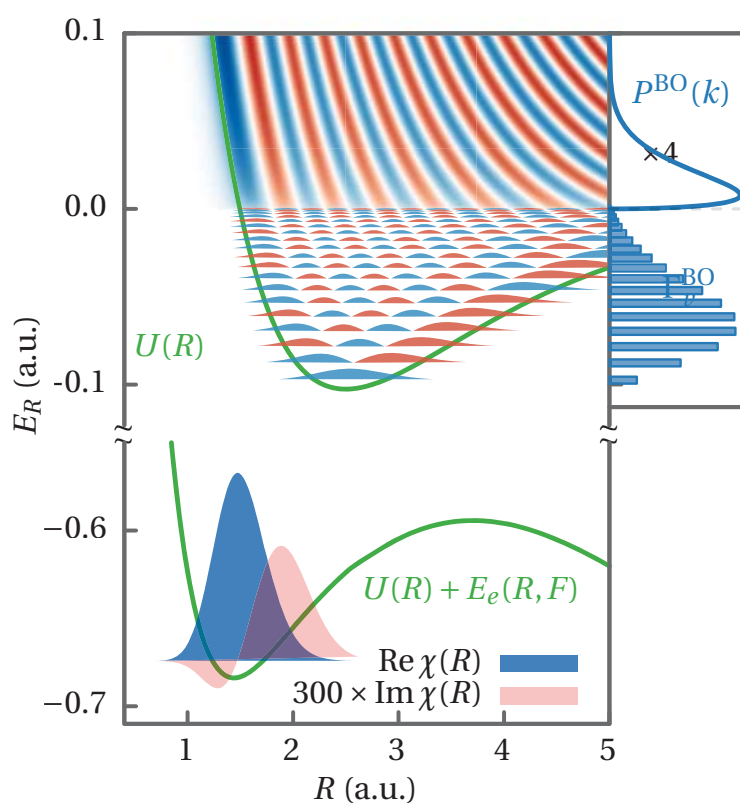
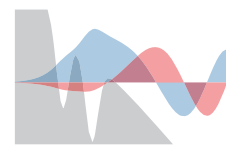


Figure 9.16: Same as Fig. 9.4, but using the potentials of M3.



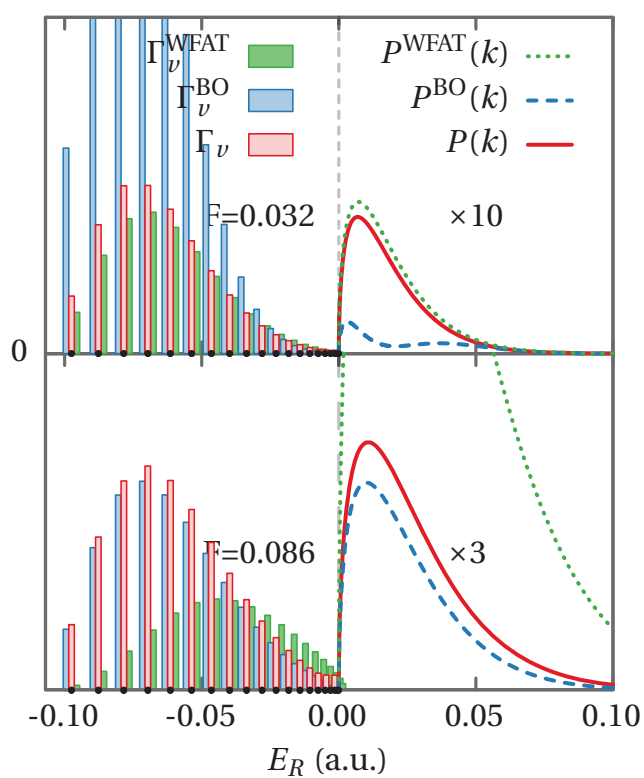
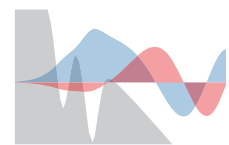


Figure 9.17: Same as Fig. 9.5, but using the potentials of M3.



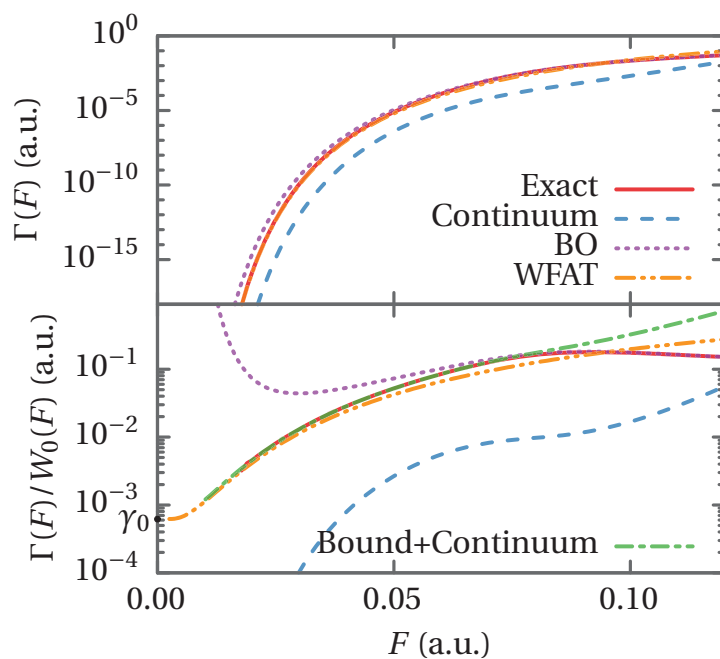


Figure 9.18: Same as Fig. 9.6, but using the potentials of M3.

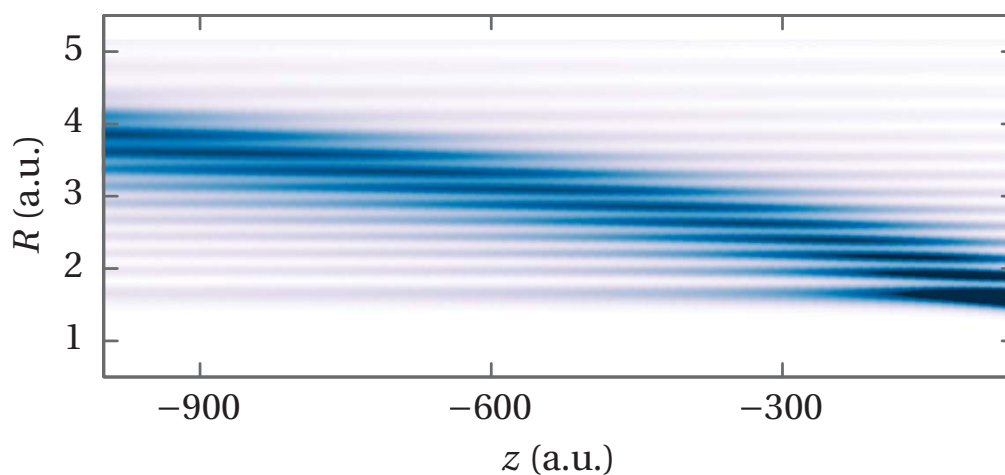
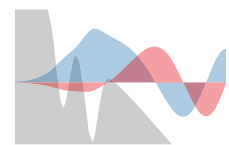


Figure 9.19: Same as Fig. 9.7 at $F = 0.08$, but using the potentials of M3.



A Asymptotic Expansion

In this appendix we will solve the differential equation

$$\left[\frac{d^2}{dx^2} + c_4 x + c_3 + \frac{c_2}{x} + \frac{c_1}{x^2} \right] f(x) = 0 \quad (\text{A.1})$$

for large values of x by means of an asymptotic expansion. We will also determine the integral

$$I(x) = \int_x^\infty f^2(\tilde{x}) d\tilde{x}, \quad (\text{A.2})$$

where $f(x)$ is the solution to Eq. (A.1). This integral is needed for normalizing the wave function. The derivative of the $f(x)$ are needed to calculate the R-matrix, so these will also be presented. In this appendix we only consider large positive x . By performing the substitutions $x \rightarrow -x$, $c_2 \rightarrow -c_2$ and $c_4 \rightarrow -c_4$ in Eq. (A.1) the results for large negative x can be obtained by the same expansions, since Eq. (A.1) is unchanged under this set of substitutions. The asymptotic expansions for the cases $c_4 = 0$ and $c_4 \neq 0$ are rather different, so we will consider these two cases separately. This appendix is similar to Appendix A of Ref. [1].

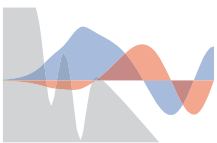
A.1 The $c_4 = 0$ Case

We start by making the ansatz

$$f(x) = x^\alpha e^{Ax} g(x). \quad (\text{A.3})$$

Inserting this ansatz in Eq. (A.1) we obtain

$$\frac{d^2 g(x)}{dx^2} + 2 \left(A + \frac{\alpha}{x} \right) \frac{dg(x)}{dx} + \left(A^2 + c_3 + \frac{2\alpha A + c_2}{x} + \frac{\alpha(\alpha - 1) + c_1}{x^2} \right) g(x) = 0 \quad (\text{A.4})$$



If we choose the ansatz coefficients and define the new coefficient B

$$A^2 = -c_3, \quad (\text{A.5a})$$

$$\alpha = \frac{-c_2}{2A}, \quad (\text{A.5b})$$

$$B \equiv \alpha(\alpha - 1) + c_1 \quad (\text{A.5c})$$

we can write Eq. (A.4)

$$0 = \left[\frac{d^2}{dx^2} + 2 \left(A + \frac{\alpha}{x} \right) \frac{d}{dx} + \frac{B}{x^2} \right] g(x). \quad (\text{A.6})$$

We now assume that $g(x)$ is of the form

$$g(x) = \sum_{n=0}^{\infty} \frac{g_n}{x^n}. \quad (\text{A.7})$$

Inserting this in Eq. (A.6) yields the recursive relation

$$g_n = -\frac{(n-1)(n-2\alpha) + B}{2nA} g_{n-1}. \quad (\text{A.8})$$

This concludes the construction of the asymptotic expansion. The derivative can be written

$$\frac{d}{dx} f(x) = x^\alpha e^{Ax} \left[\left(\frac{\alpha}{x} + A \right) \sum_{n=0}^{\infty} \frac{g_n}{x^n} - \sum_{n=1}^{\infty} \frac{n g_n}{x^{n+1}} \right]. \quad (\text{A.9})$$

Note that nothing fixes the coefficient g_0 . The freedom in choosing this coefficient corresponds to multiplying a constant on the full solution $f(x)$, as can be seen by the form of the recursion Eq. (A.8).

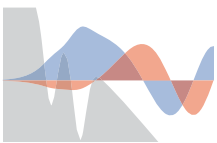
We now find an expansion for the integral Eq. (A.2). First we write

$$f^2(x) = x^{2\alpha} e^{2Ax} \sum_{k=0}^{\infty} \frac{G_k}{x^k}, \quad (\text{A.10a})$$

$$G_k = \sum_{m=0}^k g_{k-m} g_m. \quad (\text{A.10b})$$

Suppose now that the integral Eq. (A.2) is of the form

$$I(x) = -x^{2\alpha} e^{2Ax} \sum_{k=0}^{\infty} \frac{h_k}{x^k}. \quad (\text{A.11})$$



From Eq. (A.2) we get that $I'(x) = -f^2(x)$, so to check if the above expansion in fact correctly describes $I(x)$ let us calculate the derivative

$$I'(x) = -x^{2\alpha} e^{2Ax} \left[\frac{2Ah_0}{x^0} + \sum_{k=1}^{\infty} \frac{[2\alpha - (k-1)]h_{k-1} + 2Ah_k}{x^k} \right]. \quad (\text{A.12})$$

This is indeed of the same form as Eq. (A.10a). We can match the G_k coefficients to this expression and thereby obtain the recursion

$$h_0 = \frac{G_0}{2A}, \quad (\text{A.13a})$$

$$h_k = \frac{G_k - [2\alpha - (k-1)]h_{k-1}}{2A} \quad k = 1, 2, \dots \quad (\text{A.13b})$$

A.2 The $c_4 \neq 0$ Case

In this case we start by introducing a new variable

$$z^2 = x. \quad (\text{A.14})$$

In terms of this variable Eq. (A.1) becomes

$$\left[\frac{d^2}{dz^2} - \frac{1}{z} \frac{d}{dz} + 4c_4 z^4 + 4c_3 z^2 + 4c_2 + 4 \frac{c_1}{z^2} \right] f(z) = 0. \quad (\text{A.15})$$

We now make the ansatz

$$f(z) = z^{-1/2} \exp\left(\frac{1}{6}Dz^3 + \frac{1}{2}Bz\right) g(z). \quad (\text{A.16})$$

Inserting this in Eq. (A.15) yields

$$\left[\frac{d}{dz^2} + \left(-\frac{2}{z} + Dz^2 + B\right) \frac{d}{dz} + A - \frac{B}{z} + \frac{C}{z^2} \right] g(z) = 0, \quad (\text{A.17})$$

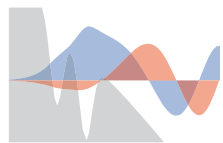
where the following coefficients have been chosen or introduced

$$D^2 = -4^2 c_4, \quad (\text{A.18a})$$

$$B = \frac{-8c_3}{D}, \quad (\text{A.18b})$$

$$A = \frac{1}{4}B^2 + 4c_2, \quad (\text{A.18c})$$

$$C = 4c_1 + \frac{5}{4}. \quad (\text{A.18d})$$



Inserting the expansion

$$g(z) = \sum_{n=0}^{\infty} \frac{g_n}{z^n} \quad (\text{A.19})$$

in Eq. (A.17) yields

$$0 = \sum_{n=3}^{\infty} \frac{((n-3)n+C)}{z^{n-1}} g_{n-3} - \sum_{n=2}^{\infty} \frac{B(n-1)}{z^{n-1}} g_{n-2} + \sum_{n=1}^{\infty} \frac{A}{z^{n-1}} g_{n-1} - \sum_{n=0}^{\infty} \frac{nD}{z^{n-1}} g_n \quad (\text{A.20})$$

From this we obtain the recursion

$$g_1 = g_0 \frac{A}{D}, \quad (\text{A.21a})$$

$$g_2 = \frac{Ag_1 - Bg_0}{2D}, \quad (\text{A.21b})$$

$$g_n = \frac{[n(n-3)+C]g_{n-3} - (n-1)Bg_{n-2} + Ag_{n-1}}{nD} \quad n = 3, 4, \dots \quad (\text{A.21c})$$

The derivative of this solution is

$$\frac{df(z)}{dz} = z^{-1/2} \exp\left(\frac{1}{6}Dz^3 + \frac{B}{2}z\right) \left(\left[-\frac{1}{2z} + \frac{D}{2}z^2 + \frac{B}{2} \right] \sum_{n=0}^{\infty} \frac{g_n}{z^n} - \sum_{n=1}^{\infty} \frac{ng_n}{z^{n+1}} \right), \quad (\text{A.22a})$$

$$\frac{df(x)}{dx} = \frac{z^{-3/2}}{2} \exp\left(\frac{1}{6}Dz^3 + \frac{B}{2}z\right) \left(\left[-\frac{1}{2z} + \frac{D}{2}z^2 + \frac{B}{2} \right] \sum_{n=0}^{\infty} \frac{g_n}{z^n} - \sum_{n=1}^{\infty} \frac{ng_n}{z^{n+1}} \right). \quad (\text{A.22b})$$

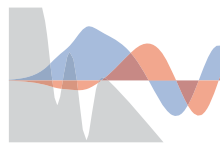
In order to calculate the $I(x)$ integral Eq. (A.2) we first make a change of variable

$$I(x) = \int_x^{\infty} f^2(\tilde{x}) d\tilde{x} = \int_z^{\infty} f^2(x(z)) 2z dz. \quad (\text{A.23})$$

The integrand is of the form

$$f^2(x(z)) 2z = 2 \exp\left(\frac{1}{3}Dz^3 + Bz\right) \sum_{k=0}^{\infty} \frac{G_k}{z^k}, \quad (\text{A.24a})$$

$$G_k = \sum_{m=0}^k g_{k-m} g_m. \quad (\text{A.24b})$$



We proceed similarly as in the $c_4 = 0$ case and assume the integral to be of the form

$$I(z) = \exp\left(\frac{1}{3}Dz^3 + Bz\right) \sum_{k=0}^{\infty} \frac{h_k}{z^k}. \quad (\text{A.25})$$

The derivative of this is given by

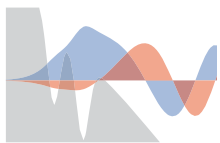
$$\frac{d}{dz}I(z) = \exp\left(\frac{1}{3}Dz^3 + Bz\right) \left(\sum_{k=0}^2 \frac{Dh_k}{z^{k-2}} + \frac{Bh_0}{z^0} + \sum_{k=1}^{\infty} \frac{Dh_{k+2} + Bh_k - (k-1)h_{k-1}}{z^k} \right). \quad (\text{A.26})$$

This is indeed of the same form as Eq. (A.24a), and by matching the coefficients we obtain

$$h_0 = h_1 = 0, \quad (\text{A.27a})$$

$$h_2 = \frac{1}{D}2G_0, \quad (\text{A.27b})$$

$$h_k = \frac{1}{D}(2G_{k-2} - Bh_{k-2} + (k-3)h_{k-3}) \quad k = 3, 4, \dots \quad (\text{A.27c})$$



B WKB Approximation

In this appendix the Wentzel-Kramers-Brillouin (WKB) theory will be derived. The structure of this appendix is inspired by Landau and Lifshitz' book [14]. The basic idea of the WKB approximation is to expand solutions to the time-independent Schrödinger equation (TISE) in orders of the Planck constant \hbar . The Planck constant is in some sense a measure of how 'classical' a system is, when this constant is small compared to other characteristics of the system a system behaves in a classical manner. WKB theory is also sometimes referred to as semi-classical theory. In this appendix we do not put \hbar to 1, unlike the rest of the thesis.

We start by writing the TISE in the form

$$\left[\hbar^2 \frac{d^2}{dx^2} + p^2(x) \right] \psi(x) = 0. \quad (\text{B.1})$$

Into this we insert the ansatz

$$\psi(x) = C e^{if(x)/\hbar}, \quad (\text{B.2})$$

which yields [for $\psi(x) \neq 0$]

$$0 = -(f'(x))^2 + i\hbar f''(x) + p^2(x). \quad (\text{B.3})$$

We now expand f in powers of \hbar

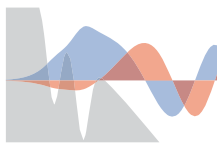
$$f(x) = f_0(x) + \hbar f_1(x) + \hbar^2 f_2(x) + \dots \quad (\text{B.4})$$

This expansion is inserted in Eq. (B.3). Collecting terms to zeroth order in \hbar we get

$$f_0(x) = \pm \int dx p(x). \quad (\text{B.5})$$

$f_0(x)$ is a fair approximation to $f(x)$ if the second term in equation (B.3) is a lot smaller than the first one

$$1 \gg \left| \frac{\hbar f''}{(f')^2} \right| = \left| \frac{d}{dx} \left(\frac{\hbar}{f'} \right) \right| = \left| \frac{d}{dx} \left(\frac{\hbar}{p} \right) \right|. \quad (\text{B.6})$$



If we continue the derivation and collect to first order we get

$$0 = -2f_0'(x)f_1'(x) + if_0''(x) \quad (\text{B.7})$$

$$f_1(x) = i\frac{1}{2} \ln p(x) \quad (\text{B.8})$$

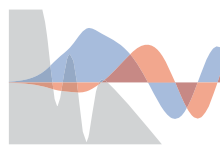
The wave function to first order in $\hbar = 1$ then becomes:

$$\psi(x) = Ce^{i(f_0(x)+f_1(x))} \quad (\text{B.9})$$

$$= \frac{C}{p^{1/2}(x)} e^{\pm i \int dx p(x)} \quad (\text{B.10})$$

The integration in the exponential carries an arbitrary constant. Different choices of this constant can be absorbed into to the constant C . Often one chooses the integration to start at a classical turning point defined by $p(x_t) = 0$, thereby fixing the value of C

$$\psi(x) = \frac{C}{p^{1/2}(x)} e^{\pm i \int_{x_t}^x dx' p(x')}. \quad (\text{B.11})$$



C Reflection Approximation

In this appendix we will derive the reflection approximation. The reflection approximation provides a convenient way of evaluating integrals of the form

$$C(k) = \int_0^\infty dR \varphi(R) g(R, k), \quad (\text{C.1})$$

where $\varphi(R)$ is some function and $g(R, k)$ are continuum state solutions of the eigenvalue problem

$$\left[-\frac{1}{2M} \frac{d^2}{dR^2} + U(R) - E_R \right] g(R, k) = 0, \quad (\text{C.2})$$

where it is assumed that $U(R)|_{R \rightarrow \infty} = 0$, $E_R > 0$ and the energy is parametrized by the wave number $E_R = \frac{k^2}{2M}$. The continuum states are normalized according to

$$g(R, k)|_{R \rightarrow \infty} = 2 \sin(kR + \delta), \quad (\text{C.3})$$

and we impose the boundary condition $g(R = 0, k) = 0$. We assume that the potential $U(R)$ for a given k has exactly one turning point R_t

$$U(R_t) = E_R = \frac{k^2}{2M}. \quad (\text{C.4})$$

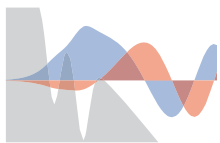
We expand the potential $U(R)$ to first order around this turning point

$$U(R) \approx U(R_t) + U'(R_t) \Delta R, \quad (\text{C.5})$$

where $\Delta R = R - R_t$.

We define the variable

$$z = -\alpha \Delta R, \quad (\text{C.6})$$



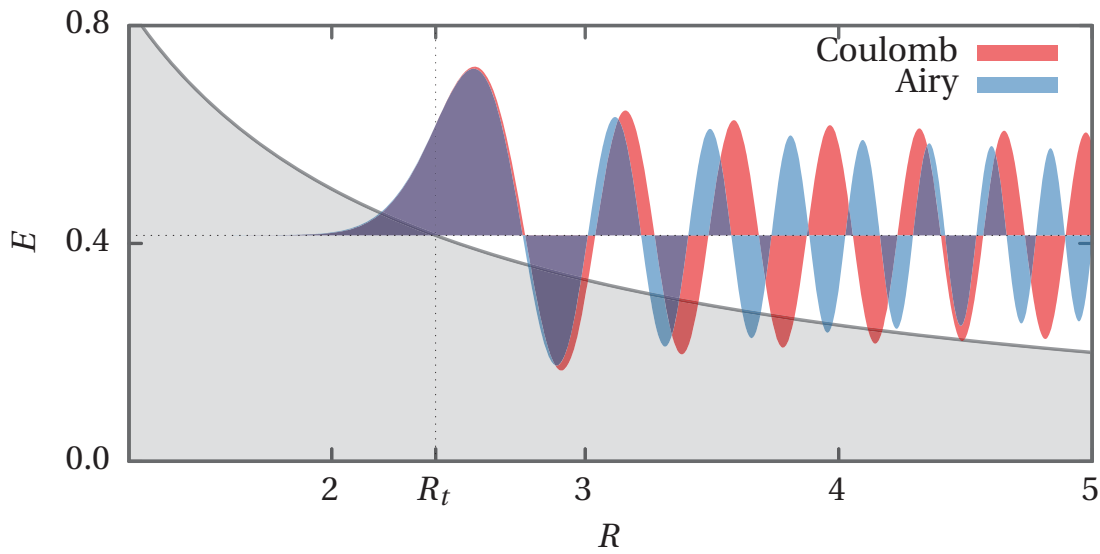


Figure C.1: Airy function in a Coulomb potential $U(R) = 1/R$, based on a linear expansion of the potential around $R_t = 2.4$. Also shown is the corresponding Coulomb wave. They agree well around the turning point R_t .

where

$$\alpha = (-2MU'(R_t))^{1/3}. \quad (\text{C.7})$$

The eigenvalue problem (C.2) can be written in terms of the z variable as

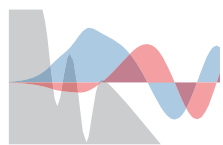
$$\left[\frac{d^2}{dz^2} - z \right] g(R, k) = 0. \quad (\text{C.8})$$

This is the Airy equation, the solution of which is the Airy function¹ [22]

$$g(R) = AAi(z), \quad (\text{C.9})$$

where A is a normalization constant. In the following we will determine this normalization constant by relating it to the normalization condition (C.3). The problem is that the Airy solution is only valid near the turning point, and not at $R \rightarrow \infty$ where the normalization condition applies. To

¹The second order differential equation (C.2) of course have two linearly independent solutions. We choose to consider the regular solution, which is the Airy function. Since $Ai(\infty) = 0$ we should in principle consider the limit $R \rightarrow -\infty$ instead of $R = 0$, but the numerical difference between these is small.



connect these conditions we will use WKB theory [see App. B]. The WKB wave function is of the form

$$g(R) = \frac{C_1}{p^{1/2}(R)} e^{i \int_{R_t}^R dR' p(R')} + \frac{C_2}{p^{1/2}(R)} e^{-i \int_{R_t}^R dR' p(R')} \quad (\text{C.10})$$

where the classical momentum given by

$$p(R) = \sqrt{2M(E_R - U(R))}. \quad (\text{C.11})$$

We consider the regular solution $g(R=0) = 0$, and for this it can be shown [14, §47] that in the classically allowed region

$$g(R) = \frac{C}{p^{1/2}(R)} \cos \left(\left| \int_{R_t}^R dR' p(R') \right| - \frac{\pi}{4} \right). \quad (\text{C.12})$$

This we want to match with the asymptotic normalization condition (C.3). The phase of the WKB approximation (C.12) is not going to match that of the exact solution, so will not care about this, only the constant in front of the trigonometric function will concern us here. We have that $p(R)|_{R \rightarrow \infty} = k$, so matching the normalization condition with the WKB wave function yields

$$C = 2\sqrt{k}. \quad (\text{C.13})$$

Now we wish to match the WKB wave function (C.12) to the Airy function (C.9). The problem is that the Airy function is only accurate near the turning point, but here the WKB wave function is not valid. We will therefore do the matching in a region close to, but still far away from the turning point. First we expand the classical momentum around the turning point (remember that $\Delta R = R - R_t$)

$$p_R = \sqrt{\Delta R} \sqrt{2M} \sqrt{\frac{E_R - \sum_{n=0}^{\infty} \frac{1}{n!} U^{(n)}(R_t) \Delta R^n}{\Delta R}} \quad (\text{C.14a})$$

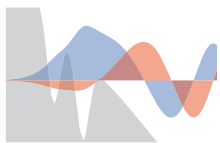
$$= \sqrt{\Delta R} \sqrt{2M} \left(\sqrt{-U'(R_t)} + O(\Delta R) \right) \quad (\text{C.14b})$$

$$= \alpha^{3/2} \sqrt{\Delta R} + O(\Delta R^{3/2}) \quad (\text{C.14c})$$

$$\int_{R_t}^R dR p_R = \frac{2}{3} (\alpha \Delta R)^{3/2} + O(\Delta R^{5/2}). \quad (\text{C.14d})$$

The WKB wave function (C.12) can then be written near the turning point

$$g(R) = \frac{2\sqrt{k}}{(\alpha^3 \Delta R)^{1/4}} \cos \left(\left| \frac{2}{3} (\alpha \Delta R)^{3/2} \right| - \frac{\pi}{4} \right). \quad (\text{C.15})$$



We will match this to the asymptotic of the Airy function (C.9) for large arguments [22]

$$g(R)|_{R \rightarrow \infty} = A \frac{\cos\left(\frac{2}{3}\alpha^{3/2}(\Delta R)^{3/2} - \frac{1}{4}\pi\right)}{\sqrt{\pi}(\alpha\Delta R)^{1/4}}. \quad (\text{C.16})$$

Matching these yields

$$A = 2\sqrt{\frac{k\pi}{\alpha}}. \quad (\text{C.17})$$

Figure C.1 shows an Airy function with this normalization in a Coulomb potential compared to the Coulomb wave that is the exact solution of Eq. (C.2) for that potential.

Delta Limit

From Ref. [38] we have the following representation of the delta function in terms of Airy functions

$$\delta(x) = \lim_{\varepsilon \rightarrow 0} \frac{1}{\varepsilon} \text{Ai}\left(\frac{x}{\varepsilon}\right). \quad (\text{C.18})$$

We can write the solution (C.9) as

$$g(R) = 2\sqrt{\frac{k\pi}{\alpha^3}} \frac{1}{\alpha^{-1}} \text{Ai}\left(-\frac{\Delta R}{\alpha^{-1}}\right). \quad (\text{C.19})$$

In the limit $M \rightarrow \infty$ we have $\alpha^{-1} \rightarrow 0$, and thus obtain

$$g(R) = 2\sqrt{\frac{k\pi}{\alpha^3}} \delta(\Delta R). \quad (\text{C.20})$$

If we note that

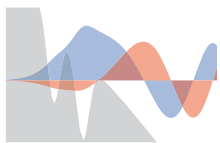
$$\frac{dR}{dk} = \frac{k}{MU'(R_t)}, \quad (\text{C.21})$$

this can be written as

$$g(R) = \sqrt{-2\pi \frac{dR}{dk}} \delta(R - R_t). \quad (\text{C.22})$$

Using this approximation for $g(R)$ the integral (C.1) can be approximately evaluated

$$\tilde{C}(k) = \sqrt{-2\pi \frac{dR_t}{dk}} \varphi(R_t). \quad (\text{C.23})$$



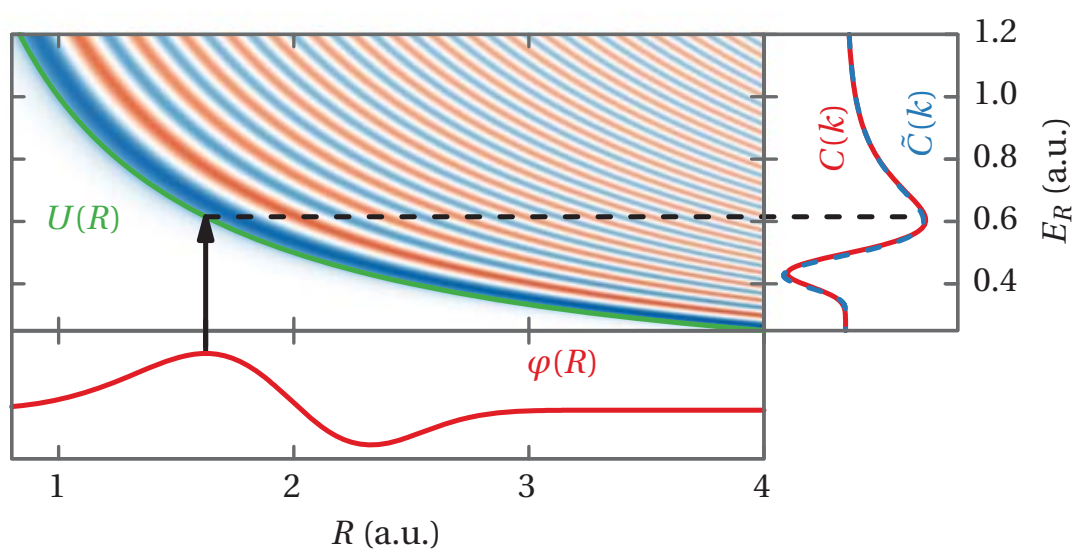
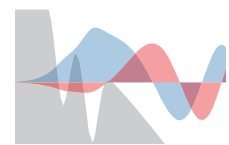


Figure C.2: An example function $\varphi(R) = e^{3 \cdot (R-1.8)^2} - e^{6 \cdot (R-2.2)^2}$. Solid (red) line: Direct numerical projection of $\varphi(R)$ on Coulomb waves with $M = 1836/2$. Dashed dotted (blue) line: Approximation to this based on Eq. (C.23).



D Continuum Normalization

In this Appendix we will show that the asymptotic normalization condition

$$g(R, k)|_{R \rightarrow \infty} = 2 \sin(kR + \delta_k) \quad (\text{D.1})$$

is equivalent with the delta normalization condition

$$\int_0^\infty g(R, k)g(R, k') = 2\pi\delta(k - k'), \quad (\text{D.2})$$

where $g(R, k)$ is a continuum state solution of the eigenvalue problem

$$\left(-\frac{1}{2M} \frac{d^2}{dR^2} + U(R) \right) g(R, k) = E g(R, k), \quad (\text{D.3})$$

with $E = \frac{k^2}{2M}$ and the boundary condition $g(R=0, k) = 0$. It is assumed that $U(R)|_{R \rightarrow \infty} = 0$. The derivation in this appendix was inspired by a note by Haruhide Miyagi.

We start by considering two solutions g_k and $g_{k'}$ to Eq. (D.3) with energies E and E' . Equation (D.3) for each of these states is multiplied with the other state, then these are subtracted from each other to obtain

$$-\frac{1}{2M} \left(g_{k'} \frac{d^2}{dR^2} g_k - g_k \frac{d^2}{dR^2} g_{k'} \right) = (E - E') g_k g_{k'}, \quad (\text{D.4})$$

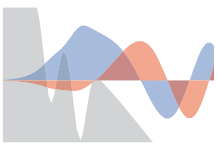
where we introduced the short-hand notation $g_k = g(R, k)$. Now integrating this over R yields

$$(E - E') \int_0^\infty g_k g_{k'} dR = \frac{1}{2M} \lim_{R \rightarrow \infty} \left(g_k \frac{d}{dR} g_{k'} - g_{k'} \frac{d}{dR} g_k \right). \quad (\text{D.5})$$

Inserting the asymptotic normalization condition (D.1) and applying trigonometric addition rules yields

$$\int_0^\infty g_k g_{k'} dR = \frac{1}{k^2 - k'^2} \lim_{R \rightarrow \infty} \left(g_k \frac{d}{dR} g_{k'} - g_{k'} \frac{d}{dR} g_k \right) \quad (\text{D.6})$$

$$= 2 \lim_{R \rightarrow \infty} \left[\frac{\sin((k - k')R + \delta_k - \delta_{k'})}{k - k'} - \frac{\sin((k + k')R + \delta_k + \delta_{k'})}{k + k'} \right]. \quad (\text{D.7})$$



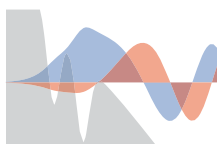
By using the representation of the delta function as the limit of a sine function

$$\delta(x) = \lim_{a \rightarrow \infty} \frac{\sin ax}{\pi x} \quad (\text{D.8})$$

we obtain that

$$\int_0^\infty g_k g_{k'} dR = 2\pi \delta(k - k'), \quad (\text{D.9})$$

which establishes the equivalence of Eqs. (D.1) and (D.2).



E Soft-coulomb Potential

We have used soft-coulomb potentials of the form [34–36]

$$V(z, R) = - \sum_{\pm} \frac{1}{\sqrt{\left(z \pm \frac{R}{2}\right)^2 + a(R)}}, \quad (\text{E.1})$$

where the parameter $a(R)$ has been chosen such that $U(R)$ and $U(R) + E_e(R)$ coincides with a given set of BO curves, where the electronic energy is found by solving the problem

$$[H - E_e(R)] \psi_e(z; R) = 0, \quad (\text{E.2})$$

where

$$H = -\frac{1}{2} \frac{d^2}{dz^2} + V(z, R). \quad (\text{E.3})$$

Given two sets of BO curves $U(R)$ and $U_l(R)$, this could, e.g., be the BO curves of H_2 and H_2^+ , we thus want to find values of $a(R)$ such that $E_e(R)$ is the same as the difference of the BO potentials

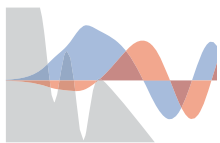
$$E_{\text{target}}(R) = U_l(R) - U(R). \quad (\text{E.4})$$

In the following we consider a given value of R , and will therefore drop it in all notation. We can consider the electronic energy of the ground state as a function of the softening parameter $E_e^0(a)$. Consider the function

$$f(a) = E_{\text{target}} - E_e^0(a). \quad (\text{E.5})$$

We wish to find a zero for this function. For this we can use the Newton-Raphson method, where the following sequence is evaluated until convergence

$$a_{n+1} = a_n - \frac{f(a_n)}{f'(a_n)}. \quad (\text{E.6})$$



The function $f(a_n)$ can be evaluated by diagonalizing the Hamiltonian of Eq. (E.2). The derivative $f'(a_n)$ is slightly more tricky. We could use a numerical derivative, as discussed right after Eq. (6.105), but there is another way to determine this derivative. Consider Eq. (E.2) derived with respect to a

$$[H(a) - E_e(a)] \frac{\partial}{\partial a} \psi_e(z, a) + \left[\frac{\partial}{\partial a} H(a) - E'_e(a) \right] \psi_e(z, a) = 0. \quad (\text{E.7})$$

By projecting this with $\int_{-\infty}^{\infty} dz \psi_e(z, a)$ and using the hermicity of $H(a)$ we obtain

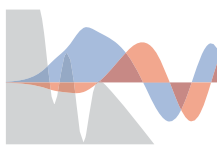
$$\int \psi_e(z, a) \left[\frac{\partial}{\partial a} V(z, a) - E'_e(a) \right] \psi_e(z, a) dz = 0, \quad (\text{E.8})$$

which assuming the normalization $\int \psi_e^2(z, a) dz = 1$ can be written

$$E'_e(a) = \int \psi_e^2(z, a) \frac{\partial}{\partial a} V(z, a) dz. \quad (\text{E.9})$$

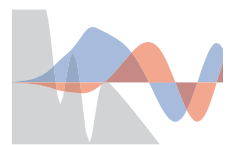
Note that this is a version of the Hellman-Feynman theorem. We can thus calculate the Newton-Raphson steps by finding the smallest eigenvalue of $H(a_n)$ and the corresponding eigenvector and using Eq. (E.9).

Since the potential $V(z, R)$ should be smooth in R , the same should be the case for softening parameter $a(R)$. It can therefore be a good idea to use the $a(R)$ obtained at one value of R as initial guess for $a(R)$ at the next R considered.

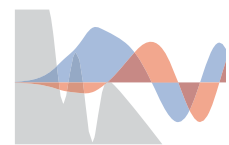


Bibliography

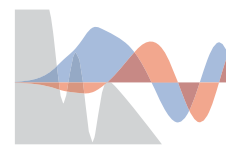
- [1] J. Svensmark, O. I. Tolstikhin, and L. B. Madsen, *Coulomb and dipole effects in tunneling ionization of molecules including nuclear motion*, Phys. Rev. A **91**, 013408 (2015).
- [2] J. Svensmark, O. I. Tolstikhin, and L. B. Madsen, *Theory of dissociative tunneling ionization*, Phys. Rev. A **93**, 053426 (2016).
- [3] F. Krausz and M. Ivanov, *Attosecond physics*, Rev. Mod. Phys. **81**, 163 (2009).
- [4] A. McPherson, G. Gibson, H. Jara, U. Johann, T. S. Luk, I. A. McIntyre, K. Boyer, and C. K. Rhodes, *Studies of multiphoton production of vacuum-ultraviolet radiation in the rare gases*, J. Opt. Soc. Am. B **4**, 595 (1987).
- [5] P. B. Corkum, *Plasma perspective on strong field multiphoton ionization*, Phys. Rev. Lett. **71**, 1994 (1993).
- [6] L. V. Keldysh, *Ionization in the Field of a Strong Electromagnetic Wave*, Zh. Eksp. Teor. Fiz. **47**, 1945 (1964), [Sov. Phys. JETP **20**, 1307 (1965)].
- [7] A. J. F. Siegert, *On the Derivation of the Dispersion Formula for Nuclear Reactions*, Phys. Rev. **56**, 750 (1939).
- [8] O. I. Tolstikhin, V. N. Ostrovsky, and H. Nakamura, *Siegert pseudostate formulation of scattering theory: One-channel case*, Phys. Rev. A **58**, 2077 (1998).
- [9] P. A. Batishchev, O. I. Tolstikhin, and T. Morishita, *Atomic Siegert states in an electric field: Transverse momentum distribution of the ionized electrons*, Phys. Rev. A **82**, 023416 (2010).



- [10] O. I. Tolstikhin and L. B. Madsen, *Retardation Effects and the Born-Oppenheimer Approximation: Theory of Tunneling Ionization of Molecules Revisited*, Phys. Rev. Lett. **111**, 153003 (2013).
- [11] O. I. Tolstikhin, T. Morishita, and L. B. Madsen, *Theory of tunneling ionization of molecules: Weak-field asymptotics including dipole effects*, Phys. Rev. A **84**, 053423 (2011).
- [12] O. I. Tolstikhin, L. B. Madsen, and T. Morishita, *Weak-field asymptotic theory of tunneling ionization in many-electron atomic and molecular systems*, Phys. Rev. A **89**, 013421 (2014).
- [13] O. I. Tolstikhin, *Siegert-state expansion for nonstationary systems: Coupled equations in the one-channel case*, Phys. Rev. A **73**, 062705 (2006).
- [14] L. D. Landau and E. M. Lifshitz, *Quantum Mechanics, Non-Relativistic Theory* (Pergamon, Oxford, 1977).
- [15] D. J. Griffiths, *Introduction to Quantum Mechanics* (Pearson, 2005).
- [16] E. U. Condon, *Nuclear Motions Associated with Electron Transitions in Diatomic Molecules*, Phys. Rev. **32**, 858 (1928).
- [17] E. A. Gislason, *Series expansions for Franck-Condon factors. I. Linear potential and the reflection approximation*, J. Chem. Phys. **58**, 3702 (1973).
- [18] S. Chelkowski, P. B. Corkum, and A. D. Bandrauk, *Femtosecond Coulomb Explosion Imaging of Vibrational Wave Functions*, Phys. Rev. Lett. **82**, 3416 (1999).
- [19] L. P. H. Schmidt, T. Jahnke, A. Czasch, M. Schöffler, H. Schmidt-Böcking, and R. Dörner, *Spatial Imaging of the H_2^+ Vibrational Wave Function at the Quantum Limit*, Phys. Rev. Lett. **108**, 073202 (2012).
- [20] H. Stapelfeldt and T. Seideman, *Colloquium : Aligning molecules with strong laser pulses*, Rev. Mod. Phys. **75**, 543 (2003).
- [21] J. C. Light, I. P. Hamilton, and J. V. Lill, *Generalized discrete variable approximation in quantum mechanics*, The Journal of Chemical Physics **82**, 1400 (1985).



- [22] M. Abramowitz and I. A. Stegun, *Handbook of Mathematical Functions* (Dover Publications Inc., New York, 1972).
- [23] J. T. Muckerman, *Some useful discrete variable representations for problems in time-dependent and time-independent quantum mechanics*, Chem. Phys. Lett. **173**, 200 (1990).
- [24] DLMF, *NIST Digital Library of Mathematical Functions*, <http://dlmf.nist.gov/>, online version of [22].
- [25] O. I. Tolstikhin and C. Namba, *CTBC. A program to solve the collinear three-body Coulomb problem. Bound states and scattering below the three-body disintegration threshold*, Tech. Rep. NIFS-779 (National Institute for Fusion Science, 2003).
- [26] O. I. Tolstikhin, S. Watanabe, and M. Matsuzawa, 'Slow' variable discretization: a novel approach for Hamiltonians allowing adiabatic separation of variables, J. Phys. B **29**, L389 (1996).
- [27] H. Wind, *Electron Energy for H_2^+ in the Ground State*, J. Chem. Phys. **42**, 2371 (1965).
- [28] W. Kolos and L. Wolniewicz, *Accurate Adiabatic Treatment of the Ground State of the Hydrogen Molecule*, J. Chem. Phys. **41**, 3663 (1964).
- [29] K. Pachucki, *Born-Oppenheimer potential for H_2* , Phys. Rev. A **82**, 032509 (2010).
- [30] V. H. Trinh, O. I. Tolstikhin, L. B. Madsen, and T. Morishita, *First-order correction terms in the weak-field asymptotic theory of tunneling ionization*, Phys. Rev. A **87**, 043426 (2013).
- [31] H. Ohmura, N. Saito, and T. Morishita, *Quantum control of molecular tunneling ionization in the spatiotemporal domain*, Phys. Rev. A **83**, 063407 (2011).
- [32] H. Li, D. Ray, S. De, I. Znakovskaya, W. Cao, G. Laurent, Z. Wang, M. F. Kling, A. T. Le, and C. L. Cocke, *Orientation dependence of the ionization of CO and NO in an intense femtosecond two-color laser field*, Phys. Rev. A **84**, 043429 (2011).
- [33] J. Wu, L. P. H. Schmidt, M. Kunitski, M. Meckel, S. Voss, H. Sann, H. Kim, T. Jahnke, A. Czasch, and R. Dörner, *Multiorbital Tunneling Ionization of the CO Molecule*, Phys. Rev. Lett. **108**, 183001 (2012).



- [34] K. C. Kulander, F. H. Mies, and K. J. Schafer, *Model for studies of laser-induced nonlinear processes in molecules*, Phys. Rev. A **53**, 2562 (1996).
- [35] B. Feuerstein and U. Thumm, *Fragmentation of H_2^+ in strong 800-nm laser pulses: Initial-vibrational-state dependence*, Phys. Rev. A **67**, 043405 (2003).
- [36] S. Saugout, C. Cornaggia, A. Suzor-Weiner, and E. Charron, *Ultrafast Electronuclear Dynamics of H_2 Double Ionization*, Phys. Rev. Lett. **98**, 253003 (2007).
- [37] E. Condon, *A Theory of Intensity Distribution in Band Systems*, Phys. Rev. **28**, 1182 (1926).
- [38] O. Vallée and M. Soares, *Airy Functions and Applications to Physics*, EBSCO ebook academic collection (World Scientific, 2004).

